MECHANICAL BEHAVIOR OF LOW DENSITY POLYMERIC FOAMS UNDER MULTIPLE LOADING AND UNLOADING

by

Umud Esat Öztürk

B.S., Mechanical Engineering, Boğaziçi University, 1998

M.S., Mechanical Engineering, Boğaziçi University, 2001

Submitted to the Institute for Graduate Studies in
Science and Engineering in partial fulfillment of
the requirements for the degree of
Doctor of Philosophy

Graduate Program in Mechanical Engineering

Boğaziçi University

2008

ACKNOWLEDGEMENTS

This study has been supported by Boğaziçi University Research Found through grant 07A–604 D and the Research and Development Center of Arçelik A.Ş. I am indebted to Boğaziçi University for the numerical analysis and to Arçelik A.Ş. for the experimental work.

I would like to express my gratitude to my thesis supervisor, Professor Günay Anlaş for his advice, support, encouragement, and enthusiasm during this study. It was a pleasure to know him and to work with him.

I wish to thank Mr. Yasin Yılmaz, Mr. Murat Tursun, and all other fellow graduate students, for their friendly support and motivation during long winter nights throughout my PhD studies.

I would like to thank Mr. Emin Bulak, Washing Machine Product Development Manager and Mr. Ertan Çetinkaya, Dryer Product Development Manager for granting me the chance to engage in this study. I am thankful to Mr. Gürhan Kuzgun, Mr. Ömer Akbaş, Mrs. Sibel Odabaş, Dr. Can Meydanlı, and Dr. Osman G. Ersoy from Research and Development Center, and Mr. İbrahim Yıldırım from Washing Machine Product Development Department of Arçelik A. Ş. for their help and advice for the experimental studies, and further many thanks to those who helped me greatly with utilizing laboratory equipment, computer, and software for making them available when required.

I would also like to thank Professor Akın Tezel and Professor Ali Rana Atılgan, members of my thesis committee, for their contributions and kind advices throughout my PhD study, and Assistant Professor Nuri Ersoy and Assistant Professor Hilmi Luş for their helpful comments and review of the thesis.

Finally, I would like to thank my parents for growing me in such a lovely environment and to let me focus on my academic career, and for their continuous support and encouragement.

ABSTRACT

MECHANICAL BEHAVIOR OF LOW DENSITY POLYMERIC FOAMS UNDER MULTIPLE LOADING AND UNLOADING

In this thesis, mechanical behavior and energy absorption characteristics of low density polymeric foams under multiple loading and unloading are investigated for uniaxial and hydrostatic compression, uniaxial tension, simple shear, and cylinder and block indentation.

Constitutive models and energy absorption diagrams available in literature for uniaxial compressive loading are reviewed. A new phenomenological constitutive model for accurate calculation of load, deformation, and absorbed energy is proposed for multiple loading and unloading. Results of the available and the new models are compared to those of experiments for expanded polystyrene (EPS) and polyethylene (PE) foams. A design procedure for multiple compressive loading and unloading is presented.

A drop test rig for measuring uniaxial compressive behavior of foams at high loading speed and a hydrostatic compression test setup to study the mechanical behavior of foams under multiple hydrostatic loading and unloading are built. Tools to be used with Zwick Z020 universal tensile testing machine are prepared for uniaxial tension, simple shear, and cylinder and block indentation tests. Stress–strain results are presented for EPS and PE foam specimens.

Finite element simulations of EPS and PE foam specimens under multiple loading and unloading for uniaxial and hydrostatic compression, uniaxial tension, simple shear, and cylinder and block indentation are performed using Abaqus finite element package for volumetric and isotropic hardening. The results of finite element simulations are compared to those of experiments.

ÖZET

DÜŞÜK YOĞUNLUKLU POLİMER KÖPÜK MALZEMELERİN BİRDEN FAZLA YÜKLEME ALTINDAKİ MEKANİK DAVRANIŞI

Bu çalışmada, düşük yoğunluklu polimer köpük malzemelerin, tek eksen ve hidrostatik basma, tek eksen çekme, basit kayma, silindir ve blok basma yükleme durumları için birden fazla yükleme altındaki mekanik davranışı ve enerji sönümleme özellikleri incelenmiştir.

Literatürdeki tek eksen basma yükü altındaki köpük malzemeler için geliştirilmiş bünye modelleri ve enerji sönümleme diyagramları incelenmiştir. Tek eksen basma durumunda birden fazla yükleme ve boşaltma için kuvvet, deformasyon ve sönümlenen enerjinin doğru bir şekilde hesaplanmasında kullanılmak üzere yeni bir bünye modeli önerilmiştir. Mevcut ve yeni modelin sonuçları, şişirilmiş polistiren (EPS) ve polietilen (PE) köpük malzemeleri için deneysel sonuçlar ile karşılaştırılmıştır. Yeni model kullanılarak bir tasarım prosedürü önerilmiştir.

Köpük malzemelerin yüksek hızda tek eksen basma durumundaki ve düşük hızda hidrostatik basma durumunda çok sayıda yükleme ve boşaltma altındaki davranışlarını ölçmek için test düzenekleri kurulmuştur. Zwick Z020 çekme test cihazında tek eksen çekme, basit kayma, silindir ve blok basma deneylerini yapabilmek için aparatlar hazırlanmış ve EPS ve PE köpük malzemeler için gerilme ve uzama sonuçları sunulmuştur.

Sonlu elemanlar yöntemi ile tek eksen ve hidrostatik basma, tek eksen çekme, basit kayma, silindir ve blok basma durumlarında çok sayıda yükleme deneyleri simülasyonu, volümetrik ve izotropik sertleşme için Abaqus sonlu elemanlar paket programı kullanılarak yapılmıştır. Simülasyon sonuçları, deneysel sonuçlar ile karşılaştırılmıştır.

TABLE OF CONTENTS

LIST OF FIGURES

LIST OF TABLES

LIST OF SYMBOLS / ABBREVIATIONS

A	Size of the horizontal axis of the yield ellipse
B	Size of the vertical axis of the yield ellipse
E	Elastic modulus
E_0	Initial elastic modulus
F	Yield surface function
F_0	Initial value of the yield surface function
G	Flow potential
k	Compression yield stress ratio
k_t	Hydrostatic yield stress ratio
M	Mass
P	Potential energy
p	Hydrostatic pressure stress
p_0	Center of the yield ellipse
p_c	Yield stress in hydrostatic compression
p_c^0	Initial yield stress in hydrostatic compression.
p_t	Strength of material in hydrostatic tension
q	Von Mises stress
S12	Shear stress
W	Absorbed energy
α	Shape factor of the yield ellipse
ε	Strain
ε_i	Incident strain
ε_r	Reflected strain
ε_t	Transmitted strain
$\dot{\varepsilon}$	Strain rate
$\dot{\varepsilon}_0$	Quasi–static strain rate

$\dot{\varepsilon}^{pl}$	Plastic strain rate
ε_{vol}^{pl}	Volumetric compacting plastic strain
ε_{axial}^{pl}	Axial plastic strain
ε_{nom}	Engineering strain
υ	Poisson's ratio
υ_p	Poisson's ratio for plastic region
ρ	Relative density
σ	Stress
σ_c^0	Initial yield stress in uniaxial compression
σ_m	Mean stress
σ_{nom}	Engineering stress
σ_Y	Yield stress

EPS	Expanded polystyrene
FE	Finite elements
LVDT	Linear voltage displacement transducer
PE	Polyethylene
SEM	Scanning electron microscope
SPHB	Split Hopkinson pressure bar

1. INTRODUCTION

Low density polymeric foams are extensively used as energy absorbing materials in many applications because they can dissipate large amount of impact energy with low reaction forces. They are cheap, light and suitable for mass production. Design guides prepared for foams and studies available in the literature are mainly based on single compressive loading. When a helmet or foam padding in a car is subjected to impact loading, it is replaced by a new one. Foam is only loaded once in those applications, therefore unloading behavior and energy absorbing capability of the previously loaded foam part is not important. On the other hand, a packaged consumer good travels to many destinations after it leaves the plant, and the low density polymeric foam used in packaging can be subjected to impact loading many times before it reaches the consumer. During its travel, it may fall on the ground and may be subjected to impact loadings many times. Therefore there is a need to know the mechanical behavior and the energy absorbing characteristics under multiple loading and unloading.

Among many kinds of low density polymeric foams, expanded polystyrene (EPS) and polyethylene (PE) are the most used ones in packaging industry. EPS can be produced in complex shapes by molding. PE is produced by extrusion and PE sheets are cut at different geometries for packaging. EPS and PE foams with 3 different densities (EPS 12, EPS 20, EPS 30 and PE 24, PE 32 and PE 58) are used in this study. The numbers represent densities in kg/m^3. EPS used in this study is obtained from BASF and molded by a local manufacturer; PE used in this study is directly obtained from DOW (Figure 1.1). Glass transition temperatures of solid polymer polystyrene (PS) and polyethylene (PE) are around 373 K and 285 K respectively [1]. EPS foam is more crushable compared to PE foam at room temperature.

A typical stress–strain curve of low density polymeric foam for single compressive loading-unloading and double loading-unloading is given for EPS 30 in Figure 1.2. Mechanical behavior of EPS 30 under uniaxial compression can be explained in three regimes: in the elastic regime, EPS 30 exhibits a linear elastic behavior and cell walls bend elastically up to 3 per cent strain; from 3 per cent to 60 per cent strain, cell walls start to collapse with large amount of gas expelled from cells, this plateau regime is characterized by small stress increase at large strain increase; after 60 per cent strain, cell walls contact each other, and stress increases sharply during densification as shown in Figure 1.2 (a) [1]. In Figure 1.2 (b), stress-strain curve for EPS 30 that is loaded twice is given: first, the specimen is compressed up to 40 per cent strain and unloaded to 24 per cent residual strain; then, it is compressed up to 90 per cent strain and unloaded to 48 per cent residual strain. During the second loading, the load increases elastically up to 40 per cent strain, and continues non-elastically afterwards. In the non-elastic portion of the second loading from 40 to 90 per cent strain, EPS 30 follows the same loading curve of the first loading as if it were never unloaded before.

Designers should pay attention that a foam package is not compressed until densification region to avoid large stress that can result in damage. It is clear from Figure 1.2 (b) that EPS 30 may stay in plateau region under first loading but it can go into densification region in subsequent loadings, and high stress levels can be reached.

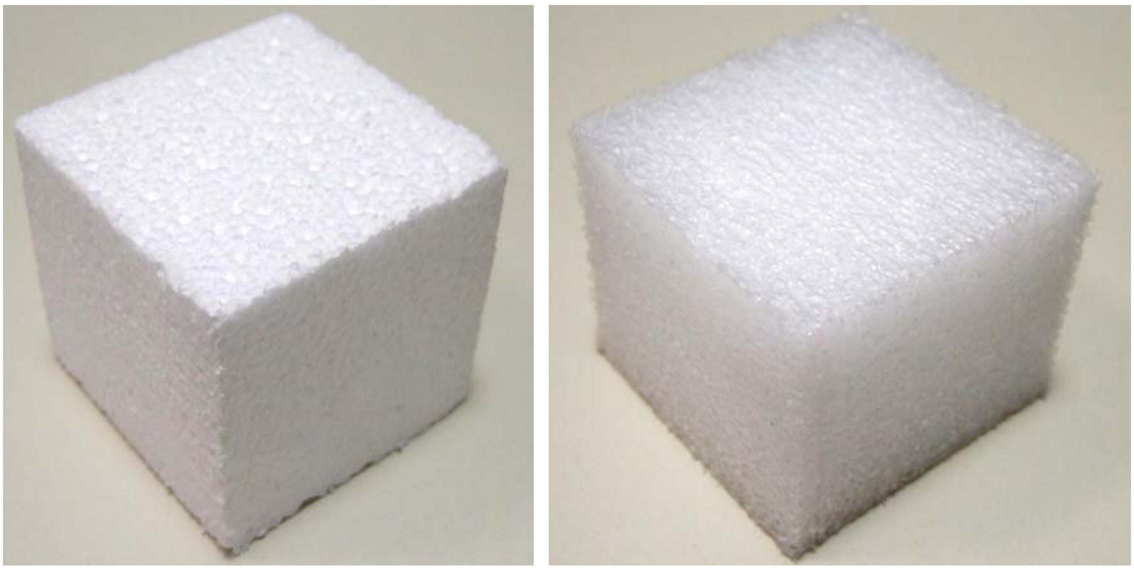

(a) (b)

Figure 1.1. Specimens: a) EPS b) PE 58

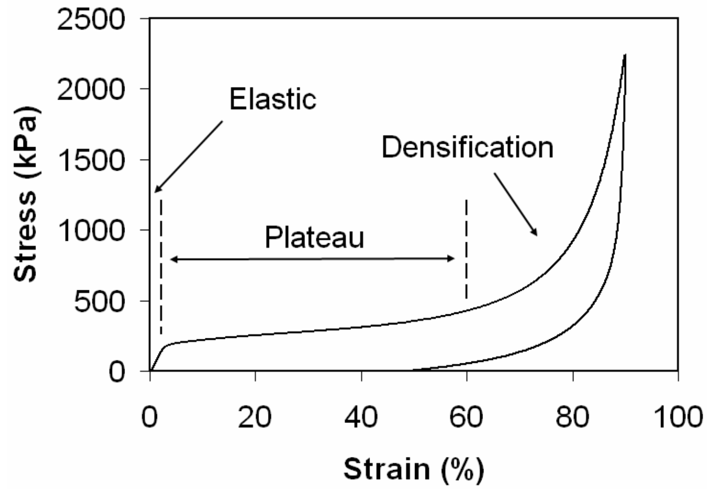

(a)

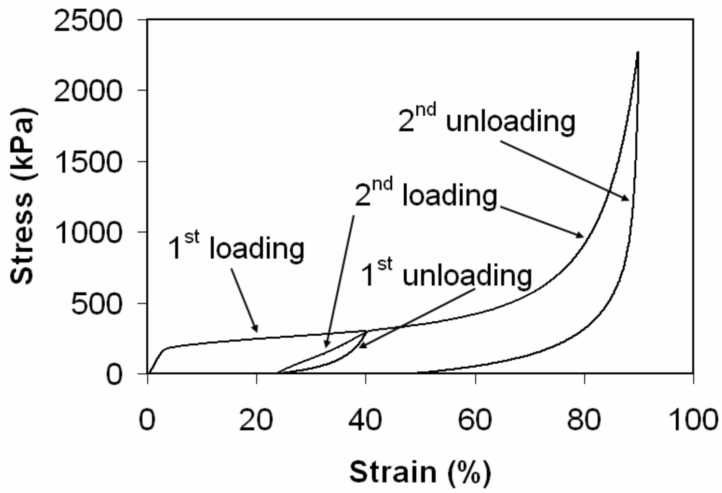

(b)

Figure 1.2. (a) Typical stress–strain curve of EPS 30 foam under compressive loading-unloading (b) Stress–strain curve of EPS 30 under double compressive loading-unloading (compression direction is taken as positive)

Scanning Electron Microscope (SEM) photographs of cellular structures of EPS and PE foams are taken both at undeformed state and at compressed state. In Figure 1.3, SEM photographs of EPS 12 at undeformed and 80 per cent compressed states, and in Figure 1.4, SEM photographs of PE 24 at undeformed, 40 and 80 per cent compressed states are given. The collapsed cell walls can be seen in compressed state SEM photographs.

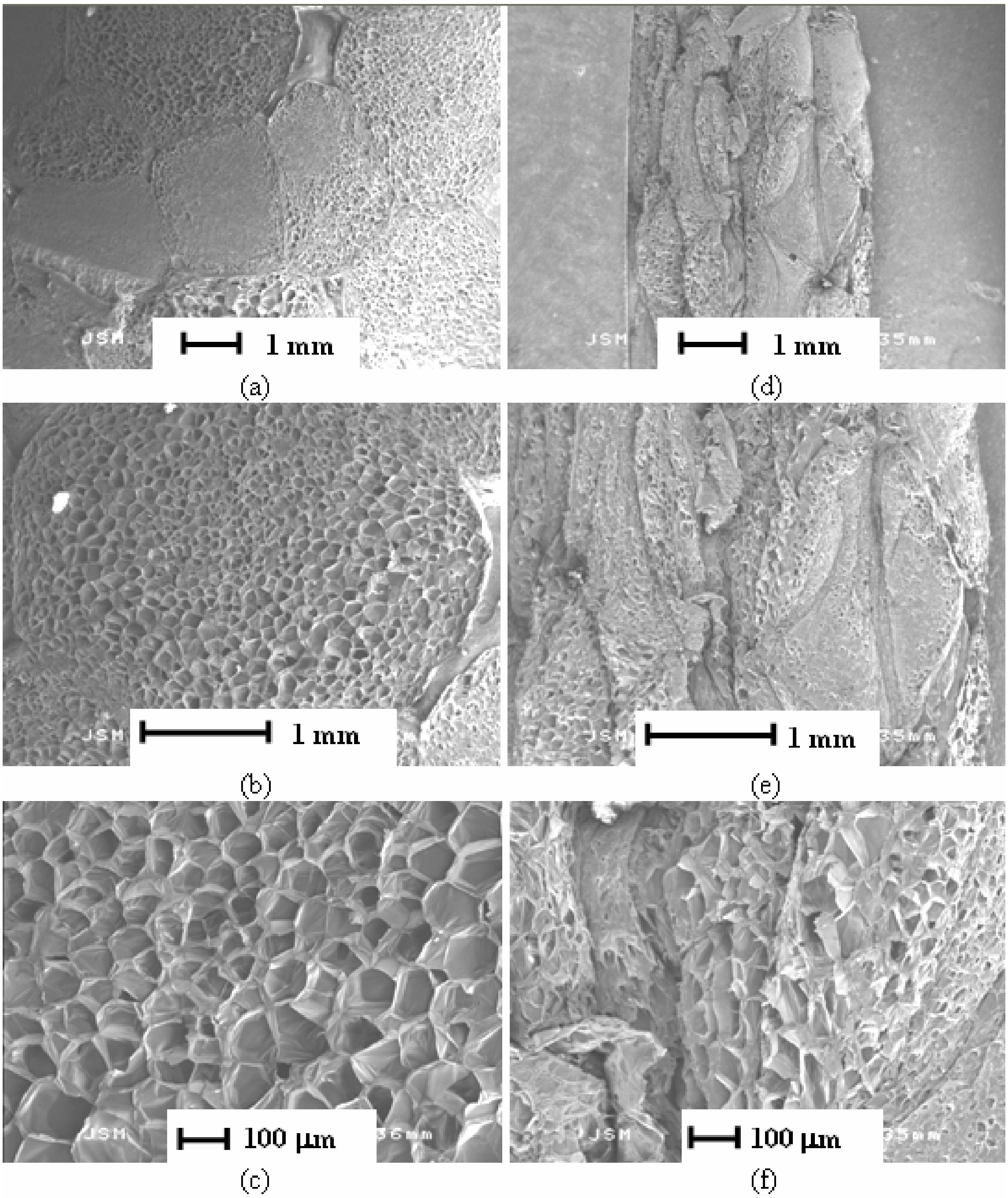

Figure 1.3. SEM photographs of: a) EPS 12, 15 times enlarged, b) EPS 12, 30 times enlarged, c) EPS 12, 100 times enlarged, d) EPS 12, compressed at 80 per cent, 15 times enlarged, e) EPS 12, compressed at 80 per cent, 30 times enlarged, f) EPS 12, compressed at 80 per cent, 100 times enlarged

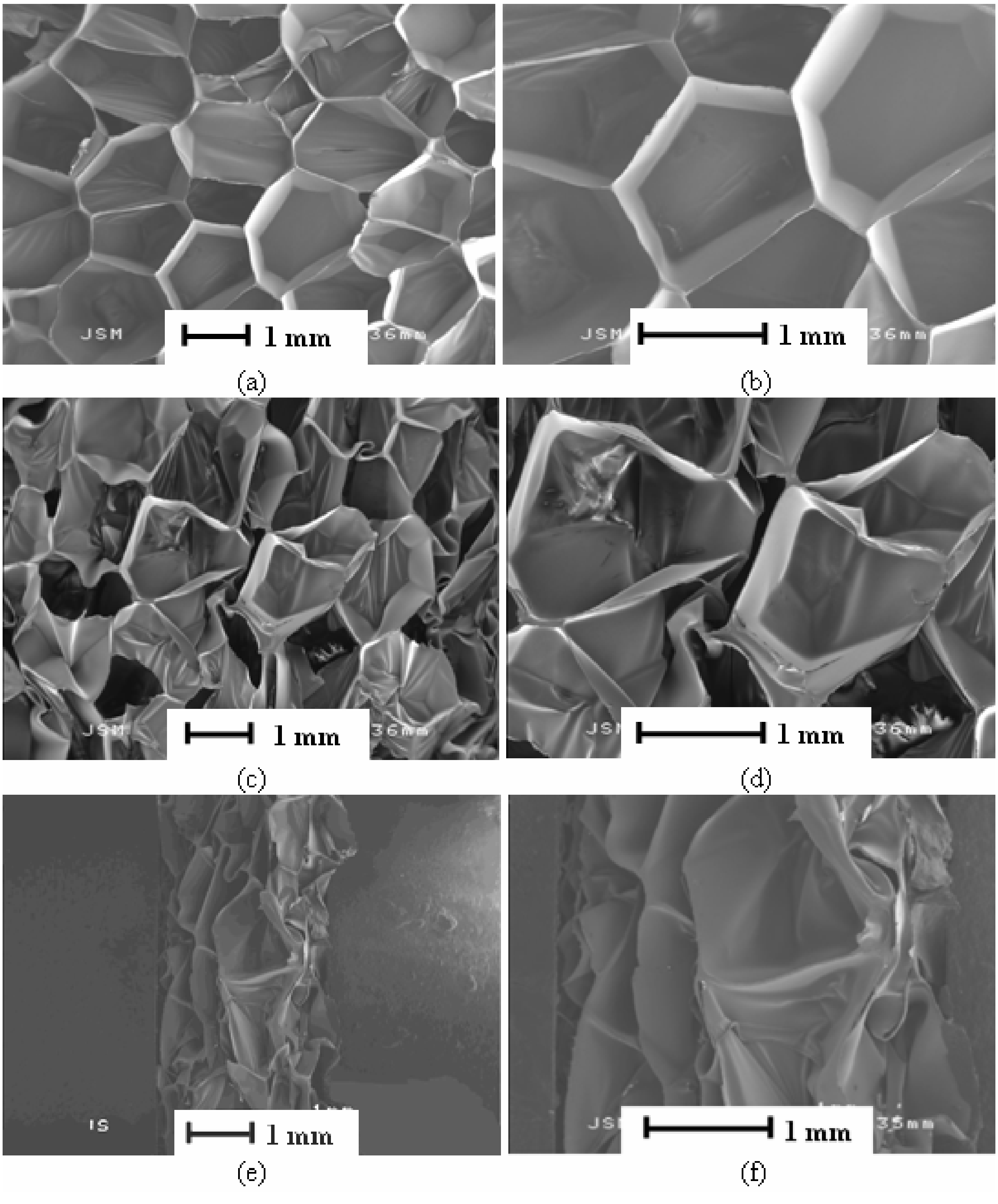

Figure 1.4. SEM photographs of: a) PE 24, 15 times enlarged, b) PE 24, 30 times enlarged, c) PE 24, compressed at 40 per cent, 15 times enlarged, d) PE 24, compressed at 40 per cent, 30 times enlarged, e) PE 24, compressed at 80 per cent, 15 times enlarged, f) PE 24, compressed at 80 per cent, 30 times enlarged

Mechanical behavior of low density polymeric foams can easily be affected by testing conditions and specimen properties. For the sake of repeatability and accuracy of test results, tests should be performed considering those parameters. There are international standards for uniaxial compressive and tensile testing of foams. Researchers can get use of the previous studies in the literature for testing foams in simple shear, hydrostatic compression, and indentation tests. Foams can be tested in uniaxial compression according to DIN 53421, ASTM C 165-83, and ASTM D 1621-73/79 standards, and in uniaxial tension according to the DIN 53430 standard. Stress–strain response of foams may change depending on the specimen dimensions, ambient temperature, loading speed, loading direction, cell orientation, and aging [1-2]. It is stated in the literature that compressive yield strength of foams may decrease with increasing area of the specimen. It does not change much with the thickness of the specimen [2]. Compressive yield strength usually increases with increasing loading speed and decreasing temperature [1-2]. Compressive yield strength of EPS also depends on the age of the specimen; it increases about 10 per cent in 8 weeks after the production date [2]. Compressive yield strength also depends on the shape, size, and orientation of the cells. Loading direction is important, higher compressive yield strength is obtained along the direction where the cells are stretched [2]. PE sheets are produced by extrusion; hence the cells are oriented along the extrusion direction. During the expansion of EPS foam material inside the mold, the cells close to the mold wall are flattened, and the regions close to the mold walls have higher densities. The regions close to the top and bottom surfaces of PE foam sheets have higher density than the inner regions. Compressive yield strength increases with increasing density, and specimens cut from different locations of the sheet may have different densities and different compressive yield strengths.

1.1. Literature Review

There are many works in the literature that model the mechanical behavior of foam in compression based on macroscopic observations. This approach is often referred as phenomenological constitutive modeling. Microstructures of low density polymeric foams used in packaging like EPS and PE are random, and it is not practically possible to model their mechanical behavior through micro-mechanical models.

There are lots of works for phenomenological constitutive modeling of uniaxial compressive loading in literature but they are not developed and tested for unloading and reloading. If a foam package that is subjected to drops more than once is to be studied, a constitutive model developed for single loading only is not satisfactory. Accurate modeling of unloading is also necessary to determine the residual strain at which subsequent loading starts.

Foams used for energy absorbing purposes are usually loaded at high loading speeds and test rigs are developed to measure the stress–strain response of foams at high strain rates.

Constitutive models for general loading and yield criteria for foams are also available in literature, but most of them have modeled elastic region in loading and unloading as linear without considering hysteresis and other nonlinear effects. The models that considered nonlinear elastic behavior during unloading do not give accurate results for residual deformation. Therefore it is not possible to calculate accurately reloading behavior. Researchers performed multi–axial loading tests such as simple shear, uniaxial tension, hydrostatic compression and tension, and bi-axial and axisymmetric loading to develop failure criteria. Some of them implemented their constitutive model and yield criteria into finite element codes. They have done sphere, cylinder, and block indentation tests to validate their proposed models. All of those studies are for the mechanical behavior of single loading only. They are not developed and tested for reloading. There are very few experimental data about the uniaxial compressive unloading and reloading of foams in literature, but it is not used for developing a constitutive model and failure criteria or for validation of any existing model.

1.1.1. Models Developed for Uniaxial Compression

Foams used for energy absorbing purposes are usually loaded in compression, and models developed for uniaxial compression can successfully be used for calculation of load, deformation, and absorbed energy in most loading cases [2-3].

First constitutive model for polymeric foam under uniaxial compression is presented in 1969 by Rusch [4-6]. Rusch proposed the following relationship for uniaxial compressive loading of foams

$$\sigma = E_0 f(\varepsilon), \tag{1.1}$$

where σ is the stress, E_0 is the initial compressive modulus of the foam, and ε is the non-linear strain. The strain function $f(\varepsilon)$ has the following form

$$f(\varepsilon) = \varepsilon\left(a\varepsilon^{-c} + b\varepsilon^{d}\right), \tag{1.2}$$

where a, b, c, and d are empirically determined constants.

In 1970, Meinecke and Schwaber proposed initial elastic modulus E_0 to be a function of strain rate as [7]

$$\sigma = E_0(\dot{\varepsilon})\, f(\varepsilon), \tag{1.3}$$

with

$$E_0(\dot{\varepsilon}) = K\dot{\varepsilon}^{\alpha}, \tag{1.4}$$

and

$$f(\varepsilon) = \sum_{n=0}^{10} A_n \varepsilon^{n}. \tag{1.5}$$

K and α are constants selected for the strain-rate sensitivity of E_0 as a function of strain rate. The strain function in this model is expressed in terms of polynomials $f(\varepsilon)$ that fit the stress-strain relationship.

In 1974, Nagy et al. [8] modified Meinecke and Schwaber's model, by considering the strain-rate effect with coupling of strain and strain-rate in the following form

$$\sigma = E_0(\dot{\varepsilon}) M(\varepsilon, \dot{\varepsilon}), \tag{1.6}$$

with

$$M(\varepsilon, \dot{\varepsilon}) = \left(\frac{\dot{\varepsilon}}{\dot{\varepsilon}_0} \right)^{n(\varepsilon)}, \tag{1.7}$$

and

$$n(\varepsilon) = a + b\varepsilon . \tag{1.8}$$

$\dot{\varepsilon}_0$ can be either an arbitrary quasi-static strain rate or a referenced strain rate, a and b are empirical constants.

The constitutive models given above are applicable to foams with a given density; they cannot be used to study the effect of density on the stress–strain response under uniaxial compression. In 1992, Sherwood et al. [9] developed the Nagy's model by adding the effects of temperature and density as following

$$\sigma = H(T) G(\rho) M(\varepsilon, \dot{\varepsilon}) f(\varepsilon), \tag{1.9}$$

where $H(T)$ and $G(T)$ are expressed as bi-linear functions of temperature and density respectively. The temperature and density functions are separable and independent. Another modification is also made in the shape function Equation (1.5) by summing the power series beginning with $n = 1$.

Chou et al. [10] proposed in 1998 a constitutive model by taking the temperature and strain rate effects as a coupled, inseparable function $H(\dot{\varepsilon},T)$. The model assumes the following form

$$\sigma = H(\dot{\varepsilon},T)G(\rho)f(\varepsilon), \tag{1.10}$$

where $G(\rho)$ again is a density function.

Gibson and Ashby [1] proposed in 1997 a micro-mechanical model, and its formulation is defined by dividing the compressive stress–strain response into three regions.

In linear elastic region,

$$\sigma_{nom} = E\varepsilon_{nom} \text{ if } \sigma_{nom} \le \sigma_Y , \tag{1.11}$$

in plateau region,

$$\sigma_{nom} = \sigma_Y \text{ if } \varepsilon_Y \le \varepsilon_{nom} \le \varepsilon_D \left(1 - D^{-1/m}\right), \tag{1.12}$$

, and in densification region,

$$\sigma_{nom} = \sigma_Y \frac{1}{D}\left(\frac{\varepsilon_D}{\varepsilon_D - \varepsilon_{nom}}\right)^m \text{ if } \varepsilon > \varepsilon_D \left(1 - D^{-1/m}\right), \tag{1.13}$$

where σ_{nom} and ε_{nom} are engineering stress and engineering strain, respectively, considered positive in compression. The model has five parameters: E, the slope of the elastic part of the curve, σ_Y, the yield stress, ε_D, the strain value characteristic of the densification phase, D and m, empirical constants.

Liu and Subhash [11] proposed in 2004 a constitutive model which is applicable in both compressive and tensile loading as

$$\sigma = A\frac{e^{K\varepsilon}-1}{B+e^{L\varepsilon}}+e^{C}\left(e^{M\varepsilon}-1\right), \tag{1.14}$$

where parameters A, B, C, K, L, and M are constants for a given initial density and strain rate, parameter A has units of stress and other parameters do not have units.

Liu et al. [12] revised Equation (1.14) in 2005 by making the parameters in the constitutive model as a function of density, and proposed the following model

$$\sigma\left(\rho,\varepsilon\right) = A\left(\rho\right)\frac{e^{K(\rho)\varepsilon}-1}{1+e^{L(\rho)\varepsilon}}+e^{C(\rho)}\left(e^{M(\rho)\varepsilon}-1\right), \tag{1.15}$$

In the equation above, the first term is for elastic and plateau regions and the second term accounts for densification region. In their model, the parameters A, C, K, L, and M are density (ρ) dependent. Liu et al. performed multiple loading experiments to produce specimens with higher densities to be able to set the relationship between the parameters used in Equation (1.15) and density, so that they can work with less number of specimens. They also stated that due to the differences between the elastic loading response of a virgin specimen and the deformed specimen, it is not fully justified to consider a deformed specimen to be equivalent to a virgin specimen with increased initial bulk density. Liu et al.'s study does not include unloading behavior of foams. It will be shown later in this study that the elastic behavior in subsequent loadings change a lot from linear to nonlinear as the deformation level increases for EPS and PE. The energy absorbed in elastic region in subsequent loadings is important, especially at high residual strain levels. Therefore the elastic region in multiple loading should be modeled accurately.

Avalle et al. [13] developed the following constitutive model in 2007 for polymeric foams

$$\sigma(\varepsilon) = A\left(1 - e^{(-E/A)\varepsilon(1-\varepsilon)^m}\right) + B\left(\frac{\varepsilon}{1-\varepsilon}\right)^n, \tag{1.16}$$

where A can be considered as the stress level in plateau region, and E as the elastic modulus. They tried to set a relationship between the parameters of their model and the density of foam. They worked with different densities of expanded polypropylene foam (EPP), expanded polystyrene foam (EPS), expanded polyurethane foam (PUR), and polyphenylene oxide/polystyrene foam (PPO/PS).

Constitutive relations developed for compressive loading can be used for energy absorption calculations. Avalle et al. [15] and Miltz et al. [14] calculated energy absorption diagrams and efficiency diagrams defined by Gibson et al. [1] for the case of single loading of foams. They proposed a method for using those diagrams in the design of energy absorbing components. They have not analyzed energy absorption for multiple compressive loading and unloading.

1.1.2. Studies for High Speed Compressive Loading

Energy absorbing cellular materials are usually loaded at high loading speeds. Those loading speeds cannot be reached by conventional universal tensile testing machines. Therefore other kinds of test rigs are needed to test and measure load and deformation of the specimen at strain rates which occur at energy absorbing applications.

Juntikka and Hallstrom [16] developed a weight-balanced drop test rig to evaluate the response of cellular materials subject to dynamic compression. Shim and Yap [17] used a similar drop tower to test foam–plate sandwich systems. At those test rigs, a free falling weight is dropped from a certain height on to the test specimen. Reaction force is measured by accelerometer or load cell, and displacement is measured by laser displacement sensor.

Split Hopkinson pressure bar (SPHB) is another method to test and measure dynamic compressive stress–strain response of most materials. It consists of a striker bar, an incident bar, a transmission bar. The sample is placed between the incident and transmission bars. A gas gun launches the striker bar at the incident bar, and that impact causes an elastic compression wave to travel in the incident bar toward the sample. When the impedance of the sample is less than that of the bars, an elastic tensile wave is reflected into the incident bar and an elastic compression wave is transmitted into the transmission bar. If the elastic stress pulses in the bars are non dispersive, the elementary theory for wave propagation in bars can be used to calculate the sample response from measurements taken with strain gages mounted on the incident and transmission bars. Strain gages mounted on the incident bar measure the incident ε_i and reflected ε_r strain pulses, and strain gages mounted on the transmission bar measure the transmitted ε_t strain pulse [18]. SHPB is successfully used to test metals, concrete, ceramics, and hard polymers. However, if the specimen is a soft material with low mechanical impedance, such as silicone rubbers and polymeric foams, the conventional Split Hopkinson pressure bar technique needs to be modified before reliable dynamic data can be produced [19-23].

1.1.3. Studies for Yield Criteria Under General Loading

Although compression is the dominant loading mode in most of the energy absorbing applications of low density polymeric foams, other loading modes occur even in an indentation type of loading. Hence there is a need for constitutive models and failure criteria for general loading.

Gibson et al. [24] modeled the elastic buckling, plastic yield, and brittle fracture of cellular solids under multi-axial stresses to develop equations describing their failure surfaces in 1989. Triantafillou et al. [25] performed uniaxial, biaxial, axisymmetric, and hydrostatic loading tests, and compared experimental results to those calculated by the model proposed by Gibson et al. [24]. Studies of Gibson et al. [24] and Triantafillou et al. [25] are focused on the failure in single loading; they have not analyzed unloading and reloading behavior of cellular materials. Triantafillou et al. [25] proposed the following yield surface as

$$F \equiv \pm \frac{q}{\sigma_Y} + 0.81\rho\left(\frac{\sigma_m}{\sigma_Y}\right)^2 - 1 \le 0\,, \tag{1.17}$$

where σ_Y is the uniaxial tensile or compressive strength, ρ, the density, q, the Von Mises effective stress, and σ_m, the mean stress. This yield surface assumes that the foams deform by plastic bending of the cell walls under deviatoric loading and stretching of the cell walls under hydrostatic loading. They also analyzed the elastic buckling of cell walls and added a buckling cap to the above yield surface.

Deshpande and Fleck [26] have given experimental data for the multi-axial yield behavior of open and closed cell aluminium alloy foams and proposed the following phenomenological yield surface

$$F \equiv \frac{1}{\left[1+\left(\frac{\alpha}{3}\right)^2\right]} + \left[q^2 + \alpha^2 \sigma_m^2\right] - \sigma_Y^2 \leq 0\,, \tag{1.18}$$

where σ_Y is the uniaxial tensile or compressive yield strength of the foam. The parameter α defines the shape of the yield surface and is the ratio of the shear to hydrostatic yield strengths. Their model is also used in the foam crushable foam model in Abaqus finite element software package.

Zhang et al. [27-28] have performed uniaxial and hydrostatic compression experiments, and shear experiments with polystyrene (PS), polyurethane (PU), and polypropylene (PP) foams. They proposed a yield surface and implemented it into finite element code Ls-Dyna 3D. They used foam specimens with dimensions of 50 × 50 × 50 mm^3 for compression and tension tests, and 50 × 50 × 100 mm^3 for simple shear tests according to ASTM Standard D1621. For simple shear tests, foam specimens are glued in between two L-shaped loading fixtures made of steel. It is seen that there is not much difference in stress–strain results between loading speeds 4.45 m/s and 0.229 m/s for PS foam with 32 kg/m^3 density, however big difference for PP foam with 98 kg/m^3 density. For hydrostatic compression tests, foam specimens are wrapped by latex rubber and immersed into a specially designed hydrostatic compression chamber filled with water. Air is allowed to escape from the specimens through an air vent on the lid of the chamber. They have also studied the temperature effect on the constitutive behavior of PP foam by using the following William et al.'s model [29]. Zhan et al. [27] proposed a yield surface based on their experimental data. The yield surface is defined by an ellipse on the plane of Von Mises stress q and the hydrostatic pressure p as

$$F - F_o = \frac{\left[p - x_o(\varepsilon_{vol}^{p}) \right]^2}{a(\varepsilon_{vol}^{p})} + \frac{q^2}{b(\varepsilon_{vol}^{p})} - 1 = 0\,, \tag{1.19}$$

where $x_o(\varepsilon_{vol}^{p})$, $a(\varepsilon_{vol}^{p})$ and $b(\varepsilon_{vol}^{p})$ defines the center, the lengths of the major and minor axes of the yield ellipse respectively. Those parameters are functions of total plastic volumetric strain ε_{vol}^{p}. When foam is consolidated, the yield ellipse extends in the q - p stress space. In their study, those three consolidation variables are defined by means of three experiments: uniaxial compression, hydrostatic compression, and simple shear. They have implemented their model into Ls-Dyna 3D code using a user defined subroutine and compared results of model to the hemi-sphere indentation test. They have found that the numerical simulation predicts well the loading phase but there is large deviation for unloading. Zhang et al. [27] have not analyzed multiple loading and unloading in their study.

Deshpande and Fleck [30] studied the plastic yield and elastic buckling behavior for two densities (100 kg/m^3 and 200 kg/m^3) of PVC foam. Experiments including various combinations of axial and radial compression, tension, and shear tests have been performed. The results are used to determine the yield surface and to validate the existing yield models. They used two multi–axial loading systems to investigate the axisymmetric behavior of the foams under different combinations of axial, radial tension and compression. A high pressure tri-axial system is used to measure the axisymmetric stress versus strain response under different combinations of axial tension, compression, and radial compression. It consists of a pressure cell, with hydraulic fluid as the pressurizing medium, and a piston for the application of axial force. In order to apply an axial load on the specimen, the piston of the tri-axial cell is moved by a screw-driven test machine. The axial load is measured using a load cell internal to the tri-axial cell and the axial displacement is measured with a linear voltage displacement transducer (LVDT) on the test machine cross head. Circumferential strains are measured using a strain gauge glued onto the specimen, and it is assumed that the radial strain equals the circumferential strain. The axial force, axial displacement, and circumferential strains are recorded using a data logger. The oil pressure is recorded manually from a pressure gauge. They have also performed biaxial tension and hydrostatic tension tests. The specimens are loaded along the vertical axis using a screw driven testing machine while loading along the lateral axes are applied by manually turning the loading nuts. Strain gauges on the screws in lateral directions are calibrated to give the load in those directions. The load in the vertical direction is measured from the load cell of the testing machine and the displacement is measured with a LVDT on the test machine cross-head. They have performed uniaxial compression and tension tests by using a standard screw driven test machine. In order to determine the plastic Poisson's ratio, the specimens are compressed in increments of approximately 5 per cent axial plastic strain and the diameter is measured at three points along the length of the specimen using a micrometer. They have also performed hydrostatic compression and tension tests by using the tri-axial cell. Equi-biaxial tension tests are also performed using the same test setup.

Deshpande and Fleck [30] have performed shear tests using the test setup suggested by Arcan et al. [31]. Arcan et al. [31] have used a plane circular specimen with anti-symmetric cutouts. Experimental analysis of the specimen has been performed by photoelastic and strain gage methods for the cases of pure shear and general plane stress.

Deshpande and Fleck [30] recommended as a future topic of research that for situations where multiple loading occurs, the viscoelastic behavior of foams is important and needs to be taken into account in the constitutive model.

Moreu and Mills [40] have developed a test rig for hydrostatic compression testing of foam materials. They used a three liter reservoir that contains air at relative pressure between -100 kPa and 700 kPa. This reservoir is connected to a pressure chamber of 0.25 liter by a valve. The pressure can be increased in 10 seconds by opening the valve of the pressure chamber. The displacements can be measured by a linear voltage displacement transducer (LVDT) with 10 mm range.

Cridland and Wood [33] have proposed a method for testing materials in hydrostatic tension using a spherical specimen bonded into the center of a cube matrix material which has tensile loads applied to the faces of the cube. The materials are chosen such that failure first occurs in the test material, in which the stress can be estimated by elastic theory. Failure is detected from the edge displacement of the cube face.

For crushable and hysteretic foams, Faruque et al. [34] formulated a strain rate and temperature dependent constitutive model and implemented it into an explicit dynamic finite element code developed at Ford Motor Company in 1997. Their model considers strain rate effect on Young's modulus and yield strength, hardening of Young's modulus with volumetric strain and tension cut-off. They have not analyzed and tested their model for unloading and reloading behavior of foams.

Chou et al. [35] did some experimental studies in 1995 to study the mechanical behavior of the three types of foams: Dylite foam (expanded polystyrene), Arpro foam (expanded polyethylene), Dytherm (expandable copolymer of styrene and maleic anhyride) from Arco Chemicals. They used Ls-Dyna 3D software package to make finite element (FE) simulations of different loading conditions including the static compression, indentation, tensile tests, and dynamic impacts with a spherical head form. To observe the unloading and hysteresis behavior in uniaxial compressive loading, they loaded, unloaded and reloaded foams in compression at 30 per cent, 60 per cent ad 90 per cent of their original height. Although Chou et al. [35] measured loading and unloading behavior for uniaxial compressive loading; they have not analyzed loading and unloading behavior for tension, shear, multi–axial, and other types of loadings. They have not studied multiple loading and unloading effects for energy absorption calculation purposes and used finite element software packages to simulate multiple loading and unloading of foams.

In the indentation tests performed by Chou et al. [35], they have noted that the stresses of indentation are much higher than those of compression. They have commented that the shear and tensile strengths are believed to play an important role in providing additional resistance to the deformation. They used material type no 57 developed in Ls-Dyna 3D for foam modeling. The material model is capable of simulating hysteresis of foam materials but not the residual strain. Although there is approximately 0.35 residual strain after unloading for uniaxial compression of APRO foam, all of the deformation is completely recovered in the FE simulation performed by Chou et al. [35]. Therefore material type no 57 in Ls-Dyna 3D is not appropriate for simulation of multiple loading and unloading.

Gilchrist and Mills [36] used the Abaqus Finite Element (FE) program to model the impact response of low-density polystyrene (PS 35) foam with a measured density of 28.3 ± 0.3 kg/cm^3. They have given experimental results of PS foam for compressive stress–strain, tensile stress–strain, and simple shear stress–strain. They used compression test data of PS 35 foam for foam hardening. They have found that in a single uniaxial compression loading–unloading simulation, in which the foam is forced to return to its original dimensions, simulation results show metal-like reverse yielding at high tensile stresses, quite different from the experimental unloading response of PS 35. The foam is predicted by Abaqus to yield in tension at a slightly smaller stress than in compression, and further yield occurs without hardening. They have found that the predicted simple shear response by Abaqus shows no hardening after yield. However, using shear plus compression impact equipment, they showed shear strain hardening on loading for EPS foam of density 60 kg/m^3. They have taken Poisson's ratio in the elastic region to be the same as that for an EPS of density 20 kg/m^3, measured as 0.09 by Mills and Gilchrist [38]. They used uniaxial and hydrostatic compression responses measured by Bilkhu et al. [39] for EPS foam of 40 kg/m^3 density. Their data shows that hydrostatic and uniaxial compression collapse started at stresses of 0.21 and 0.34 MPa respectively. They have commented that hydrostatic compression collapse involves only the buckling of cell faces, whereas uniaxial compression collapse also involves cell face tensile yielding, therefore the difference in collapse stresses in hydrostatic and uniaxial compression is meaningful. They used the Abaqus Finite Element program for simulation of cylinder and cube indentation tests for PS 35 foam. To describe the yield surface used in Abaqus, they used as yield pressure in hydrostatic compression, p_c = 0.15 MPa, initial yield pressure in hydrostatic compression, p_{c0} = 0.29 MPa, and strength in hydrostatic tension, p_t = 0.15MPa. They stated that the uniaxial tension result does not fit on the yield ellipse. Abaqus calculates the initial yield surface from the parameters p_{c0}, σ_{c0}, and p_t for "foam" command, then calculates relative hardening from the tabular data with "foam hardening" command, using the first value in the table as a reference value. They have given the comparison of results calculated by Abaqus and experimental measurements for cube indentation force versus displacement data of PS 35 foam. Although the difference between the simulation and the experimental results for force–displacement curve have been found to be acceptable during loading, the deviation increased when crack occurred in the tested foam specimen. Gilchrist and Mills [36] have recommended that Abaqus model should be improved for foam hardening in tension and shear, unloading response, and anisotropy. They have not studied reloading behavior of foam.

1.2. Motivation and Objectives of the Study

In most of the energy absorbing applications, low density polymeric foams are only loaded once. It is important to make accurate calculations of absorbed energy, stress, and strain during loading. Energy release from foam during unloading and reloading behavior is not important in most of the applications because foam parts are usually replaced by a new one once they are loaded. Hence, most of the studies available in literature have proposed constitutive models and yield criteria for foams that are loaded only once. Experimental studies show that unloading behavior is not calculated accurately with available models. Reloading behavior has not been studied at all.

In packaging applications of consumer goods however, a packaged product can be subjected to several impact loadings until it reaches to the consumer's house. Hence, it is important to make accurate calculations of multiple loading and unloading behavior of foams. Therefore in this study, it is aimed to test EPS and PE foams and measure their mechanical behavior at various multiple loading and unloading conditions, to propose an accurate method for energy absorption calculations for multiple compressive loading and unloading, and to compare the experimental results to the results of models developed previously for multiple general loading and unloading.

1.3. Thesis Outline

The thesis consists of four main chapters. In Chapter 2, mechanical behavior and energy absorbing characteristics of foams under multiple uniaxial compressive loading and unloading are measured experimentally. Existing constitutive models for uniaxial compression are used to calculate the stress-strain in multiple loading and their results are compared to experimental results. A new model for uniaxial compressive loading and unloading is proposed. A design procedure using the new proposed model for foams that are subjected to multiple loading and unloading is presented. In Chapter 3, the test rig built for measuring uniaxial compressive loading and unloading behavior at high strain rates is presented and experimental results are given. In Chapter 4, mechanical behaviors of foams under multiple loading and unloading for uniaxial tension, simple shear, hydrostatic compression, cylinder indentation, and block indentation, which are measured by specially prepared test rigs are presented. In Chapter 5, test results presented in chapter four are compared to finite element simulation results obtained by using Abaqus Explicit version 6.7 for multiple loading and unloading.

2. UNIAXIAL COMPRESSIVE LOADING AND UNLOADING BEHAVIOR OF LOW DENSITY POLYMERIC FOAMS

Most of the studies available in the literature are for uniaxial compressive loading because in most of the energy absorption applications, it is the dominant loading [1-16]. In this chapter, multiple loading and unloading behavior of EPS and PE foam is experimentally analyzed under uniaxial compression using Zwick Z020 universal tensile testing machine (Figure 2.1). Empirical calculations of load, deformation, and absorbed energy based on experimental measurements are presented. Existing constitutive models for uniaxial compression are used to calculate the stress-strain in multiple loading and their results are compared to experimental results. A new model for accurate calculation of stress, strain, and absorbed energy for uniaxial compressive loading, unloading, and reloading is proposed. A design procedure using the new proposed model for foams that are subjected to multiple loading and unloading is presented.

EPS and PE foams with 3 different densities (EPS 12, EPS 20, EPS 30 and PE 24, PE 32 and PE 58) are used in uniaxial compression tests. The numbers represent densities in kg/m^3. EPS is obtained from BASF and molded by a local manufacturer; PE is directly obtained from DOW.

Zwick Z020 universal tensile testing machine is used to test specimens with 50 mm $\times$ 50 mm $\times$ 50 mm dimensions at 3 different constant cross-head speeds for loading and unloading: 5 mm/min, 100 mm/min and 1000 mm/min. Corresponding strain rates are calculated by dividing the crosshead speed by the height of the specimen (H). Specimen properties and strain rates are tabulated in Table 2.1. Tests are performed at room temperature. EPS sheets are produced by molding, and PE sheets are produced by extrusion. The compression loading direction in tests is vertical to the EPS and PE sheet surface (*z* direction in Figure 2.2). When it is specified that loading is in parallel and perpendicular directions, it is meant that the specimen is loaded along the *x* and *y* directions respectively in Figure 2.2. The test results are given positive for compression unless otherwise specified.

Figure 2.1. Zwick Z020 universal tensile testing machine

Densities of specimens are measured by dividing the mass of the specimen by its volume. During the expansion of EPS foam material inside the mold, the cells close to the mold wall are flattened, and the regions close to the mold walls have higher densities. The regions close to the top and bottom surfaces of PE foam sheets have higher density than the inner regions. Therefore specimens cut from different locations on the sheets may have different densities and different compressive yield strength. EPS and PE sheets are cut in around 5 mm slices and the density change through the thickness is measured in Figure 2.3 and 2.4 for EPS 30 and PE 58 respectively. It is seen that the difference in density between the outer regions and middle of foam sheet is approximately 20 per cent for PE 58 and 10 per cent for EPS 30. Compression tests repeatability is very good when specimens with more or less equal densities are used.

Table 2.1. EPS and PE foam specimen properties and strain rates used in uniaxial compression tests

	Density given by manufacturer [kg/m^3]	Measured density [kg/m^3]	Dimensions (L x W x H) [mm^3]	Strain rates [s^{-1}]		
EPS	12	13.8	50x50x50	$1.70\text{x}10^{-3}$	$3.39\text{x}10^{-2}$	$3.39\text{x}10^{-1}$
	20	17.9	50x50x50	$1.66\text{x}10^{-3}$	$3.33\text{x}10^{-2}$	$3.33\text{x}10^{-1}$
	30	27.6	50x50x50	$1.66\text{x}10^{-3}$	$3.33\text{x}10^{-2}$	$3.33\text{x}10^{-1}$
PE	24	23.2	50x50x47	$1.78\text{x}10^{-3}$	$3.56\text{x}10^{-2}$	$3.56\text{x}10^{-1}$
	32	33.7	50x50x56	$1.49\text{x}10^{-3}$	$2.97\text{x}10^{-2}$	$2.97\text{x}10^{-1}$
	58	55.8	50x50x46	$1.84\text{x}10^{-3}$	$3.67\text{x}10^{-2}$	$3.67\text{x}10^{-1}$

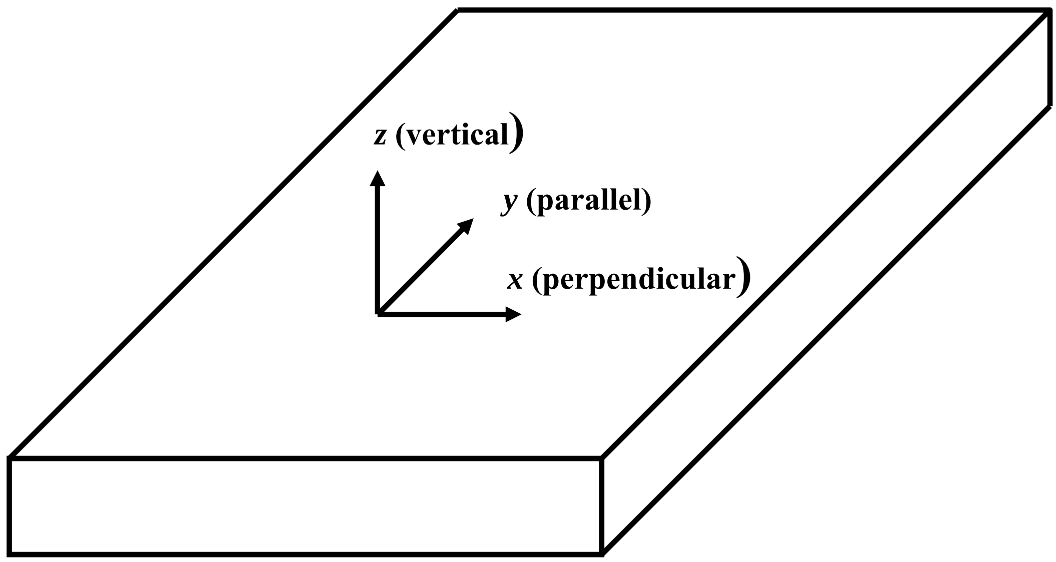

Figure 2.2. Loading directions of test specimen shown on foam sheet

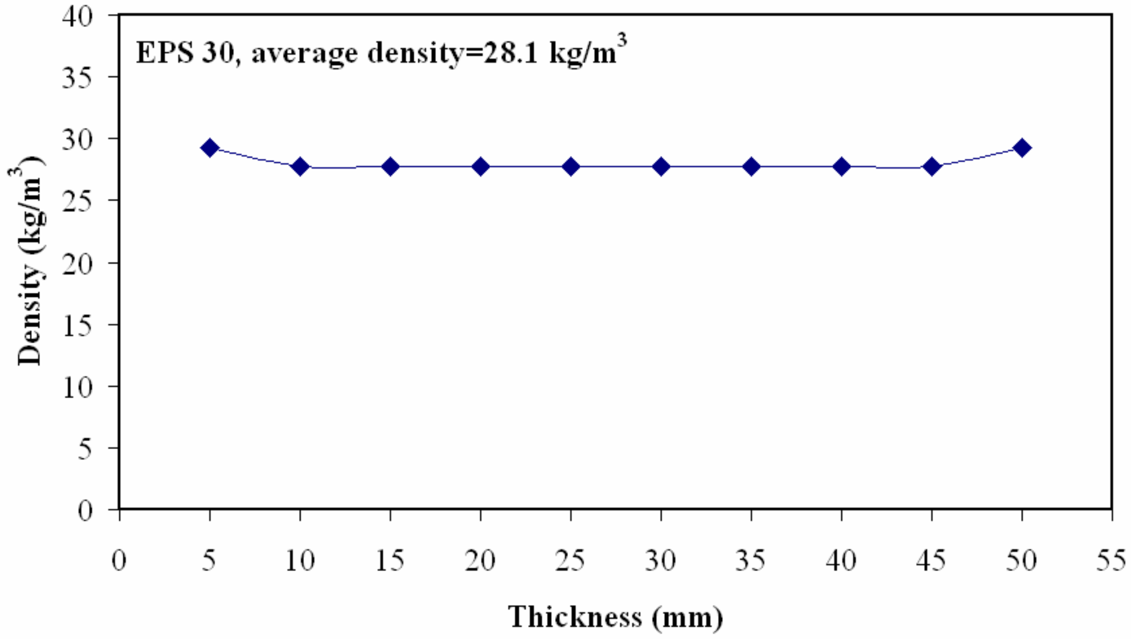

Figure 2.3. Density variation through the thickness of EPS 30 test specimen

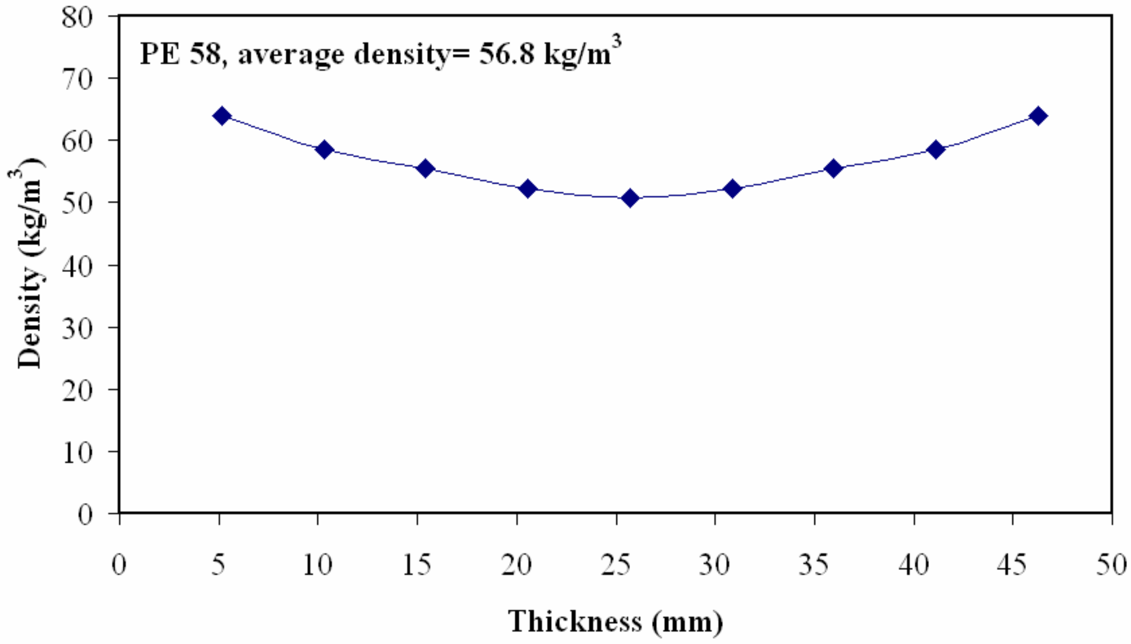

Figure 2.4. Density variation through the thickness of PE 58 test specimen

In Figure 2.5–2.7, force versus displacement curves for EPS 12, EPS 20, and EPS 30 are given for cross head speeds of 5 mm/dk, 100 mm/dk, and 1000 mm/dk respectively. In Figure 2.8–2.10, force versus displacement curves for PE 24, PE 32, and PE 58 are given for cross head speeds of 5 mm/dk, 100 mm/dk, and 1000 mm/dk respectively. Mechanical behavior of a polymeric foam depends on strain rate because of the viscoelastic characteristics of solid material and the gas expelled as it is compressed [1]. There is a considerable difference in loads applied to obtain the same amount of displacement for cross head speeds of 5 mm/min and 1000 mm/min. However, there is almost no difference between load versus displacement curves of EPS and PE for cross head speeds 100 mm/min and 1000 mm/min. Strain rate dependency of load–displacement response decreses with increasing density.

Chou et al. [35] classified foams as crushable and resilient according to their ratio of residual deformation to total deformation. If the ratio is greater than 0.6, the foam is considered crushable, and if it is less than 0.2, resilient. In Table 2.2, the ratios of residual deformation to total deformation calculated for 3 different cross head speeds and 3 different densities of EPS and PE are given. The residual deformation of EPS at 45 mm of compression is larger for 5 mm/min cross head speed than those obtained at 100 mm/min and 1000 mm/min cross head speeds. At 5 mm/min, the ratio of residual deformation to total deformation is greater than 0.6 for all EPS s tested, but the ratio is 0.34, 0.37 and 0.47 for EPS 12, EPS 20 and EPS 30 respectively at 1000 mm/min. For PE foam, this ratio does not vary considerably with density and cross head speed. In all cases, the ratio is between 0.2 and 0.24. PE foam is resilient for all cases and EPS foam is crushable at 5 mm/min, but shows less crushable behavior at higher cross head speeds. For all foams tested, 5 mm deformation is beyond the yield point. Load measured at 5 mm deformation is given in Table 2.2 to show how the reaction forces of foams tested vary with density and cross head speed. It is observed that the reaction force increases with density and with cross head speed.

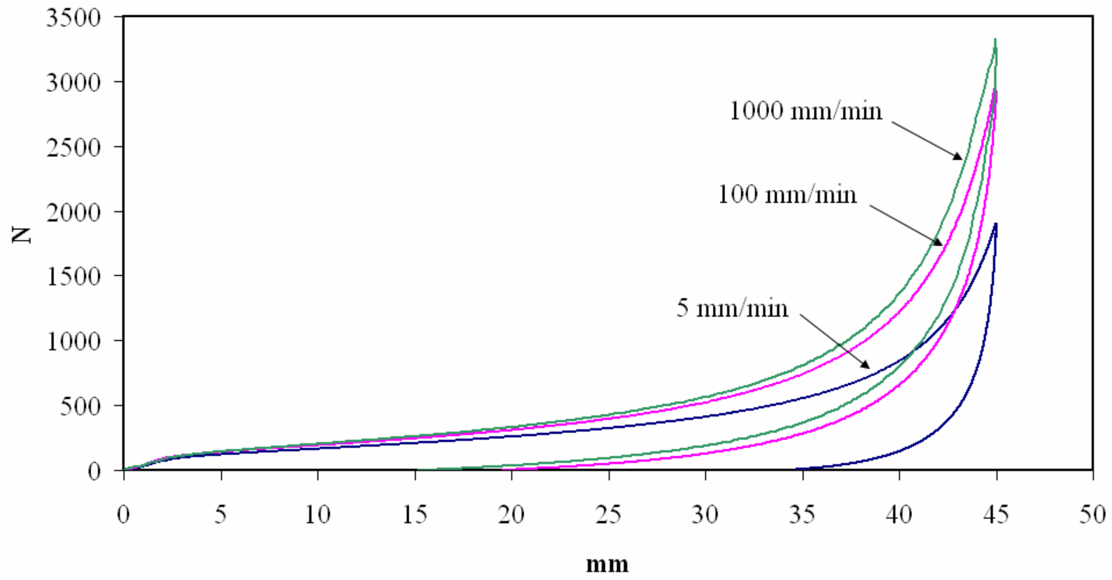

Figure 2.5. Load and cross head displacement curves for compressive loading and unloading of EPS 12 at 5 mm/min, 100 mm/min, and 1000 mm/min cross head speeds (compression direction is taken as positive)

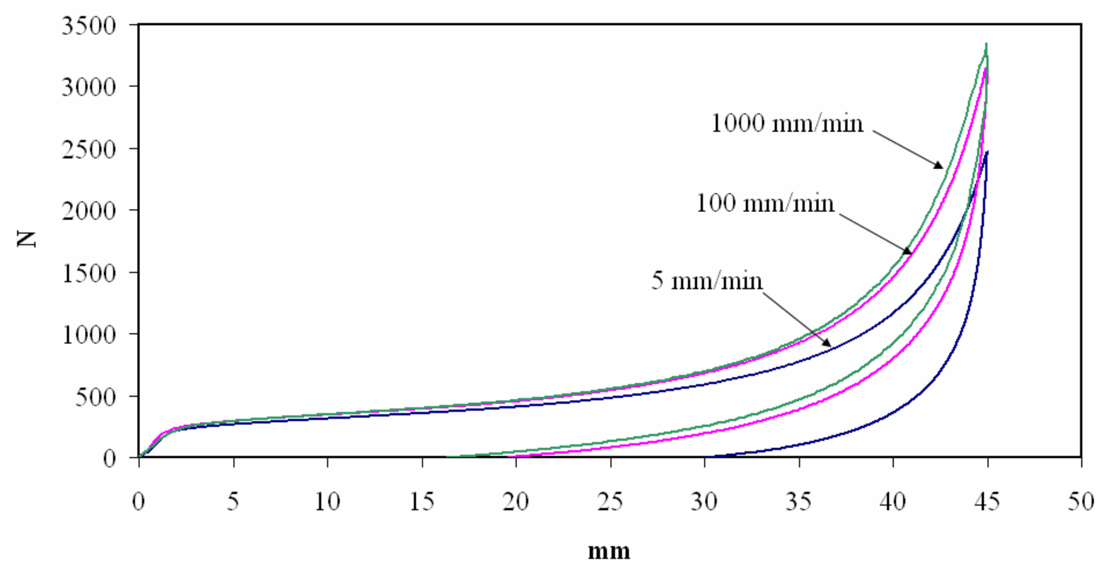

Figure 2.6. Load and cross head displacement curves for compressive loading and unloading of EPS 20 at 5 mm/min, 100 mm/min, and 1000 mm/min cross head speeds (compression direction is taken as positive)

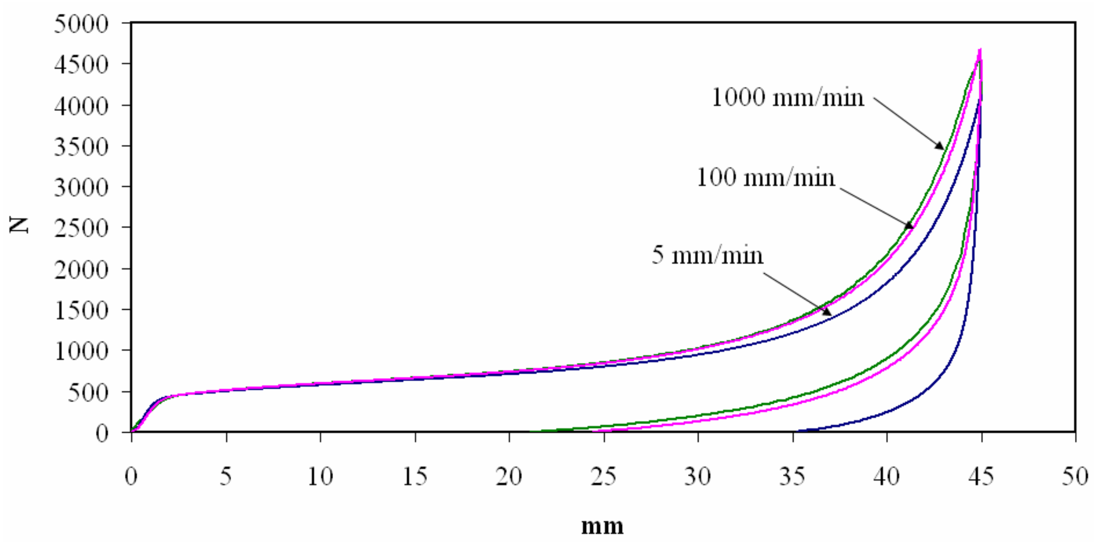

Figure 2.7. Load and cross head displacement curves for compressive loading and unloading of EPS 30 at 5 mm/min, 100 mm/min, and 1000 mm/min cross head speeds (compression direction is taken as positive)

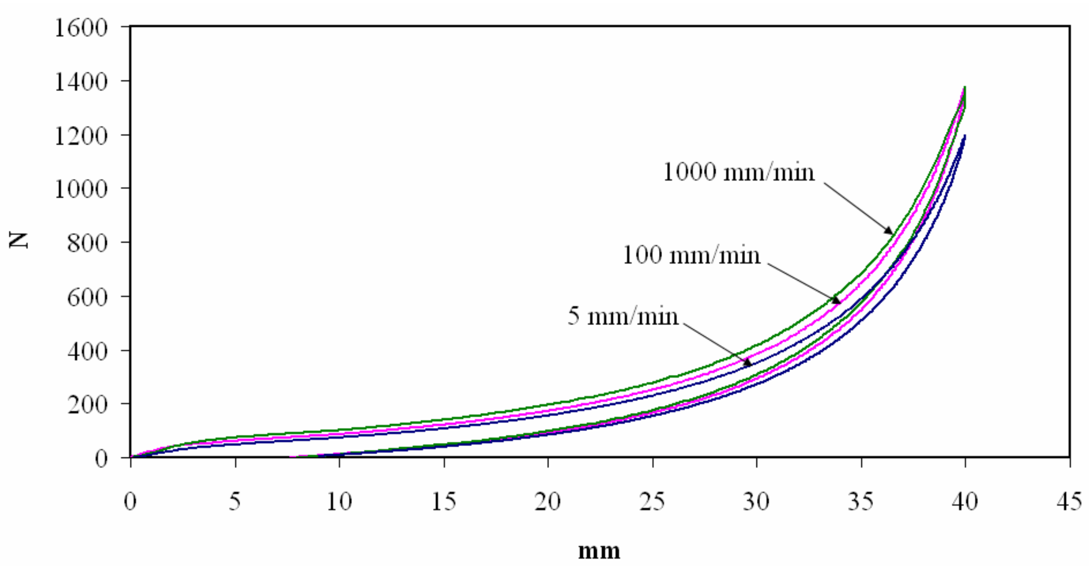

Figure 2.8. Load and cross head displacement curves for compressive loading and unloading of PE 24 at 5 mm/min, 100 mm/min, and 1000 mm/min cross head speeds (compression direction is taken as positive)

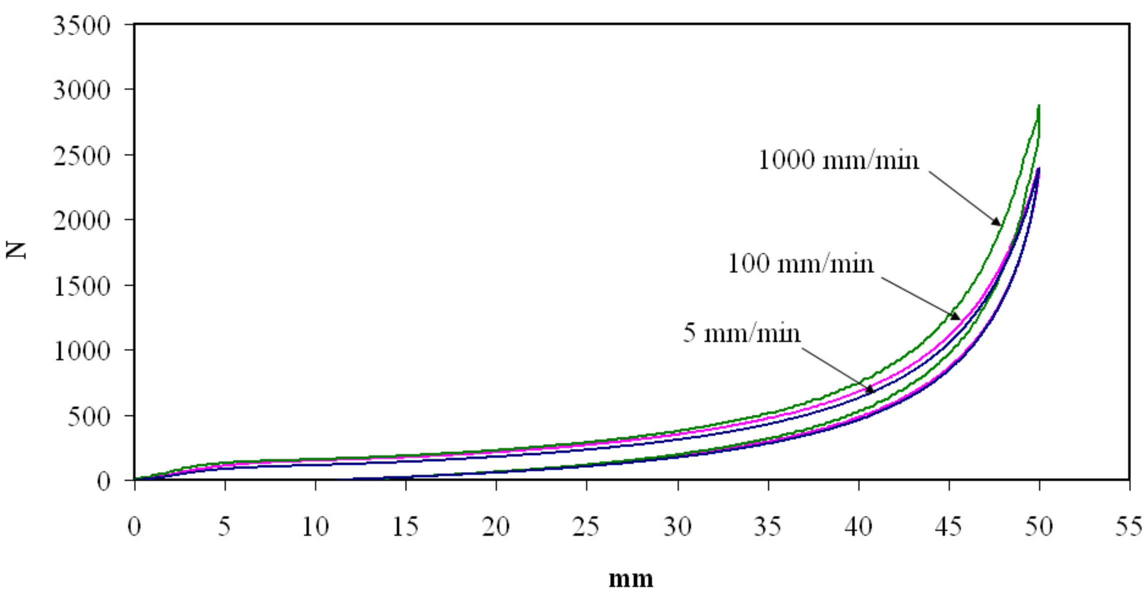

Figure 2.9. Load and cross head displacement curves for compressive loading and unloading of PE 32 at 5 mm/min, 100 mm/min, and 1000 mm/min cross head speeds (compression direction is taken as positive)

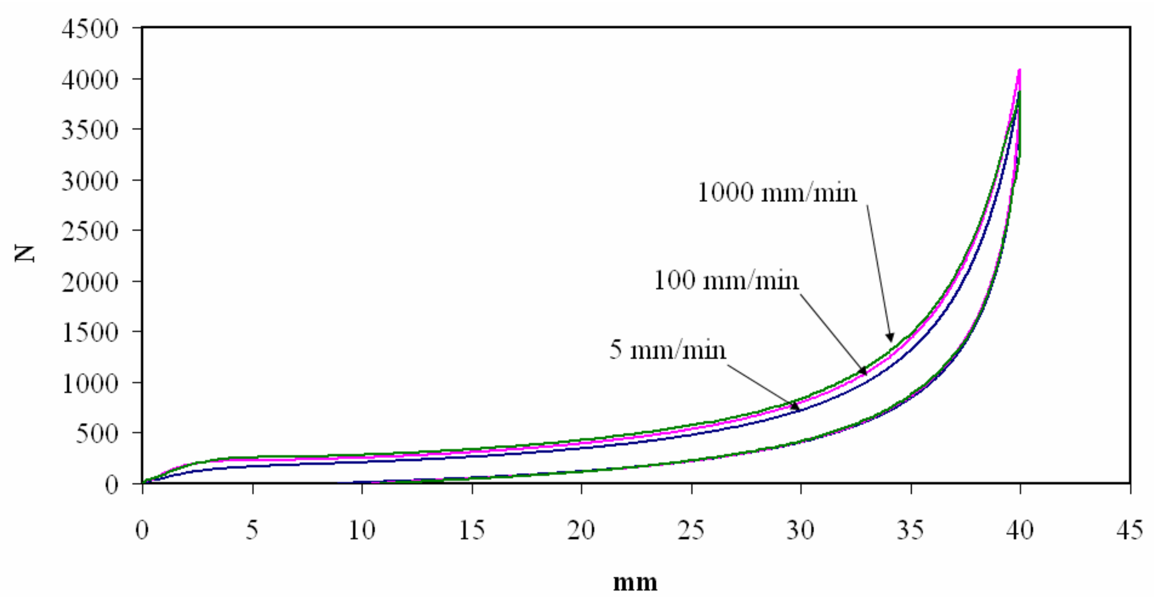

Figure 2.10. Load and cross head displacement curves for compressive loading and unloading of PE 58 at 5 mm/min, 100 mm/min, and 1000 mm/min cross head speeds (compression direction is taken as positive)

Masso-Moreu and Mills [40] reported that the yield stress of EPS increases at most by 18 per cent when the strain rate is increased from $4x10^{-3}$ s^{-1} to impact strain rates. In the study of Zhang et al. [27-28], it is seen that stress of EPS varies approximately 10 per cent for the same strain level when the strain rate increases from $8x10^{-1}$ s^{-1} to $8.8x10^{1}$ s^{-1}. Therefore, although the 1000 mm/min cross head speed and the corresponding strain rates used in the tests presented in this article (from 10^{-3} to $3x10^{-1}$ s^{-1}) are lower than impact strain rates, results and discussions are valid for impact behavior of EPS and PE foams.

For EPS 30, in vertical (z) direction, there is not a considerable difference in yield stress between 5 mm/min, 100 mm/min, and 1000 mm/min cross head speeds. Repeatibility of 100 mm/min test results is good. In parallel (y) and perpendicular (x) directions, compression curves are very similar and yield stress is around 20 per cent higher than the one in vertical direction. This result can be due to the fact that the EPS is expanded during production, and the region close to the mold wall has higher density than the inner regions. Therefore it is more difficult to compress EPS at parallel and perpendicular directions.

In Figures 2.11 and 2.12, stress versus strain for compressive loading and unloading of EPS 30 at 5 mm/min, 100 mm/min, and 1000 mm/min cross head speeds. In Figures 2.13 and 2.14, stress versus strain for compressive loading and unloading of three EPS 30 specimens tested in vertical direction are given at 100 mm/min speed, and good repeatibility is achieved for the three specimens tested. In Figures 2.15 and 2.16, stress versus strain for compressive loading and unloading of EPS 30 in vertical, parallel and perpendicular directions at 100 mm/min speed are given. Considering the test results given for three specimen in vertical direction at 100 mm/min speed, there is not a considerable difference in yield stress between 5 mm/min, 100 mm/min, and 1000 mm/min speeds. In parallel (y) and perpendicular (x) directions, compression curves are very similar and yield stress is around 20 per cent higher than the one in vertical direction. This result can be due to the fact that the local densities at close to mold surfaces are higher for EPS.

Table 2.2. Total deformation, residual deformation, and corresponding load at 5 mm compression at 3 different cross head speeds

	Cross head speed [mm/min]	Residual deformation [mm]	Residual / Total deformation	Load at 5 mm compression [N]
EPS 12	5	34.7	0.77	122
	100	19.3	0.43	140
	1000	15.1	0.34	143
EPS 20	5	30.1	0.67	268
	100	19.6	0.44	291
	1000	16.7	0.37	291
EPS 30	5	35.2	0.78	512
	100	24.4	0.54	512
	1000	21.3	0.47	512
PE 24	5	7.9	0.20	49
	100	7.9	0.20	61
	1000	7.9	0.20	74
PE 32	5	11.2	0.20	85
	100	11.2	0.20	111
	1000	11.2	0.20	131
PE 58	5	8.9	0.20	74
	100	10.5	0.23	227
	1000	10.9	0.24	257

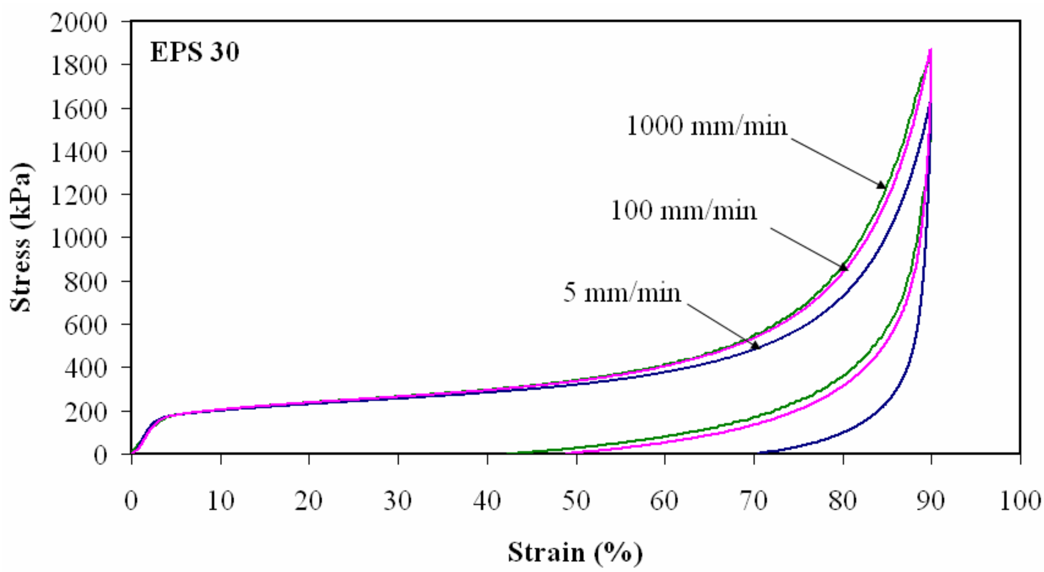

Figure 2.11. Stress versus strain for compressive loading and unloading of EPS 30 at 5 mm/min, 100 mm/min, and 1000 mm/min cross head speeds (compression direction is taken as positive)

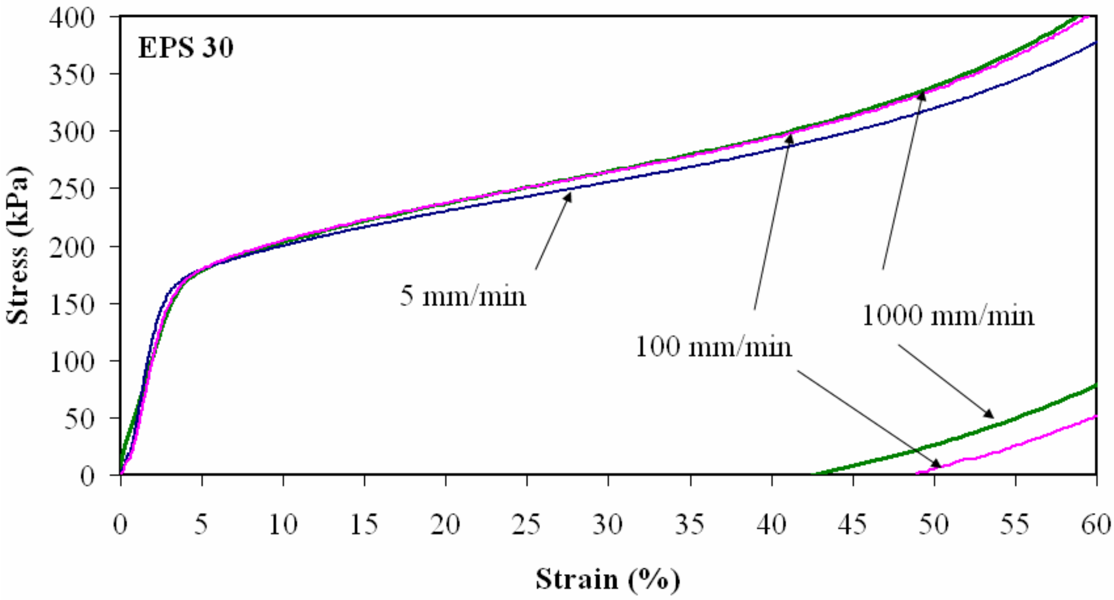

Figure 2.12. Stress (up to 400 kPa) versus strain (up to 60 per cent) for compressive loading and unloading of EPS 30 at 5 mm/min, 100 mm/min, and 1000 mm/min cross head speeds (compression direction is taken as positive)

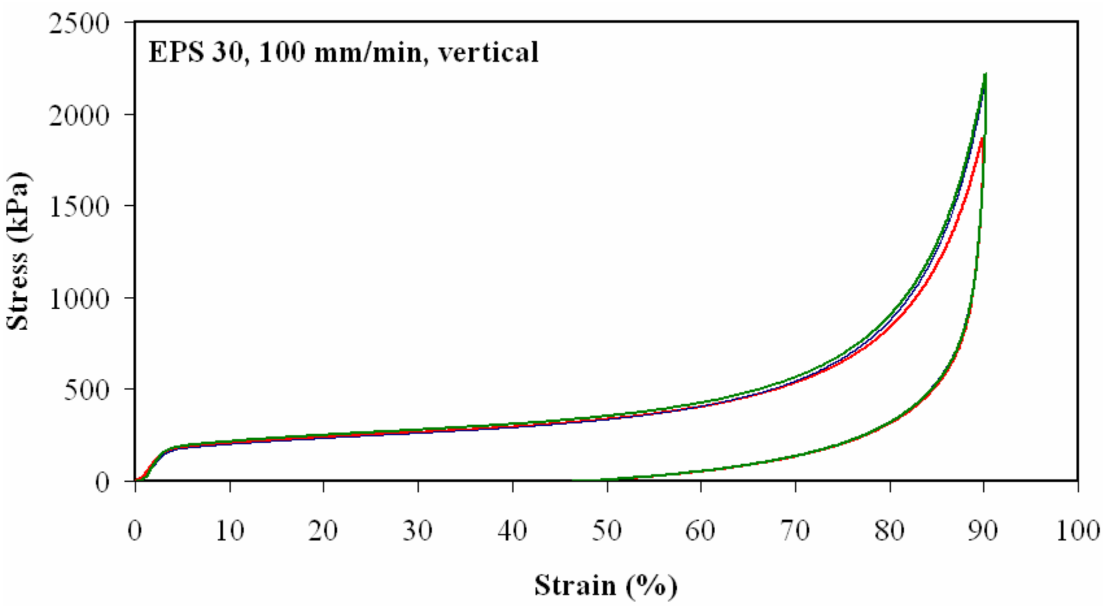

Figure 2.13. Stress versus strain for compressive loading and unloading of three EPS 30 specimens at 100 mm/min cross head speeds (compression direction is taken as positive)

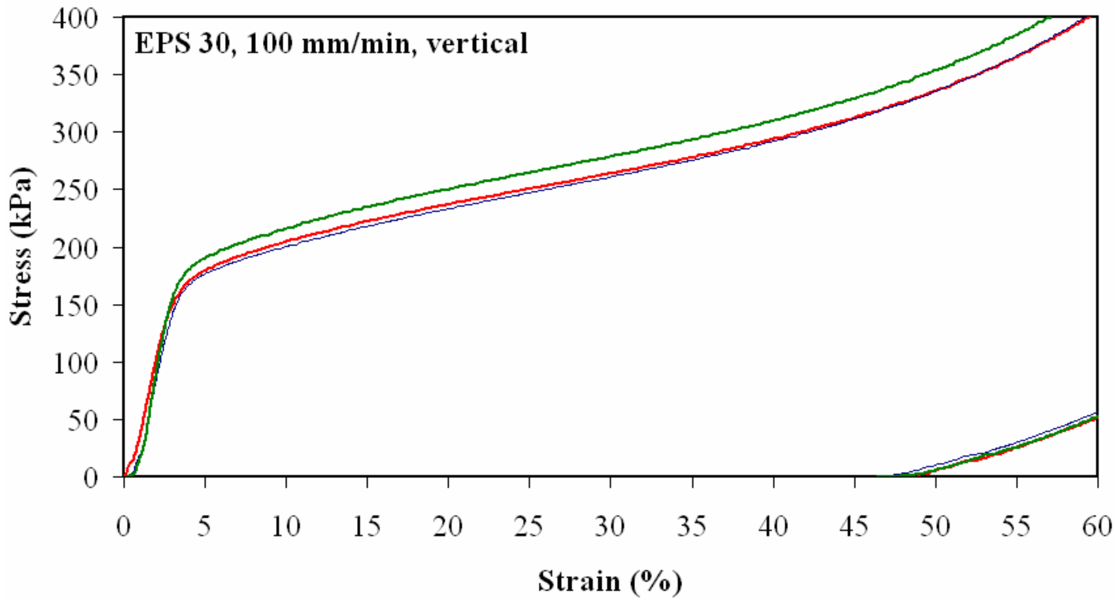

Figure 2.14. Stress (up to 400 kPa) versus strain (up to 60 per cent) for compressive loading and unloading of three EPS 30 specimens at 100 mm/min (compression direction is taken as positive)

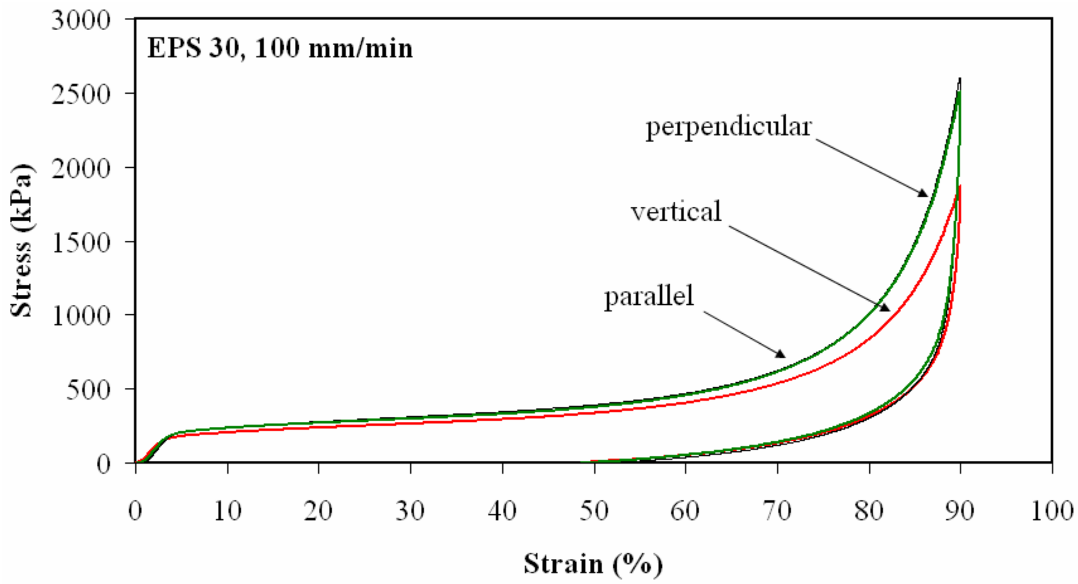

Figure 2.15. Stress versus strain for compressive loading and unloading of EPS 30 in vertical, parallel, and perpendicular directions at 100 mm/min cross head speeds (compression direction is taken as positive)

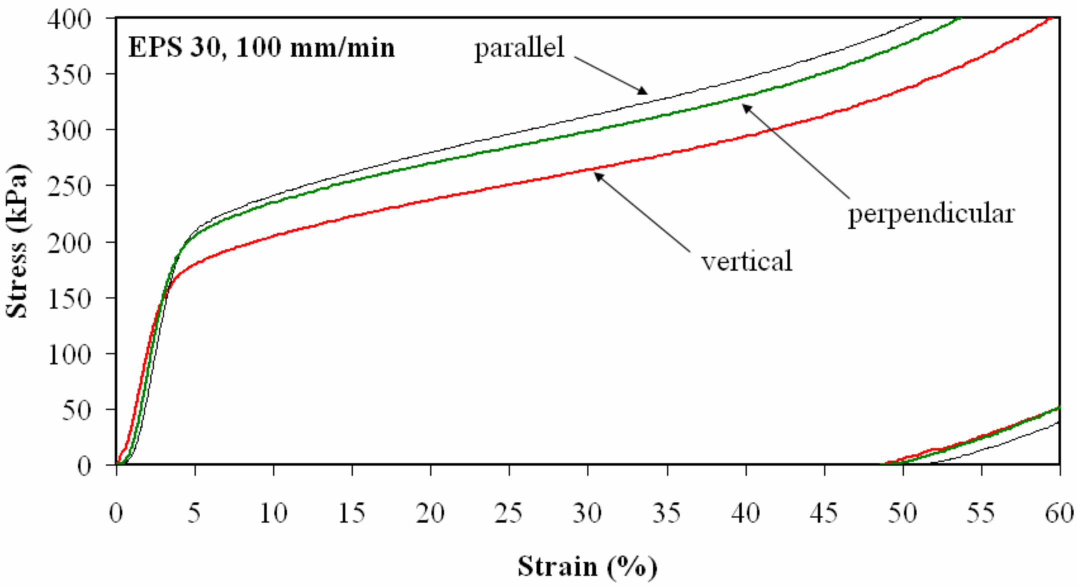

Figure 2.16. Stress (up to 400 kPa) versus strain (up to 60 per cent) for compressive loading and unloading of EPS 30 in vertical, parallel, and perpendicular directions at 100 mm/min cross head speed (compression direction is taken as positive)

In Figures 2.17 and 2.18, stress versus strain for compressive loading and unloading of PE 58 at 5 mm/min, 100 mm/min, and 1000 mm/min cross head speeds. In Figures 2.19 and 2.20, stress versus strain for compressive loading and unloading of three PE 58 specimens tested in vertical direction are given at 100 mm/min speed. In Figures 2.21 and 2.22, stress versus strain for compressive loading and unloading of PE 58 in vertical, parallel and perpendicular directions at 100 mm/min speed are given. Considering the test results given for three specimens in vertical direction at 100 mm/min speed, in vertical direction, there is a difference of about 20 per cent for yield strength of PE 58 tested at 100 mm/min and 1000 mm/min cross head speeds and about 30 per cent difference for yield strength of PE 58 tested at 5 mm/min and 100 mm/min cross head speeds. In vertical and perpendicular directions, compression curves are very similar and yield stress is around 20 per cent lower than those in parallel direction. This result can be due to the fact that the PE sheets are prepared by extrusion and the grains are strechted along the extrusion (parallel) direction. Local densities of regions close to the extrusion surface are also higher than the middle region. It is more difficult to compress PE at parallel direction compared to vertical and perpendicular directions. There is not such a dependency for parallel and perpendicular directions of EPS because it is produced by molding.

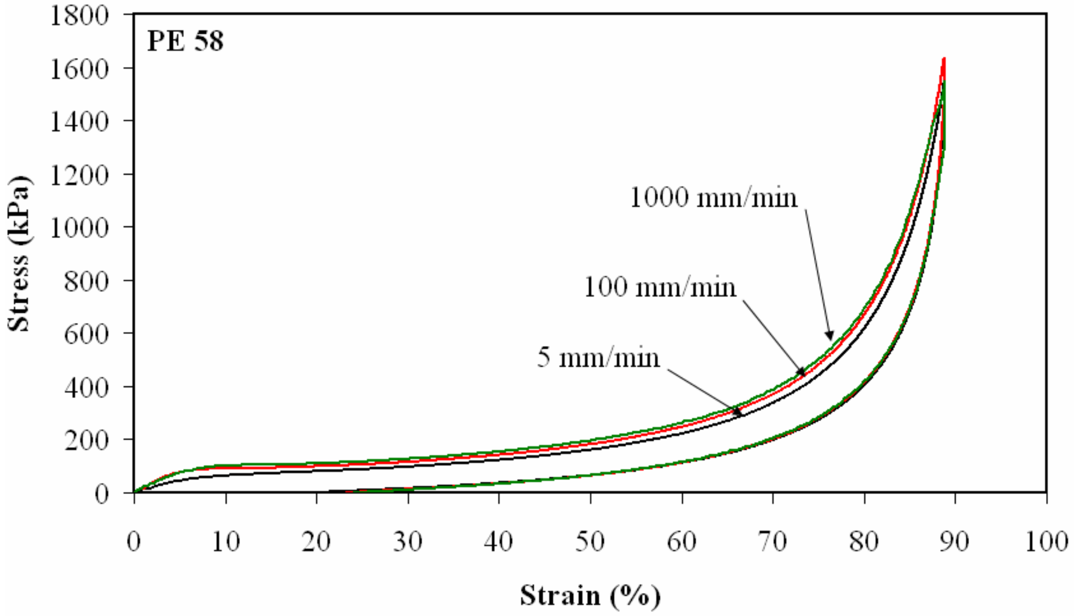

Figure 2.17. Stress versus strain for compressive loading and unloading of PE 58 at 5 mm/min, 100 mm/min, and 1000 mm/min cross head speeds (compression direction is taken as positive)

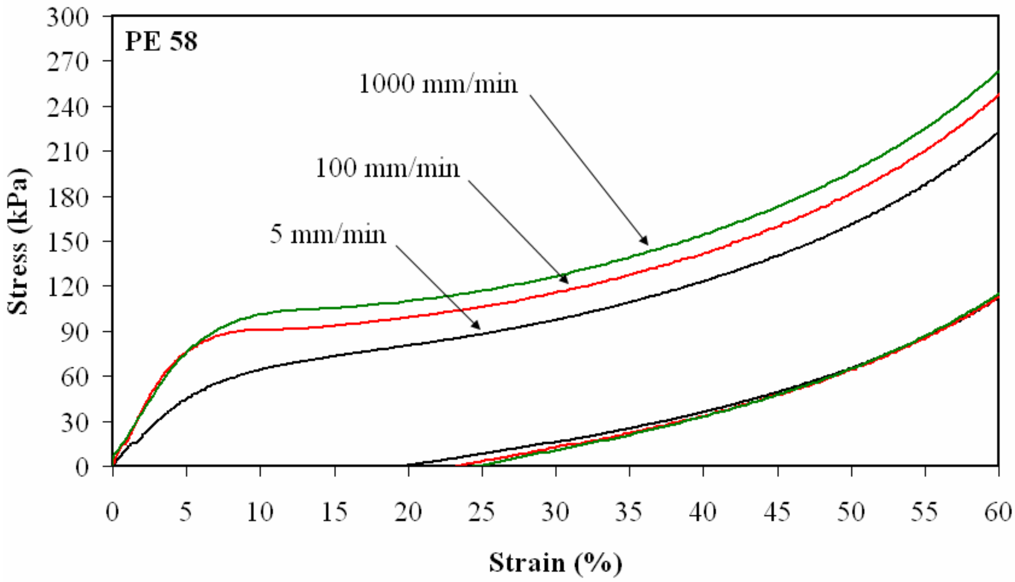

Figure 2.18. Stress (up to 300 kPa) versus strain (up to 60 per cent) for compressive loading and unloading of PE 58 at 5 mm/min, 100 mm/min, and 1000 mm/min cross head speeds (compression direction is taken as positive)

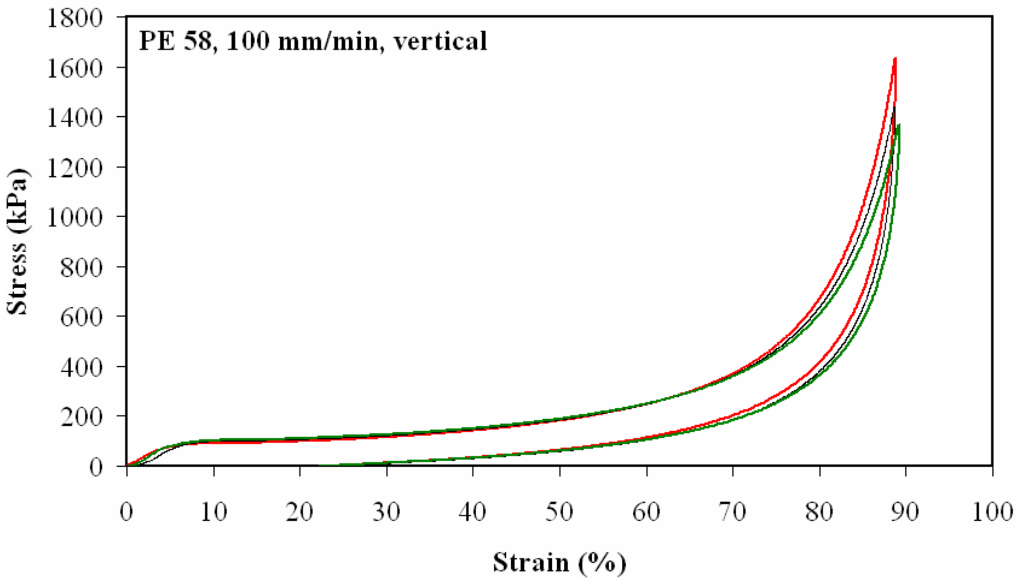

Figure 2.19. Stress versus strain for compressive loading and unloading of three PE 58 specimens in vertical direction at 100 mm/min cross head speeds (compression direction is taken as positive)

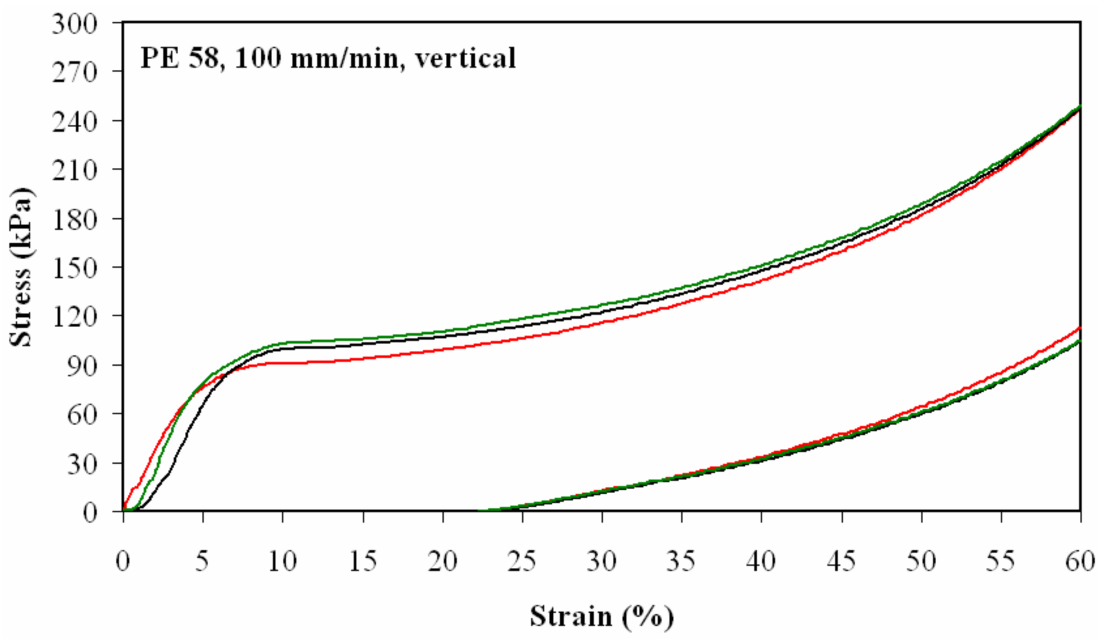

Figure 2.20. Stress versus strain for compressive loading and unloading of three PE 58 specimens in vertical direction at 100 mm/min cross head speeds (compression direction is taken as positive)

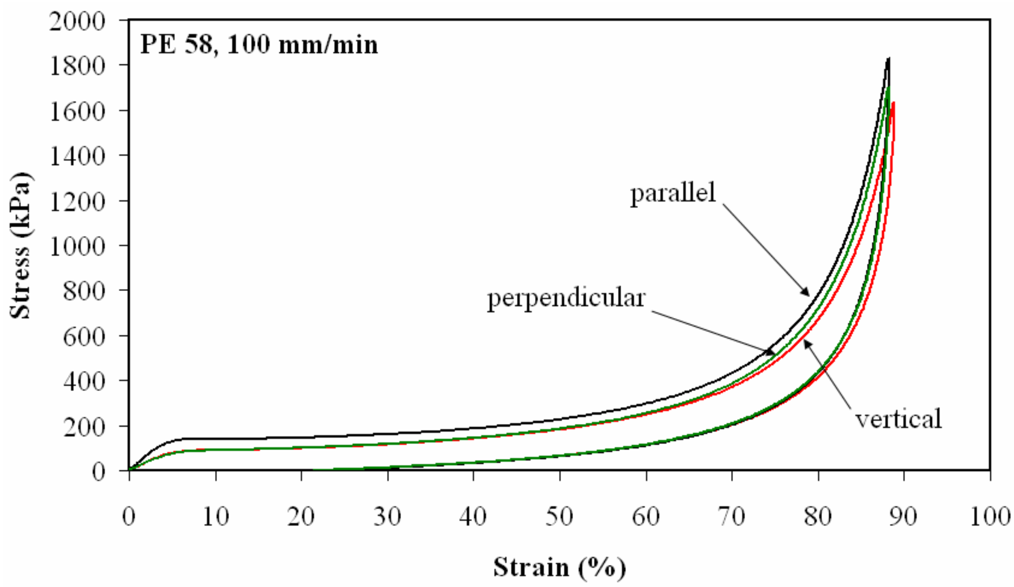

Figure 2.21. Stress versus strain for compressive loading and unloading of three PE 58 specimens in vertical, parallel, and perpendicular directions at 100 mm/min cross head speeds (compression direction is taken as positive)

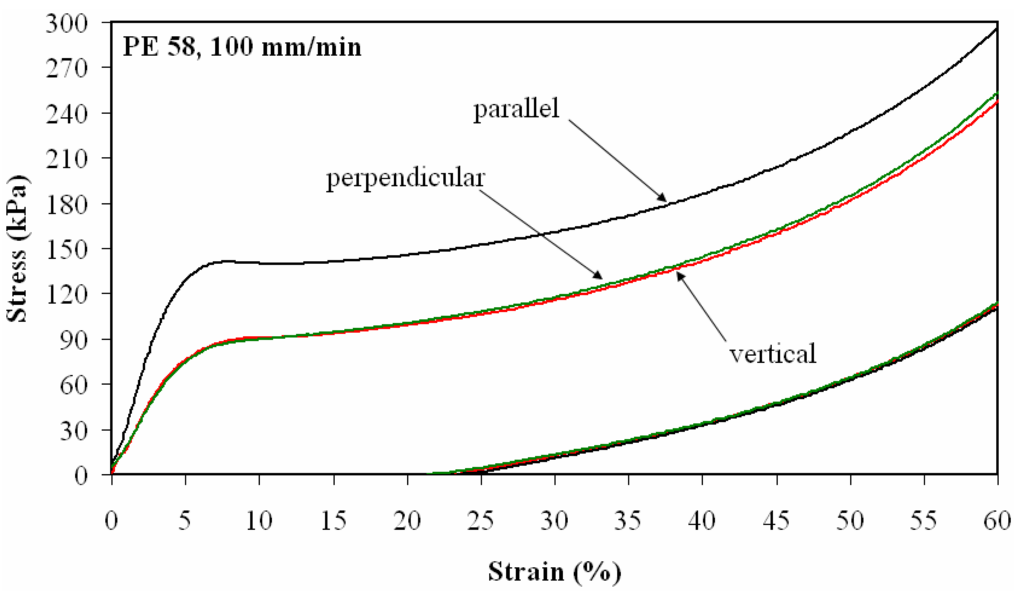

Figure 2.22. Stress (up to 300 kPa) versus strain (up to 60 per cent) for compressive loading and unloading of three PE 58 specimens in vertical, parallel, and perpendicular directions at 100 mm/min cross head speeds (compression direction is taken as positive)

2.1. Energy Absorption Characteristics Under Multiple Compressive Loading and Unloading

The primary use of foam packaging is to absorb impact energy while maintaining the reaction forces on the packaged object (stress) and the deformation of the package (strain) below design limits. The absorbed energy between two strain levels ε_0 and ε_f are defined as:

$$Energy = \int_{\varepsilon_0}^{\varepsilon_f} \sigma(\varepsilon)\, d\varepsilon \,. \tag{2.1}$$

When the absorbed energy at ε_f is divided by $\sigma(\varepsilon_f)$, efficiency of foam material is obtained [15] as shown below:

$$Efficiency = \frac{\int_{\varepsilon_0}^{\varepsilon_f} \sigma(\varepsilon)\, d\varepsilon}{\sigma(\varepsilon_f)} \,. \tag{2.2}$$

At high values of efficiency, foam absorbs larger amount of energy than the foam with low efficiency for the same stress level.

In Figures 2.23 and 2.24, stress versus strain, absorbed energy versus stress, absorbed energy versus strain, and efficiency versus stress graphs are given for different residual strain levels of second loadings for EPS 30 and PE 58 respectively. At each test, the specimen is first loaded up to a certain strain level, completely unloaded and then loaded for a second time and unloaded again. Only second loadings are plotted without plotting unloadings to make figures less crowded. For second loadings of EPS 30 in Figure 2.23, loading (I) starts from zero strain, loading (II) from 4.5 % residual strain, loading (III) from 10.8 %, loading (IV) from 17.6 %, loading (V) from 24.1 %, loading (VI) from 30.9, loading (VII) from 34.6, loading (VIII) from 38.5, and loading (IX) from 42.4 residual strain. For second loadings of PE 58 in Figure 2.24, loading (I) starts from zero strain, loading (II) from 3.0 % residual strain, loading (III) from 5.8 %, loading (IV) from 7.8 %, loading (V) from 10.0 %, loading (VI) from 12.1, loading (VII) from 14.1, and loading (VIII) from 16.5 residual strain. During the second loading of all measurements, load increases elastically up to the point where unloading in previous loading started, and then continues non-elastically as if they were never unloaded before. When a specimen is loaded up to a certain strain level, unloaded, and then loaded again, its mechanical behavior in subsequent loadings is much different from that of a virgin specimen depending on the residual strain of previous loading. The elastic deformation in second loading continues up to the point where unloading in previous loading started. Considering the same amount of energy is to be absorbed at each loading in a virgin and a previously deformed specimen, the deformation in the previously deformed specimen is much more compared to the virgin specimen.

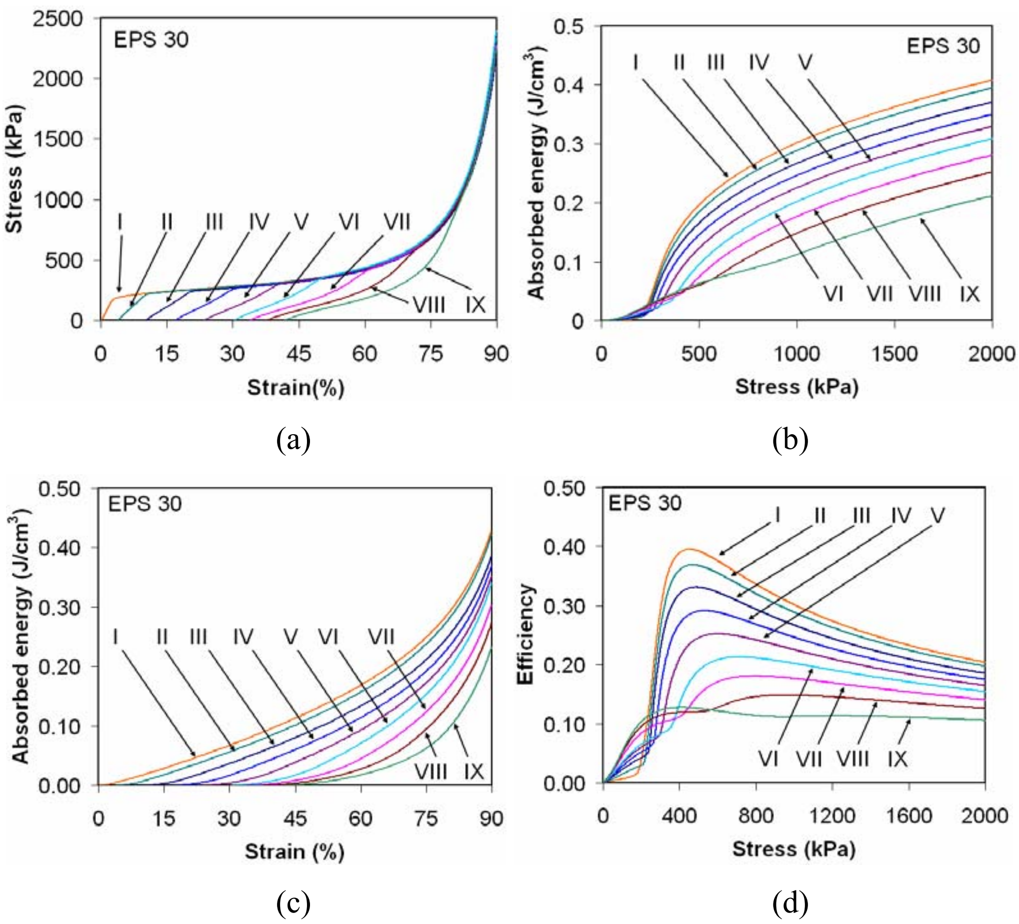

Figure 2.23. (a) Stress versus strain, (b) energy absorption versus stress, (c) energy absorption versus strain, (d) efficiency versus stress for 9 different compressive loadings (without unloading data plotted) starting at different residual strains, for EPS 30

When the residual strain level of the previously deformed specimen is high, small increases in deformation cause big increases in stress. Hence, efficiency reduces for a previously loaded specimen compared to a virgin specimen. It can be seen in Figures 2.23 (b)–2.23 (d) for EPS 30 and in Figures 2.24 (b)–2.24 (d) for PE 58 that there is a considerable decrease in absorbed energy and energy efficiency, and increase in stress and strain in second loadings for the same amount of energy absorbed. Hence foam packaging designer should consider multiple loading effects; it is clear that a foam packaged object which is not damaged in first loading can fail in subsequent loadings although same amount of energy is absorbed at each loading.

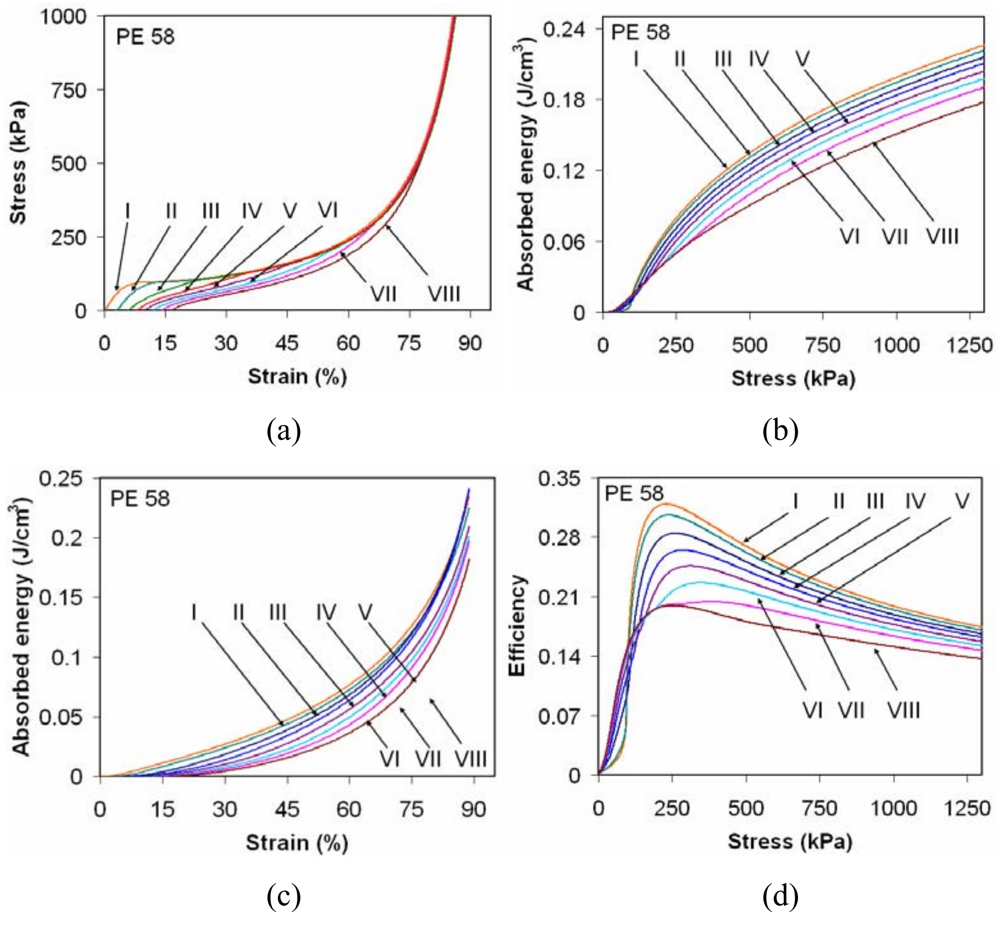

Figure 2.24. (a) Stress versus strain, (b) energy absorption versus stress, (c) energy absorption versus strain, (d) efficiency versus stress for 8 different compressive loadings (without unloading data plotted) starting at different residual strains, for PE 58

2.2. Experimental Approach for Energy Absorption Calculation Under Multiple Compressive Loading and Unloading

To study the behavior of EPS and PE foams under multiple loading and unloading in compression, the tensile testing machine is programmed so that the work done on the foam specimen by the applied load is the same at each loading. Such a loading profile is used to simulate the energy absorption of a foam package that drops multiple times from the same height. In Figure 2.25, load versus displacement data of two different tests are plotted. In the first test, EPS 30 is directly compressed up to 45 mm and then unloaded at 1000 mm/min cross head speed. In the second test, another EPS 30 specimen is compressed up to 14.4 mm and then unloaded at the same cross head speed. Then, the same specimen is compressed again, this time up to 22.3 mm (2nd loading in Figure 2.25) and unloaded. In total, 8 loadings and unloadings are performed in the second test and the work done by the force during each loading is equal to 6.7 Nm. In loadings 2 to 8, loading is elastic until the deformation level at which point the unloading of the previous step starts. Afterwards, as the loading increases, the deformation continues plastically and coincides with the loading curve of the first test.

Liu et al. [12-13] assumed that the elastic reloading curves have the same slope at all deformation levels. In the present study, however, that is not the case. Elastic modulus decreases in reloadings as the residual deformation increases. First elastic reloading curve is shown as the "2nd loading" in Figure 2.25. The elastic reloading curves (3rd, 4th, etc.) are straight at low deformation levels but gradually become curved at higher deformation levels. This behavior is observed for all densities of EPS and PE foams tested. The residual deformation at the end of each unloading is much less in PE compared to EPS. As a result, the work done during elastic loading is much higher in the case of PE when compared to EPS.

There are two important design criteria in foam packaging: The force that the package is subjected and the permanent deformation of the foam should be below specific limits. When the package drops from a certain height multiple times, the deformation of the foam and the reaction force on the package can be much higher compared to single loading as shown in Figure 2.25.

To study how load and deformation change with number of loadings from different heights, tests are conducted for up to 10 loadings, for 3 different densities of EPS and PE with work done per unit volume that ranges from 3 kJ/m^3 (5 % strain) to 200 kJ/ m^3 (90 % strain). Test results are given in Appendix A (Tables A.1–A.6). Tables A.1–A.6 are used to plot stress and strain versus number of loadings for different levels of absorbed energy per unit volume in Figures 2.26–2.37 for EPS 12, EPS 20, EPS 30, PE 24, PE 32, and PE 58. It is observed that for low values of absorbed energy, there may not be a considerable increase in stress for multiple loadings for EPS and PE foams. However as the absorbed energy amount causes the foam to deform close to densification regime, stress is increased multiple times for multiple loadings. Strain increase in multiple loading is more in first loadings and rate of increase of strain decreases with increasing number of loadings. PE has less residual deformation after unloading compared to EPS. Hence, the energy absorbed in elastic regions of reloading is much higher than EPS foams. At high levels of residual strain, the amount of absorbed energy in elastic region during reloading constitutes much of the total amount of absorbed energy for PE foams. Therefore, the increase in stress and strain at high number of loadings is less for PE foams compared to EPS foams.

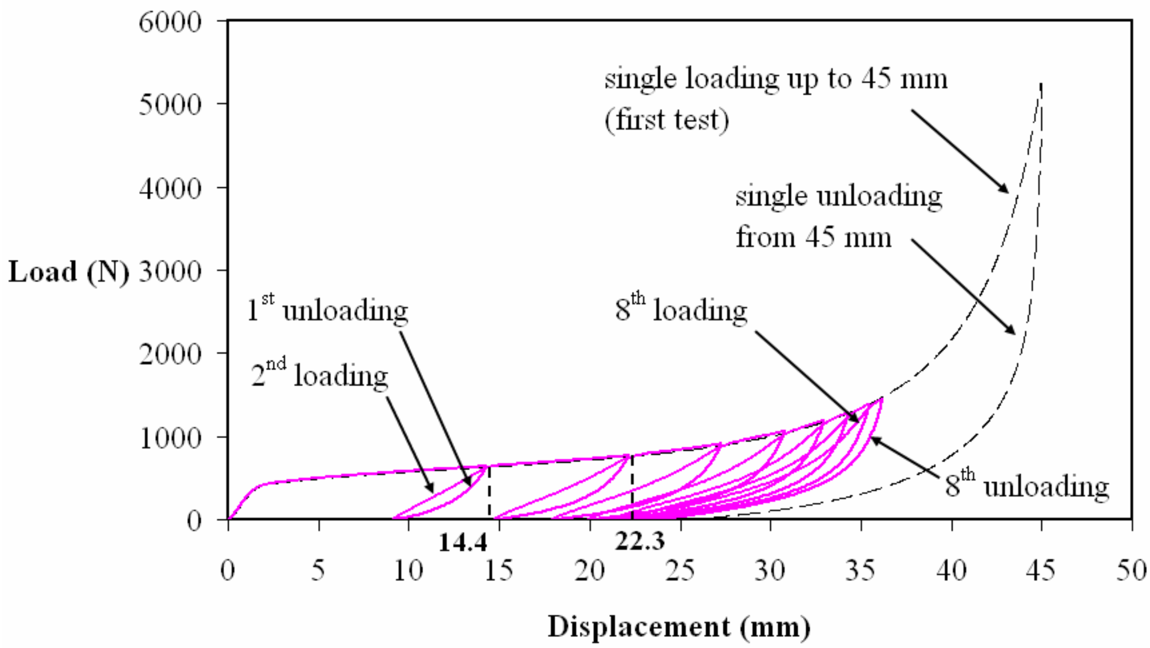

Figure 2.25. Load versus cross head displacement, single compressive loading and unloading of first test and 8 compressive loadings and unloadings of second test, for EPS 30 at 1000 mm/min cross head speed

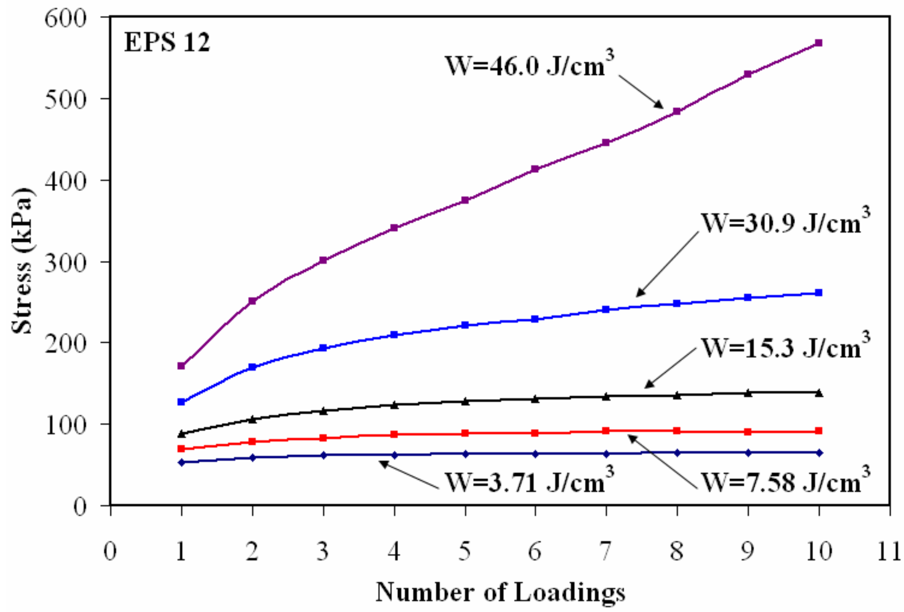

Figure 2.26. Stress versus number of loadings for EPS 12 for different levels of absorbed energy per unit volume

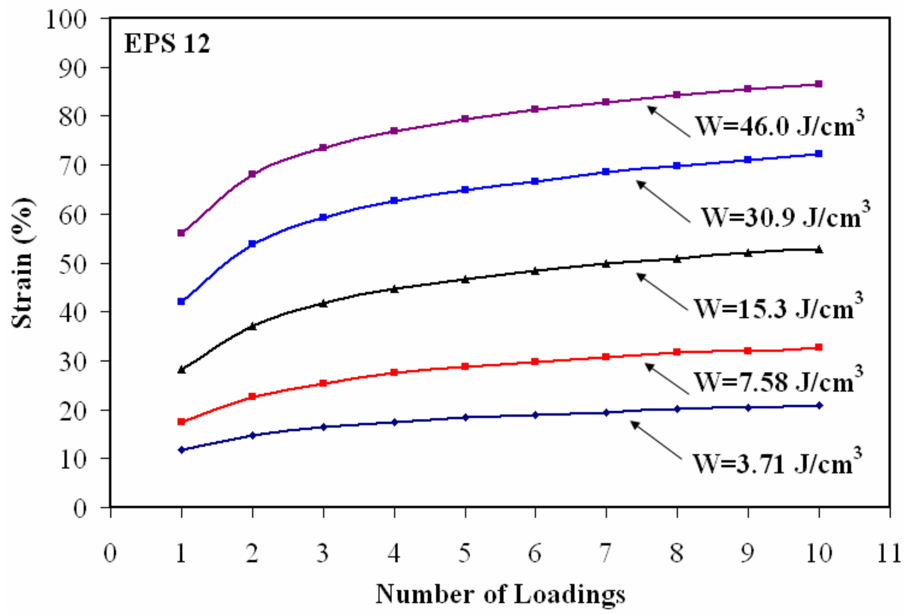

Figure 2.27. Strain versus number of loadings for EPS 12 for different levels of absorbed energy per unit volume

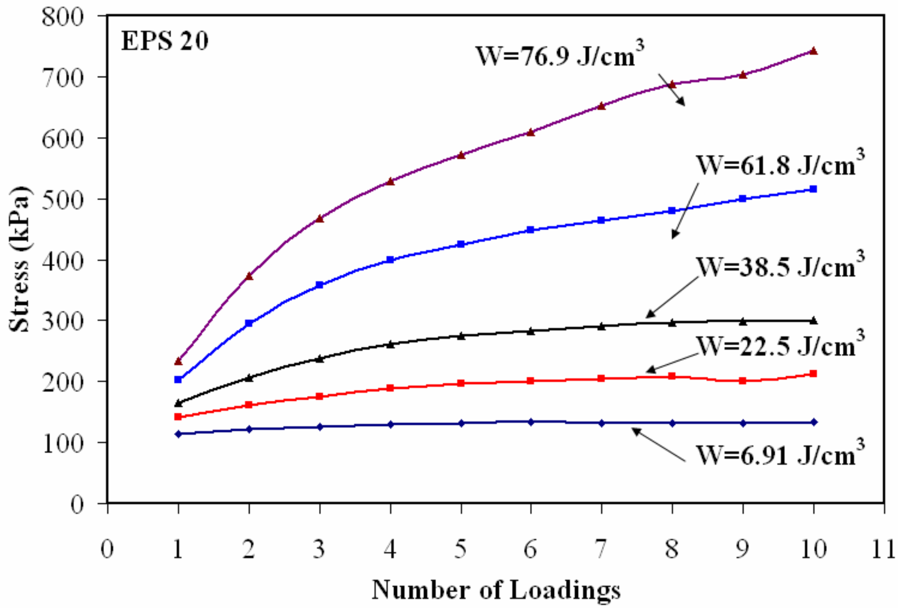

Figure 2.28. Stress versus number of loadings for EPS 20 for different levels of absorbed energy per unit volume

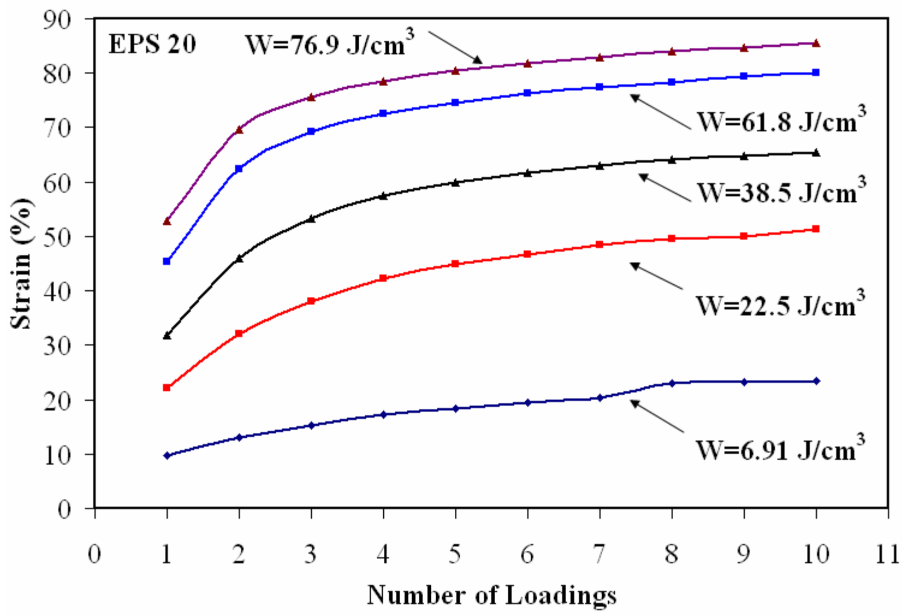

Figure 2.29. Strain versus number of loadings for EPS 20 for different levels of absorbed energy per unit volume

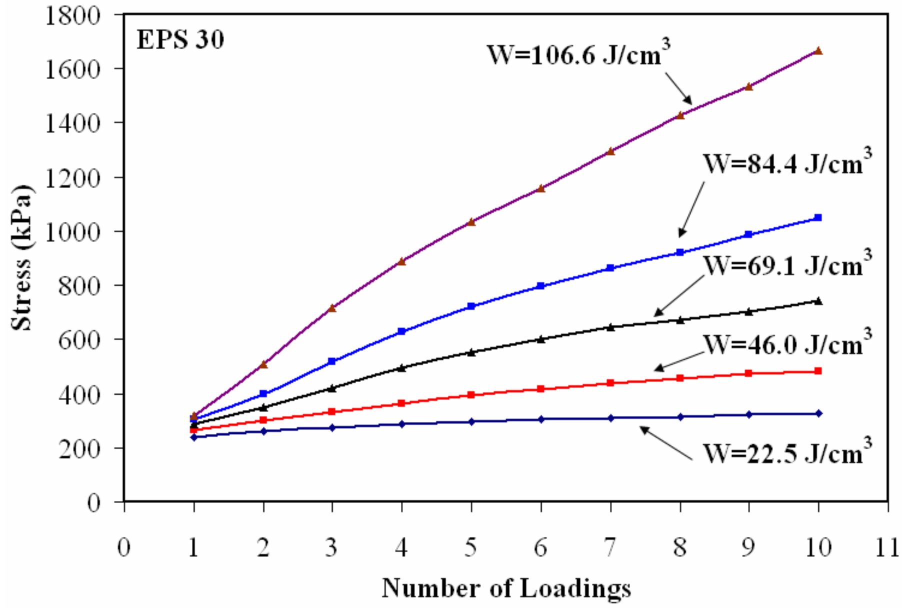

Figure 2.30. Stress versus number of loadings for EPS 30 for different levels of absorbed energy per unit volume

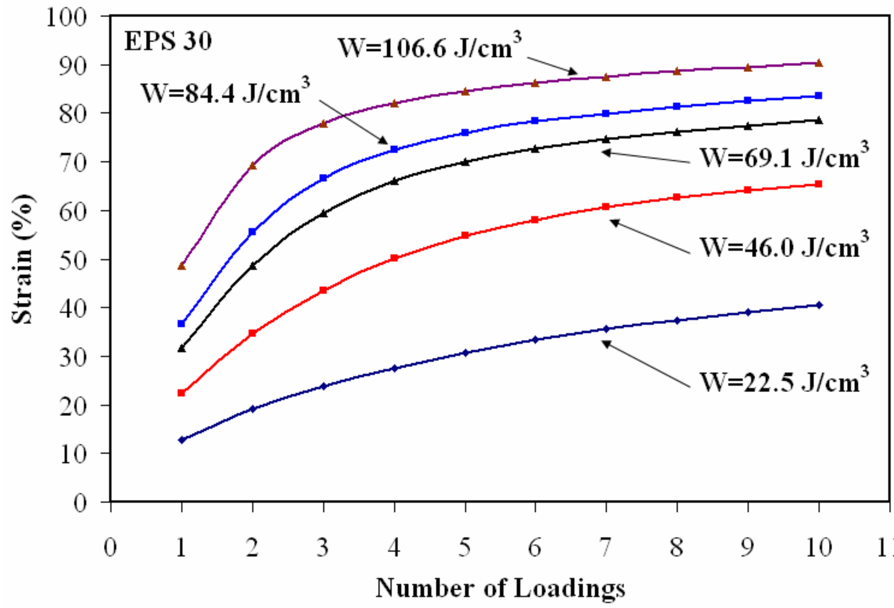

Figure 2.31. Strain versus number of loadings for EPS 30 for different levels of absorbed energy per unit volume

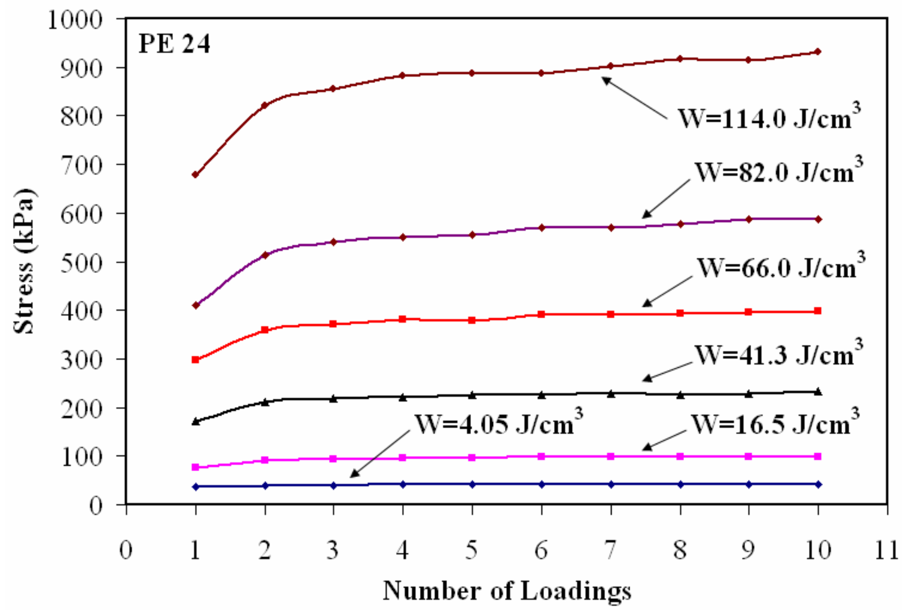

Figure 2.32. Stress versus number of loadings for PE 24 for different levels of absorbed energy per unit volume

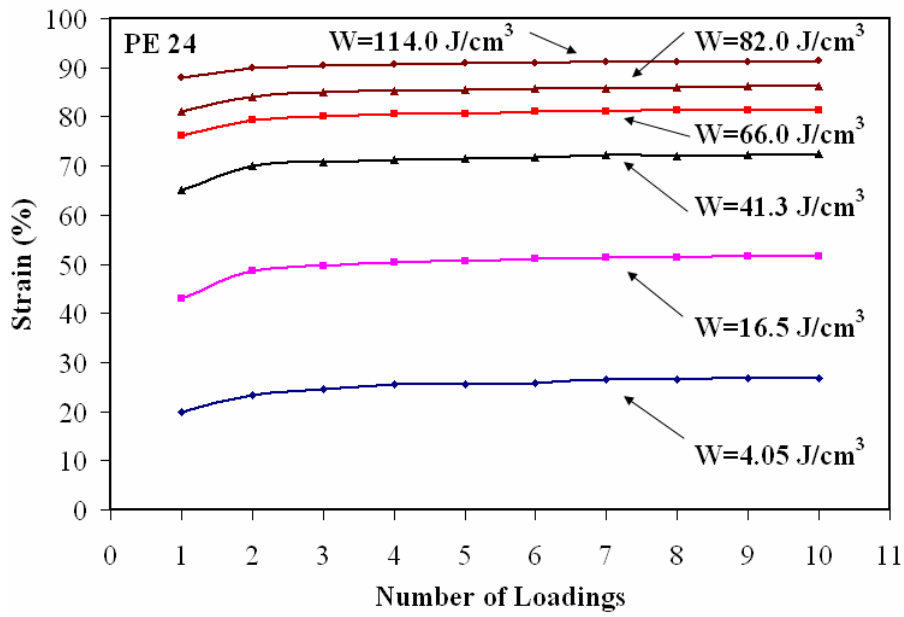

Figure 2.33. Strain versus number of loadings for PE 24 for different levels of absorbed energy per unit volume

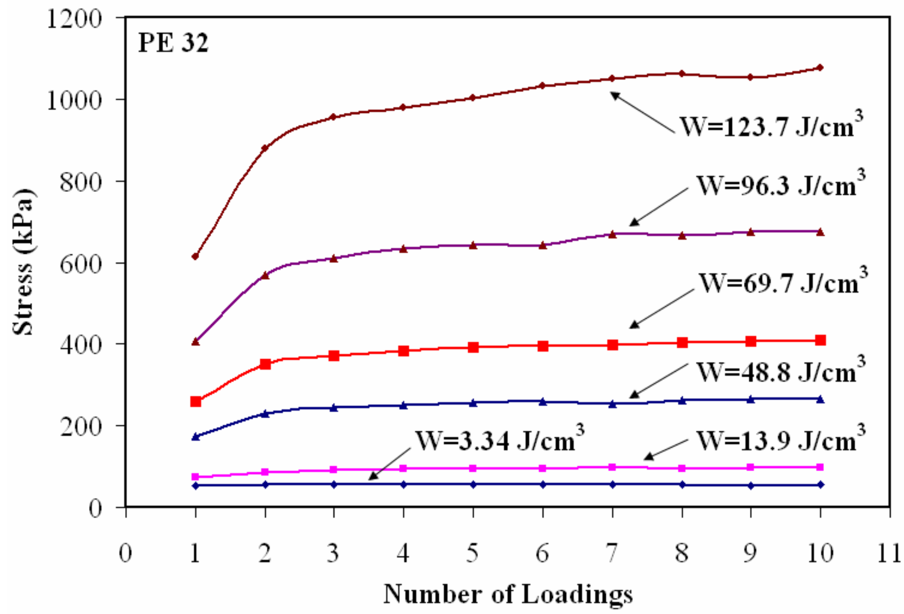

Figure 2.34. Stress versus number of loadings for PE 32 for different levels of absorbed energy per unit volume

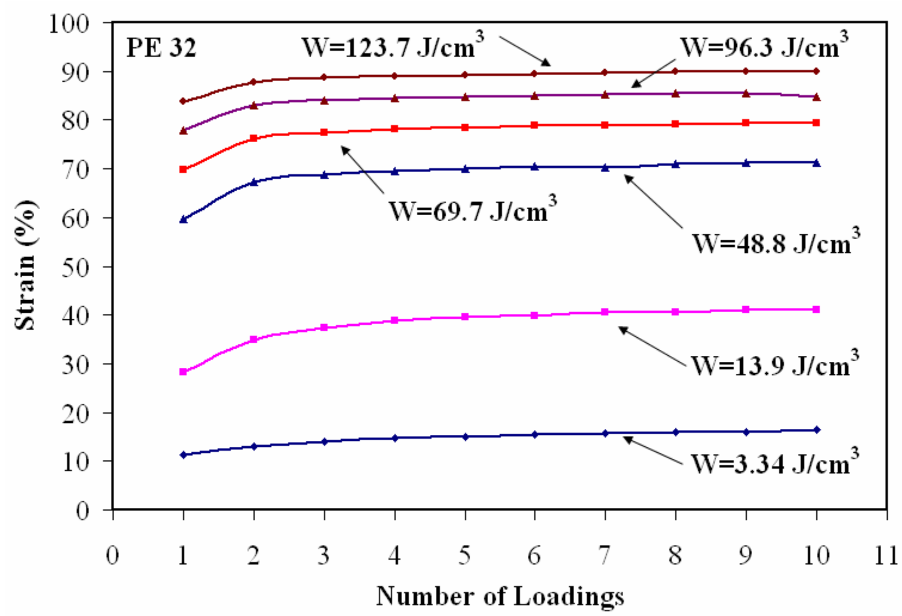

Figure 2.35. Strain versus number of loadings for PE 32 for different levels of absorbed energy per unit volume

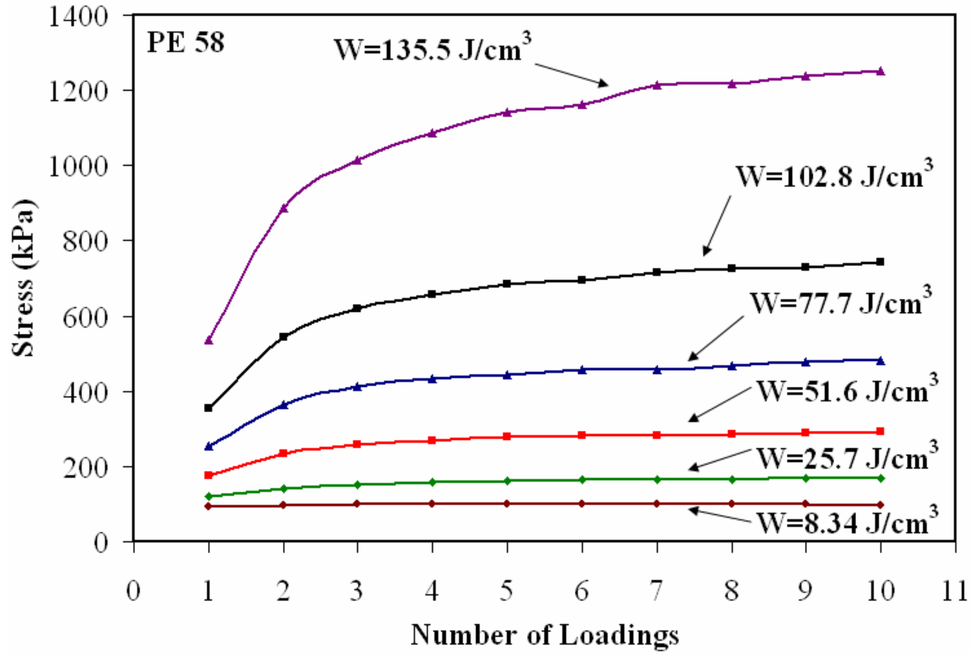

Figure 2.36. Stress versus number of loadings for PE 58 for different levels of absorbed energy per unit volume

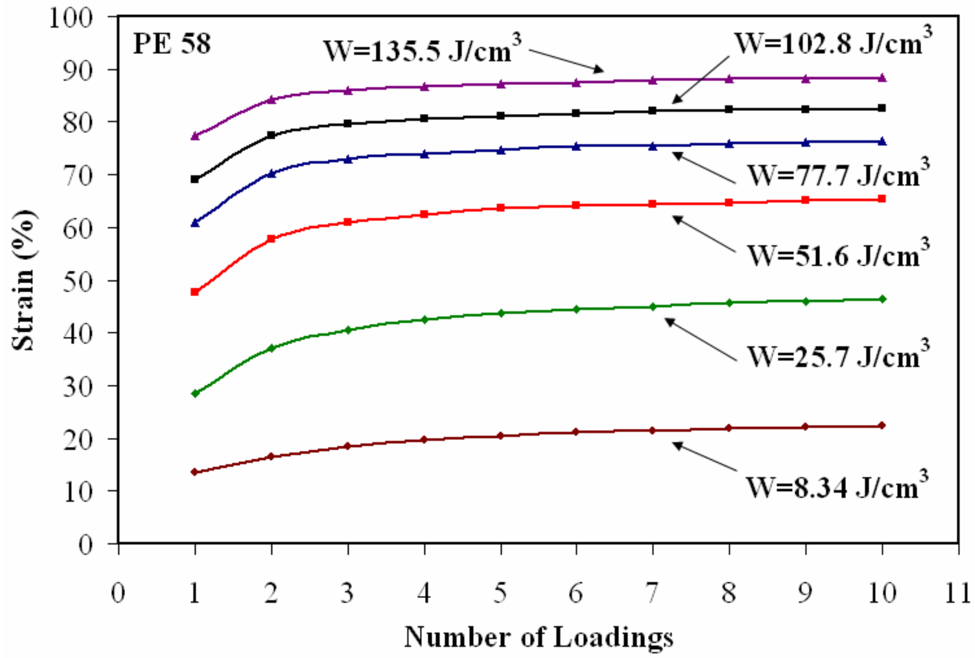

Figure 2.37. Strain versus number of loadings for PE 58 for different levels of absorbed energy per unit volume

An example of how to use those data is given in Table 2.3. Reaction forces and deformations measured for single loading and for 5 successive loadings are presented for 3 different densities of EPS and PE, for four different energy absorption cases: 86.3 kJ/m^3 , 54.9 kJ/m^3 , 23.5 kJ/m^3 ,7.8 kJ/m^3 respectively. These four cases are selected to observe the multiple compressive loading and unloading behavior of EPS and PE at low and high strain levels. At high strain levels, cell structures in foams collapse completely and the reaction force increases. This phenomenon is called densification of foams. For EPS and PE foams tested, densification occurs for strain values higher than 70 per cent. The Poisson's ratio is chosen to be zero in true stress calculations as suggested by Masso-Moreu and Mills [40].

The first case with an absorbed energy of 86.3 kJ/m^3 represents the drop of an object of mass, M, 1.1 kg from 1 m with a potential energy, P, equal to 10.8 Nm. Specimens have dimensions of 50 mm x 50 mm x 50 mm. In the first case, the reaction force of EPS at the end of the 5th loading is approximately 3 times higher than the value obtained in single loading. Strain of EPS 30 increases from 37 per cent when it is loaded once, to 76 per cent when it is loaded 5 times. At the end of 5th loading, the maximum reaction force and deformation occur for EPS 12, the minimum force occurs for EPS 20, and the minimum deformation is obtained for EPS 30. EPS 12 enters the densification region first because it is deformed more than EPS 20 and EPS 30. Therefore, the highest reaction force occurs for EPS 12. It is obvious that the lowest deformation will occur for EPS 30 and PE 58 since they have the highest densities. Similarly, the maximum force and deformations occur for PE 24, and the minimum force and deformations are obtained for PE 58.

In the second case, an object of mass 0.7 kg is assumed to drop from 1 m with a potential energy equal to 6.9 Nm. Results are similar to the first case. In the third case, an object of mass 0.3 kg is assumed to drop from 1 m with a potential energy equal to 2.9 Nm. At the end of the 5th loading, maximum compressive strains are 58 per cent and do not enter the densification region. At the end of the 5th loading, the reaction force for EPS is considerably higher than the value obtained for single loading. For EPS 30, strain increases from 13 per cent when it is loaded once, to 32 per cent when it is loaded 5 times. Maximum force and minimum deformation occur for EPS 30 whereas minimum force and maximum deformation are obtained for EPS 12 both at the end of single loading and 5 loadings. Similar respective results are obtained for PE 58 and PE 24 as well. In the fourth case, an object of mass 0.1 kg is assumed to drop from 1 m with a potential energy equal to 1.0 Nm. Results are similar to the third case. It is seen that there is not a straightforward rule for estimating which foam will have the maximum or minimum force and deformation. The results depend on strain level and number of loadings. There is a need to obtain data that are similar to those presented in Table 2.3 to estimate the multiple loading behavior of a foam.

Table 2.3. Reaction force and deformation results for single and 5 loadings tests

					single loading data				5 loadings data			
		M	P	W	strain	stress	def.	force	strain	stress	def.	force
case	foam	kg	Nm	kJ/m^3	%	kPa	mm	N	%	kPa	mm	N
1	EPS12	1.1	10.8	86.3	70.2	302	35.1	755	90.4	1052	45.2	2630
	EPS20	1.1	10.8	86.3	56.7	257	28.3	644	83.1	691	41.6	1727
	EPS30	1.1	10.8	86.3	37.0	310	18.5	776	76.4	744	38.2	1861
	PE24	1.1	10.8	86.3	82.1	441	41.0	1103	86.2	592	43.1	1481
	PE32	1.1	10.8	86.3	75.1	348	37.6	871	82.7	549	41.4	1374
	PE58	1.1	10.8	86.3	63.9	286	32.0	716	77.2	516	38.6	1290
2	EPS12	0.7	6.9	54.9	57.9	194	29.0	484	81.3	456	40.7	1140
	EPS20	0.7	6.9	54.9	41.6	191	20.8	477	66.9	349	33.5	872
	EPS30	0.7	6.9	54.9	25.7	280	12.8	699	61.0	451	30.5	1128
	PE24	0.7	6.9	54.9	71.9	239	35.9	598	77.5	317	38.8	792
	PE32	0.7	6.9	54.9	62.4	195	31.2	489	73.4	300	36.7	751
	PE58	0.7	6.9	54.9	49.9	186	24.9	464	65.3	297	32.7	742
3	EPS12	0.3	2.9	23.5	35.6	109	17.8	273	57.5	179	28.7	446
	EPS20	0.3	2.9	23.5	22.7	143	11.3	356	46.0	201	23.0	502
	EPS30	0.3	2.9	23.5	13.3	242	6.6	605	31.9	300	15.9	750
	PE24	0.3	2.9	23.5	50.6	102	25.3	256	57.9	131	29.0	327
	PE32	0.3	2.9	23.5	39.7	98	19.8	244	51.5	133	25.8	333
	PE58	0.3	2.9	23.5	26.8	118	13.4	294	41.3	154	20.7	384
4	EPS12	0.1	1.0	7.8	17.7	70	8.8	175	29.4	90	14.7	224
	EPS20	0.1	1.0	7.8	10.5	116	5.3	289	20.1	135	10.1	337
	EPS30	0.1	1.0	7.8	7.1	209	3.5	523	12.6	226	6.3	565
	PE24	0.1	1.0	7.8	28.4	48	14.2	120	35.5	58	17.7	146
	PE32	0.1	1.0	7.8	18.8	64	9.4	159	26.9	72	13.4	179
	PE58	0.1	1.0	7.8	12.9	94	6.5	234	19.3	98	9.7	245

2.3. Phenomenological Constitutive Modeling for Multiple Uniaxial Compressive Loading and Unloading

A constitutive model that gives accurate stress–strain relationship for both loading and unloading is needed at any residual strain level for calculations of stress, strain, and absorbed energy. Although unloading is not important for failure in general, accurate calculation of residual strain after loading is needed because the mechanical behavior depends on the level of residual strain in subsequent loading. In this section, results of two existing constitutive models and a new proposed constitutive model are compared to experimental measurements at different residual strain levels. Then, modeling of unloading is presented with comparisons to experimental results at different strain levels. Finally, a procedure for stress, strain, and absorbed energy calculations in multiple loading and unloading is presented.

There are many constitutive models in literature for single loading that include effects of strain rate, temperature and density [1, 4 -14], but they do not consider unloading and reloading. Most recent ones are by Liu et al. [12-13] and Avalle et al. [13]. Liu et al. [12-13] developed a constitutive model for open cell foams uniaxially compressed in a rigid confinement, and they obtained the following stress-strain relationship:

$$\sigma(\rho,\varepsilon)=A(\rho)\frac{e^{\alpha(\rho)\varepsilon}-1}{1+e^{\beta(\rho)\varepsilon}}+e^{C(\rho)}\left(e^{\gamma(\rho)\varepsilon}-1\right). \tag{2.3}$$

In the equation above, the first term is for elastic and plateau regions and the second term accounts for densification region. In their model, the parameters A, α, β, C, and γ are density (ρ) dependent. Liu et al.'s [12] performed multiple loading experiments to produce specimens with higher densities to be able to set the relationship between the parameters used in Equation (2.3) and density, so that they can work with less number of specimens. They also stated that due to the differences between the elastic loading response of a virgin specimen and the deformed specimen, it is not fully justified to consider a deformed specimen to be equivalent to a virgin specimen with increased initial bulk density. It will be shown later in this study that the elastic behavior in subsequent loadings change a lot from linear to nonlinear as the deformation level increases for EPS and PE. The energy absorbed in elastic region in subsequent loadings is important, especially at high residual strain levels. Therefore the elastic region in multiple loading should be modeled accurately.

On the other hand, Avalle et al. [13] developed the following constitutive model for polymeric foams

$$\sigma(\varepsilon) = A\left(1 - e^{(-E/A)\varepsilon(1-\varepsilon)^m}\right) + B\left(\frac{\varepsilon}{1-\varepsilon}\right)^n, \tag{2.4}$$

where A can be considered as the stress level in plateau region, and E as the elastic modulus.

The parameters in constitutive equations are found by least square fitting to experimental data. This iterative minimization procedure starts by the calculation of objective function for initial values of coefficients. Then, the objective function is minimized by changing the coefficients. This procedure can easily be done by mathematics software packages in few seconds by standard personal computers, where the default objective function is the sum of the squares of the differences between the stress calculated by constitutive model and the stress measured in experiments. Avalle et al. [13] suggested selecting the objective function as the sum of the differences between the stress calculated by the model and the experimentally measured stress divided by the experimentally measured stress.

When applying Equations (2.3) and (2.4) for modeling multiple loading behavior, one should take care of the following issues. First, both equations give zero stress at zero strain. This means that when modeling loading data with nonzero residual strain in subsequent loadings, least square fitting results for a loading path that starts from zero strain. To overcome this problem, loading data with nonzero residual strain should be shifted to zero strain, then perform the least square fitting procedure, and then transform back the loading stress–strain data to nonzero residual strain. Secondly, least square fitting procedure for Equations (2.3) and (2.4) is not straight forward. For both equations and objective functions selected, selection of the initial value for iterations of minimization procedure is important for convergence to the right local minima, which gives exact parameters of the function. To select those initial values for parameters, it is suggested by Liu and Subhash [11] to divide equations and experimental data into two portions, first portion of data includes elastic and plateau region and the second portion of data includes the densification region. Then, each divided equations are fitted separately to the divided portions of data. The parameters converged are used as initial values for the least square fitting procedure of Equations (2.3) or (2.4) to the complete experimental data. Therefore three least square fittings should be done in total to be able to find the parameters of Equations (2.3) and (2.4).

In addition to the drawbacks of Equations (2.3) and (2.4) for modeling multiple loading data, it is found out that the use of a single equation for both elastic and non-elastic regions decrease the accuracy around yield region because the transition from elastic to non-elastic region is not smooth in stress–strain curves for multiple loadings. Gibson and Ashby [1] proposed a linear model for the elastic region and a nonlinear model for densification region for single loading of foams. However, especially at high residual strain levels, the elastic behavior is not linear as seen in Figures 2.23 (a) and 2.24 (a). Therefore in this study, it is preferred to use separate equations for modeling of stress–strain response in elastic loading region, plastic loading region including plateau and densification regimes, and unloading region. Many functions are tried to give the best fit to the experimental measurements with few terms. A constitutive model consisting of high order polynomial terms, such as the 10^{th} order polynomial suggested by Sherwood and Frost [9], oscillates around the experimental stress-strain curve. Exponential terms are useful to express the high increase of stress without any oscillations in densification region. Among the many functions tried, an equation consisting of exponential and up to 3^{rd} order polynomial terms is chosen for the approximation of stress–strain data in elastic loading, plastic loading, and unloading regions with separate coefficients for each region. In elastic loading and unloading regions, the nonlinear behavior depending on the residual strain level is modeled mainly by polynomial terms, and the contribution of the exponential terms is less. In densification region however, sharp increase in stress for small strain increments is expressed mainly by the exponential terms. Equation (2.5) used for modeling stress–strain response in elastic loading region is given as

$$\sigma_{elastic} = e^{(A_{el}\varepsilon + B_{el})} + C_{el}\varepsilon^3 + D_{el}\varepsilon^2 + E_{el}\varepsilon + F_{el}\,, \tag{2.5}$$

where A_{el}, B_{el}, C_{el}, D_{el}, E_{el} and F_{el} are coefficients to be determined separately for each reloading. For plateau and densification regions, same equation as elastic region with separate coefficients is used as

$$\sigma_{plastic} = e^{(A_{pl}\varepsilon + B_{pl})} + C_{pl}\varepsilon^3 + D_{pl}\varepsilon^2 + E_{pl}\varepsilon + F_{pl}\,, \tag{2.6}$$

where A_{pl}, B_{pl}, C_{pl}, D_{pl}, E_{pl} and F_{pl} are coefficients to be determined for single loading only because the non-elastic stress-strain curve does not change with number of loadings.

Equations (2.5) and (2.6) can have nonzero strain for zero stress, therefore there is no need to arrange the multiple loading data with nonzero residual strain as needed for Equations (2.3) and (2.4). Least square fittings of Equations (2.5) and (2.6) to measured stress–strain data in multiple loading are very straightforward compared to those of Equations (2.3) and (2.4). It converges always to the exact values of coefficients whatever are the initial values of coefficients. There is no need to perform previous least square fitting procedures to find the right initial values of the coefficients before starting the least square fitting of Equations (2.3) and (2.4). Computational time needed for least square fittings of Equations (2.5) and (2.6) is just few seconds compared to that of Equations (2.3) and (2.4) in a standard personal computer. Considering all of these aspects, using Equations (2.5) and (2.6) for modeling multiple loading behavior is simpler and faster compared to using Equations (2.3) and (2.4).

In Figure 2.38, the per cent difference between the stress calculated by the three models and the experimentally measured stress are plotted for the measured per cent strain in bottom axis and the measured stress in top axis. The calculations are done for 4 different loadings (I–IV–VI–IX) given in Figure 2.23 with 0, 17.6 %, 30.9 %, and 42.4 % residual strains respectively for EPS 30. At strain levels less than 2 per cent, calculated stress values are very small, therefore per cent differences of stress are very high but their contribution to energy absorption is negligible. Largest per cent differences are observed for yield region in Figure 2.38 (b) with 18 per cent difference for Liu's model and 13 per cent difference for Avalle's model, and in Figure 2.38 (c) with 9 per cent difference for Liu's model and 10 per cent difference for Avalle's model. The new proposed model has less than 2 per cent difference for yield region in Figures 2.38 (b) and (c). Constitutive models with single equation are inadequate to model the sharp transition from elastic to non-elastic region. For low and high residual strain loading cases given in Figures 2.38 (a) and (d) respectively, this transition is smoother and the per cent differences of Liu's model and Avalle's model are less in yield region compared to those given in Figures 2.38 (b) and (c). The results of the new proposed model are still better than the others for yield region in Figures 2.38 (b) and (c). It is also seen that it is more accurate to use the new proposed model for strain levels outside the yield region for all loadings cases. Similar results are given in Figure 2.39 for PE 58 for 4 different loadings (I–III–V–VIII) given in Figure 2.24 with 0, 5.8 %, 10.0 %, and 16.5 % initial strains respectively. PE 58 shows more nonlinear behavior in elastic region in multiple loadings compared to EPS 30, and results for Liu's model and Avalle's model show larger per cent differences for PE 58 compared to EPS 30. It is found out again for PE 58 that more accurate results are obtained by the new proposed model compared to those obtained by Liu's and Avalle's models for all loading cases.

Coefficients of Equation (2.5) are calculated by using least squares fit to measured stress–strain data in elastic region at different initial strain levels. For finding out the coefficients at unmeasured residual strain values, a relationship between coefficients and residual strain can be used. This relationship can then be replaced in Equation (2.5) so that stress–strain at any residual strain can be expressed by a single equation. The relationship between coefficients and residual strain is an approximation of the measured values, and stress calculated by Equation (2.5) changes a lot with small variations in its coefficients. Hence successful evaluations of the elastic curve for any residual strain value cannot be done accurately by this method. Another way to find out the elastic loading behavior for unknown residual strain levels is to use linear interpolation between measured values of stress, and accurate results are obtained by this method.

Calculation of residual strain after unloading is important because it will give the value of initial strain for the next loading. If the residual strain is not accurately calculated, the mechanical behavior of the foam and the absorbed energy in subsequent loading cannot be determined correctly. Unloading curves are shown in Figure 2.40 (a) for EPS 30 for 18 different strain levels and in Figure 2.40 (b) for PE 58 for 10 different strain levels. Elastic loading data, except for the first loading, are not plotted in Figure 2.40 (a) and (b) to make them less crowded. Same equation used for elastic and non-elastic regions is found to be

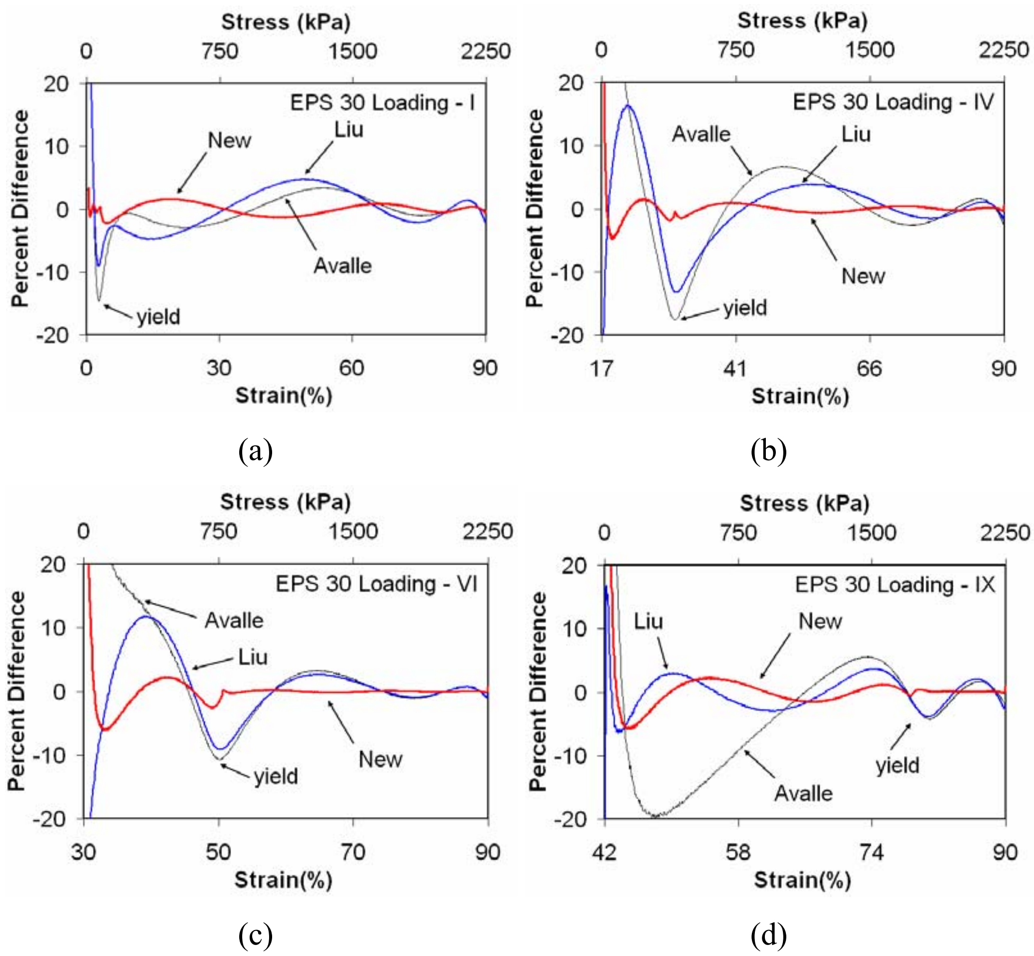

Figure 2.38. Per cent difference between experimentally measured stress and stress calculated by Liu’s model, Avalle’s model, and proposed model for (a) loading I, (b) loading IV, (c) loading VI, and (d) loading IX given in Fig. 2.23 for EPS 30

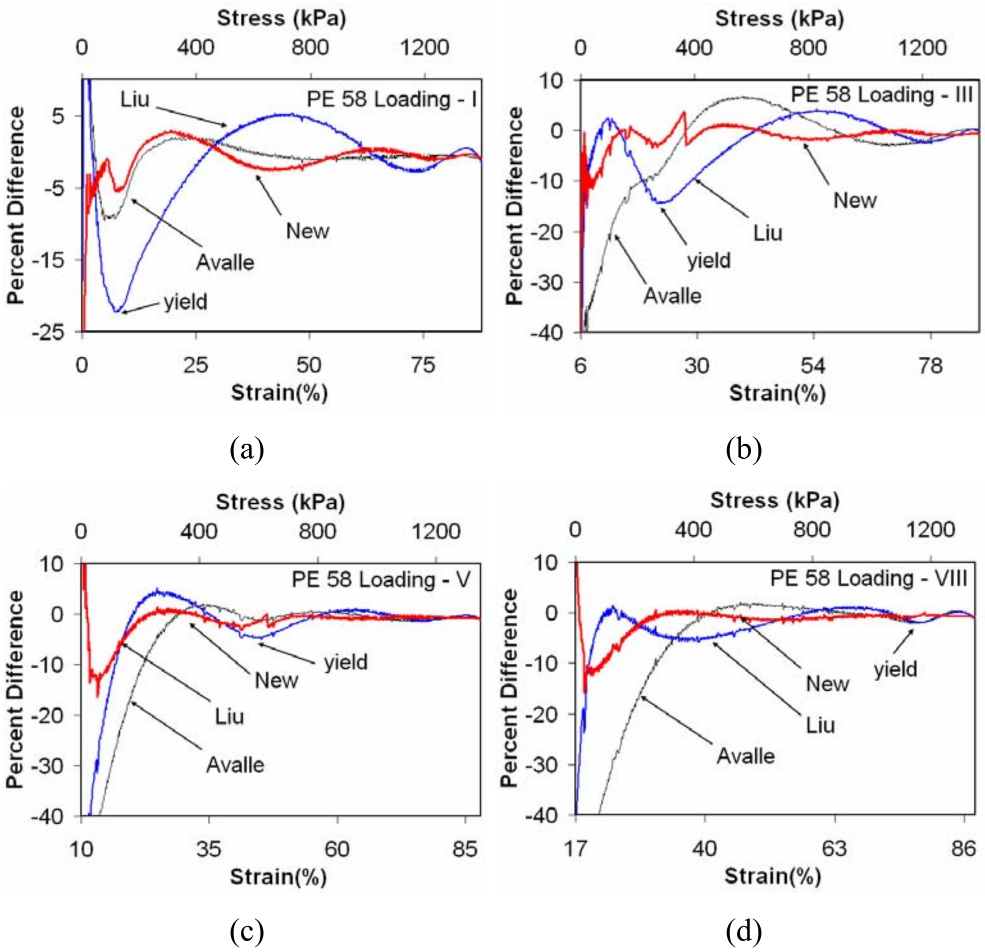

Figure 2.39. Per cent difference between experimentally measured stress and stress calculated by Liu's model, Avalle's model and new proposed model for (a) loading I, (b) loading III, (c) loading V, and (d) loading VIII given in Fig. 2.24 for PE 58

enough accurate to model the unloading stress-strain relationship as

$$\sigma_{unloading} = e^{(A_{unl}\varepsilon + B_{unl})} + C_{unl}\varepsilon^3 + D_{unl}\varepsilon^2 + E_{unl}\varepsilon + F_{unl}\,, \tag{2.7}$$

where A_{unl}, B_{unl}, C_{unl}, D_{unl}, E_{unl}, and F_{unl} are coefficients to be determined separately for each unloading. Similar to Equations (2.5) and (2.6), least square fitting of Equation (2.7) does not need special procedures like Equations (2.3) and (2.4), it is simple and fast to use it for unloading stress and strain calculations in multiple loading.

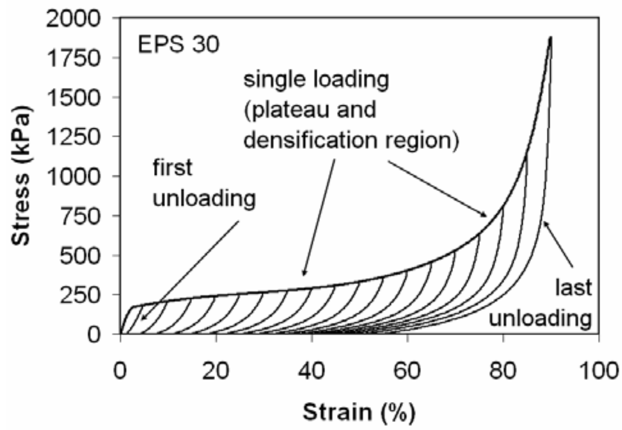

(a)

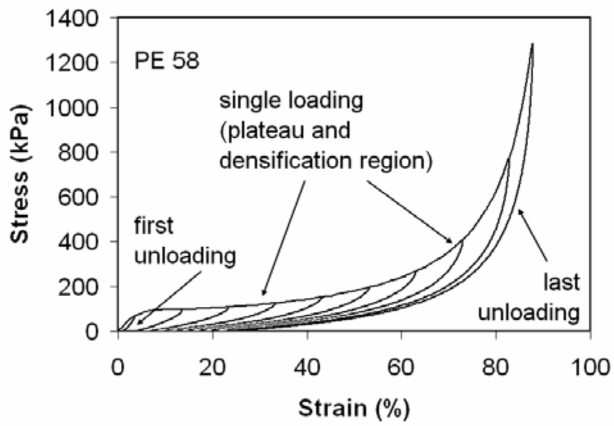

(b)

Figure 2.40. Experimentally measured stress-strain curve for single and multiple compressive unloading at different strain levels for (a) EPS 30 and (b) PE 58

Percent differences between calculated and measured stress are given for 4 different strain levels in Figure 2.41 for EPS 30 and in Figure 2.42 for PE 58. The per cent differences are higher for very small stress levels, but acceptable because absorbed energy is less. Per cent differences are much better at higher strain levels.

Similar to Equation (2.5), Equation (2.7) is very sensible to small changes in its coefficients. Therefore interpolation of measured stress and strain values is recommended to find out the unknown unloading behavior for unmeasured strain levels.

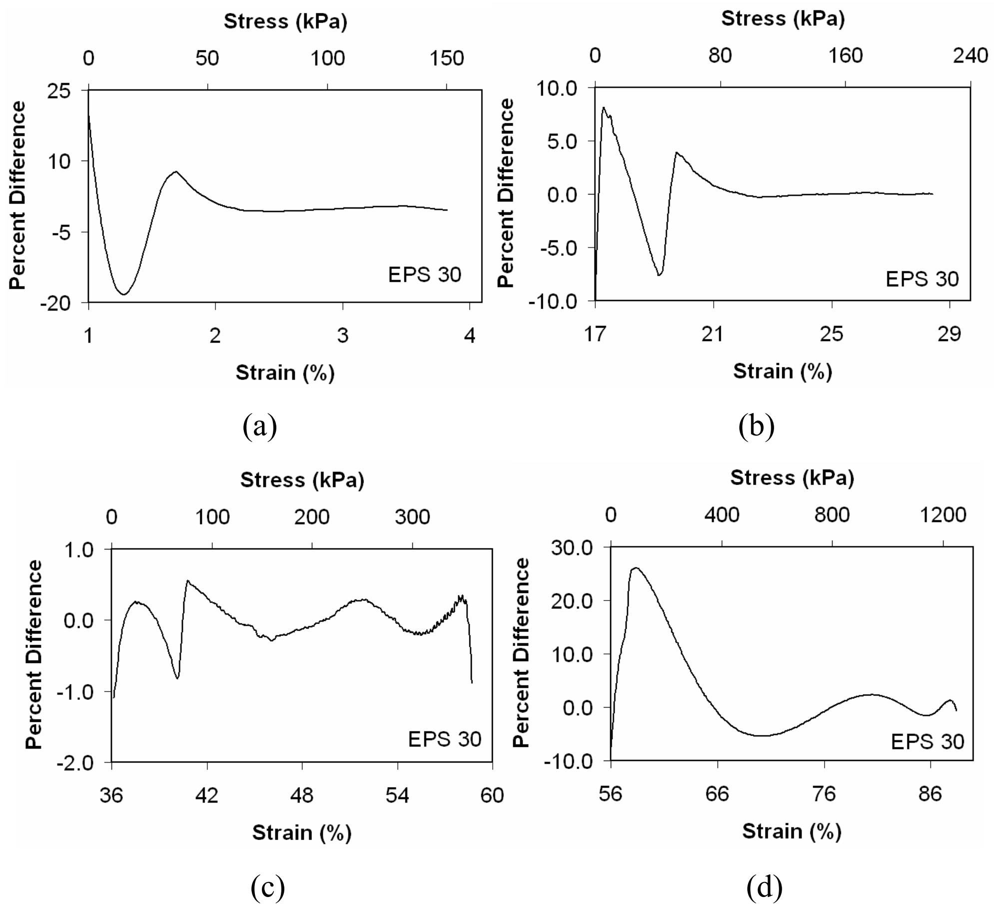

Figure 2.41. Per cent difference between calculated and experimentally measured stress versus experimentally measured stress and strain for four different residual strain levels given in Figure 2.40 (a) for EPS 30

Design guides for foam packaging and available studies in literature are focused on single loading of foam. The following steps can be followed for stress and strain calculation for a specific amount of absorbed energy and number of loadings.

1) Obtain stress-strain curve for the foam specimen under single compressive loading and unloading.

2) Load and unload twice at least 5 separate specimens and measure stress-strain with different residual strain levels for second loadings.

3) Calculate coefficients A_{el}, B_{el}, C_{el}, D_{el}, E_{el}, and F_{el} for Equation (2.5), coefficients A_{pl}, B_{pl}, C_{pl}, D_{pl}, E_{pl}, and F_{pl} for Equation (2.6), and coefficients A_{unl}, B_{unl}, C_{unl}, D_{unl}, E_{unl}, and F_{unl} for Equation (2.7) using test data.

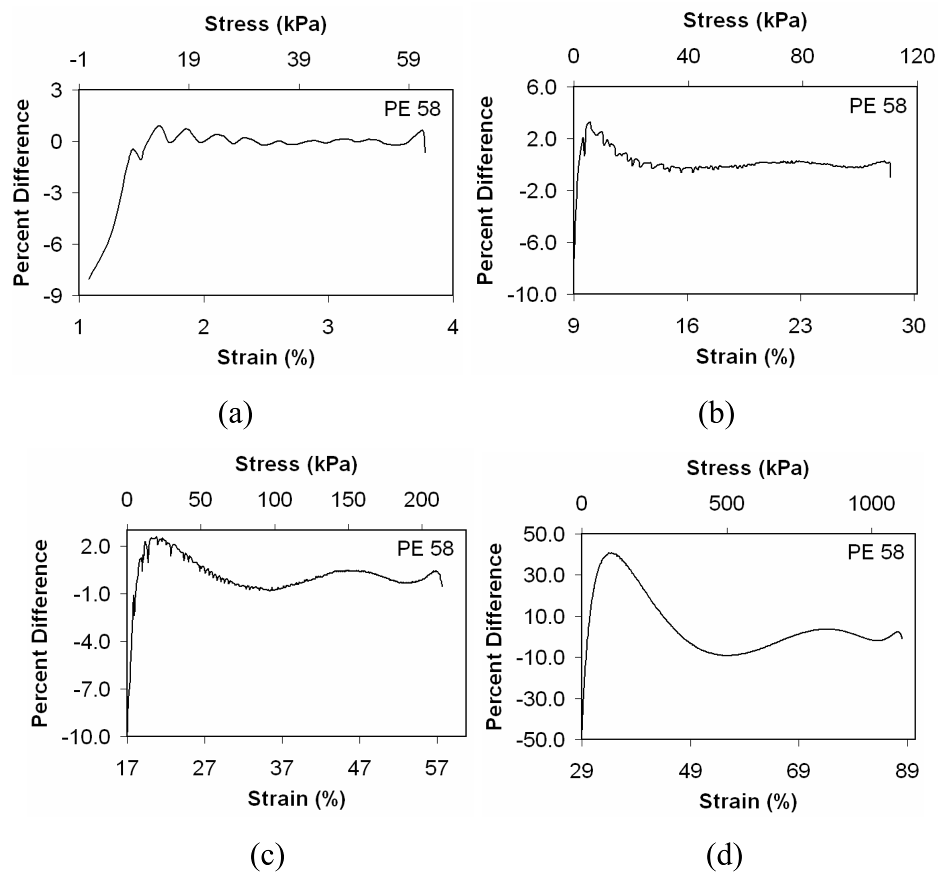

Figure 2.42. Per cent difference between calculated and experimentally measured stress versus experimentally measured stress for four different residual strain levels given in Figure 2.40 (b) for PE 58

4) Calculate stress and strain for the specific amount of absorbed energy by using Equations (2.5) and (2.6).

5) Calculate stress-strain in unloading by using interpolation of measured unloading stress-strain data. Specify the residual strain after unloading.

6) For the subsequent loading, use the residual strain as initial strain and obtain stress-strain relationship in elastic loading using interpolation of measured loading stress-strain data.

7) Calculate coefficients A_{el}, B_{el}, C_{el}, D_{el}, E_{el}, and F_{el} for Equation (2.5), from data obtained in the previous step.

8) Calculate stress and strain for the specific amount of absorbed energy by using Equation (2.5) with coefficients calculated in previous step and Equation (2.6).

9) Repeat steps 5–9 for subsequent loadings.

3. UNIAXIAL COMPRESSIVE LOADING BEHAVIOR OF LOW DENSITY POLYMERIC FOAMS AT HIGH LOADING SPEED (DROP TEST)

In general, mechanical behavior of polymeric foams are loading rate sensitive. Universal tensile testing machines like Zwick Z020 are usually driven by hydraulic systems, and their maximum loading speed (1000 mm/min) is much less than the one occurring in a drop test. An object that is falling freely from 50 cm height would reach 3.1 m/s (=186000 mm/min, 186 times of maximum speed of Zwick Z020) speed neglecting any friction effects. In the literature, there are several studies for test equipments to measure compressive stress–strain behavior at high loading speeds [16-23]. Although test data at high strain rates can be found in literature for EPS and PE, low density polymeric foam's physical properties can change considerably depending on the supplier's formulation and process. Mechanical responses of EPS and PE foams from different suppliers can be considerably different [1]. Therefore a test rig is needed to measure the load and deformation of the specimen at high loading speeds. In this chapter, a drop test rig is constructed to measure the uniaxial compressive behavior of foam specimens at high strain rates. Then, uniaxial compressive stress–strain results for EPS 30 and PE 58 obtained using the drop test rig are compared to those obtained from Zwick Z020 universal tensile testing machine.

3.1. Drop Test Rig

The test rig consists of 4 standing rails which are connected by a steel plate on the bottom and an aluminium plate on the top. Two free falling beams are attached to the rails by ball bearings. One of the free falling beams is for testing specimens up to 240 mm width, and the other is for those up to 700 mm. It is recommended by Juntikka et al. [16] to use the small beam for testing small size specimens to reduce vibrations which occur on the beam after impact. A transparent cabinet closes the test area for safety (Figures 3.1–3.4). Load cell MC3A–1000 from AMTI with 4400 N range is placed on the ground to measure the reaction force on the specimen. The test specimen with 50 x 50 mm^2 base area can be placed directly on the load cell. For larger specimens, a metal plate should be attached by screwing it on the load cell. It is better to put the specimen directly onto the load cell to have more accurate load signal. A metal plate is attached to the falling beam to compress the specimen. A light wood part is attached to the free falling beam to reflect light beam coming from the laser displacement sensor LK-G37 from Keyence with 30 ± 5 mm range. The laser sensor is placed on a standing plate so that its position can be adjusted according to specimens with different heights. The specimen height used for drop test is 20 mm with 50 x 50 mm^2 base area because the measurement range of laser displacement sensor is 30 mm. The accelerometer 356A25 is from PCB with ± 200 g measurement range is attached on the free falling beam by gluing. An electro magnet attached to a DC motor on top of the test rig is used to carry the free falling beam upward. There is an adjustable barrier on the rails on which the free falling beam carried by the magnet strikes and the beam is left to free fall. The falling height of the beam can be adjusted accurately with this method. Data are recorded at 80 kHz sampling rate by using VXI data acquisition system with a 16 channel 24 bit VT1432B card from Agilent and a desktop computer.

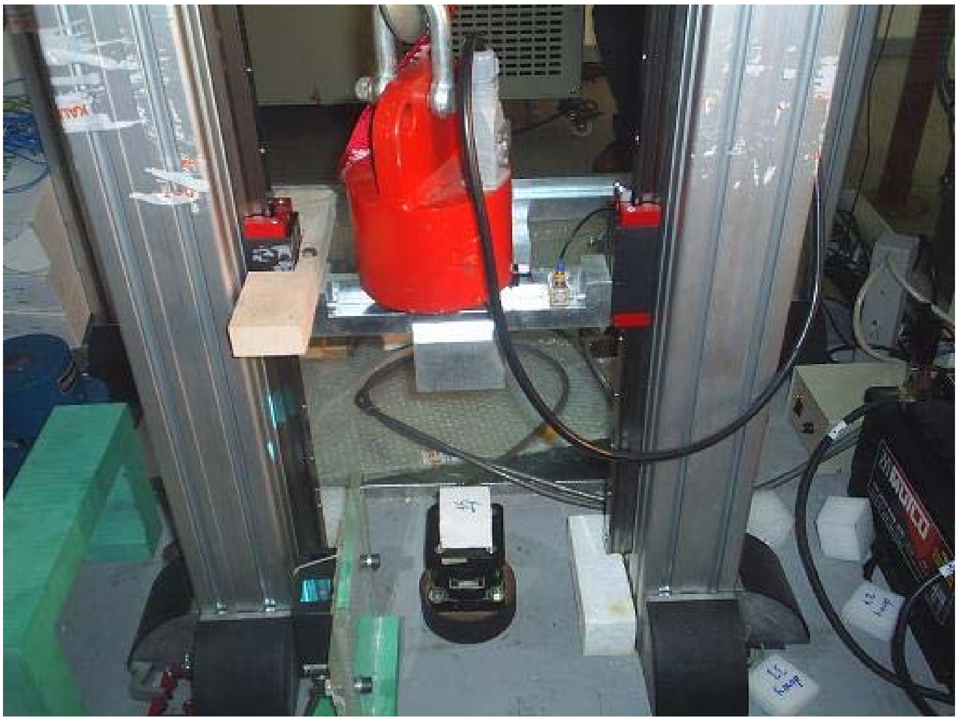

Figure 3.1. Front view of the test setup

Figure 3.2. Back view of the test setup

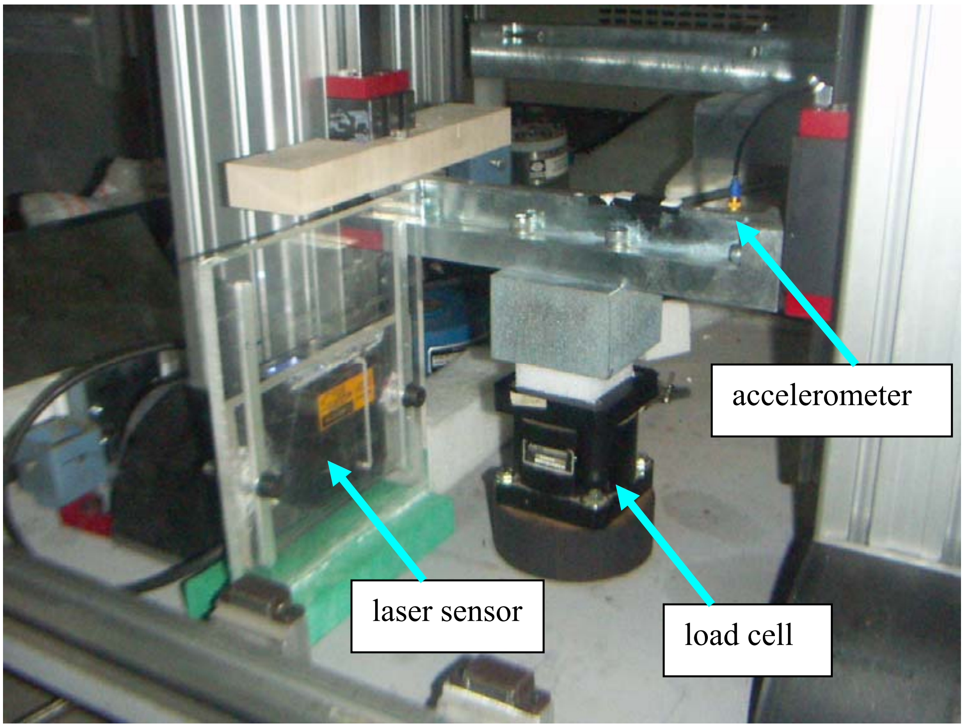

Figure 3.3. Right view of the placement of sensors

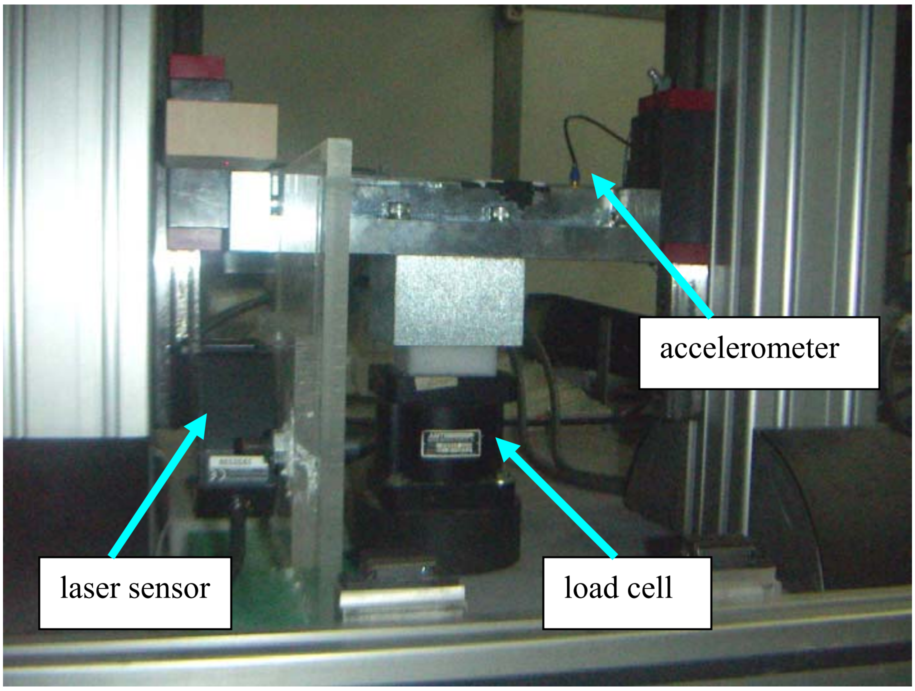

Figure 3.4. Left view of the placement of sensors

3.2. Accuracy of Sensors

Sensors used in the drop test rig have calibration information for converting the voltage output to a physical quantity such as force, displacement, and acceleration. However this conversion can be affected by ambient conditions and needs to be checked again. Measurement results of load cell are compared to those of Zwick Z020 universal tensile testing machine. Voltage output of load cell (V) versus force (N) measured by Zwick is given in Figure 3.5, and the following relationship between force and voltage is found:

$$Force = 634.94 \times Voltage - 10.00 . \tag{3.1}$$

Laser displacement sensor is calibrated by its manufacturer, and the displacement magnitude can be read directly from its display. For double checking purpose and to find out the equation for converting voltage output (V) to displacement (mm), data given in Figure 3.6 are produced by using small plates of known thickness. Equation (3.2) is obtained to convert voltage output to displacement as

$$Displacement = 1.50135 \times Voltage + 0.00242\,. \tag{3.2}$$

Accelerometer measurement is checked by using a shaker that produces a signal of amplitude 10 m/s^2 at 159.2 Hz.

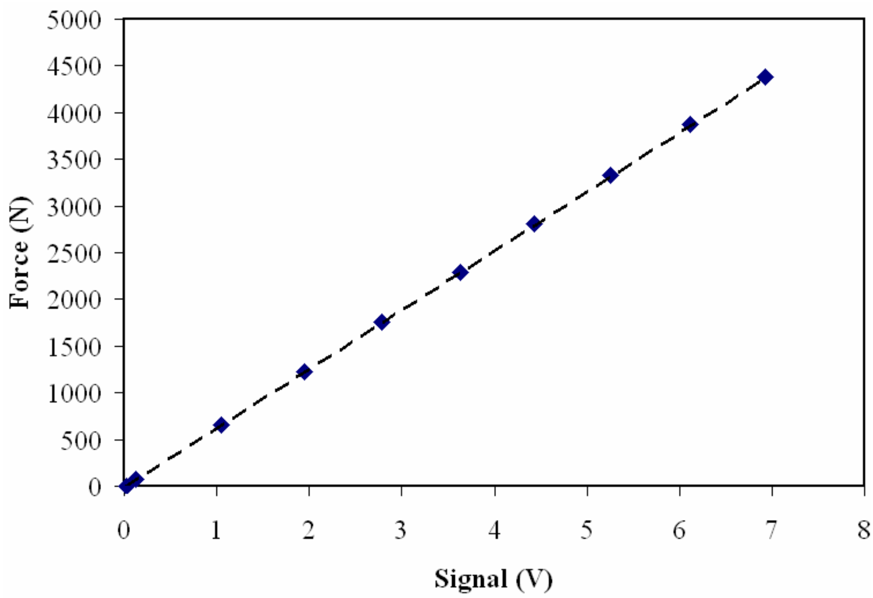

Figure 3.5. Load versus voltage output for load cell

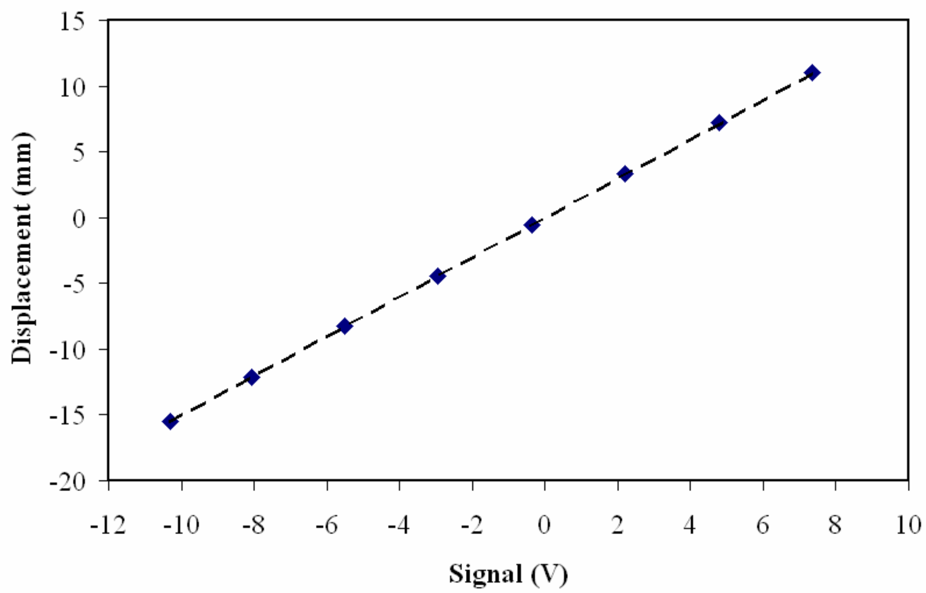

Figure 3.6. Displacement versus voltage output for laser displacement sensor

3.3. Drop Test Results

Test results for EPS 30 and PE 58 from three different falling heights (503 mm, 977 mm, and 1446 mm) are given for uniaxial compressive loading. In Figure 3.7, displacement versus time plot for EPS 30 is given for 503 mm. It is seen that after the first impact, the free falling beam bounces, and two other loadings occur. The velocity before the impact is 1.38 m/s as shown in Figure 3.8. This velocity is much lower than the expected but still much higher than the maximum loading speed (1000 mm/min= 1.67×10^{-2} m/s) in Zwick Z020 universal tensile testing machine. In Figures 3.9 and 3.10, force versus time and in Figures 3.11 and 3.12, acceleration versus time plots for EPS 30 are given. It is seen that acceleration data contain noise due to vibrations of the free falling beam while sliding over ball bearings and due to impact. Product of acceleration with falling mass would give the applied force on the specimen, however acceleration data contain noise, and data obtained from load cell are used to obtain stress versus strain plot of EPS 30 given in Figure 3.13. Test results for 977 mm are given in Figures 3.14–3.20 and similarly for 1446 mm in Figures 3.21–3.27 for EPS 30. In Figure 3.28, stress versus strain curves are plotted for the three drop tests together with the Zwick results for 1000 mm/min loading speed. It is seen that there is almost no difference between stress–strain curves of 1446 mm drop test and the Zwick 1000 mm/min test. Both of the test specimens used at these two tests have 25.9 kg/m^3 density. The initial yield stresses are higher for the drop test from 503 mm and 977 mm than the other two tests. This difference is mainly due to the difference between the densities of specimens. The EPS 30 specimens used in 503 mm and 977 mm drop tests have densities of 29.1 kg/m^3 and 27.4 kg/m^3 respectively. Therefore it is concluded that tests performed in Zwick Z020 universal tensile testing machine are valid also for loading speeds occurring in a drop test. Zhang et al. [27-28] have also shown similar results for strain rate dependency for PS foam at 32 kg/m^3 density. Mechanical response of PS foam at 32 kg/m^3 density is not loading rate sensitive after 2.29×10^{-1} m/s loading speed [27-28].

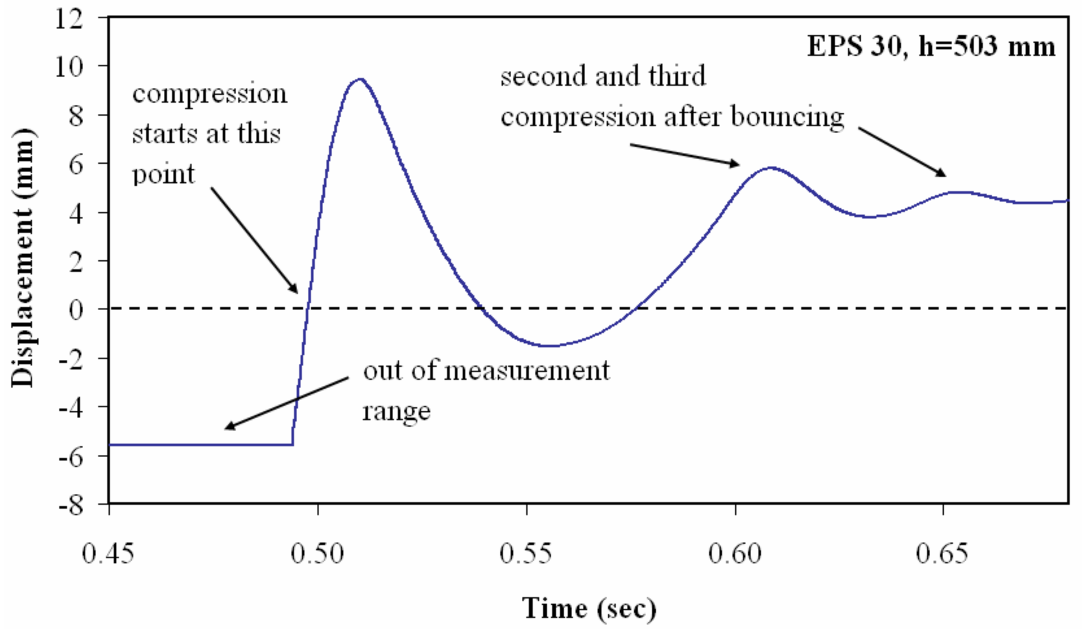

Figure 3.7. Displacement versus time for EPS 30 in drop test from 503 mm height

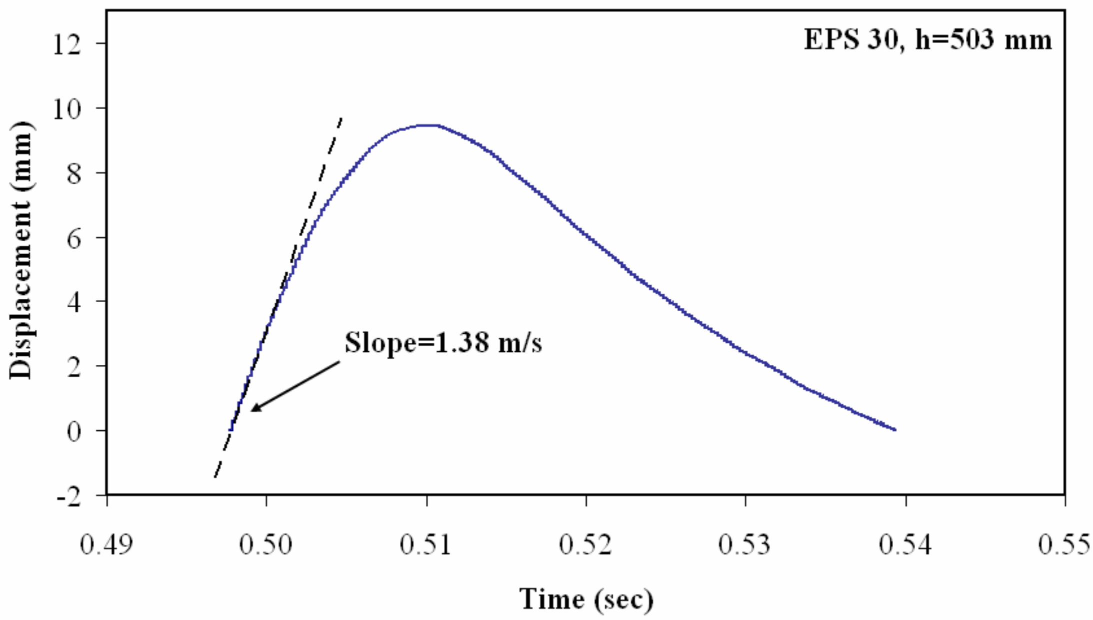

Figure 3.8. Velocity of the falling weight at the beginning of compression for EPS 30 in drop test from 503 mm height

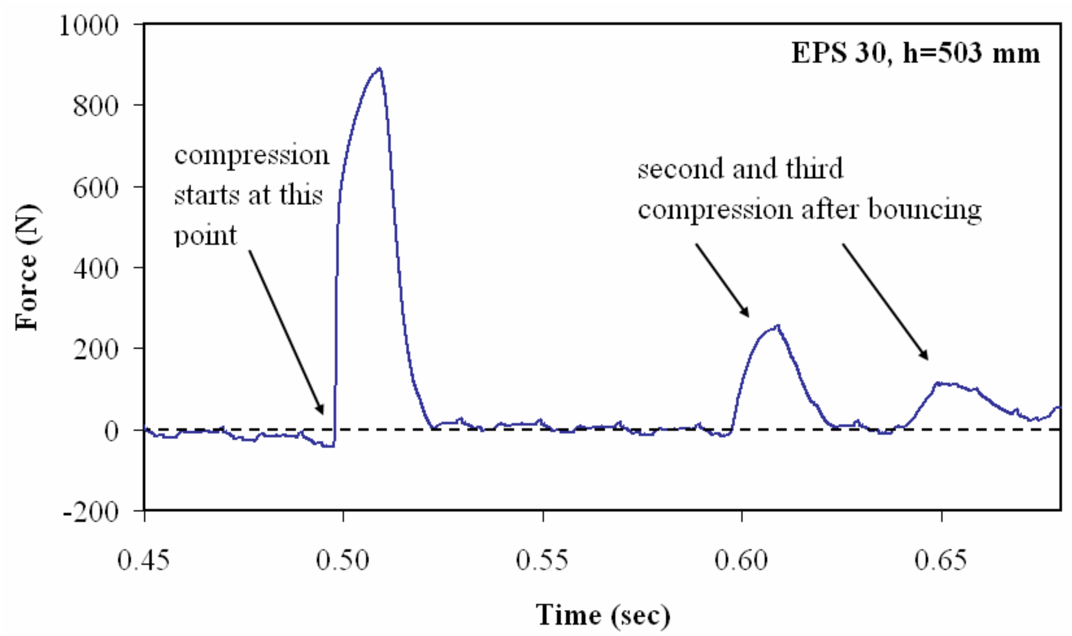

Figure 3.9. Force versus time for EPS 30 in drop test from 503 mm height

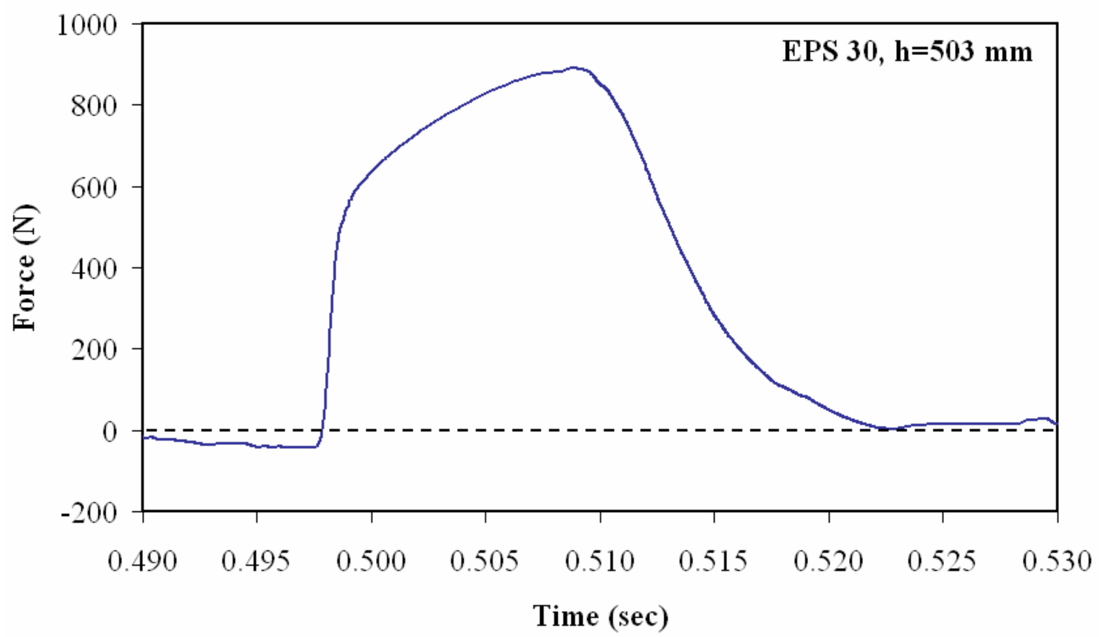

Figure 3.10. Force versus time of EPS 30 following the first impact in drop test from 503 mm height

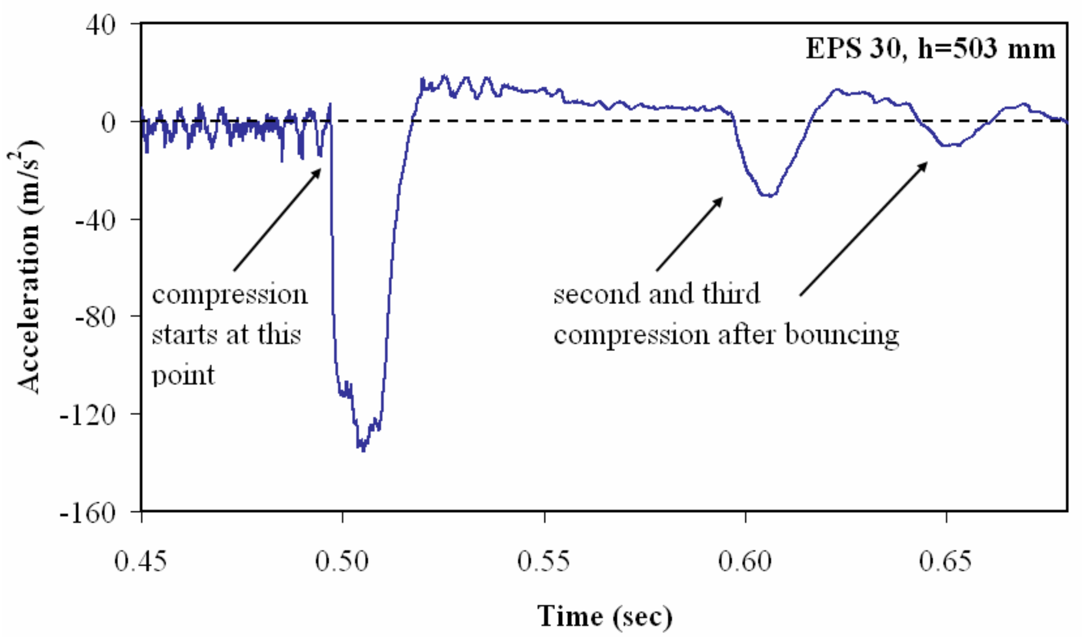

Figure 3.11. Acceleration versus time for EPS 30 in drop test from 503 mm height

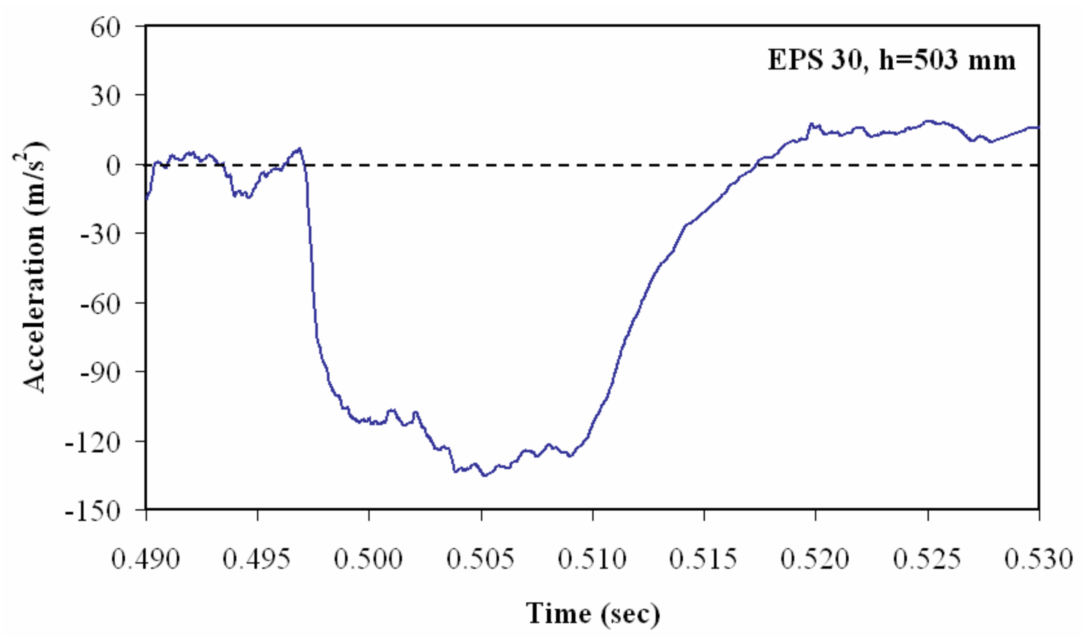

Figure 3.12. Acceleration versus time of EPS 30 following the first impact in drop test from 503 mm height

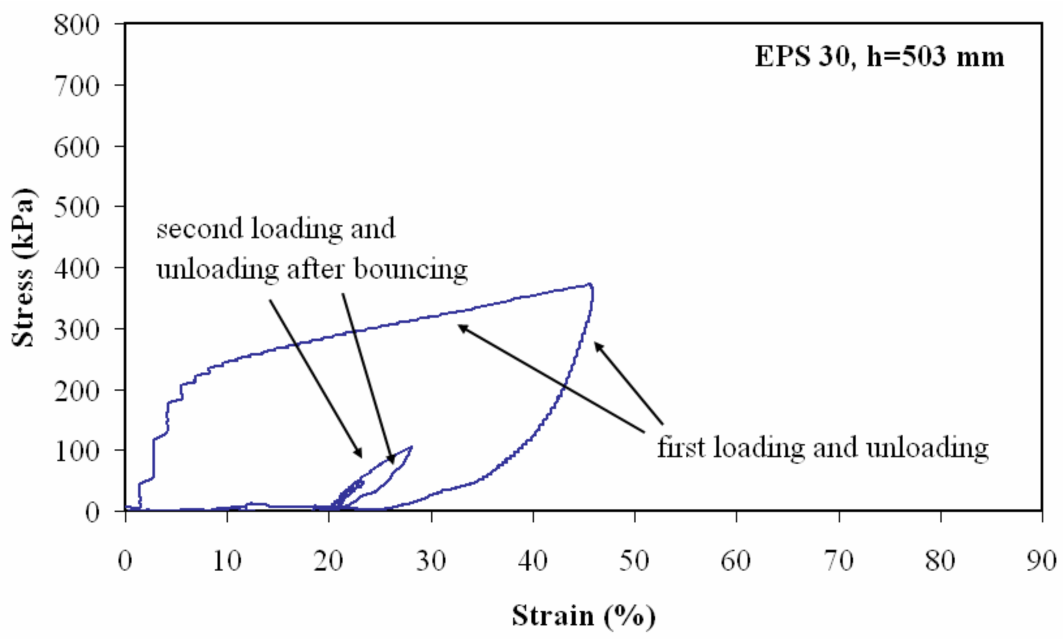

Figure 3.13. Stress versus strain for EPS 30 in drop test from 503 mm height

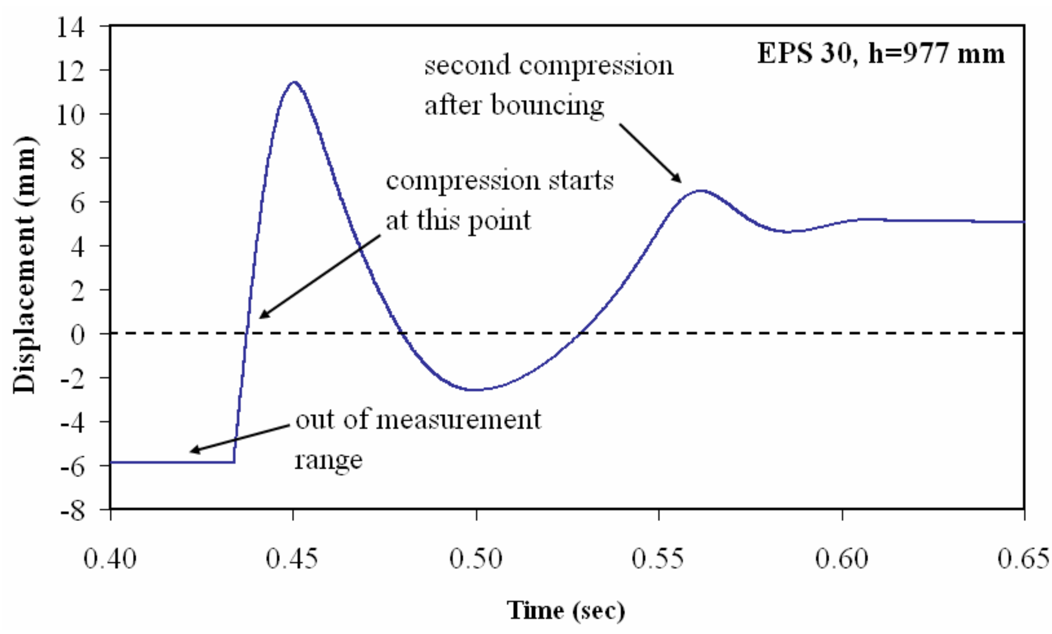

Figure 3.14. Displacement versus time for EPS 30 in drop test from 977 mm height

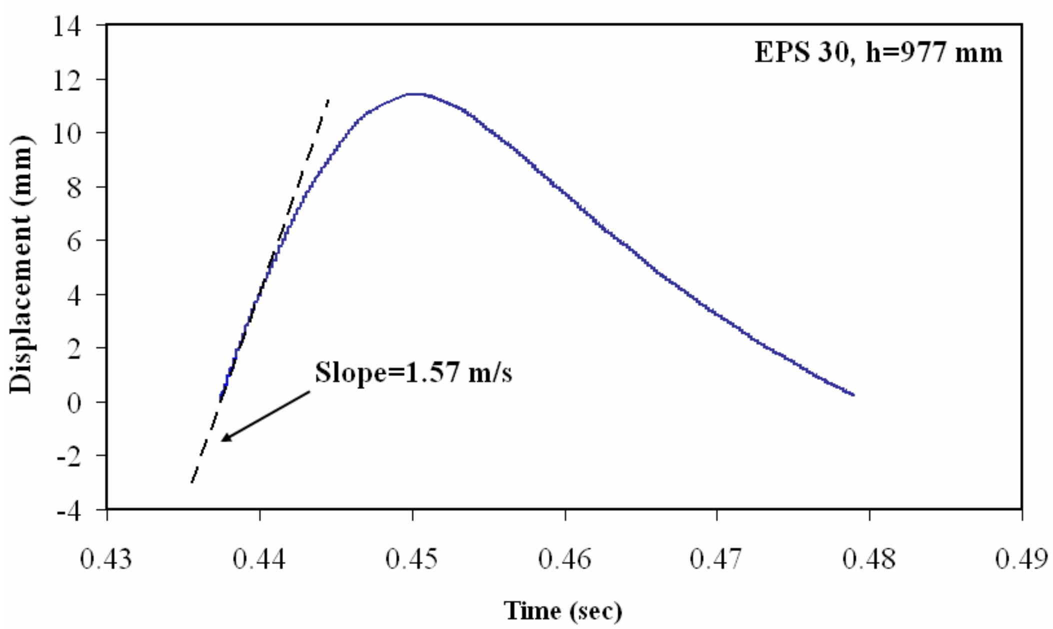

Figure 3.15. Velocity of the falling weight at the beginning of compression for EPS 30 in drop test from 977 mm height

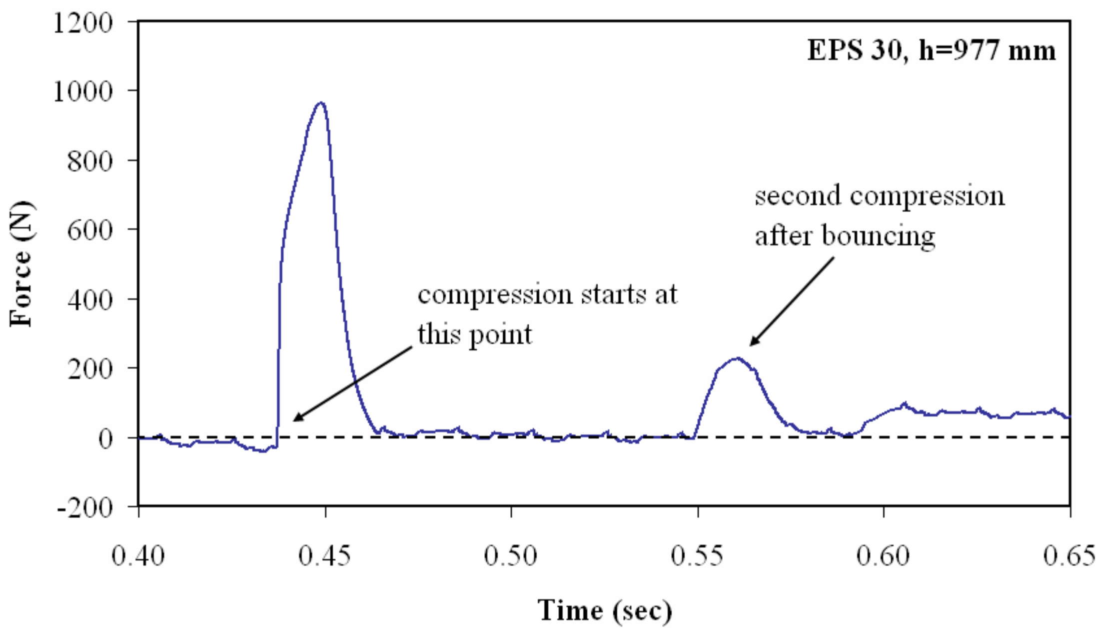

Figure 3.16. Force versus time for EPS 30 in drop test from 977 mm height

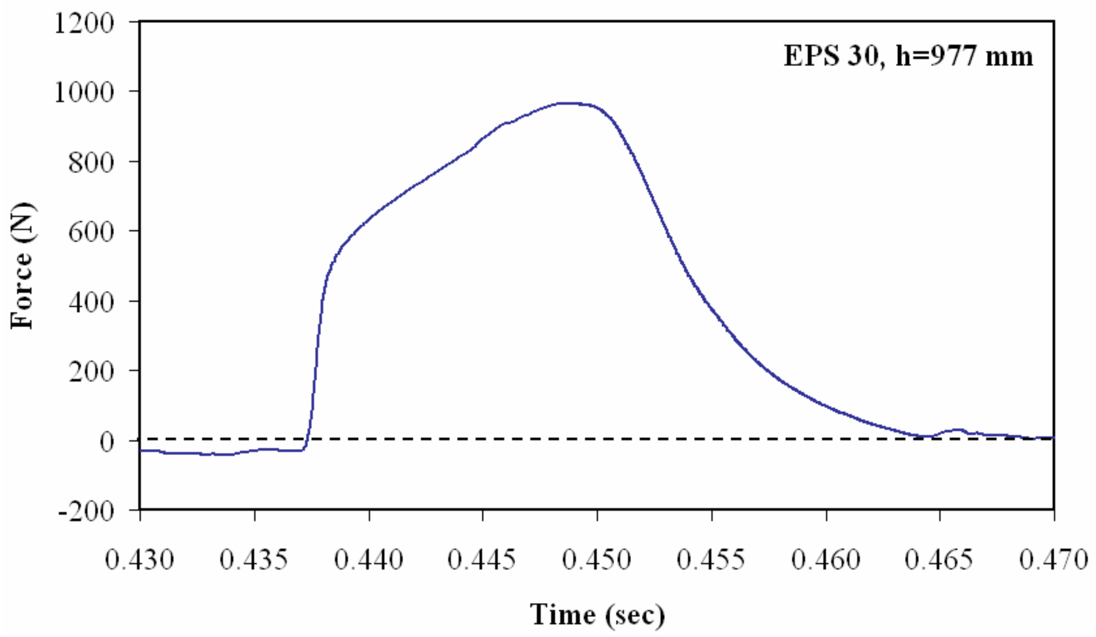

Figure 3.17. Force versus time of EPS 30 following the first impact in drop test from 977 mm height

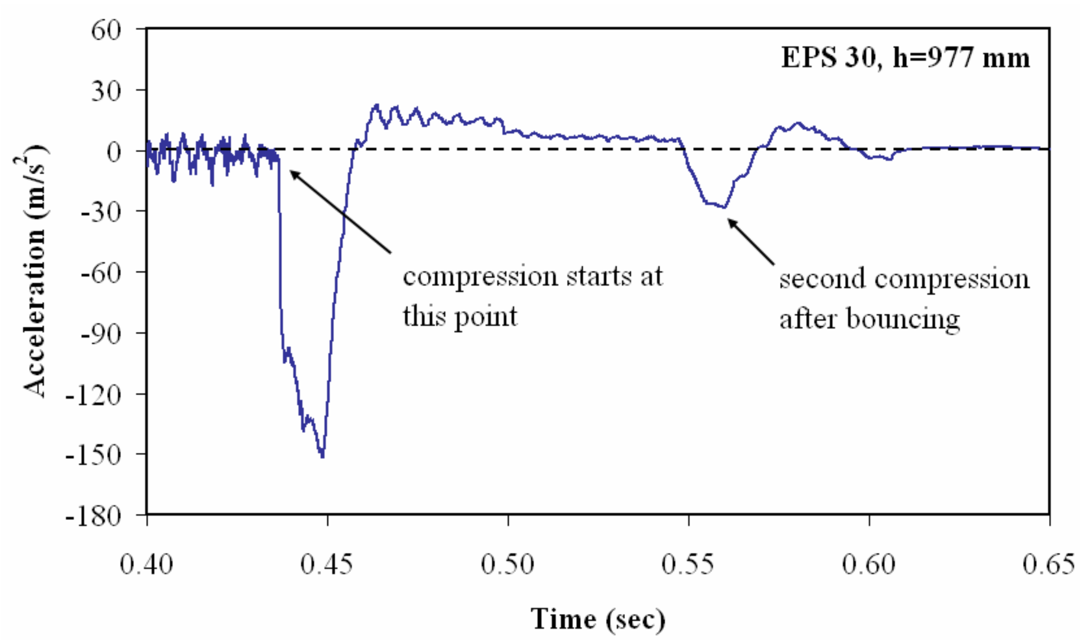

Figure 3.18. Acceleration versus time for EPS 30 in drop test from 977 mm height

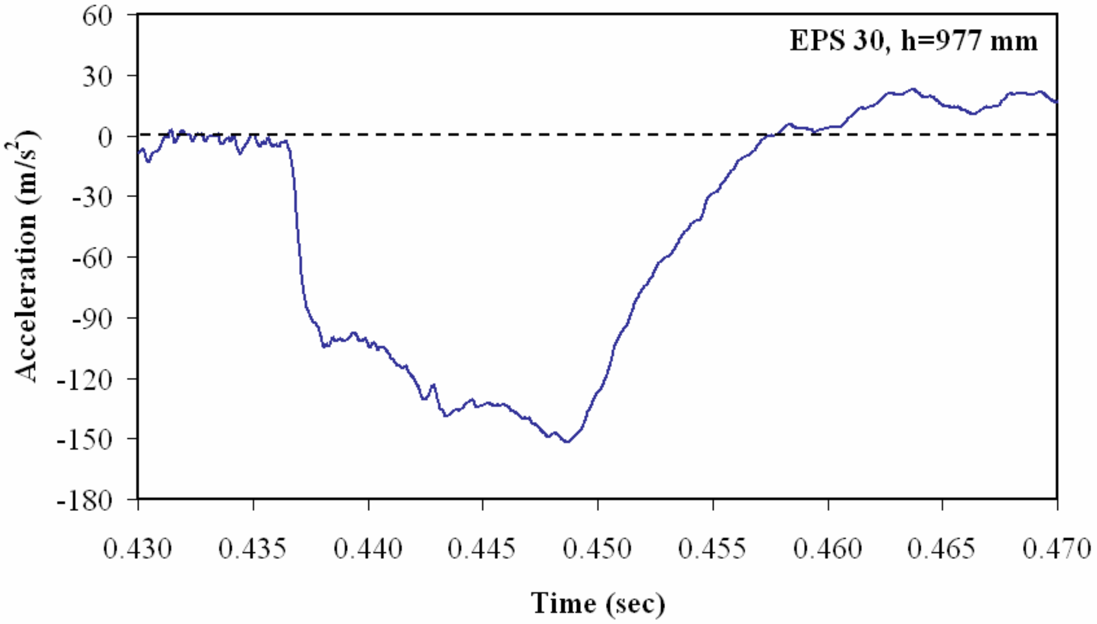

Figure 3.19. Acceleration versus time of EPS 30 following the first impact in drop test from 977 mm height

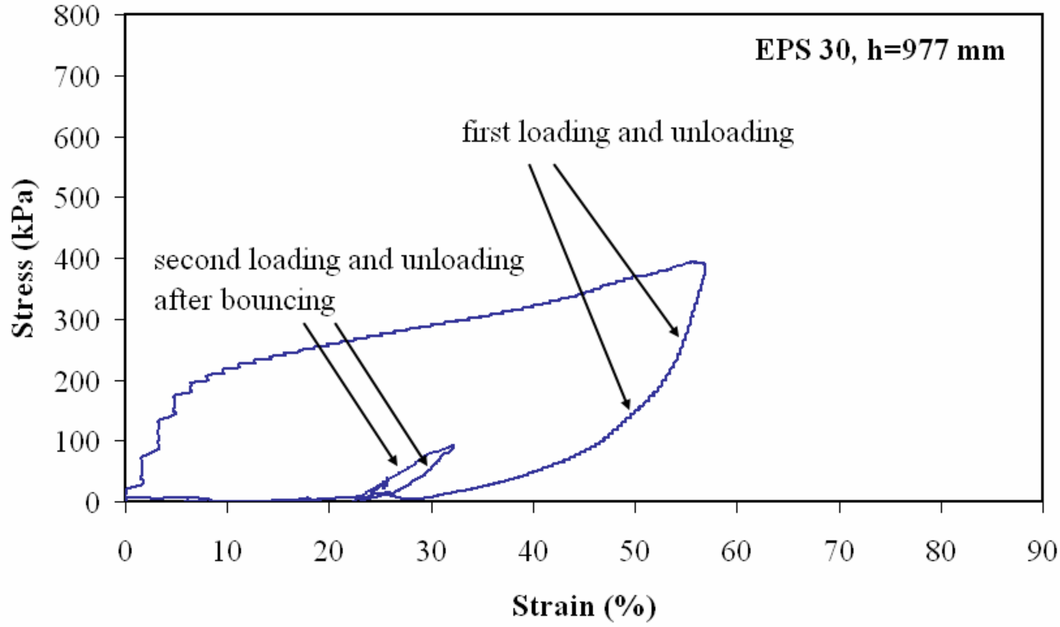

Figure 3.20. Stress versus strain for EPS 30 in drop test from 977 mm height

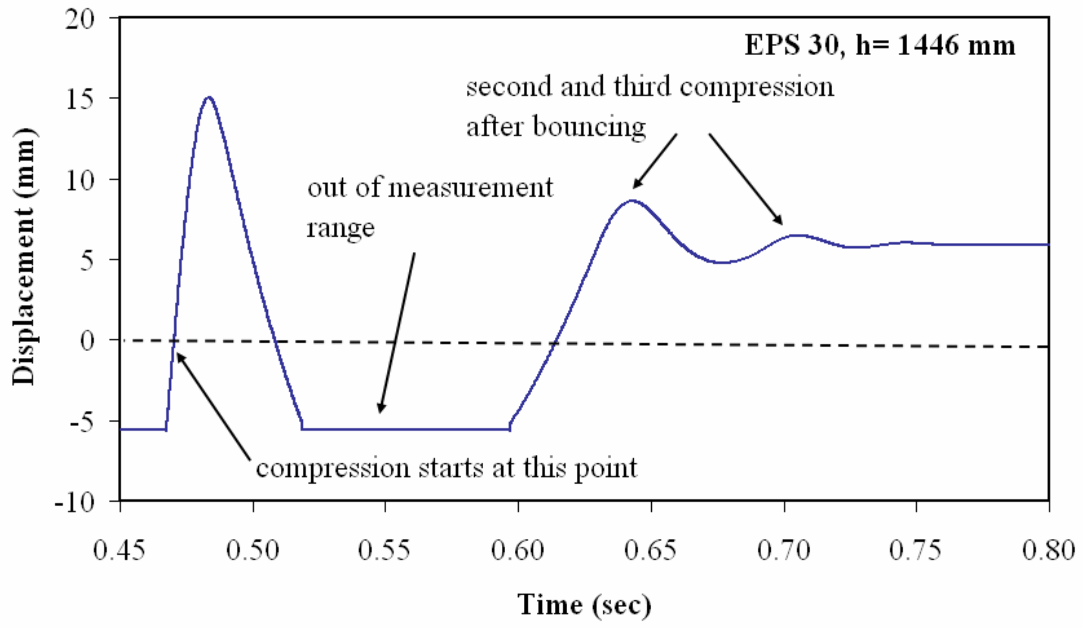

Figure 3.21. Displacement versus time for EPS 30 in drop test from 1446 mm height

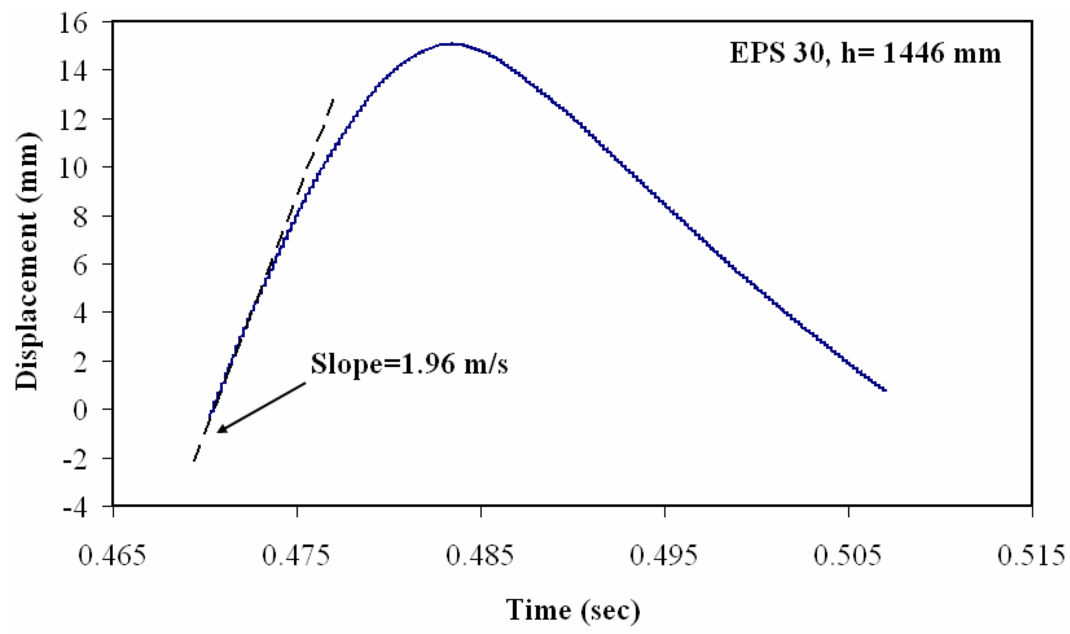

Figure 3.22. Velocity of the falling weight at the beginning of compression for EPS 30 in drop test from 1446 mm height

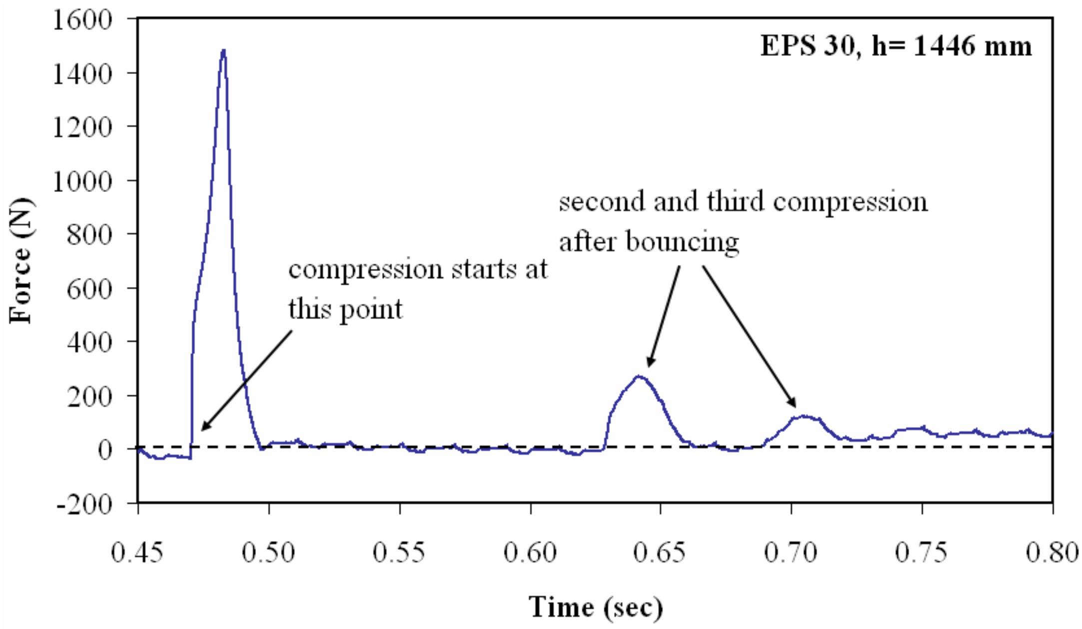

Figure 3.23. Force versus time for EPS 30 in drop test from 1446 mm height

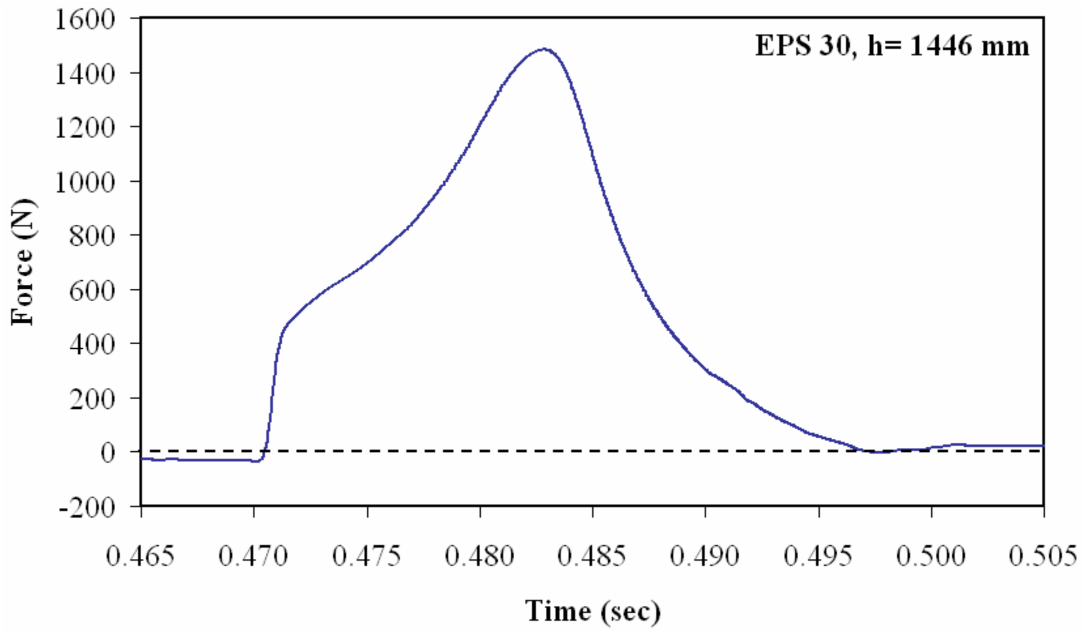

Figure 3.24. Force versus time of EPS 30 following the first impact in drop test from 1446 mm height

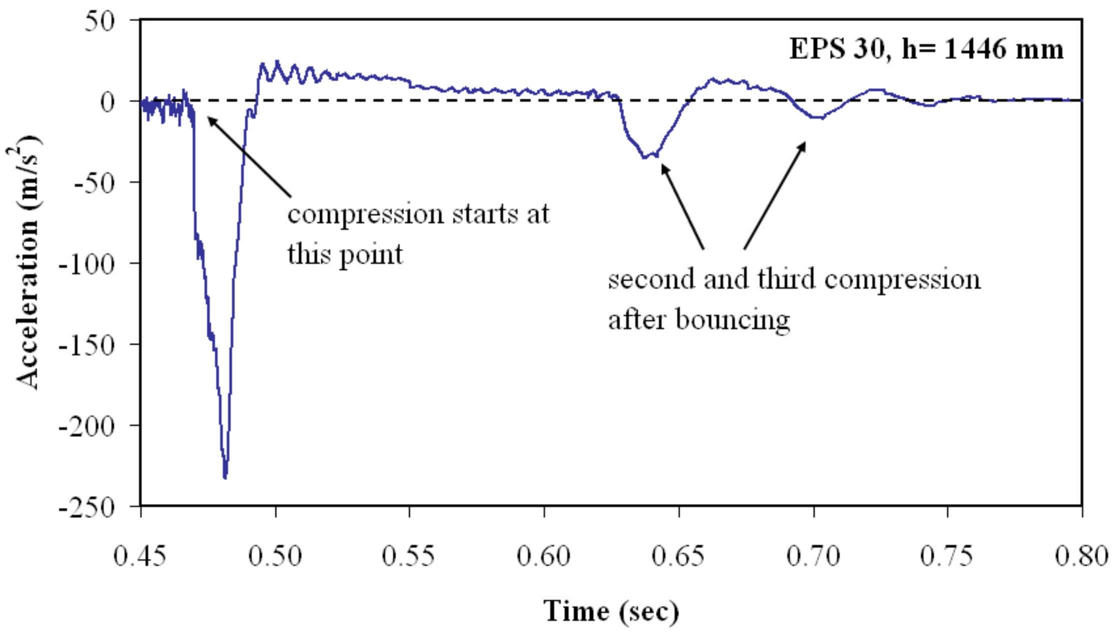

Figure 3.25. Acceleration versus time for EPS 30 in drop test from 1446 mm height

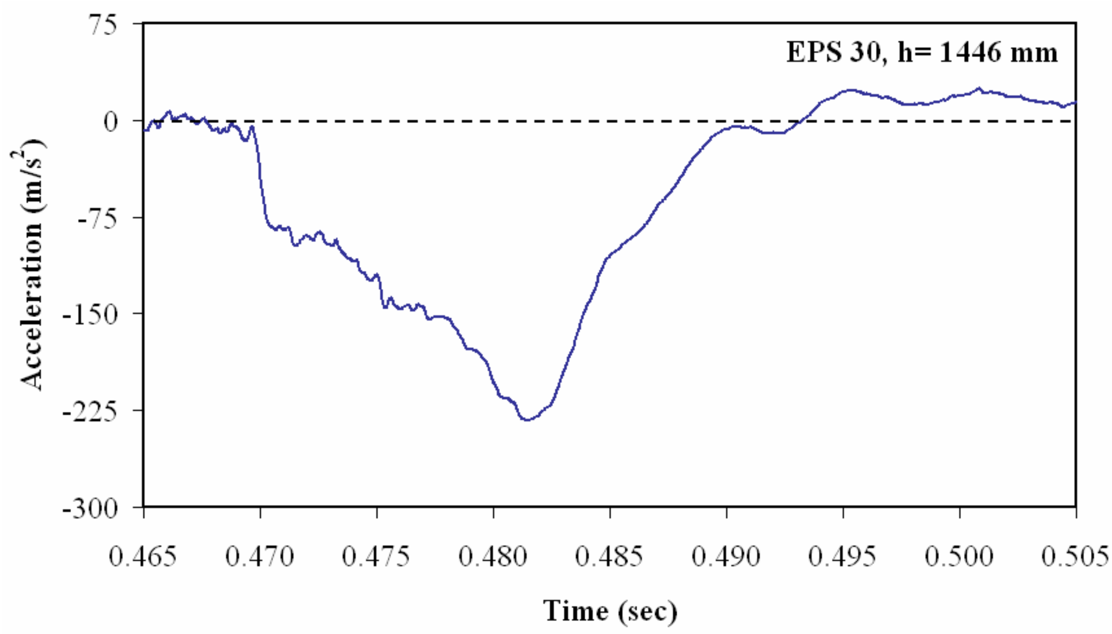

Figure 3.26. Acceleration versus time of EPS 30 following the first impact in drop test from 1446 mm height

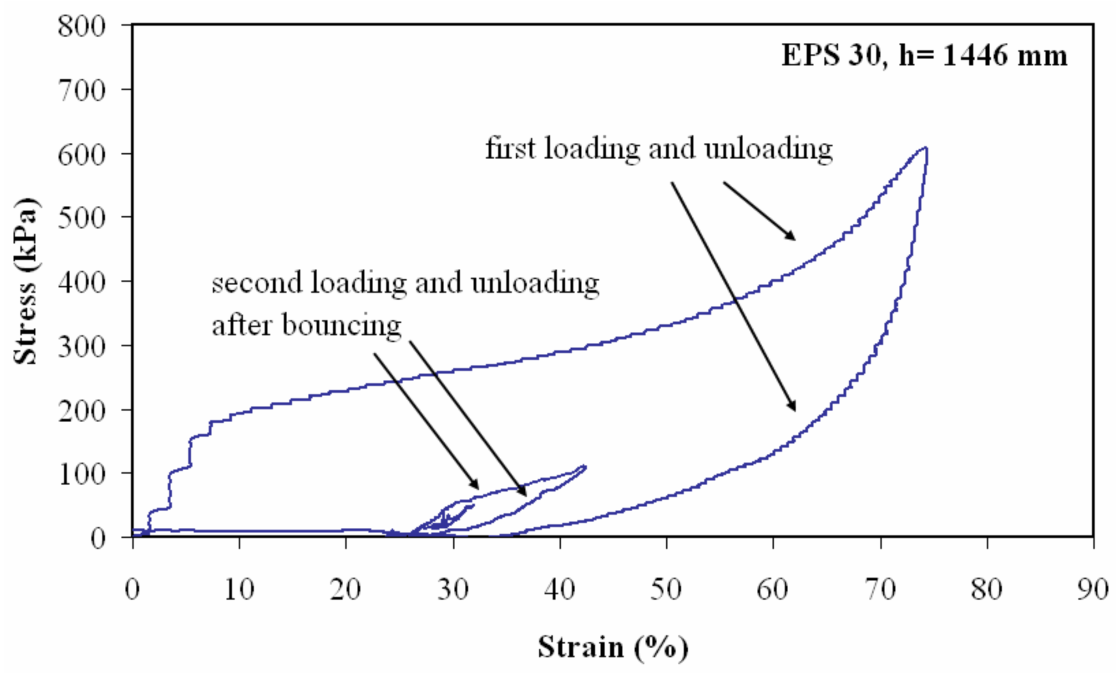

Figure 3.27. Stress versus strain for EPS 30 in drop test from 1446 mm height

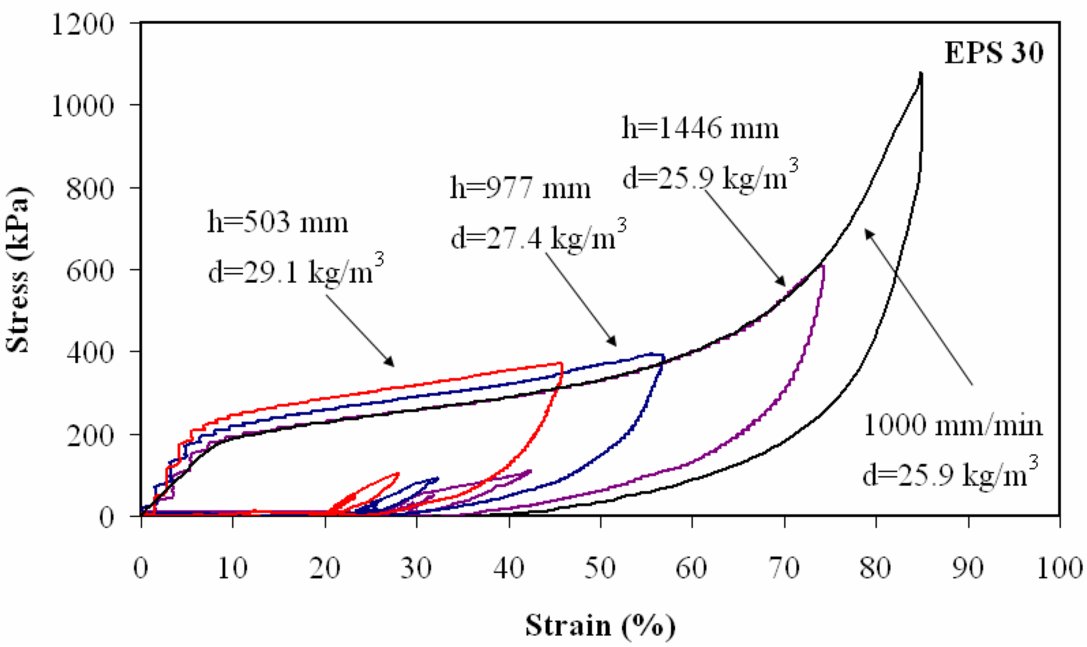

Figure 3.28. Comparison of drop test stress-strain results and results of Zwick for 1000 mm/min cross head speed for EPS 30

In Figure 3.29, displacement versus time plot for PE 58 is given for 503 mm falling height test. It is seen that after the first impact, the free falling beam bounces, and only one remarkable loading occurs. The velocity before the impact is 1.33 m/s as shown in Figure 3.30. In Figures 3.31 and 3.32, force versus time plot, and in Figures 3.33 and 3.34, acceleration versus time plot for PE 58 are given. It is seen that acceleration data contain noise due similar to EPS 30 tests. Therefore data obtained from load cell are used to obtain the stress versus strain plot of PE 58 specimen for the PE 58 test given in Figure 3.35. Similar test results are given in Figures 3.36–3.42 for the falling height of 977 mm and in Figures 3.43–3.49 for the falling height of 1446 mm for PE 58. In Figure 3.51, stress versus strain curves are given for the three tests performed in drop test rig and the test performed in Zwick Z020 universal tensile testing machine. It is seen that the three tests performed by drop test rig at high loading speeds have 10-20 per cent higher initial yield strength than the test performed in the Zwick 1000 mm/min test. The repeatability of the three tests performed in drop test rig is at the same level of Zwick Z020 tensile testing machine (see Figure 2.20) considering the differences in densities of the three test specimens. It is concluded that PE 58 have 10–20 per cent higher initial yield strength than the test performed in Zwick Z020 universal tensile testing machine at 1000 mm/min loading speed. Different multiple loading and unloading profiles can easily be set in Zwick Z020 universal tensile testing machine. Since there are not much difference in stress–strain responses of EPS and PE materials between the results of drop test rig and Zwick, mechanical tests to understand the mechanical behavior of foams under multiple loading and unloading are performed by Zwick Z020 universal tensile testing machine. Stress–strain response obtained by drop test rig can be used in hardening input data of FE simulations for drop tests.

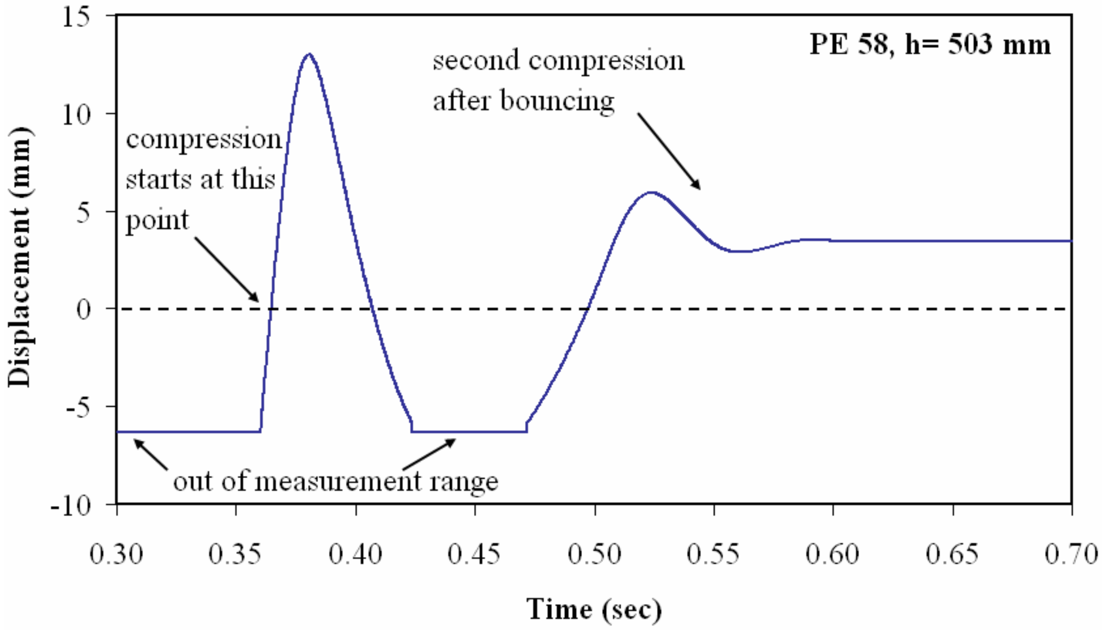

Figure 3.29. Displacement versus time for PE 58 in drop test from 503 mm height

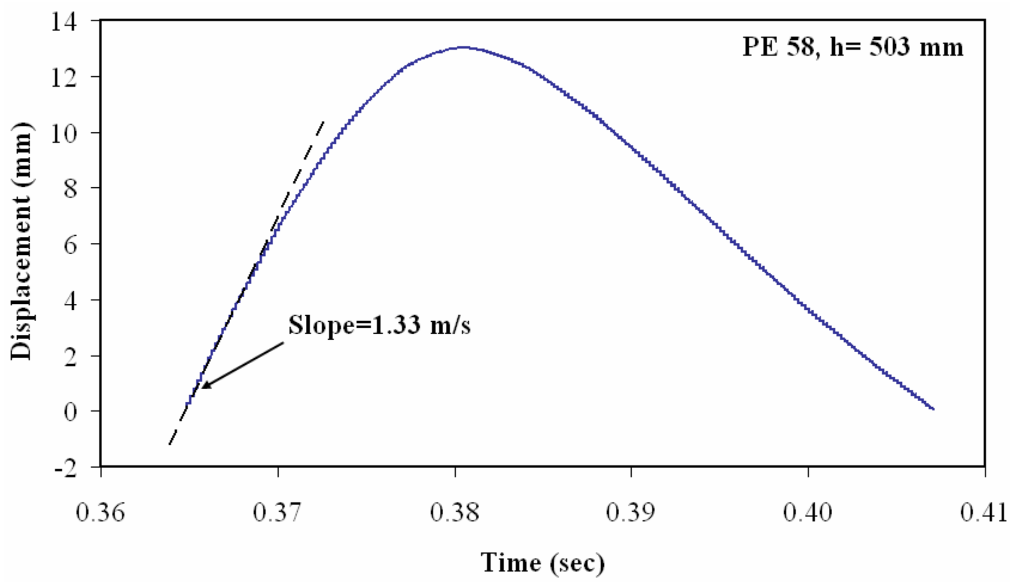

Figure 3.30. Velocity of the falling weight at the beginning of compression for PE 58 in drop test from 503 mm height

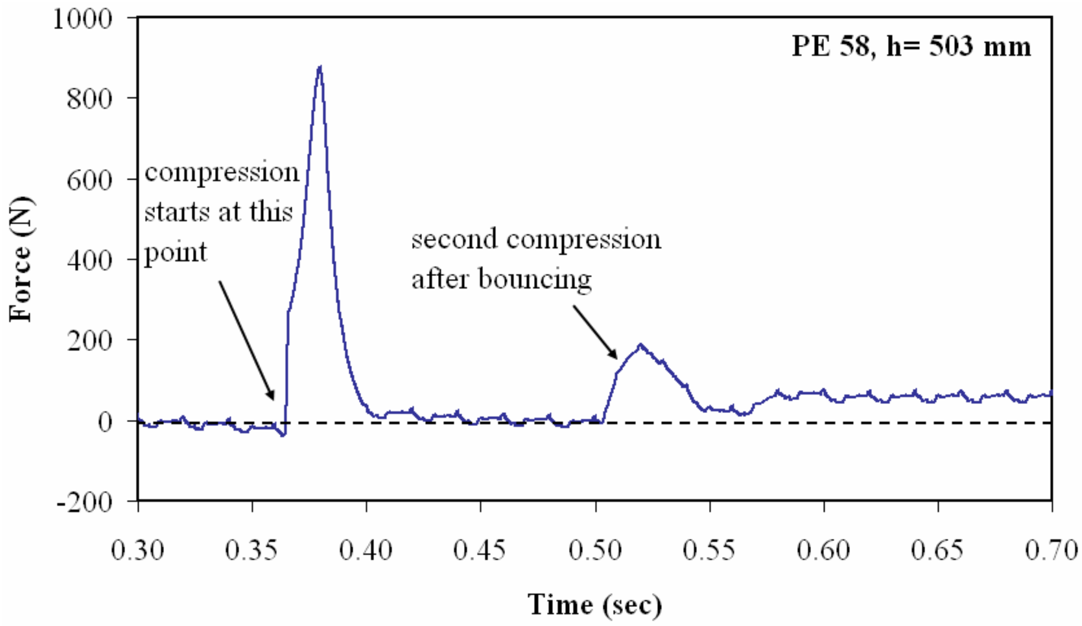

Figure 3.31. Force versus time for PE 58 in drop test from 503 mm height

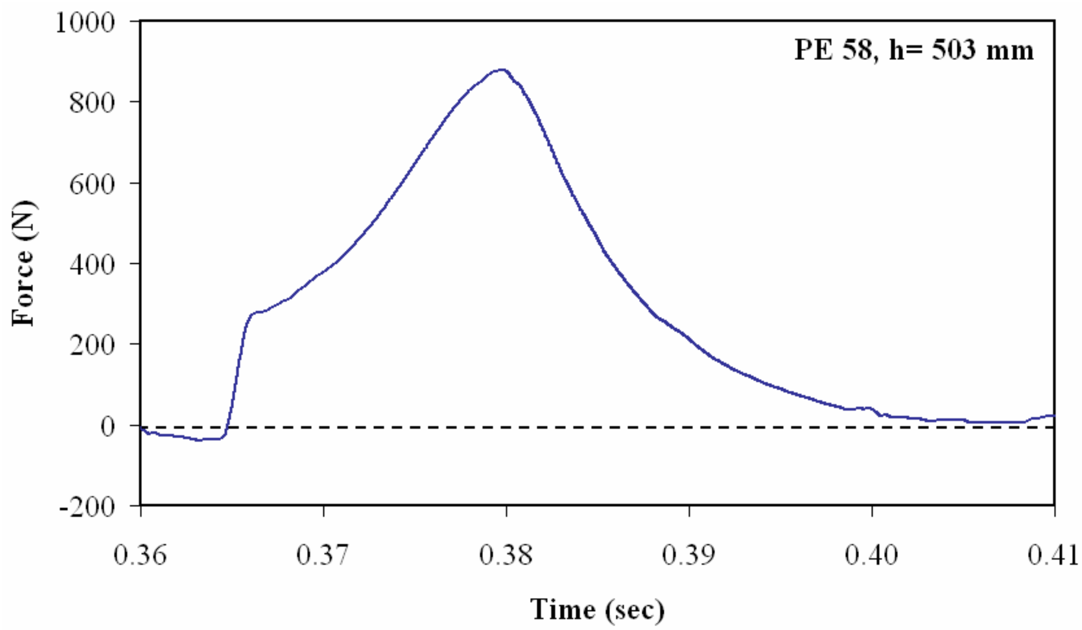

Figure 3.32. Force versus time of PE 58 following the first impact in drop test from 503 mm height

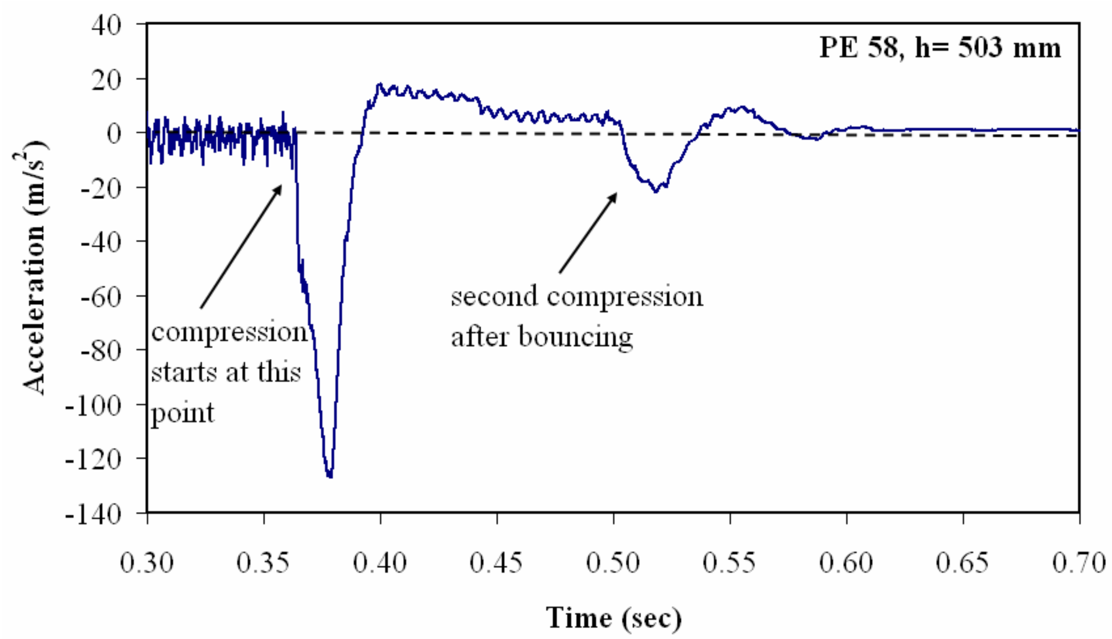

Figure 3.33. Acceleration versus time for PE 58 in drop test from 503 mm height

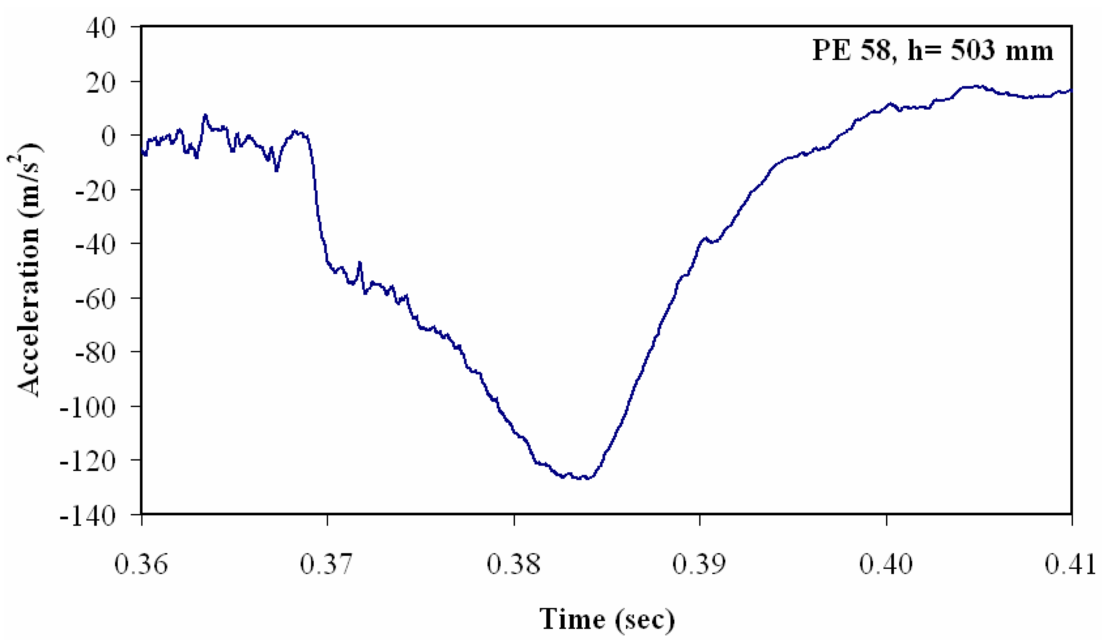

Figure 3.34. Acceleration versus time of PE 58 following the first impact in drop test from 503 mm height

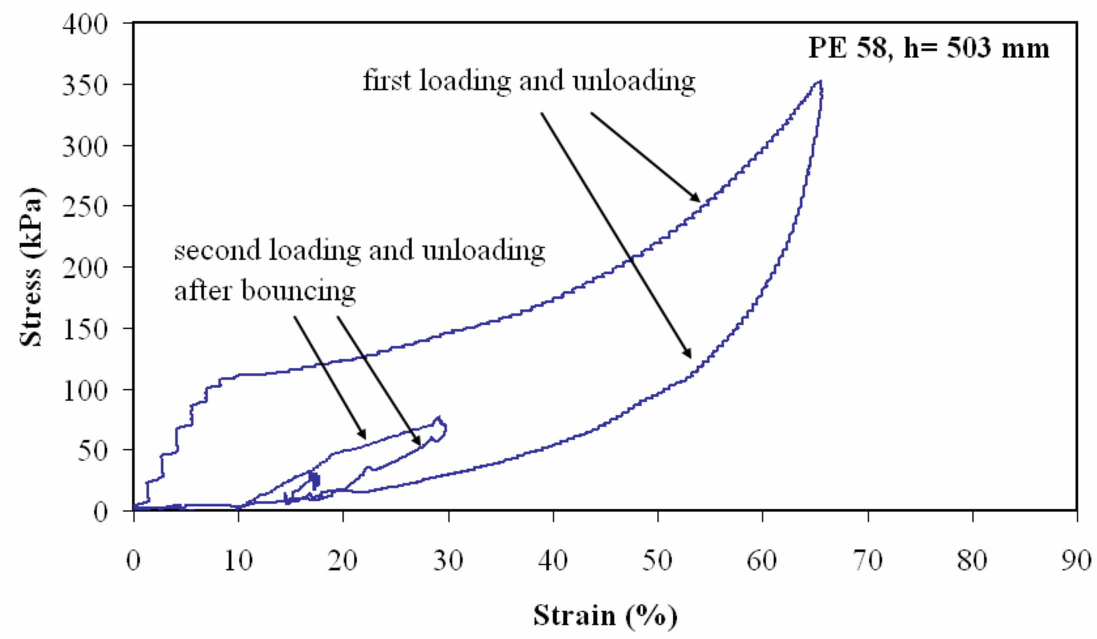

Figure 3.35. Stress versus strain for PE 58 in drop test from 503 mm height

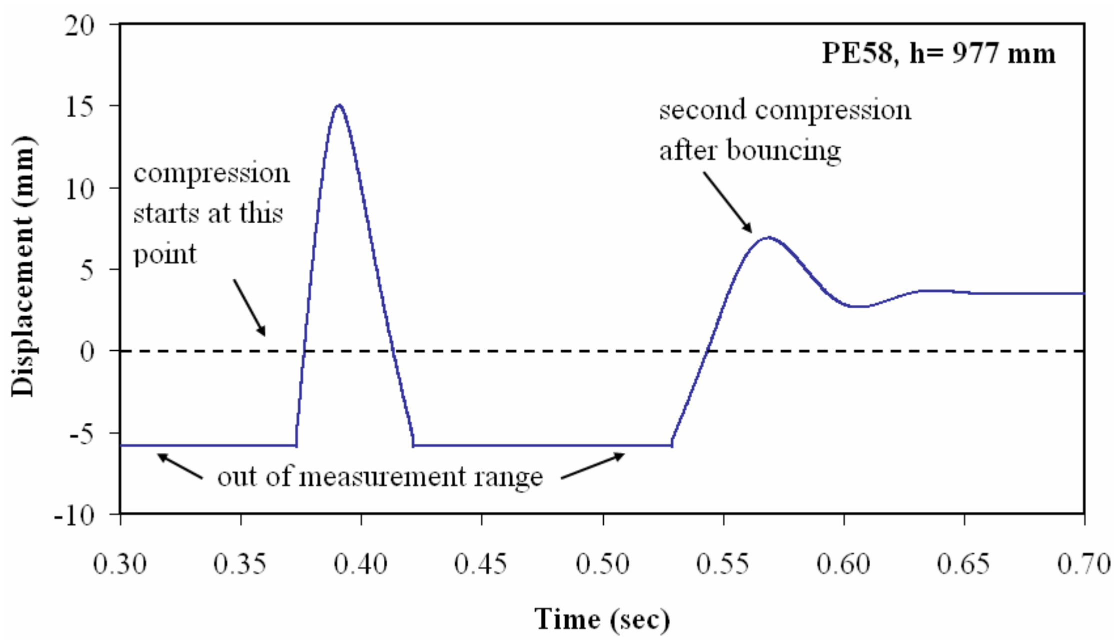

Figure 3.36. Displacement versus time for PE 58 in drop test from 977 mm height

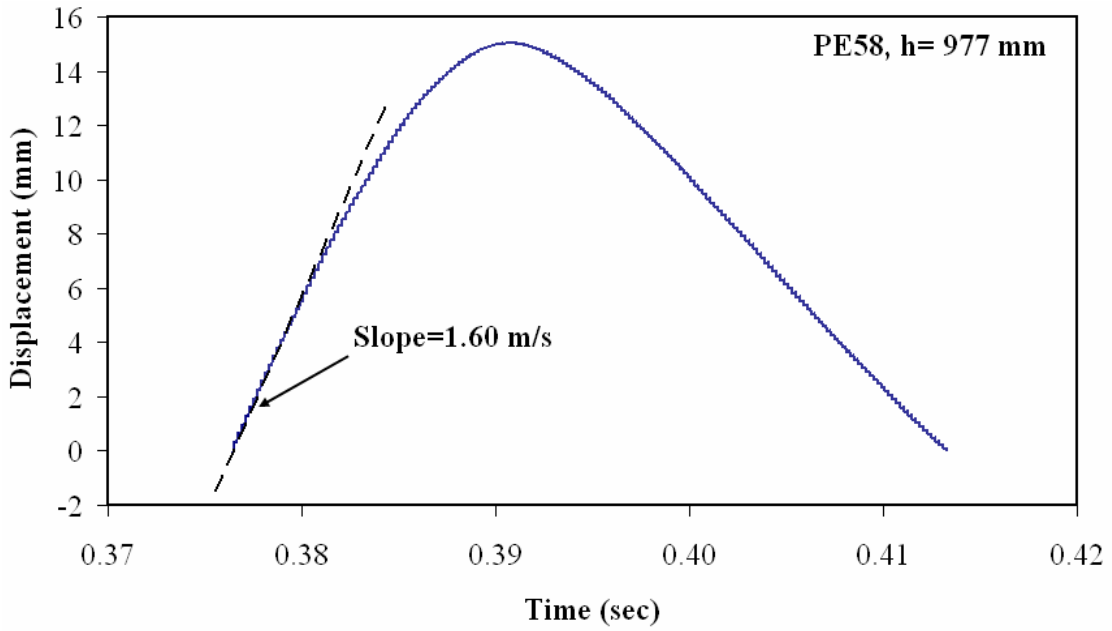

Figure 3.37. Velocity of the falling weight at the beginning of compression for PE 58 in drop test from 977 mm height

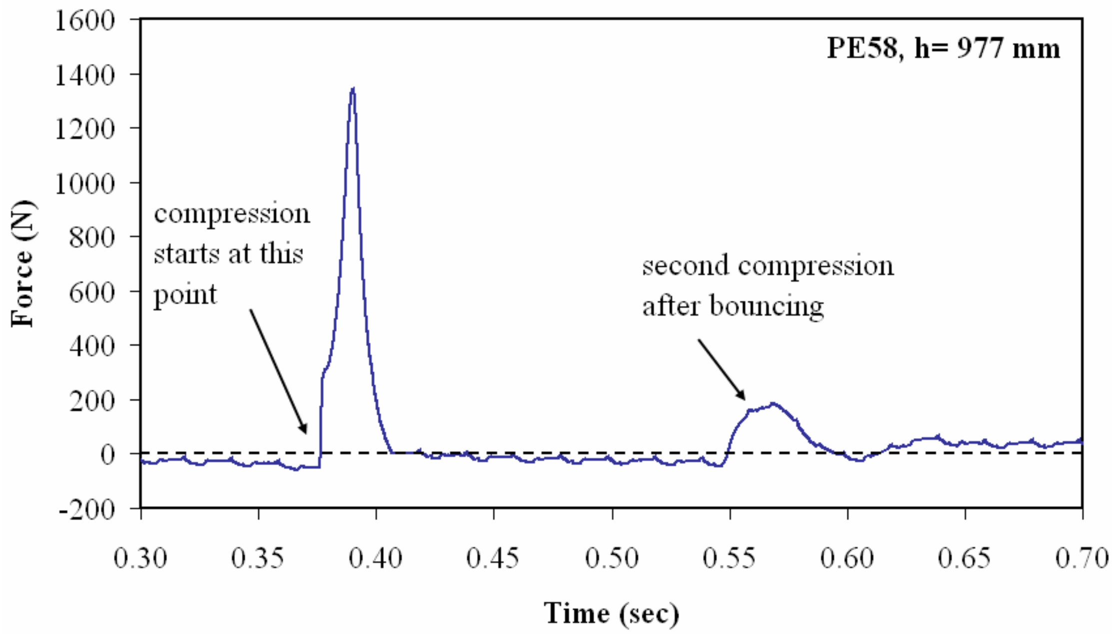

Figure 3.38. Force versus time for PE 58 in drop test from 977 mm height

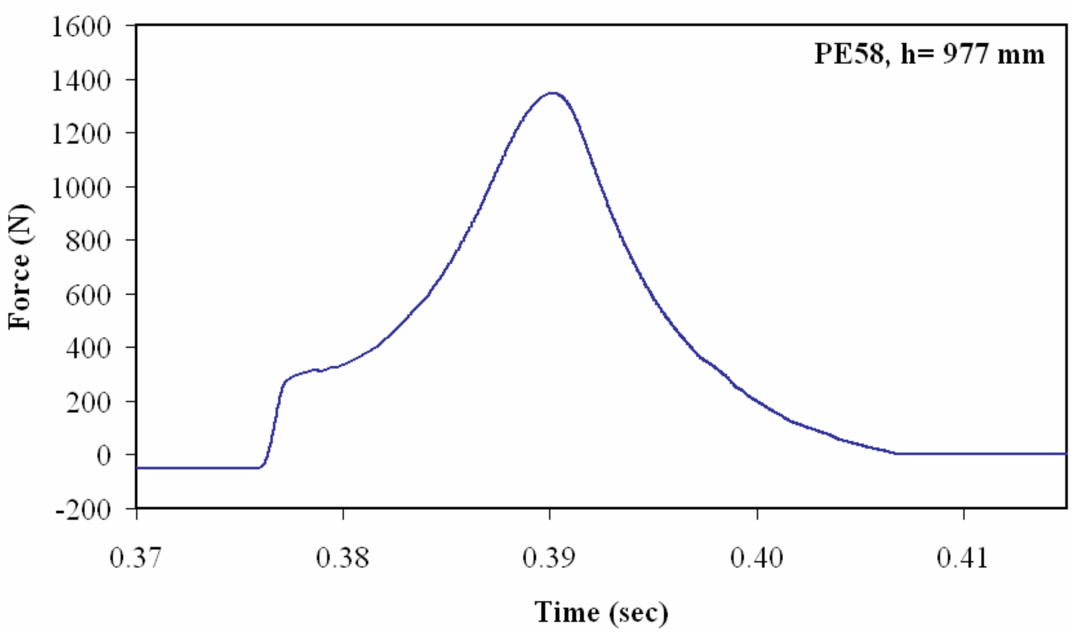

Figure 3.39. Force versus time of PE 58 following the first impact in drop test from 977 mm height

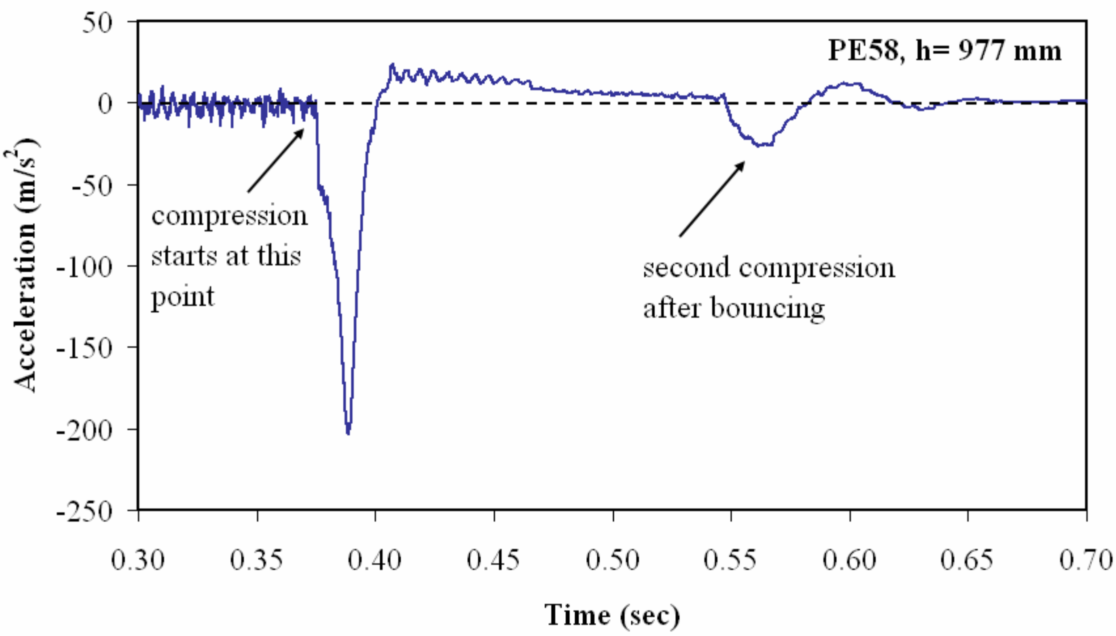

Figure 3.40. Acceleration versus time for PE 58 in drop test from 977 mm height

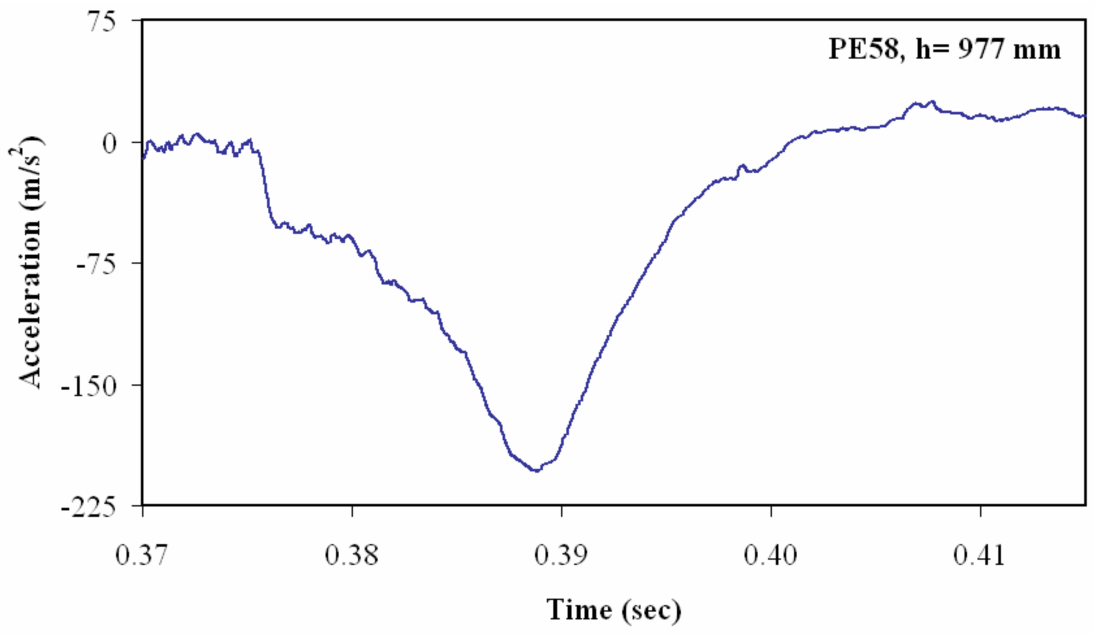

Figure 3.41. Acceleration versus time of PE 58 following the first impact in drop test from 977 mm height

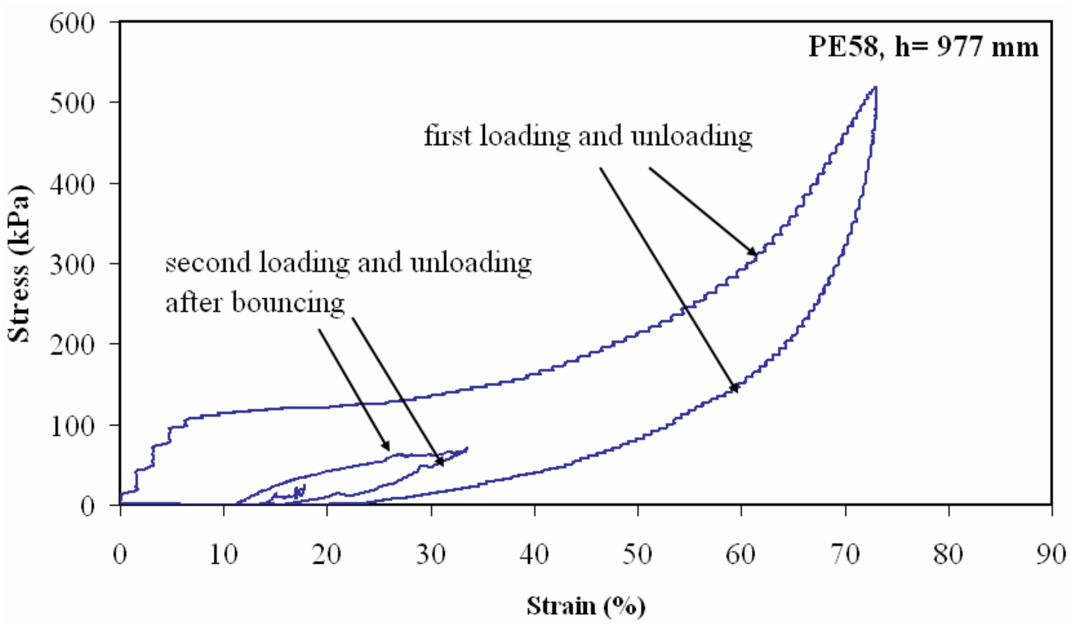

Figure 3.42. Stress versus strain for PE 58 in drop test from 977 mm height

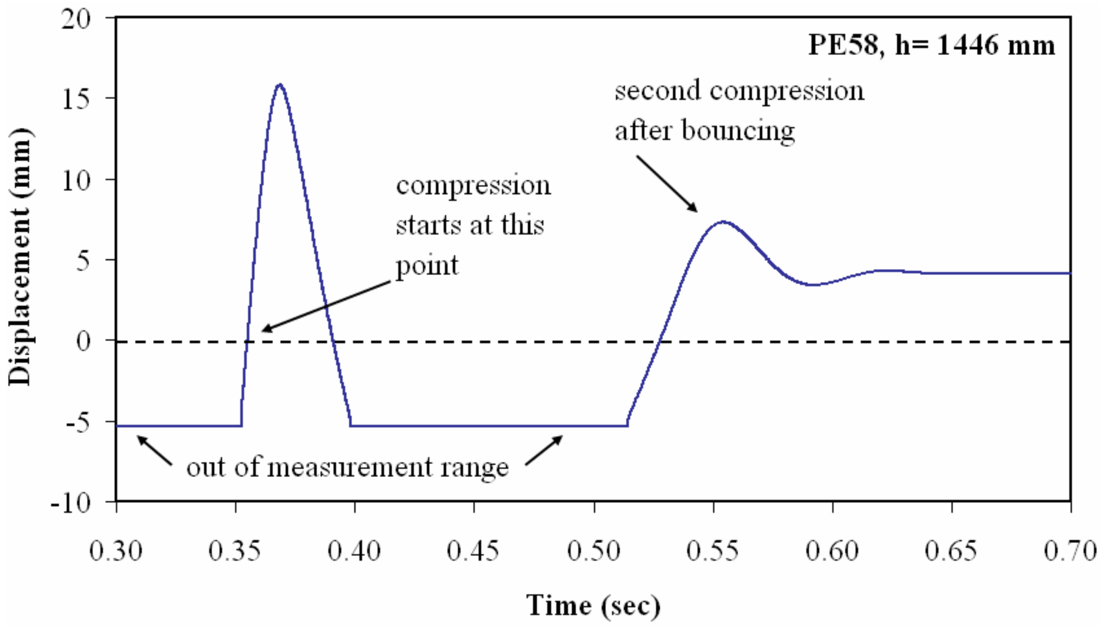

Figure 3.43. Displacement versus time for PE 58 in drop test from 1446 mm height

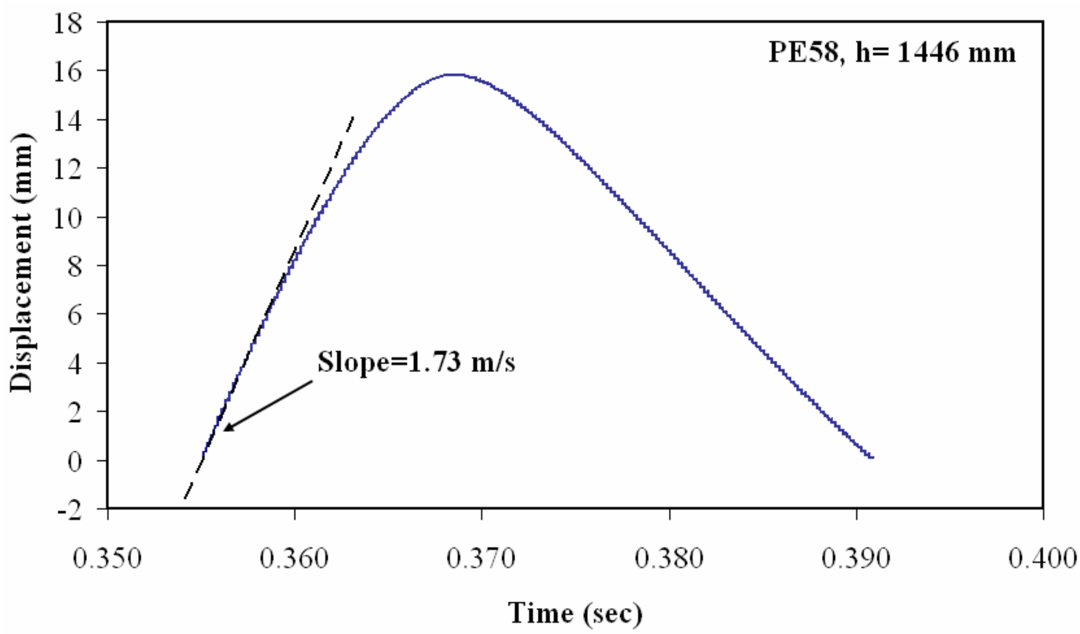

Figure 3.44. Displacement versus time for PE 58 in drop test from 1446 mm height

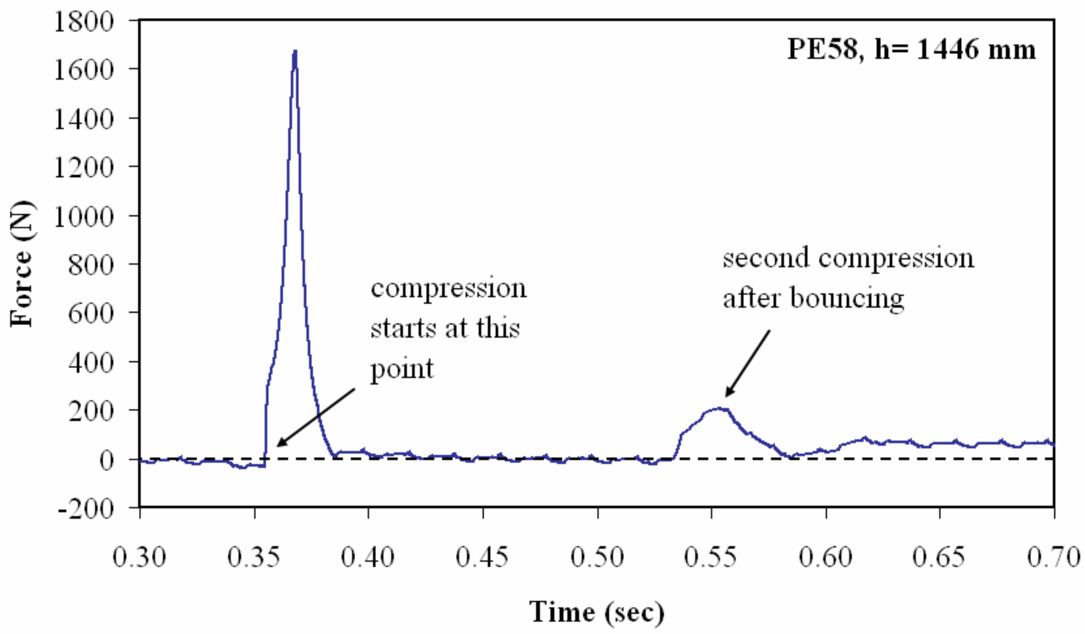

Figure 3.45. Force versus time for PE 58 in drop test from 1446 mm height

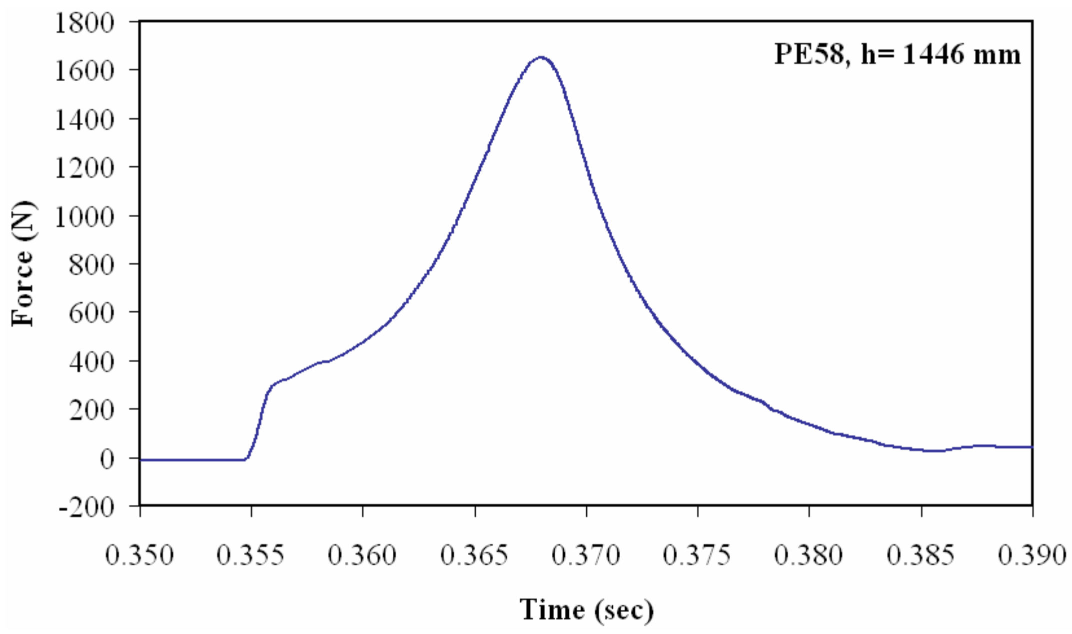

Figure 3.46. Force versus time of PE 58 following the first impact in drop test from 1446 mm height

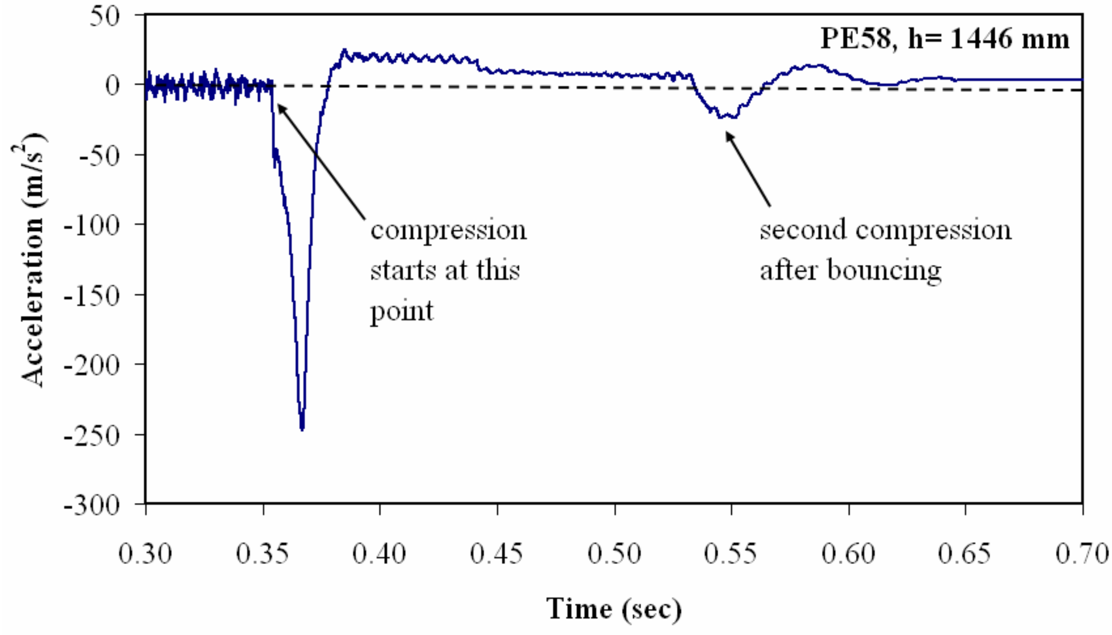

Figure 3.47. Acceleration versus time of PE 58 following the first impact in drop test from 1446 mm height

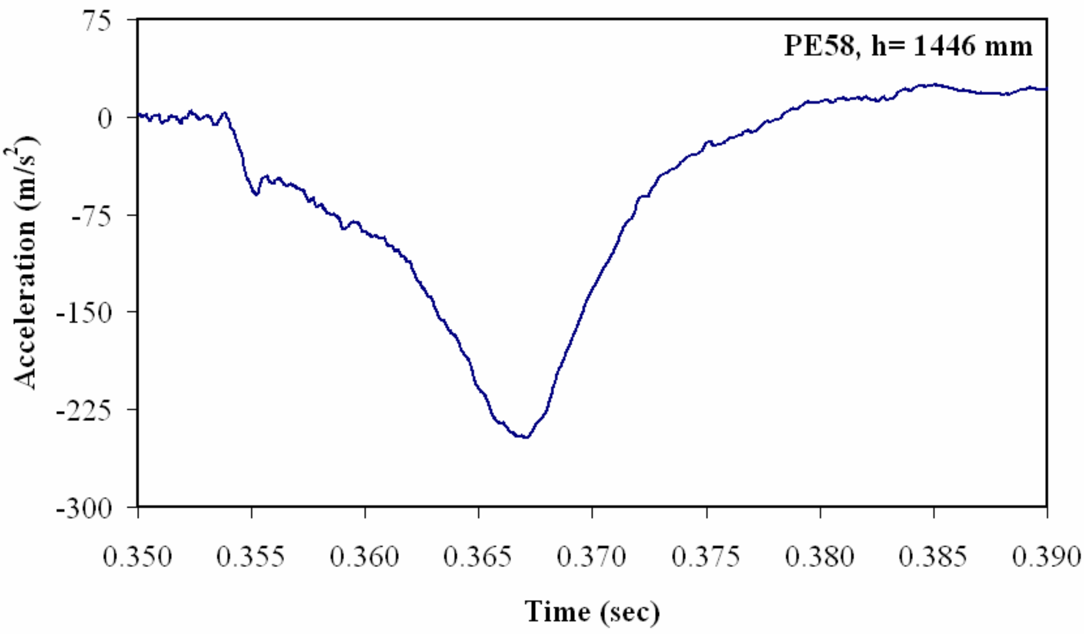

Figure 3.48. Acceleration versus time of PE 58 following the first impact in drop test from 1446 mm height

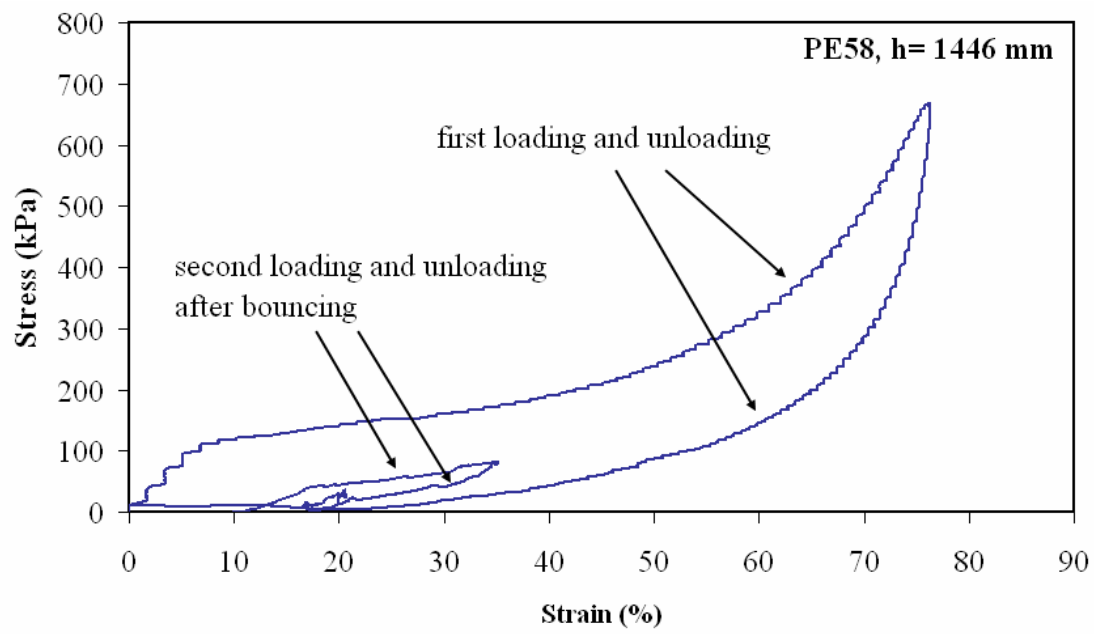

Figure 3.49. Stress versus strain for PE 58 in drop test from 1446 mm height

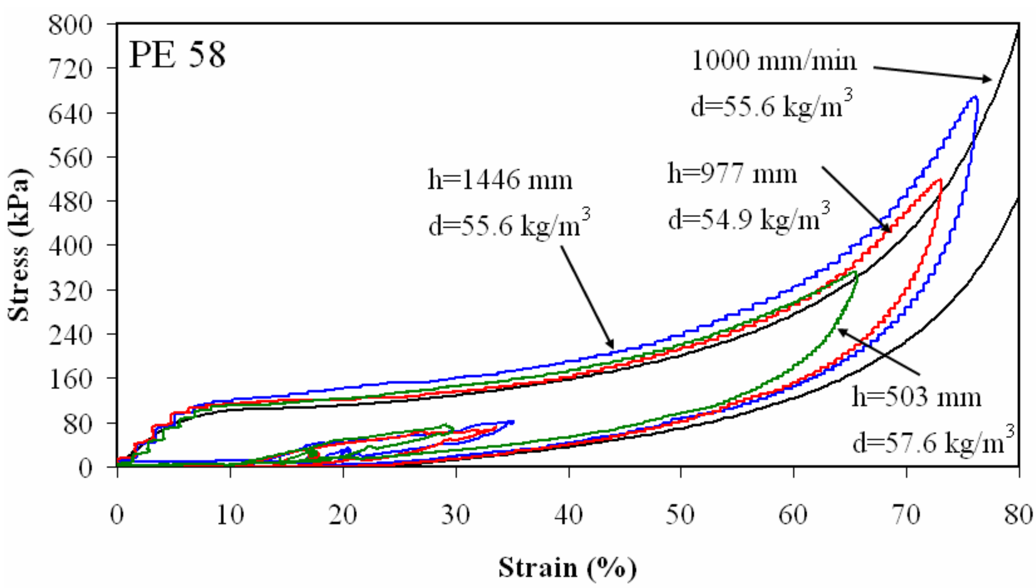

Figure 3.50. Comparison of drop test stress-strain results and results of Zwick for 1000 mm/min cross head speed for PE 58

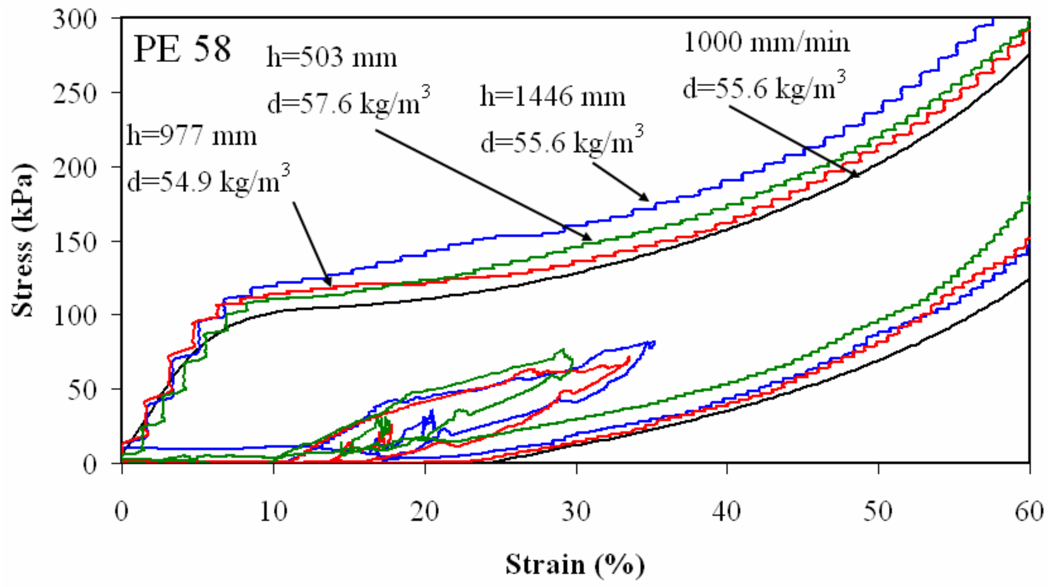

Figure 3.51. Comparison of drop test stress-strain results and results of Zwick for 1000 mm/min cross head speed for PE 58 up to 300 kPa stress and 60 per cent strain

4. MULTIPLE GENERAL LOADING AND UNLOADING BEHAVIOR OF LOW DENSITY POLYMERIC FOAMS

In most of the energy absorbing applications of foams, foam packages are not subjected to pure uniaxial compression. In an indentation type of loading, although most of the foam is under compression, tensile and shear loading modes occur around the region where the indenter penetrates. Fracture of foam occurs very frequently, and when foam is broken, it is usually divided into pieces. A broken foam package cannot function well, and it may lose most of its energy absorbing capacity for subsequent loadings. Therefore mechanical behavior of foam under uniaxial tension and simple shear is important to make accurate calculations of stress, strain, and absorbed energy, and to predict the failure. Volumetric hardening occurs for foams unlike metals. Hydrostatic compression tests and tests for different loading modes are needed to develop failure criteria for low density polymeric foams. In this chapter, multiple general loading and unloading behavior of EPS 30 and PE 58 foams are presented for uniaxial tension, simple shear, hydrostatic compression, cylinder indentation and block indentation tests. A hydrostatic compression test rig is built to study the mechanical behavior of foams under multiple hydrostatic loading and unloading. Special tools are prepared for Zwick Z020 universal tensile testing machine to perform uniaxial tension, simple shear, cylinder indentation, and block indentation tests.

4.1. Mechanical Behavior Under Uniaxial Tension

It is important to specify the loading direction of specimens according to EPS and PE sheets because stress-strain response of foam may change with loading direction. In Figure 4.1, the reference system is given for EPS and PE sheets. Throughout the text, parallel loading is used for loading the specimen in y direction, perpendicular, in x direction, and vertical, in z direction. The tensile test specimen geometry is shown in Figures 4.2 and 4.3. Shape of the specimen is according to the DIN 53430 standard. Tests are performed with Zwick Z020 universal tensile testing machine at room temperature at three different cross head speeds: 5 mm/min, 100 mm/min, and 1000 mm/min. Small additional sheet metal plates are used to increase the friction between the grips of the Zwick and the specimen.

The elongation of the specimen in its middle region is measured by using extensometers. The extensometer legs are separated 50 mm at the beginning of the test. The specimen cross section is 10×25 mm^2. In Figure 4.4, pictures of EPS 30 specimen at the beginning and at the end of the uniaxial compression tests are given. Similar picture are given for PE 58 in Figures 4.5–4.6.

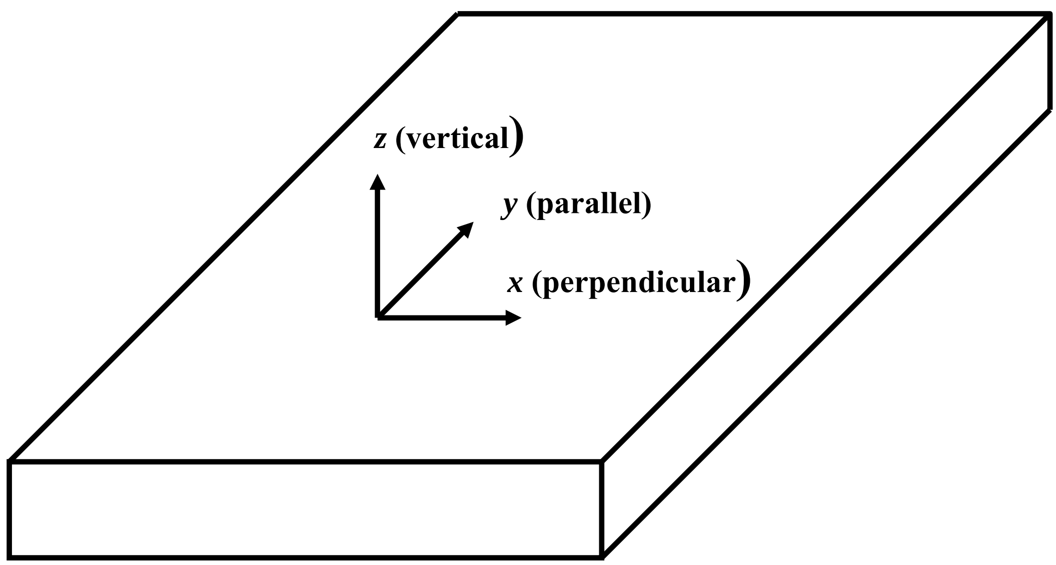

Figure 4.1. Loading directions of test specimen shown on foam sheet

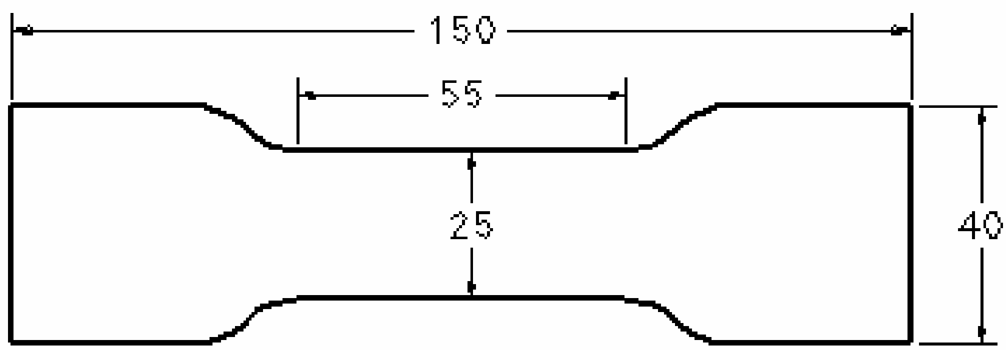

Figure 4.2. Dimensions of uniaxial tension test specimens

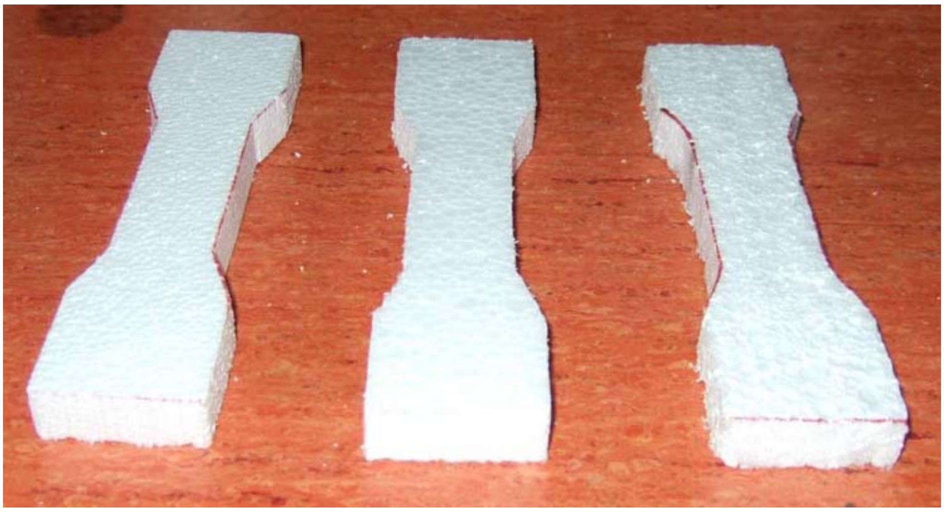

Figure 4.3. EPS 30 tensile test specimens

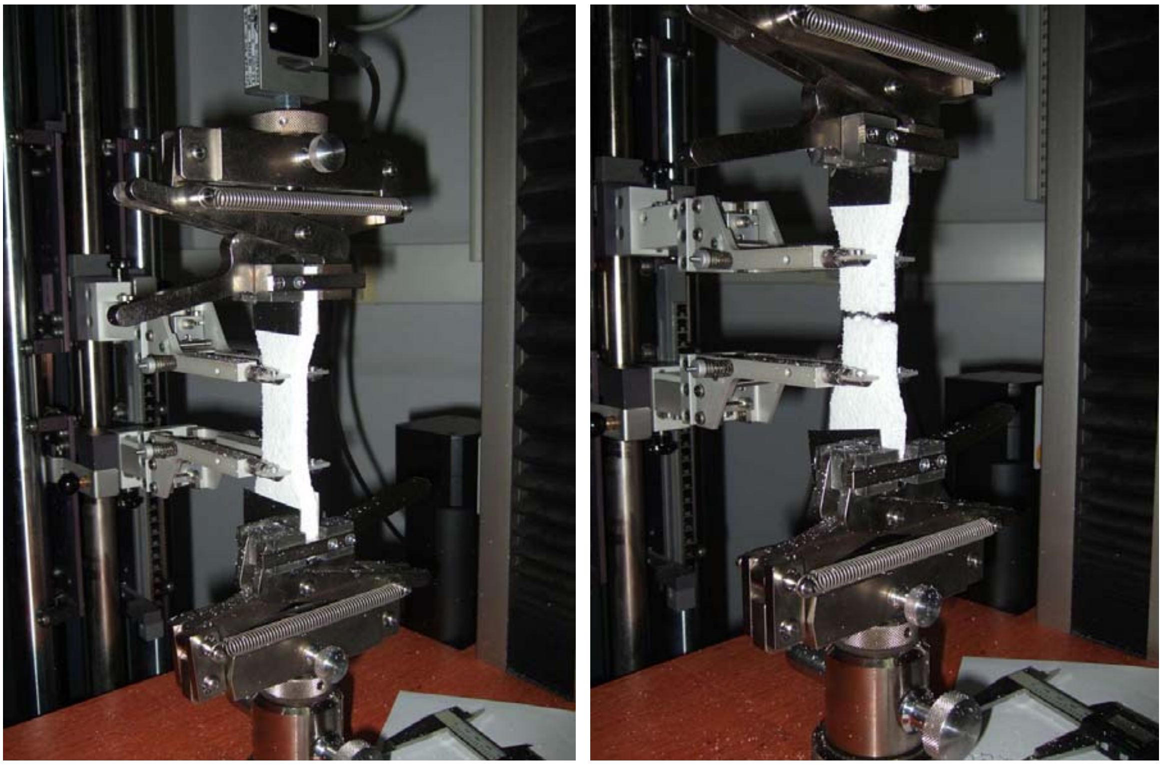

(a) (b)

Figure 4.4. EPS 30 specimen (a) at the beginning and (b) at the end of the uniaxial compression test

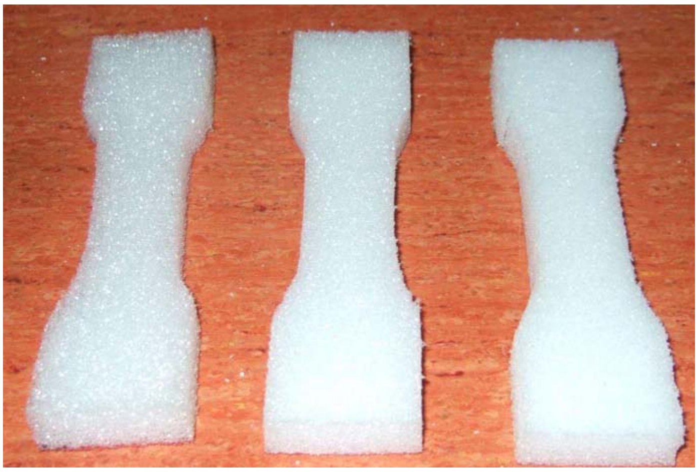

Figure 4.5. PE 58 tensile test specimens

(a) (b)

Figure 4.6. PE 58 specimen (a) at the beginning and (b) at the end of the uniaxial compression test

In Figure 4.7, tensile test results for EPS 30 are given for three different cross head speeds: 5 mm/min, 100 mm/min, and 1000 mm/min. Test results at 100 mm/min for specimens loaded in parallel and perpendicular directions are given in Figure 4.8. It is seen that tensile elastic modulus and tensile strength does not change much with loading speed and loading direction for EPS 30. In Figure 4.9, stress versus strain for multiple tension loading and unloading test of EPS 30 are given together with single loading test at 100 mm/min in perpendicular direction. It is seen that loading path in multiple loading follows the single loading path as it were never unloaded as in uniaxial compression.

In Figure 4.10, tensile test results for PE 58 are given for three different cross head speeds: 5 mm/min, 100 mm/min, and 1000 mm/min. Tensile strength increases with loading speed for PE 58. Test results at 100 mm/min for specimens loaded in parallel and perpendicular directions are given in Figure 4.11. It is seen that the specimens loaded in parallel direction have higher tensile strength than the perpendicular ones because of the stretched grains in parallel direction during extrusion process. In Figure 4.12, stress versus strain for multiple tension loading and unloading of PE 58 are given together with single loading test of two specimens tested at 100 mm/min in perpendicular direction. Similar to EPS 30 and uniaxial compression results, loading path in multiple loading follows the single loading path as it were never unloaded. Tensile test results show that EPS 30 is much more brittle compared to PE 58. PE 58 specimen ultimate tensile strain is around 60 per cent whereas it is around three per cent for EPS 30.

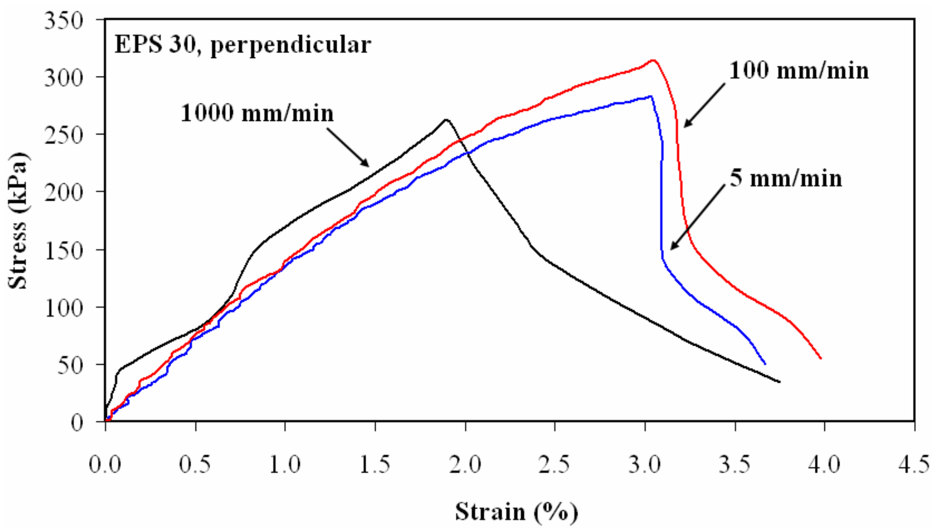

Figure 4.7. Stress versus strain for uniaxial tension of EPS 30 in perpendicular direction at 5 mm/min, 100 mm/min, and 1000 mm/min cross head speeds

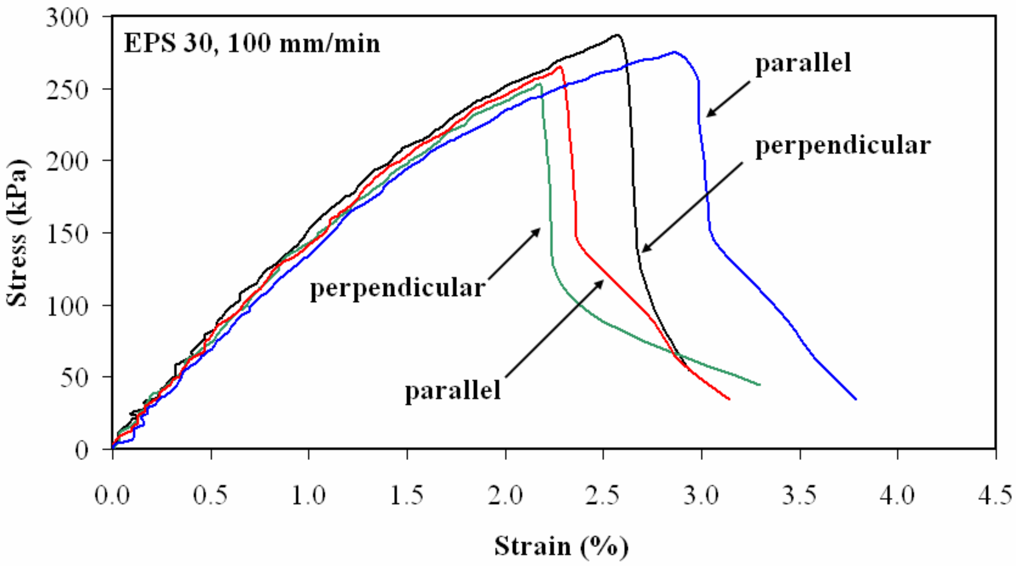

Figure 4.8. Stress versus strain for uniaxial tension of EPS 30 in parallel and perpendicular directions at 100 mm/min cross head speed

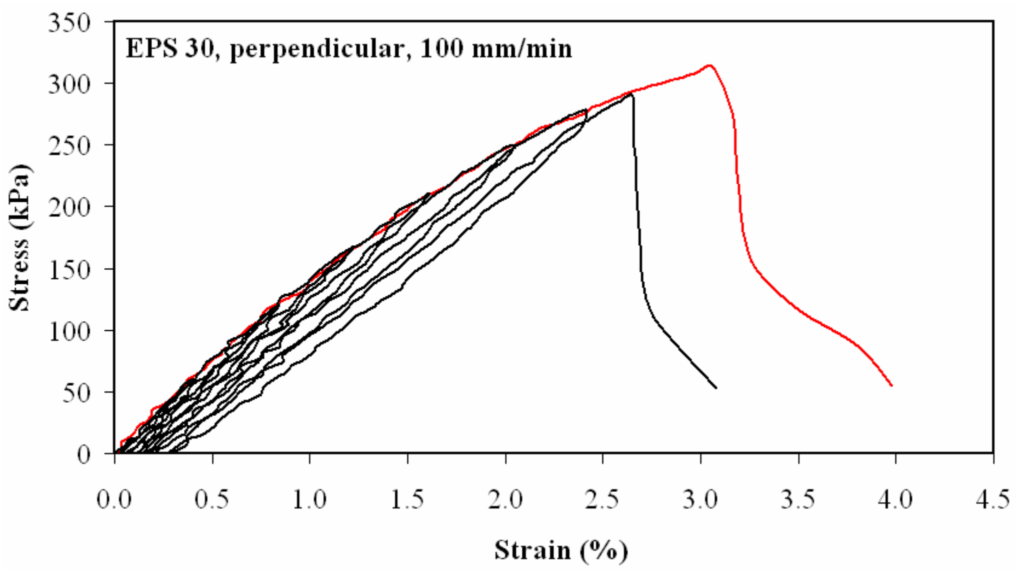

Figure 4.9. Stress versus strain for single and multiple uniaxial tensile loadings of EPS 30 in perpendicular direction at 100 mm/min cross head speed

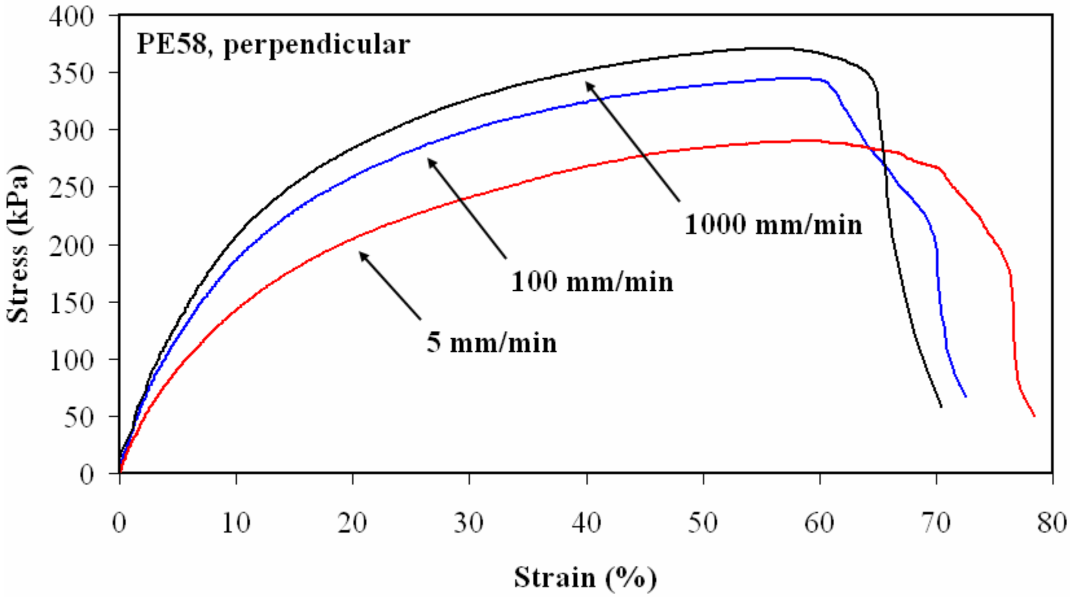

Figure 4.10. Stress versus strain for uniaxial tension of PE 58 in perpendicular direction at 5 mm/min, 100 mm/min, and 1000 mm/min cross head speeds

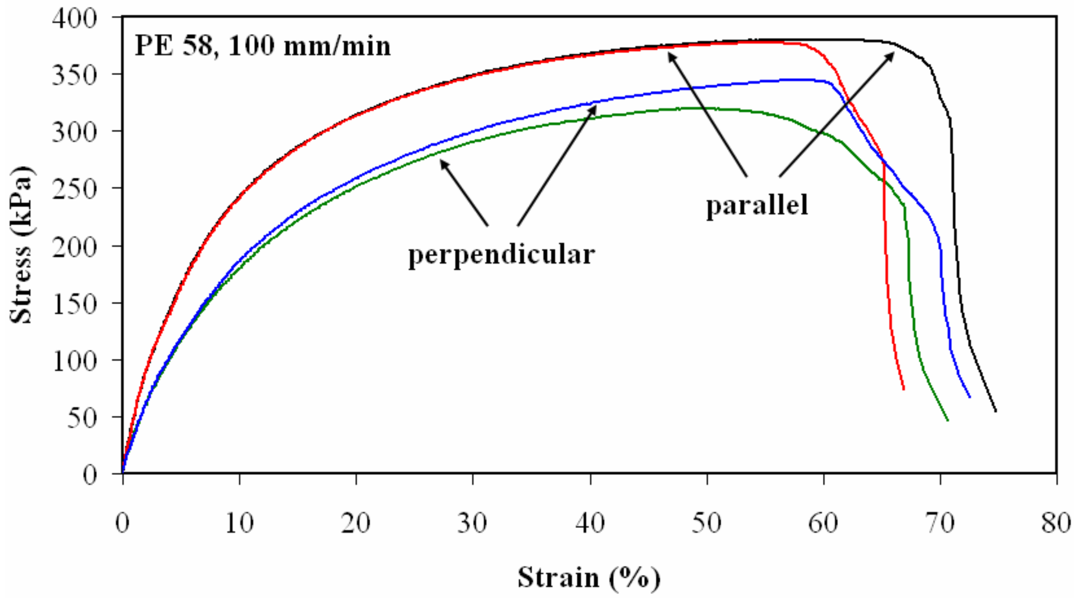

Figure 4.11. Stress versus strain for uniaxial tension of PE 58 in parallel and perpendicular directions at 100 mm/min cross head speed

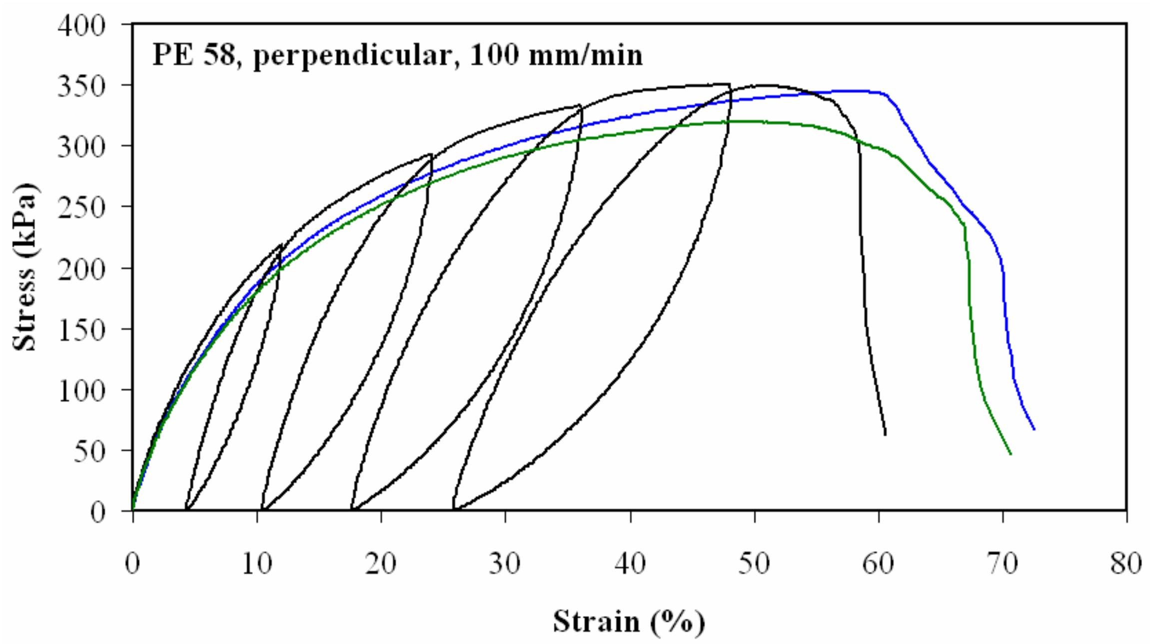

Figure 4.12. Stress versus strain for single and multiple uniaxial tensile loadings of PE 58 in perpendicular direction at 100 mm/min cross head speed

4.2. Mechanical Behavior Under Simple Shear

Simple shear tests are performed by using the Zwick Z020 universal tensile testing machine. Two L-shaped metal tools are attached to the machine, and the shear test specimen is glued to the metal apparatus. Drawing and picture of the simple shear test apparatus are given in Figure 4.13. Test specimen dimensions are $50 \times 50 \times 100$ mm^3 for EPS 30 and $45 \times 50 \times 100$ mm^3 for PE 58. Epoxy type adhesive that cures at 20 minutes is used to glue the foam specimen to the L-shaped metal plates. The position of one of the L-shaped metal tools can be adjusted horizontally so that the distance between them can be adjusted accurately according to the specimen dimensions. Pictures about the deformation pattern and fracture of the specimens in simple shear test can be seen in Figure 4.14 for EPS 30 and in Figure 4.15 for PE 58. It is observed that fracture initiates in EPS 30 foam close to the glued surface. PE 58 tears out from the glued surface at a deformation level which is much beyond the pure shear loading state.

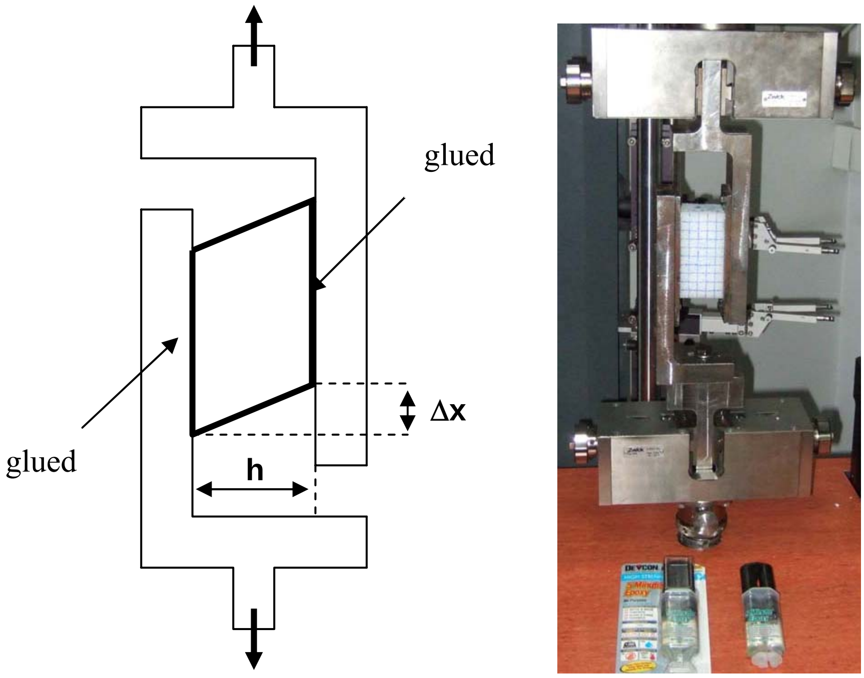

Figure 4.13. (a) Geometry of simple shear test specimen and (b) picture of simple shear test setup

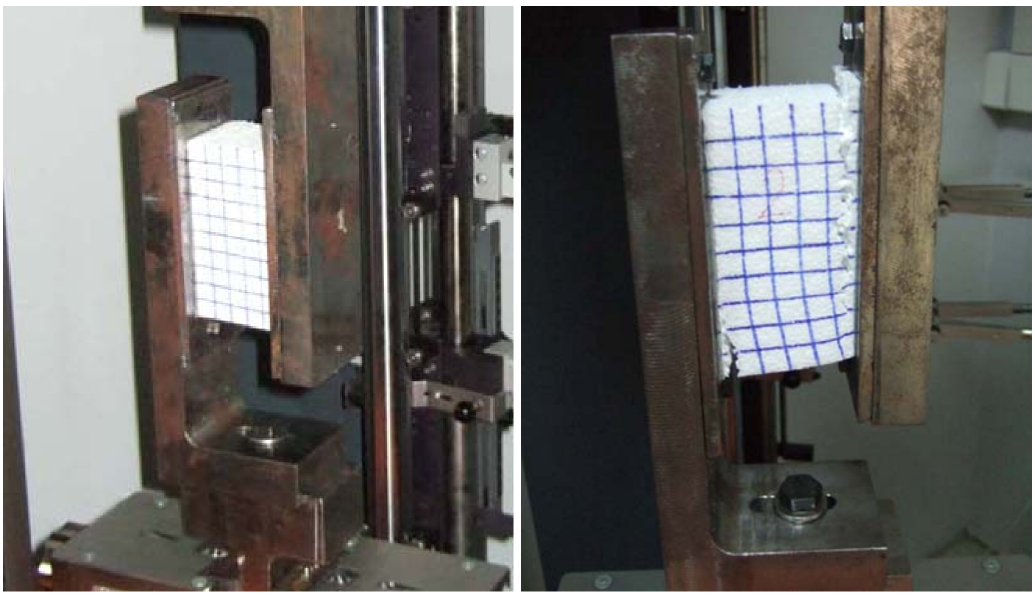

(a) (b)

Figure 4.14. EPS 30 specimen (a) at the beginning and (b) at the end of the simple shear test

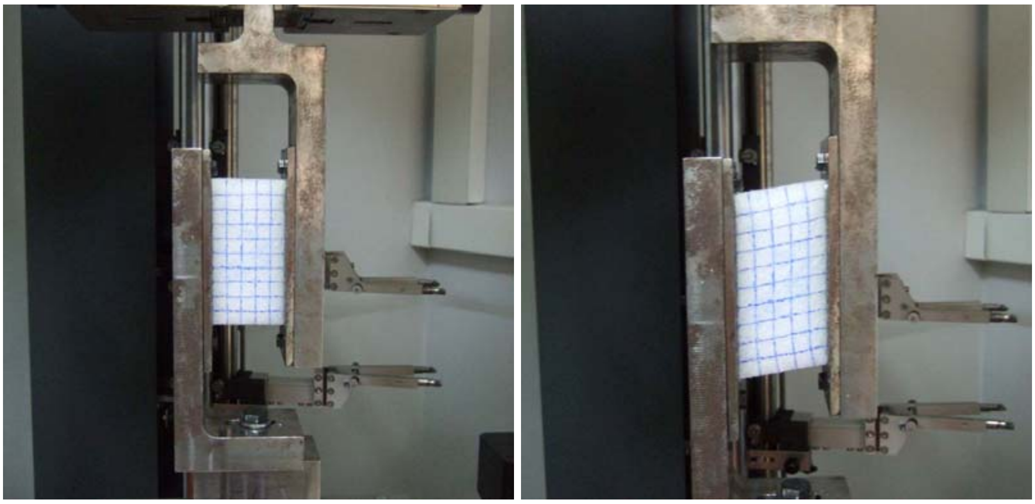

(a) (b)

Figure 4.15. (a) Undeformed and (b) deformed PE 58 specimen in the simple shear test

All test specimens for simple shear test of EPS 30 are tested in perpendicular direction because it is seen in uniaxial compression and tension tests that properties of EPS 30 do not change in parallel and perpendicular loading directions. In Figure 4.16, simple shear test results for EPS 30 are given for three different cross head speeds:5 mm/min, 100 mm/min, and 1000 mm/min. Similar to uniaxial compression and tension, it is seen that there is not a difference of shear modulus and shear strength between different loading speeds for EPS 30. In Figures 4.17 and 4.18, shear stress versus shear strain are given for multiple loading and unloading of EPS 30 together with single loading at 100 mm/min. Similar to uniaxial compression and tension, loading path in multiple shear loading follows the single loading path as it were never unloaded before.

In Figures 4.19 and 4.20, simple shear test results for PE 58 are given for three different cross head speeds: 5 mm/min, 100 mm/min, and 1000 mm/min. It is seen that the shear modulus and shear strength increase with loading speed as in compression and tension loading. From the results given in Figures 4.21, and 4.22, it is seen that there is a slight difference for simple shear test results of specimens cut and tested in parallel and perpendicular directions. In Figures 4.23 and 4.24, multiple loading and unloading of PE 58 in simple shear results are given together with single loading at 100 mm/min in perpendicular direction. In multiple loading, PE 58 specimen tears from the adhesive layer much before than single loading. Similar to uniaxial compression and tension results, loading path in multiple loading follows the single loading path as it were never unloaded. Fracture occurs in simple shear tests at corner elements. This occurs at small strains in EPS 30 compared to PE 58. Shear stress versus shear strain results are plotted for more than 100 per cent strain for PE 58 to show their behavior beyond linear region.

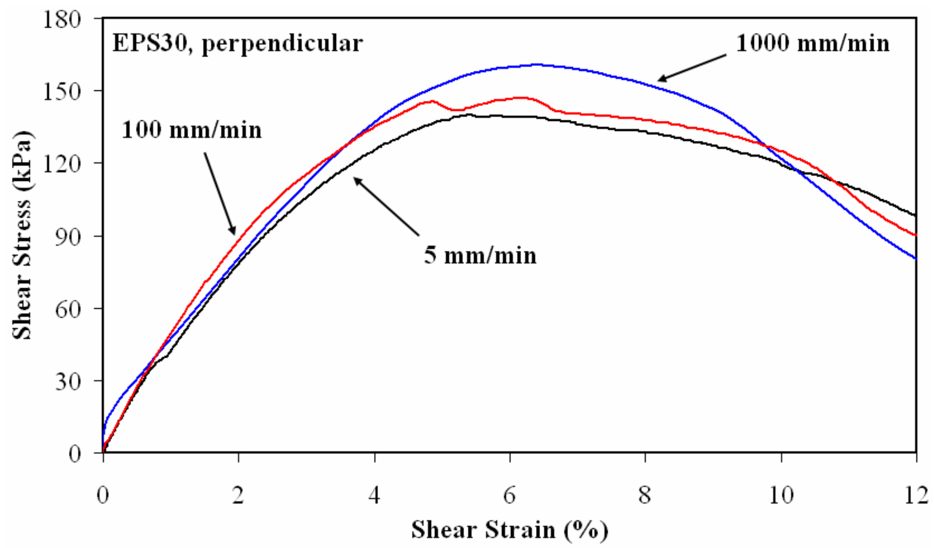

Figure 4.16. Shear stress versus shear strain for simple shear of EPS 30 in perpendicular direction at 5 mm/min, 100 mm/min, and 1000 mm/min cross head speeds

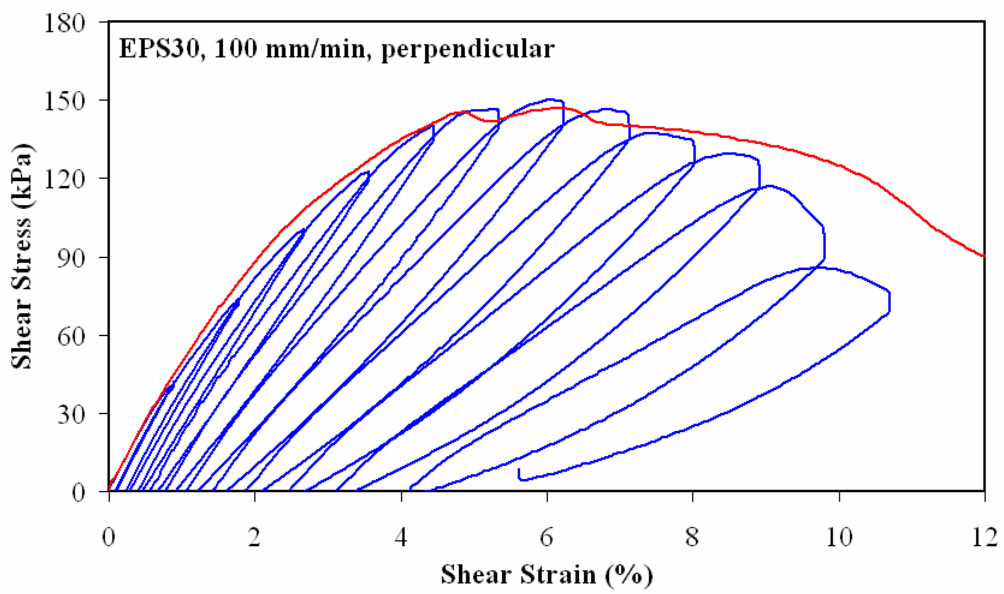

Figure 4.17. Shear stress versus shear strain for single and multiple simple shear loadings of EPS 30 in perpendicular direction at 100 mm/min cross head speed

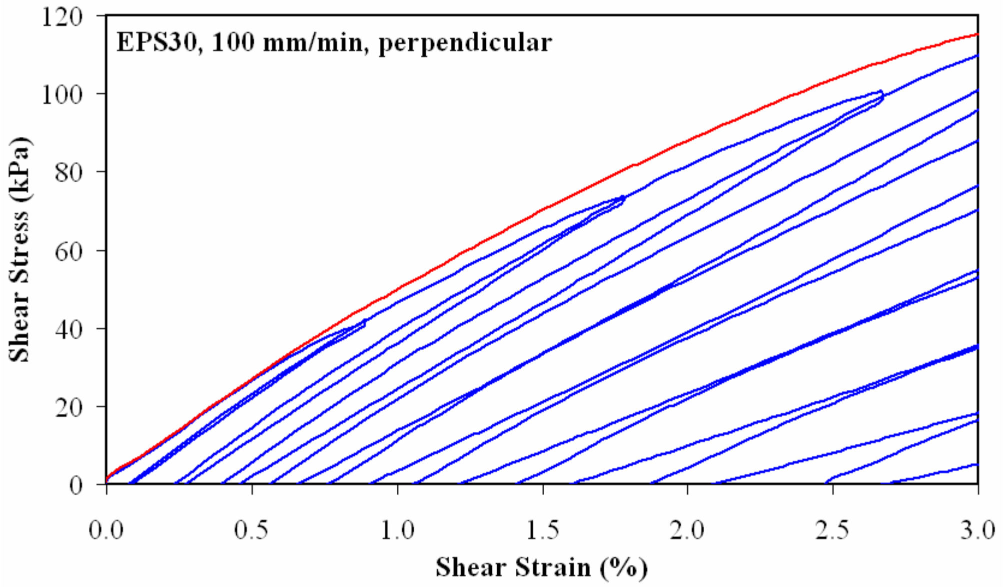

Figure 4.18. Shear stress versus shear strain for single and multiple simple shear loadings of EPS 30 in perpendicular direction at 100 mm/min cross head speed up to 3 per cent shear strain

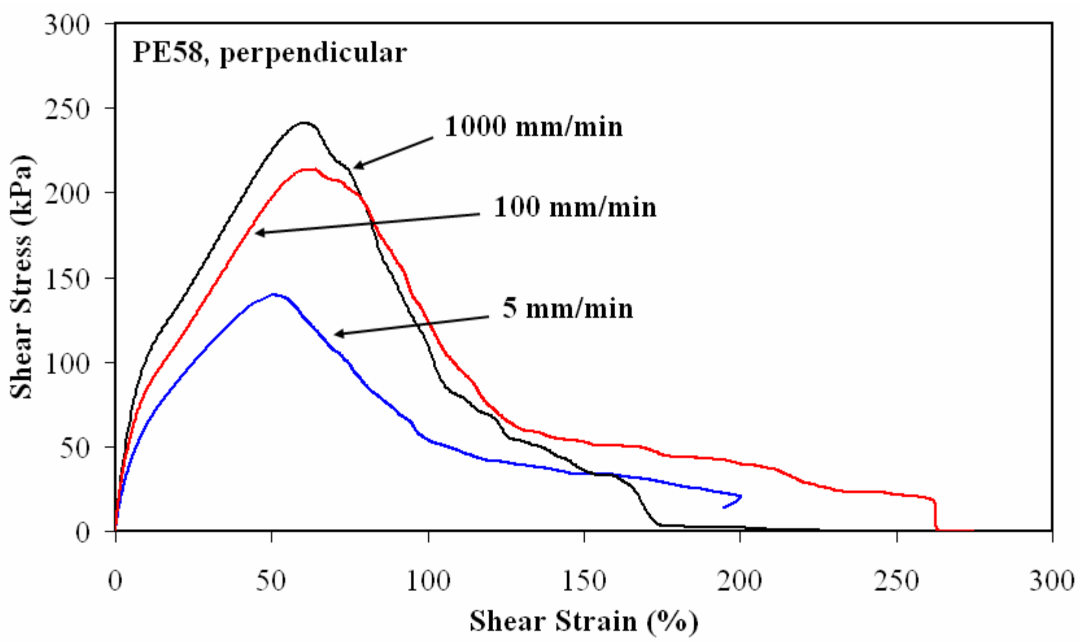

Figure 4.19. Shear stress versus shear strain for simple shear of PE 58 in perpendicular direction at 5 mm/min, 100 mm/min, and 1000 mm/min cross head speeds

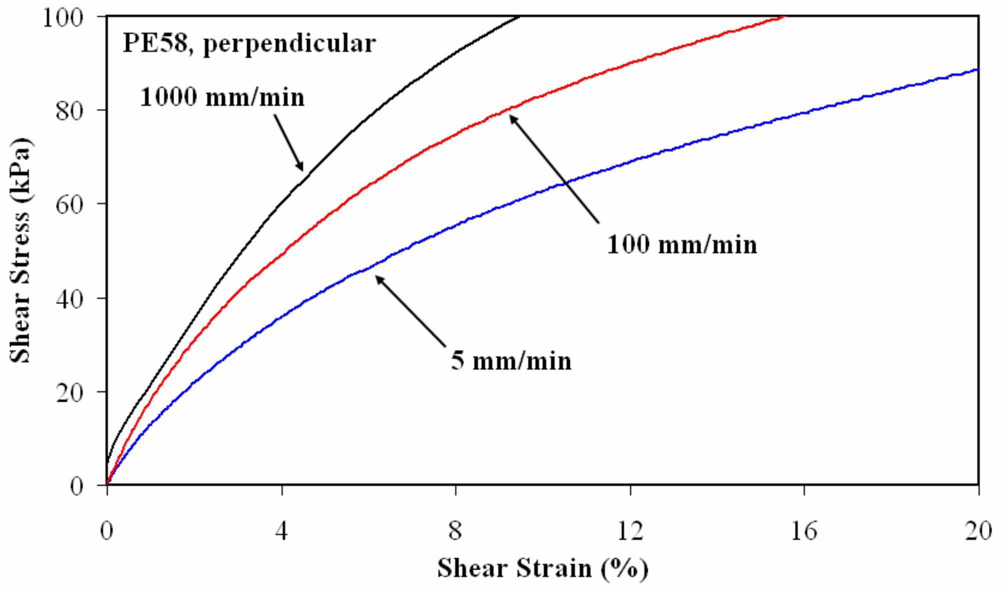

Figure 4.20. Shear stress versus shear strain for simple shear of PE 58 in perpendicular direction at 5 mm/min, 100 mm/min, and 1000 mm/min cross head speeds up to 20 per cent shear strain

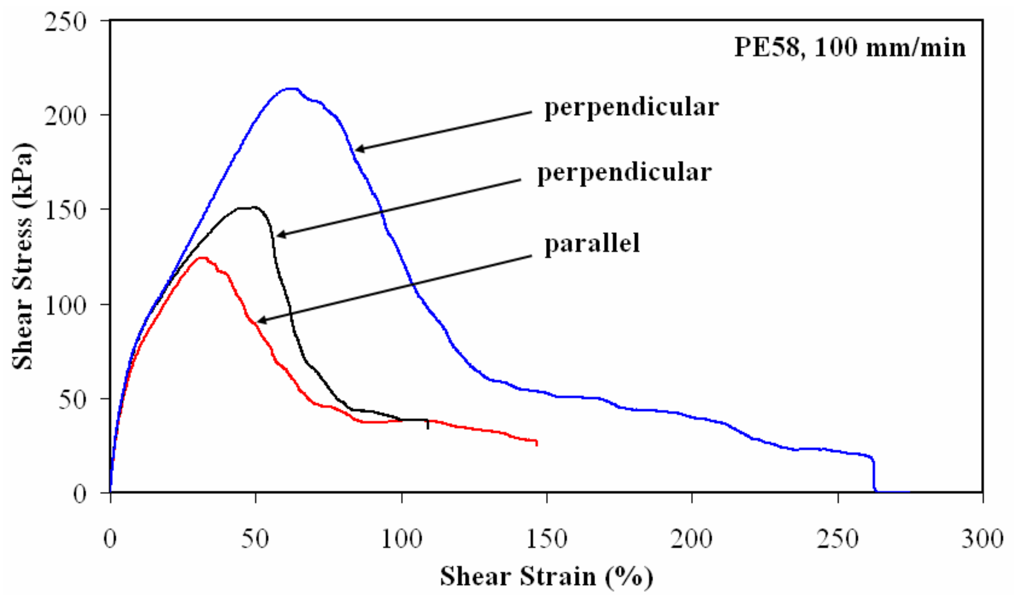

Figure 4.21. Shear stress versus shear strain for simple shear of PE 58 in parallel and perpendicular directions at 100 mm/min cross head speed.

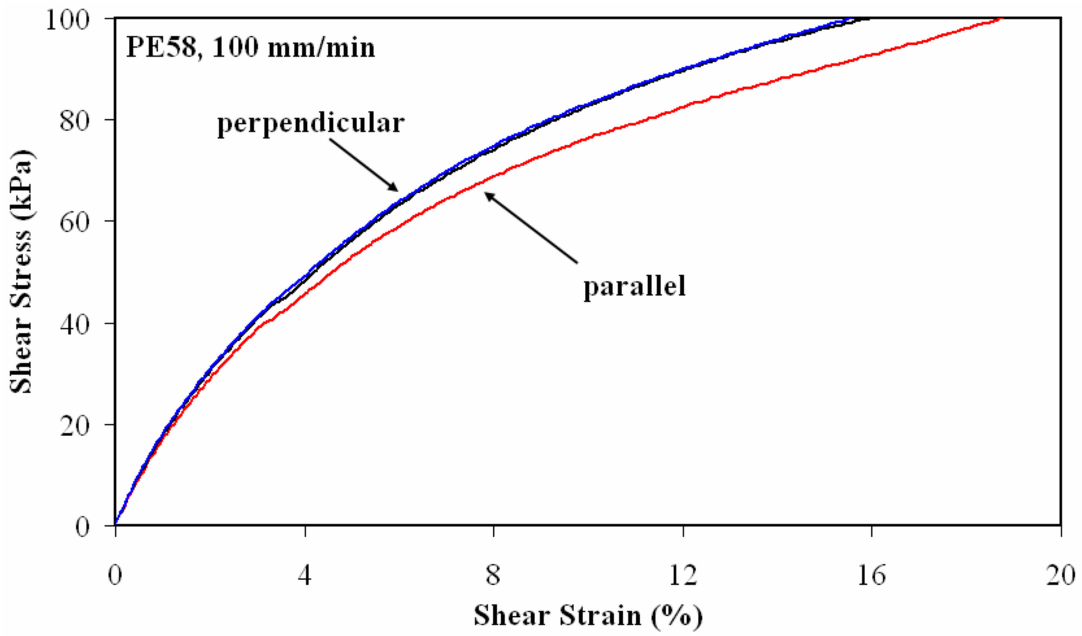

Figure 4.22. Shear stress versus shear strain for simple shear of PE 58 in parallel and perpendicular directions at 100 mm/min cross head speed up to 20 per cent shear strain

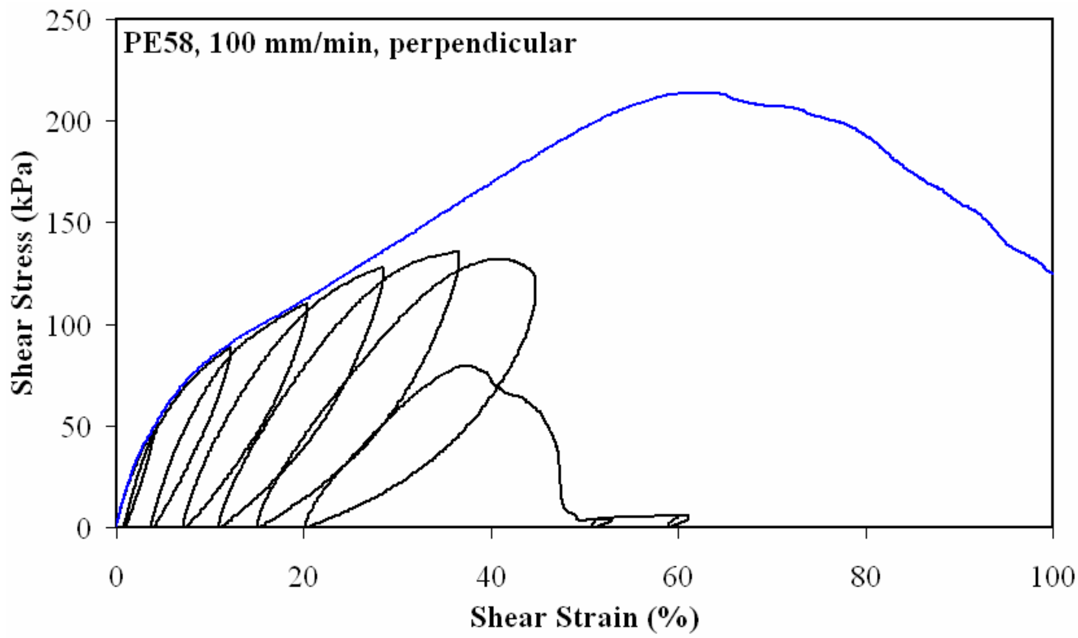

Figure 4.23. Shear stress versus shear strain for single and multiple simple shear loadings of PE 58 in perpendicular direction at 100 mm/min cross head speed

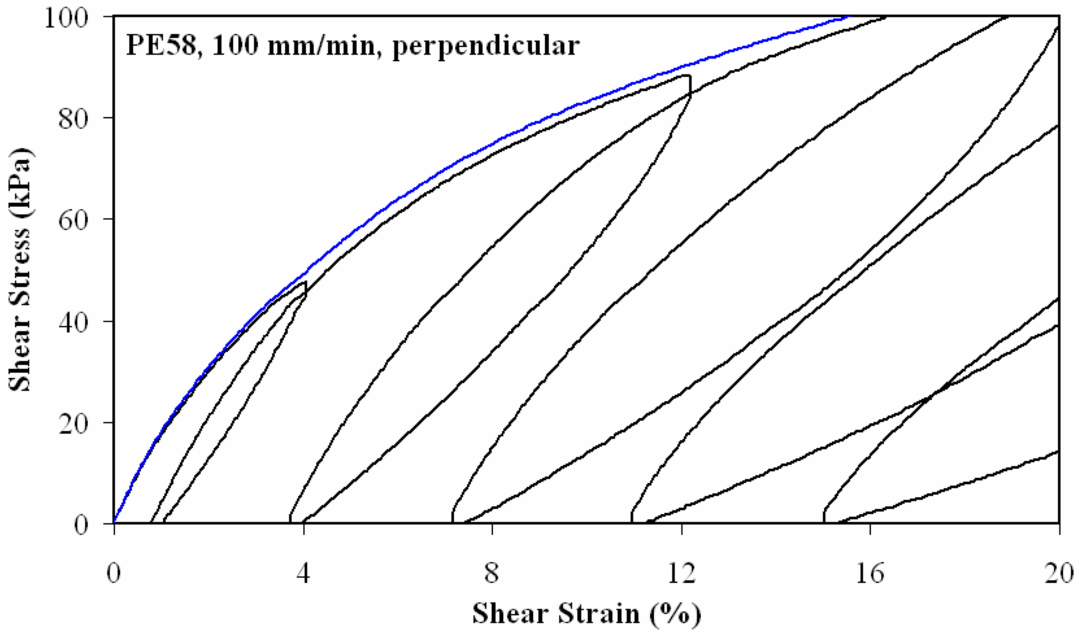

Figure 4.24. Shear stress versus shear strain for single and multiple simple shear loadings of PE 58 in perpendicular direction at 100 mm/min cross head speed up to 20 per cent shear strain

4.3. Mechanical Behavior Under Hydrostatic Compression

A test rig built for hydrostatic compression testing of low density polymeric foams as shown in Figures 4.25–4.29. Hydrostatic compression is applied by nitrogen gas. The pressure in nitrogen tank is around 230 bar when it is full, and it is connected to the test tank by a mechanical regulator, which is used to adjust the pressure inside the test tank. The test tank is $50 \times 50 \times 50$ mm^3 dimensions and made from 20 mm thick steel. Its top cover is made 20 mm thick steel where there are two windows made from 20 mm thick tempered glass of area 100×100 mm^2 for observing the deformation of the foam during the test as seen in Figures 4.26 and 4.27. Inside of the tank can be illuminated from one window and deformation of test specimen can be observed from other window. There is a mechanical pressure switch for safety that opens and exhausts the gas from tank when pressure reaches 14 bar. The tank is first checked for strength by filling it with water, and testing it for pressure up to 30 bar. In tests with nitrogen, pressure inside the test tank is increased up to 11 bar at most.

Figure 4.25. Hydrostatic test rig

A rubber seal of 8 mm diameter is used to prevent leakage from the top cover. 24 M8 bolts are used to close the top cover of the tank. Pressure transmitter ED701 from Haenni with 10 bar measurement range is used to measure the pressure inside the tank. Three linear voltage displacement transducers (LVDT) LVTG-6000 from Himmelstein with ± 25 mm measurement range are used to measure the deformation of foam specimen from three surfaces of the specimen. The foam specimen is placed at the corner of three metal plates, and the displacement sensors are fixed on those plates as seen Figure 4.28. Data cables of displacement sensors are taken out from the tank from the sealed holes on the top cover. Data cables are covered by metal tube until the connection on the top cover of the test tank so that they can resist high pressure, and no leakage occurs through the cables.

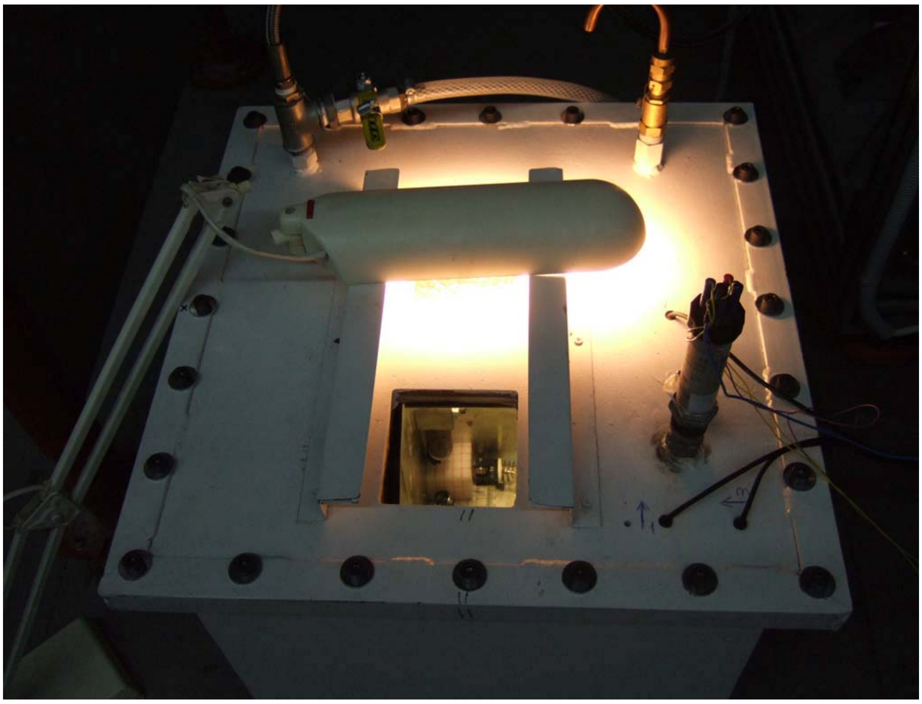

Figure 4.26. Pressure tank top cover

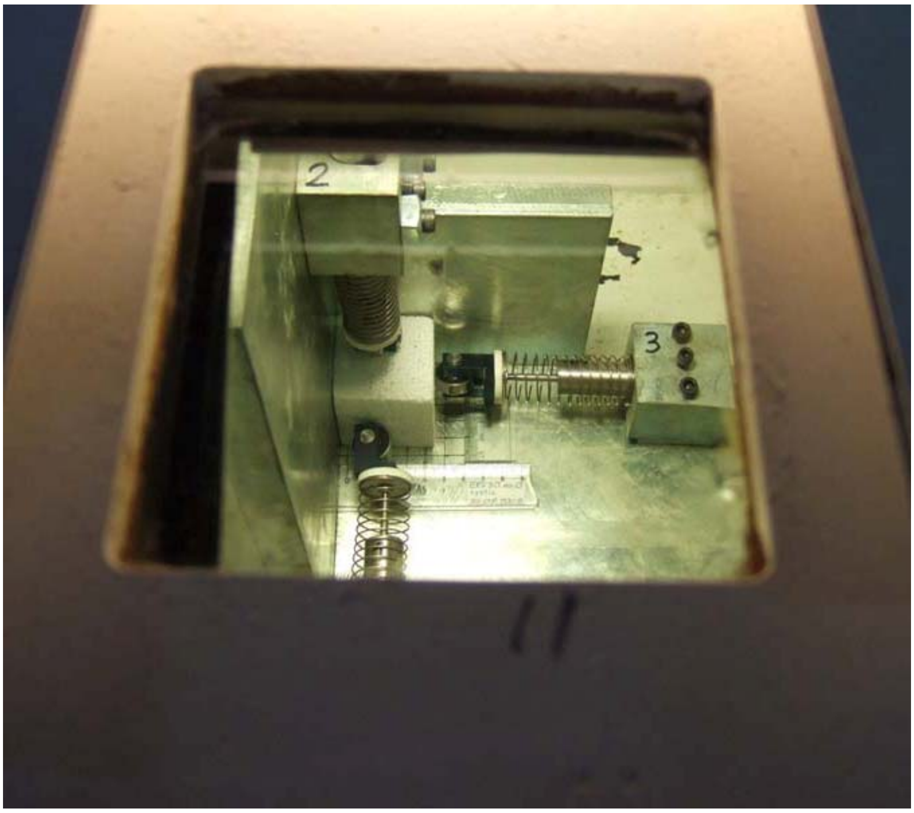

Figure 4.27. View of test specimen through glass window in hydrostatic test

From Figures 4.28 and 4.29, it can be seen how displacement sensors and the specimen is placed during testing. LVDT’s measure the displacement of the metal pin that enters into the tube. Ball bearings are attached to the metal pins so that it can slide over the surfaces of the foam during the large deformation and shrinkage of foam specimen. Helical springs are used to push the metal pins onto the foam specimen so that metal pin can follow the foam surface while the foam specimen is deformed. Helical spring exert around 200 gram force at the beginning of the test, so that the deformation due to the metal pin is negligible. A grid is drawn and a ruler is placed onto the basement to guess the magnitude of deformation from photographs. In Figure 4.28, it can be seen that the displacement sensor labeled as LVDT 2 measure the deformation normal to the basement, and LVDT 1 and 3 measure the lateral deformations.

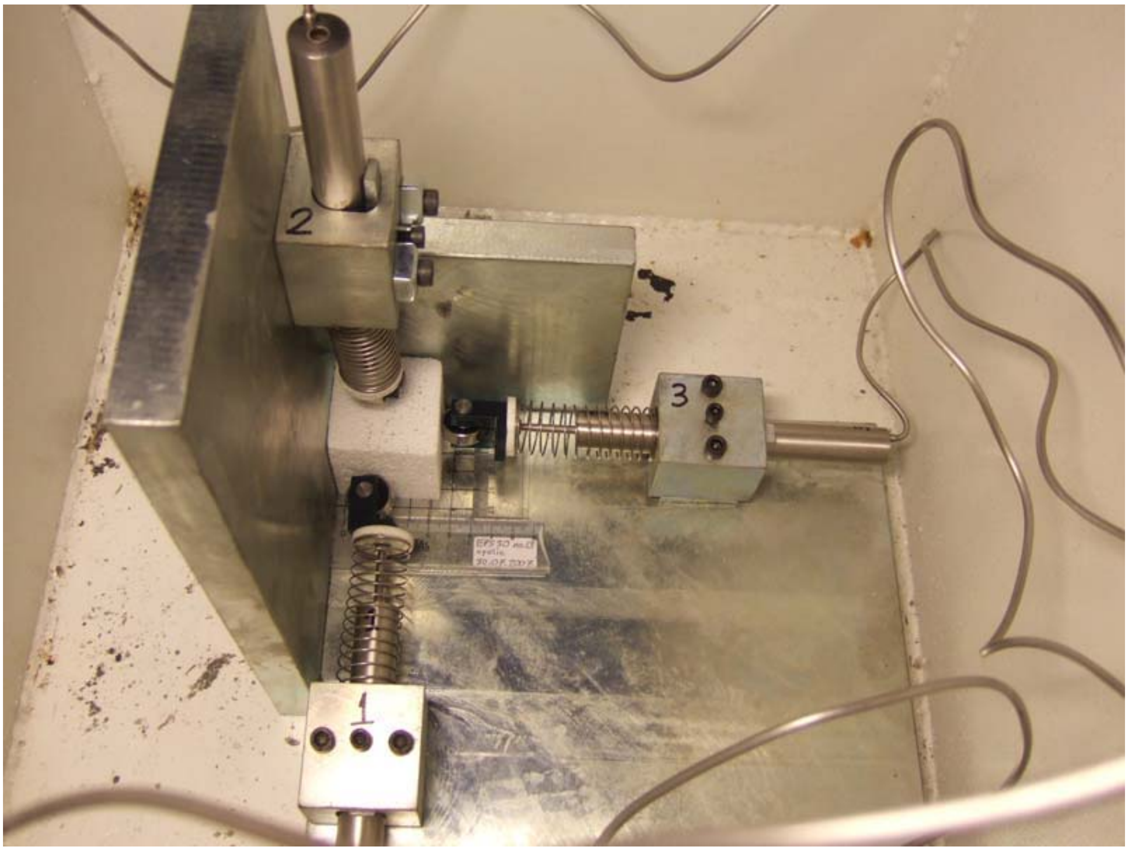

Figure 4.28. Displacement sensors in hydrostatic test

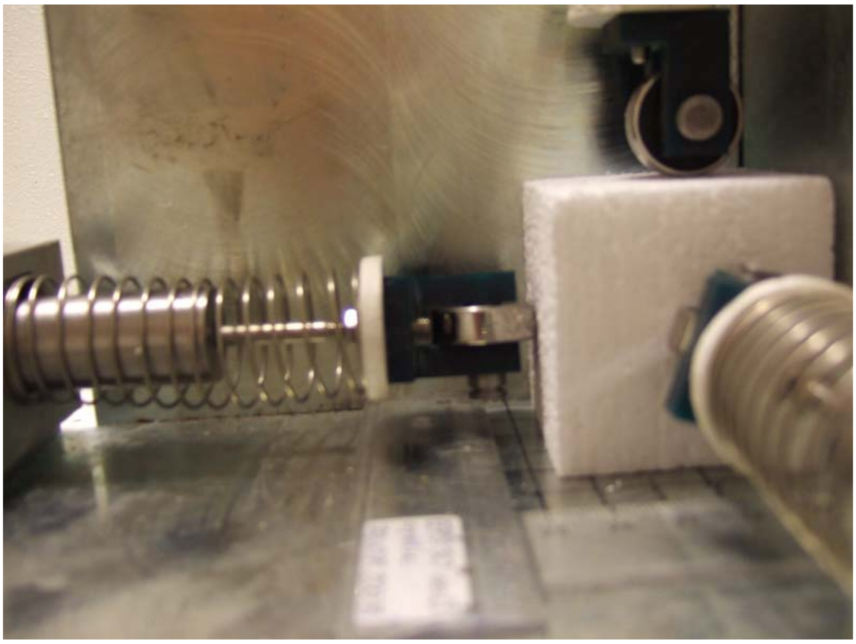

Figure 4.29. First and second displacement sensor (LVDT 1 and 2) touching on the test specimen surface

Single and multiple hydrostatic loading and unloading tests are performed for EPS 30 and PE 58. In Figure 4.30, EPS 30 specimen at the beginning of single loading test no 20 can be seen. In Figures 4.31 and 4.32, EPS 30 is deformed under maximum pressure in test no 20. It is seen that EPS 30 specimen is rotated under maximum pressure in test 20. EPS 30 specimen returns to its initial position after unloading as seen in Figure 4.33. Reasons of the rotation can be due to the friction between the foam and the metal plates, and pushing the foam with metal pins during deformation. At large deformation, the point of application of the force exerted by the metal pin is not in the middle of the foam specimen anymore, and this can lead to the rotation of the specimen. At the end of the tests of EPS 30, it is observed that there is a residual deformation of between 0.90 and 1.3 mm at the point of applications of the LVDT's on the foam.

The test specimen at the beginning of multiple loading and unloading test no 13 can be seen in Figure 4.34. In Figures 4.35 and 4.36, EPS 30 is deformed under maximum pressure in test 13. Figure 4.37 shows the deformation of EPS 30 specimen after unloading in test no 13. It is seen that EPS 30 specimen in test no 13 is not rotated as in test no 20.

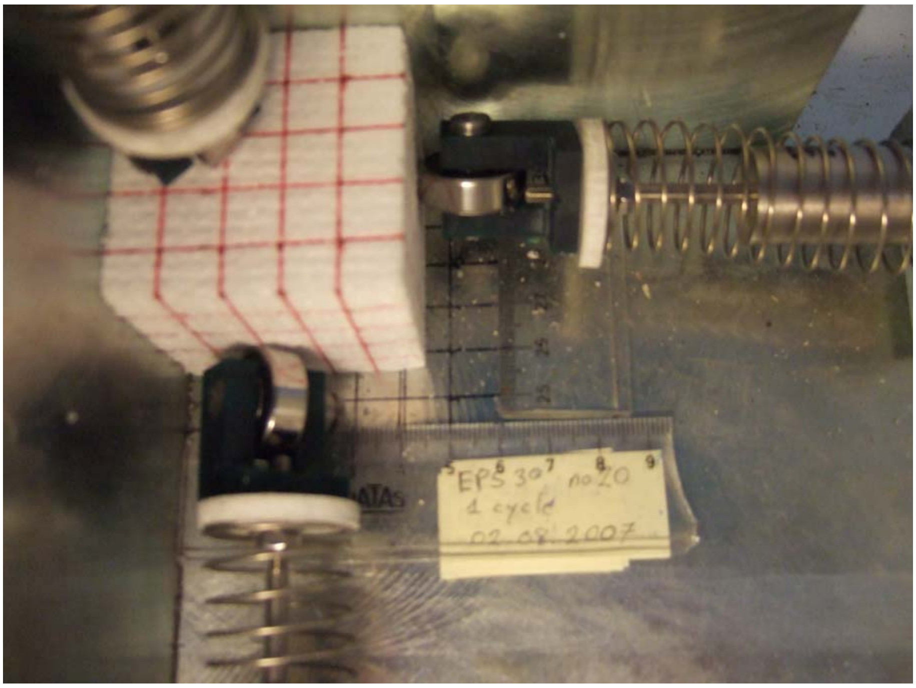

Figure 4.30. EPS 30 specimen before test no 20

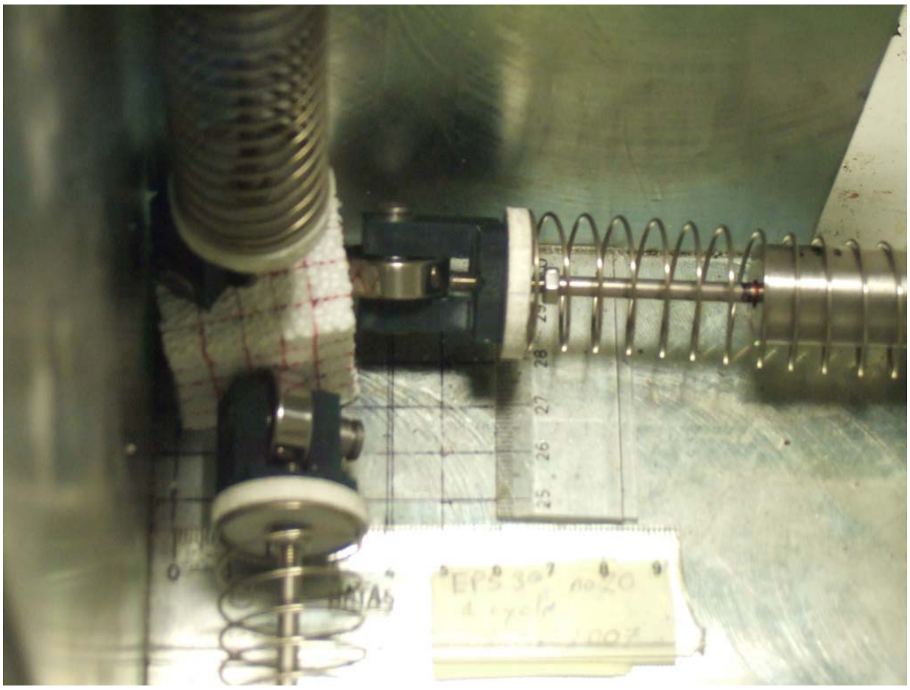

Figure 4.31. Deformation of EPS 30 specimen under maximum pressure in test no 20

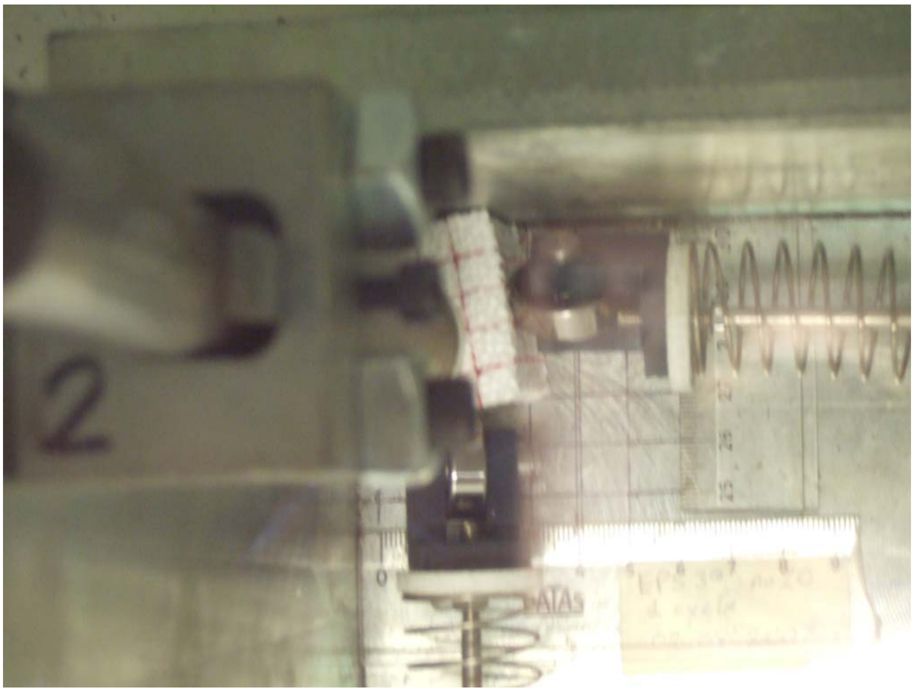

Figure 4.32. Deformation of EPS 30 specimen under maximum pressure in test no 20

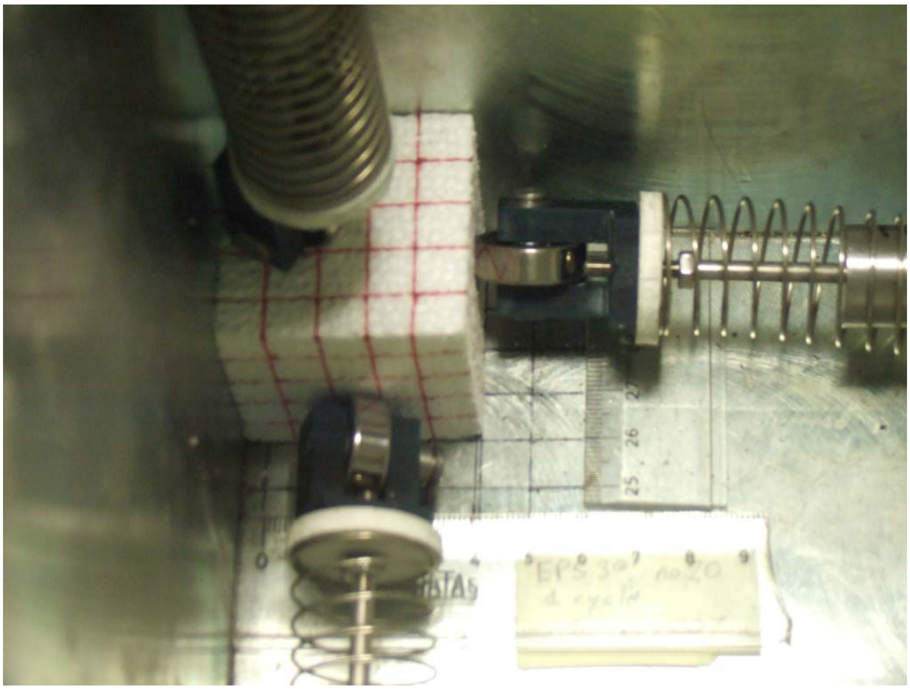

Figure 4.33. Deformation of EPS 30 specimen after unloading in test no 20

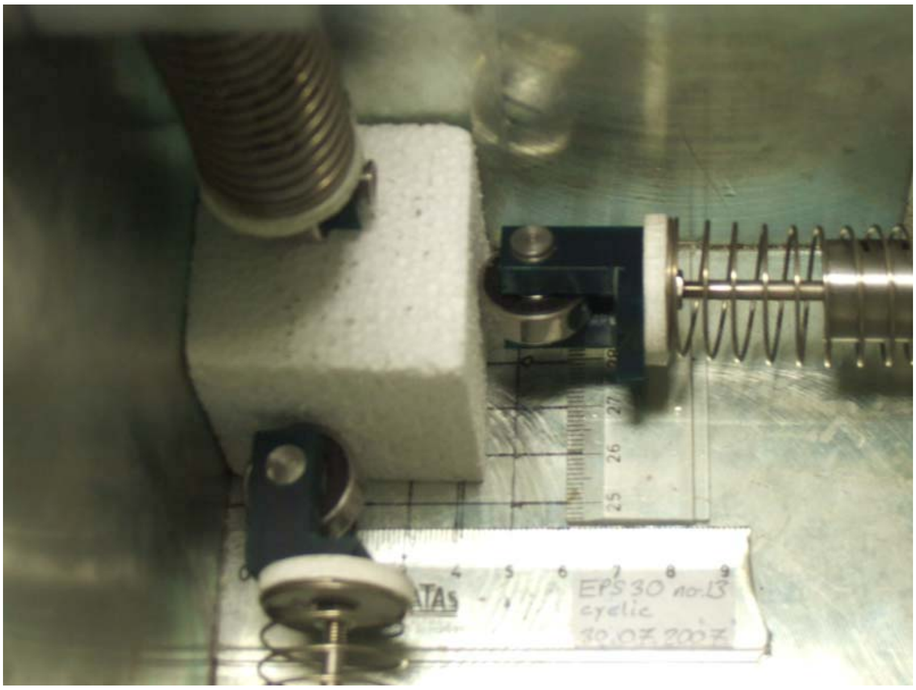

Figure 4.34. EPS 30 specimen before test no 13

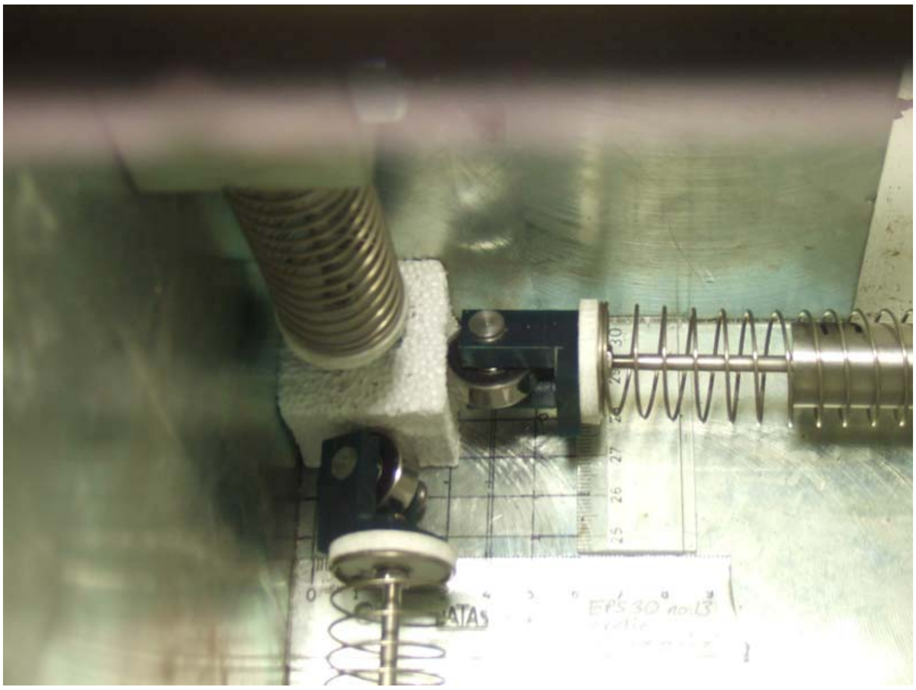

Figure 4.35. Deformation of EPS 30 specimen under maximum pressure in test no 13

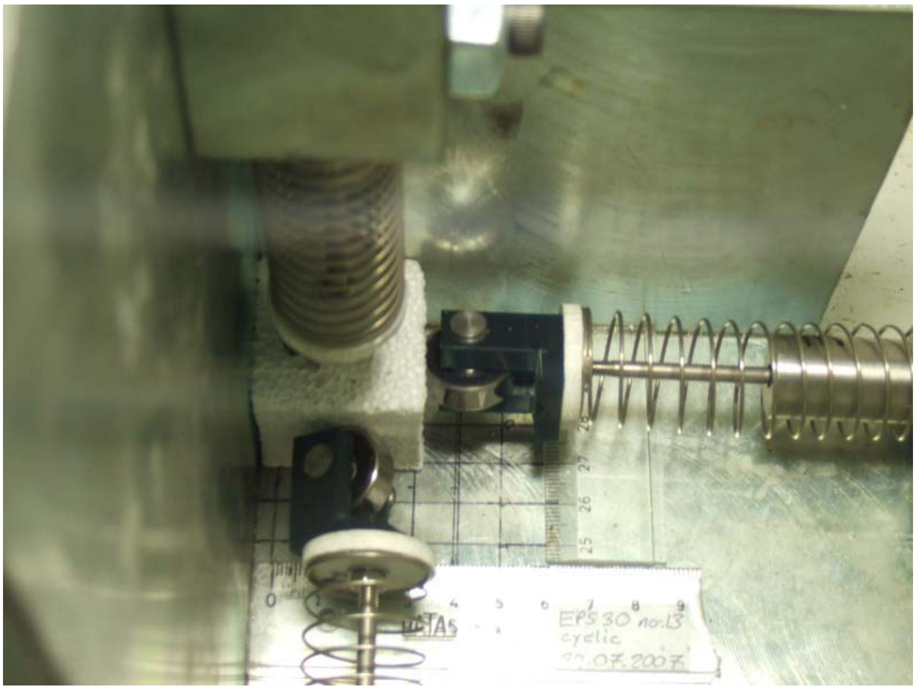

Figure 4.36. Deformation of EPS 30 specimen under maximum pressure in test no 13

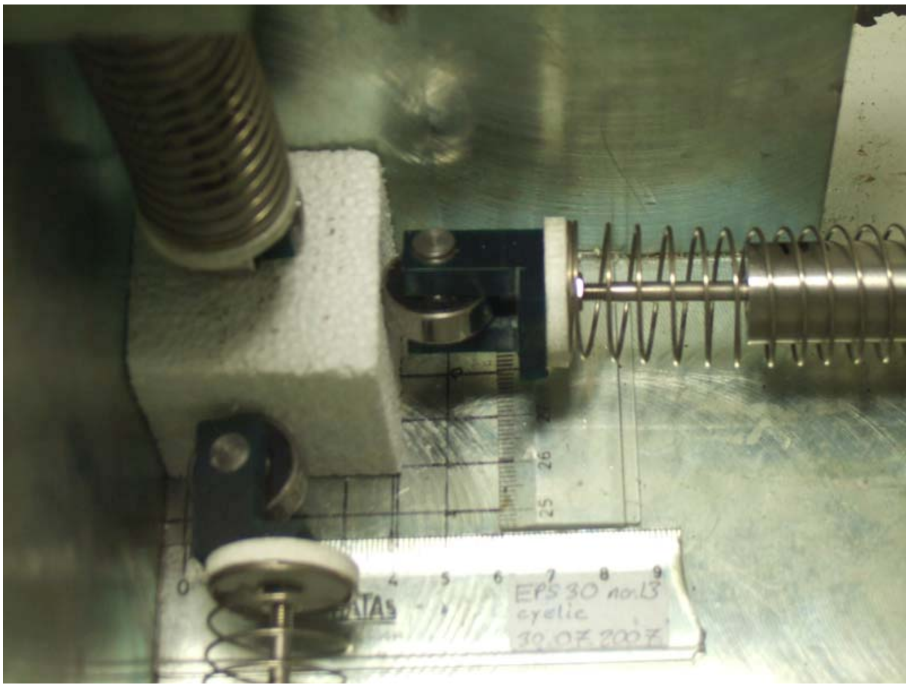

Figure 4.37. Deformation of EPS 30 specimen after unloading in test no 13

In Figure 4.38, PE 58 specimen at the beginning of single loading test no 21 can be seen. In Figures 4.39 and 4.40, PE 58 is deformed under maximum pressure in test no 21. It is seen that there is a gap of around 2 mm between the metal plate and the PE 58 specimen under maximum pressure in test 21. The PE 58 specimen is deformed much more in the perpendicular direction compared to parallel direction. Surfaces of PE 58 sheets have higher densities compared to the middle region. Therefore regions close to the top and bottom surfaces deform less than the middle region, and the surface of the foam is not flat at maximum pressure. Therefore the hydrostatic pressure versus volumetric strain results are not reliable after a certain deformation level for PE 58 tests. PE 58 specimen in test no 21 returns to its initial position, and there is no a gap anymore between the foam and the metal plate after unloading as seen in Figure 4.41. Residual deformation is around 0.3 mm after the test at the point of applications of the LVDT’s on the surface of PE 58 specimens. In Figures 4.42–4.45, single loading test no 21 of PE 58 can be seen. There is more gap between the PE 58 test no 14 and the metal plate compared to test no 21.

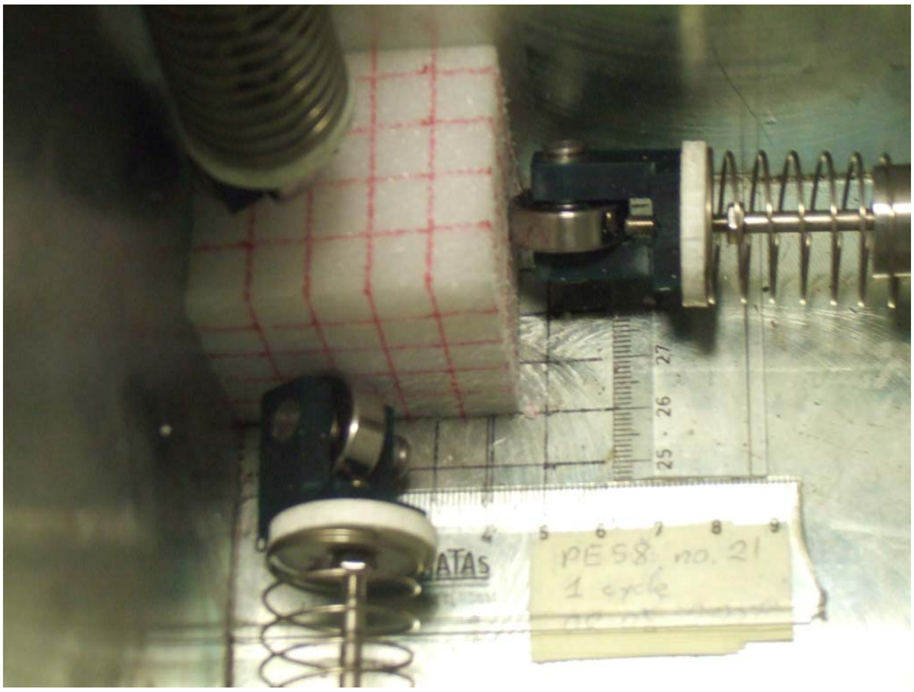

Figure 4.38. PE 58 specimen before test no 21

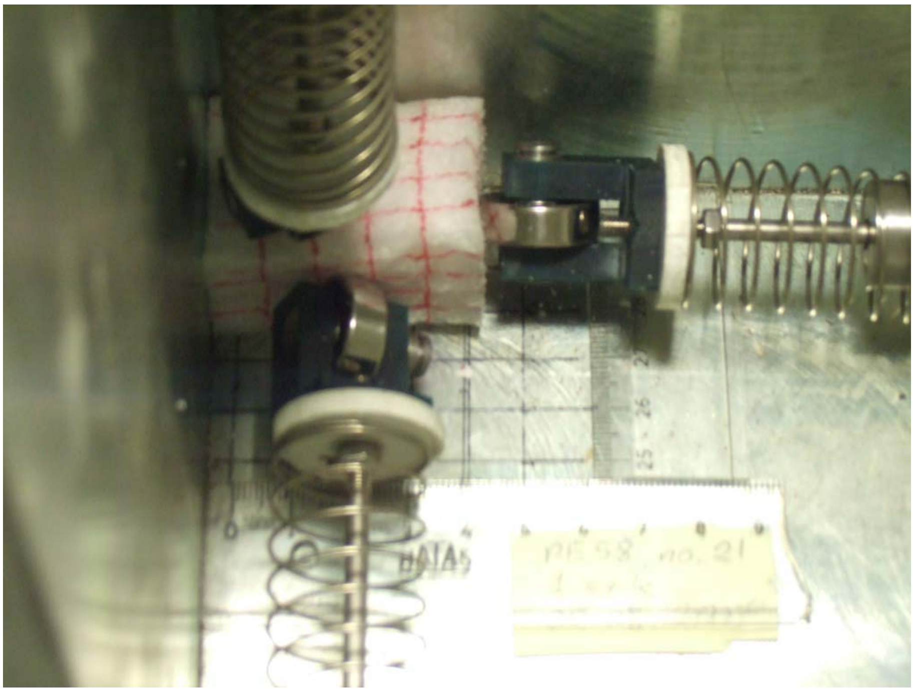

Figure 4.39. Deformation of PE 58 specimen under maximum pressure in test no 21

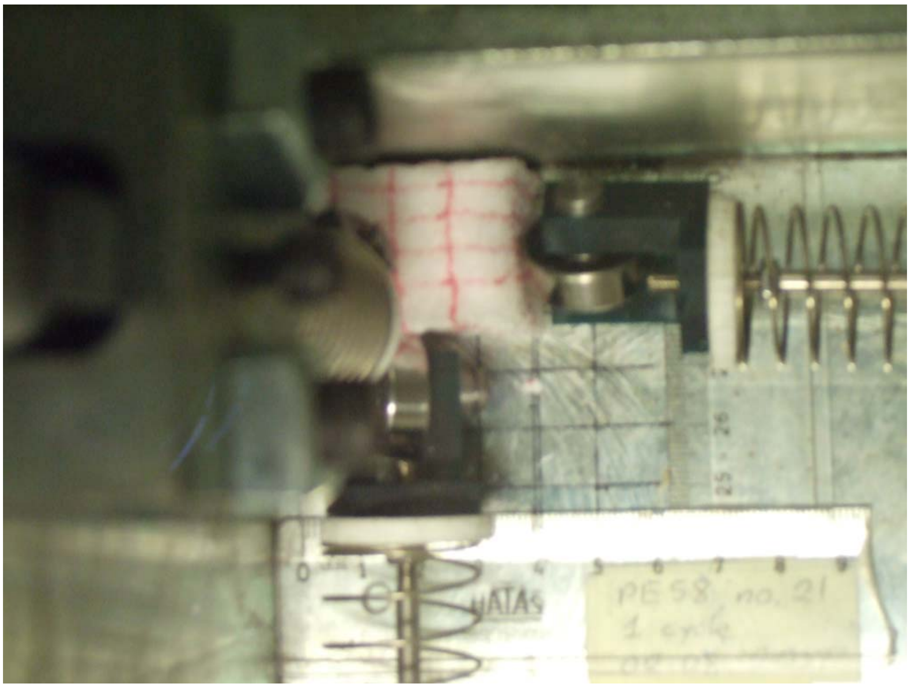

Figure 4.40. Deformation of PE 58 specimen under maximum pressure in test no 21

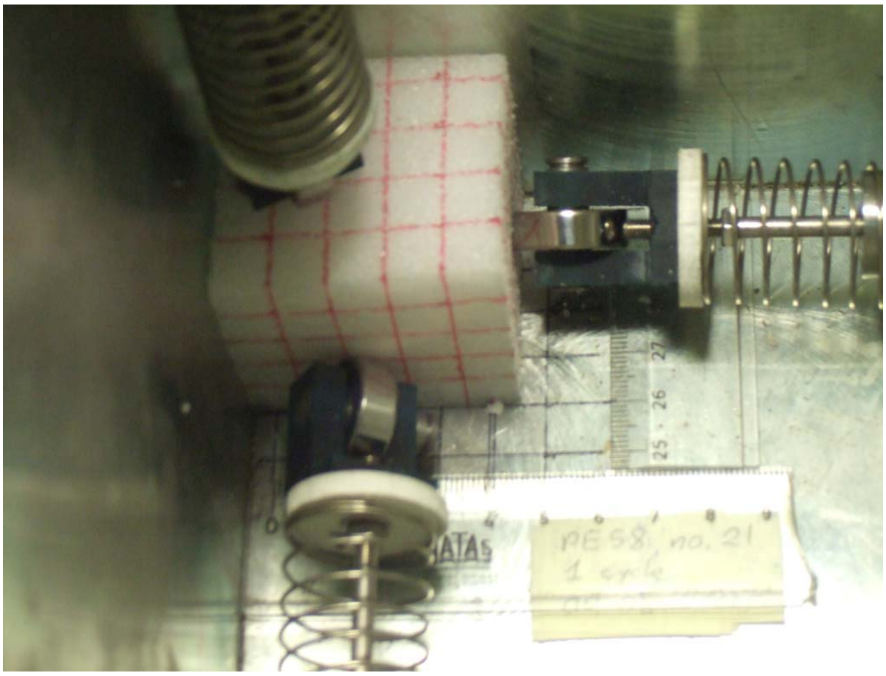

Figure 4.41. Deformation of PE 58 specimen after unloading in test no 21

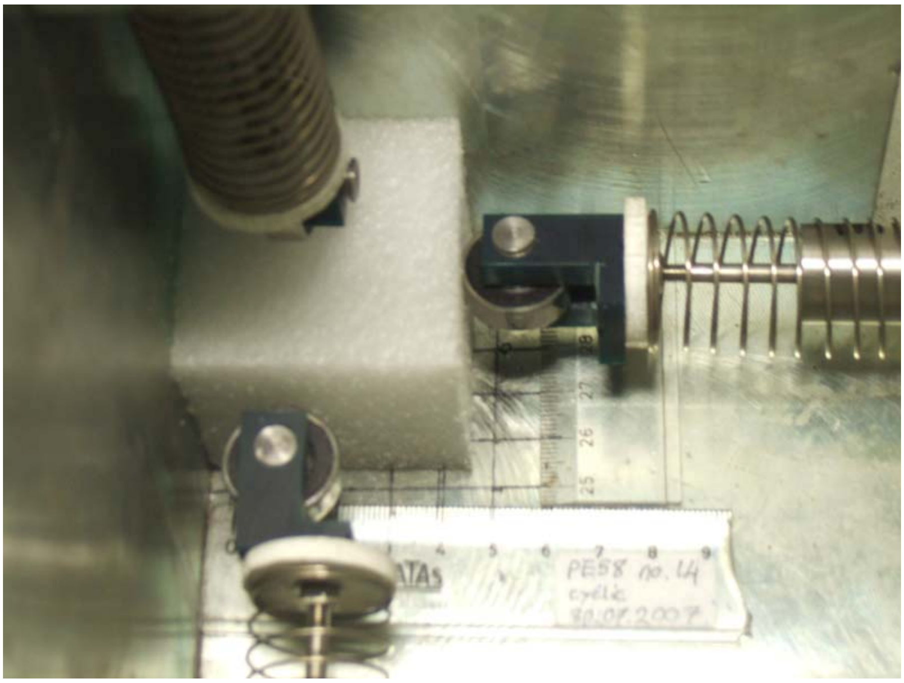

Figure 4.42. PE 58 specimen before test no 14

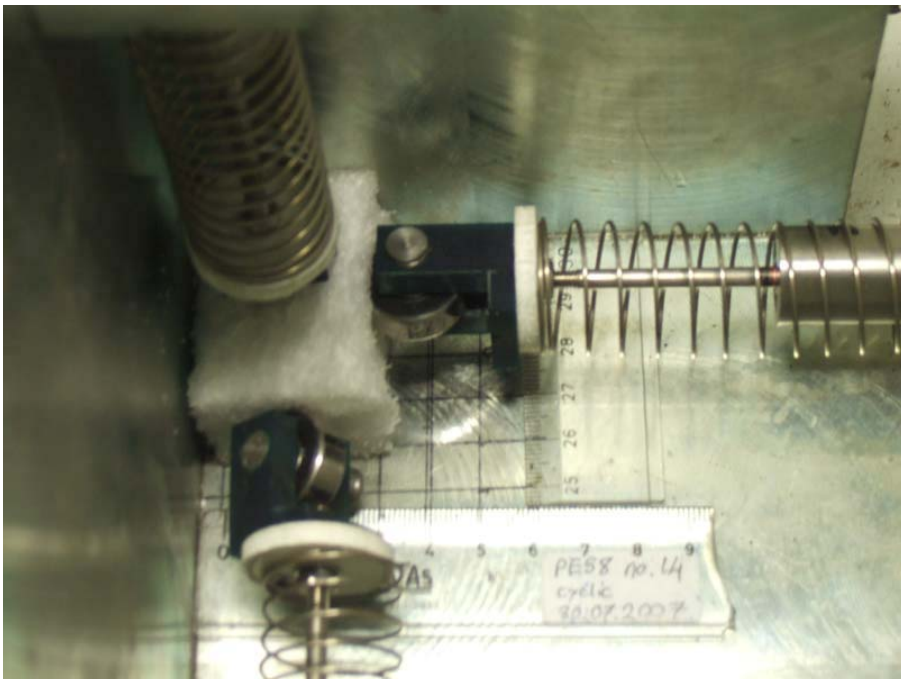

Figure 4.43. Deformation of PE 58 specimen under high pressure in test no 14

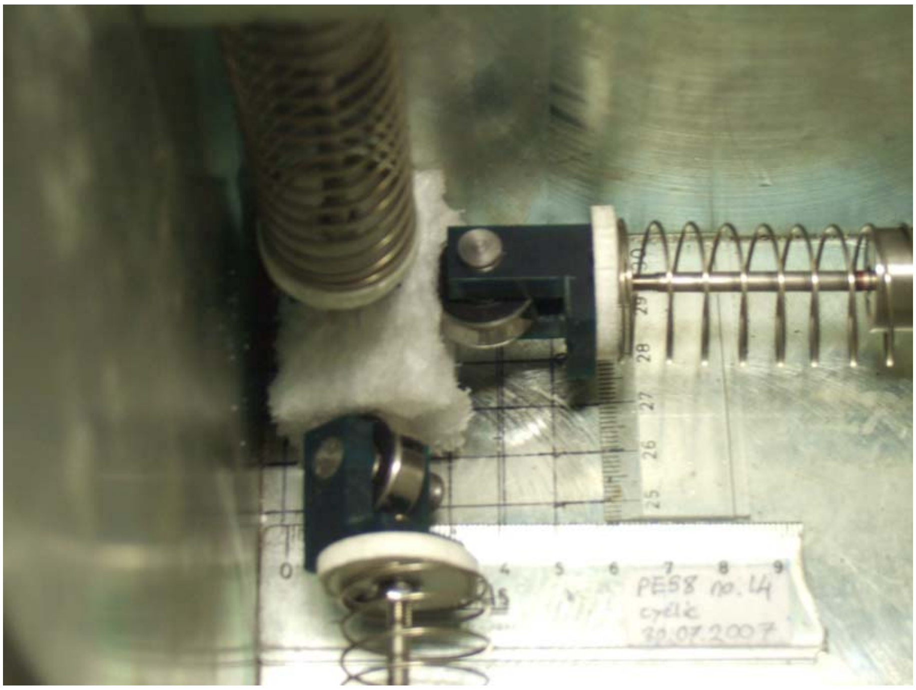

Figure 4.44. Deformation of PE 58 specimen under maximum pressure in test no 14

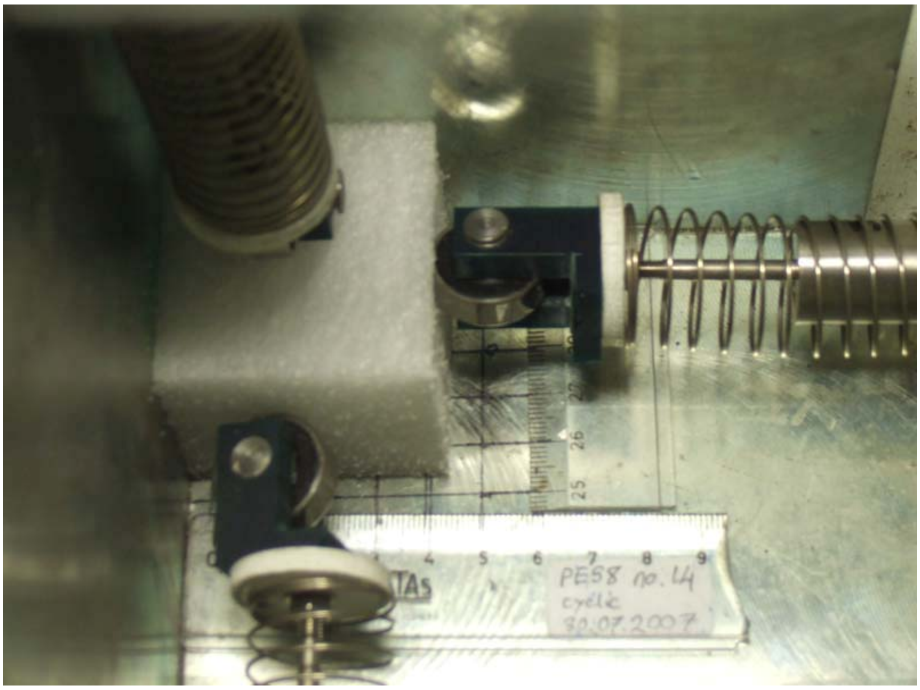

Figure 4.45. Deformation of PE 58 specimen after unloading in test no 14

Results of hydrostatic compression versus volumetric strain are given for EPS 30 test no 20 in Figures 4.46–4.49. In Figure 4.46, displacement and pressure sensors measurements are given in time scale. In Figure 4.47, the rate of deformation measured from LVDT 2 is given. Rate of deformation is around 7.3 mm/sec (438 mm/min) at the beginning of loading, and around 4 mm/sec (240 mm/min) at the end of loading. Rate of pressure increase is around 0.11 bar/sec, and remains constant during loading in test no 20. In Figure 4.48, hydrostatic pressure versus displacement results are plotted for the three displacement sensors. The EPS 30 specimen is rotated in test no 20, therefore average of LVDT 1 and 3 is used for volumetric strain calculation for test 20. Similar results are given for multiple loading and unloading of EPS 30 no 13 in Figures 4.50–4.52. Hydrostatic pressure versus volumetric strain results are plotted together for single and multiple loading tests in Figure 4.53. It is seen that single loading path follows the multiple loading path as it were never unloaded before as observed in uniaxial compression, tension, and simple shear tests.

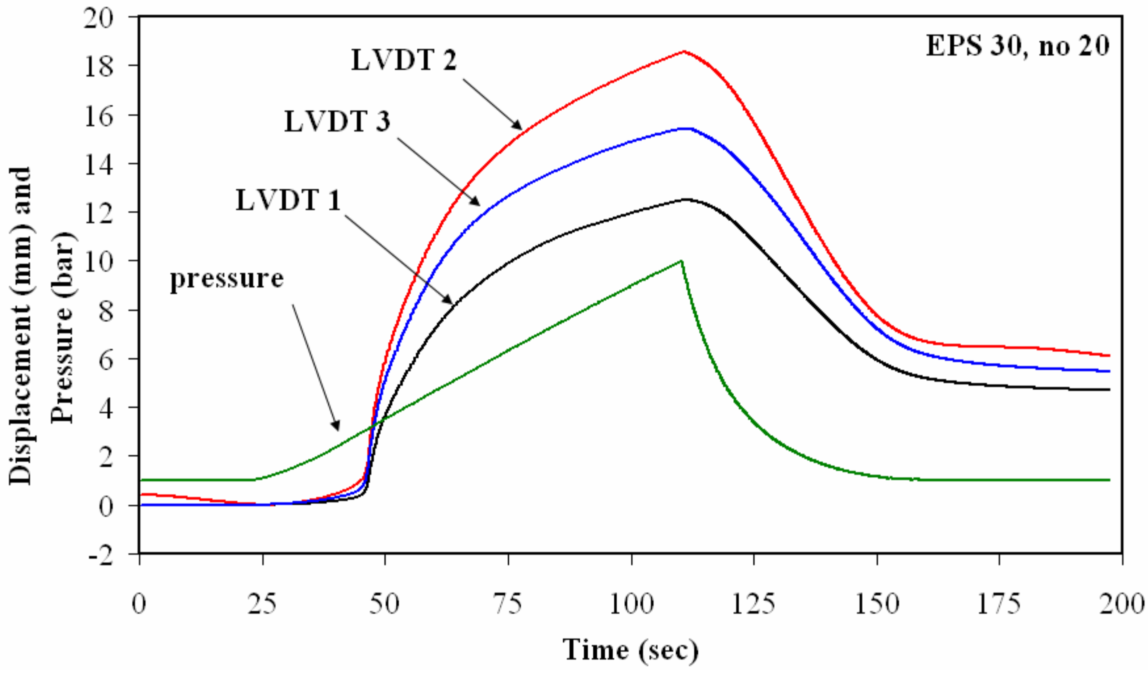

Figure 4.46. Displacement and pressure versus time in single hydrostatic loading of EPS 30 (compression direction is taken as positive)

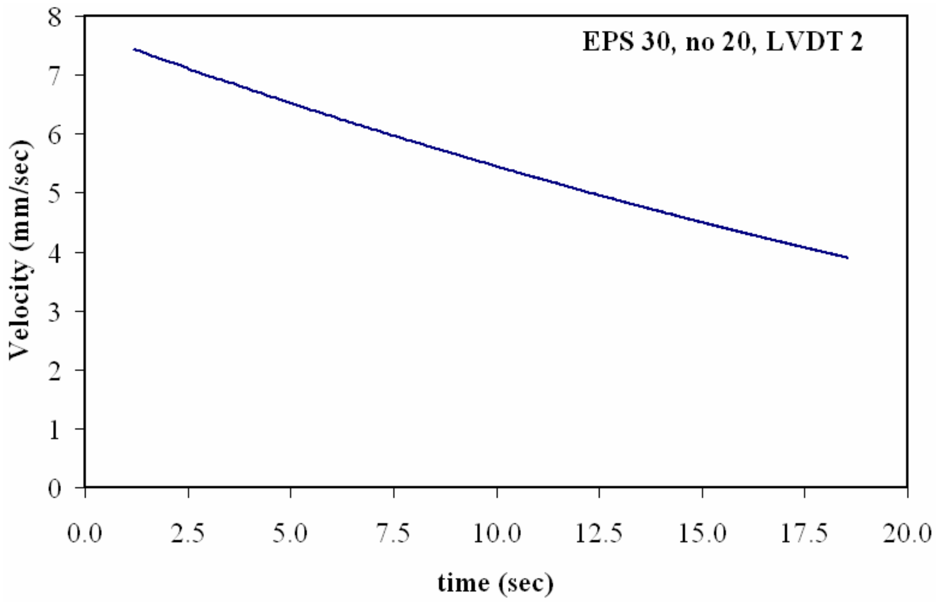

Figure 4.47. Time versus velocity along LVDT 2

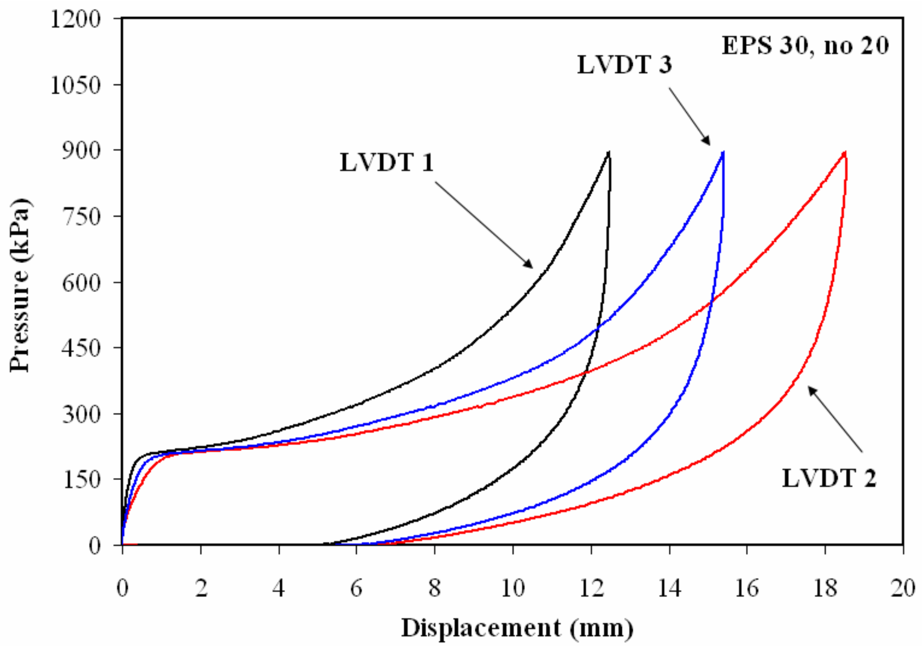

Figure 4.48. Pressure versus displacement in single hydrostatic loading of EPS 30 (compression direction is taken as positive)

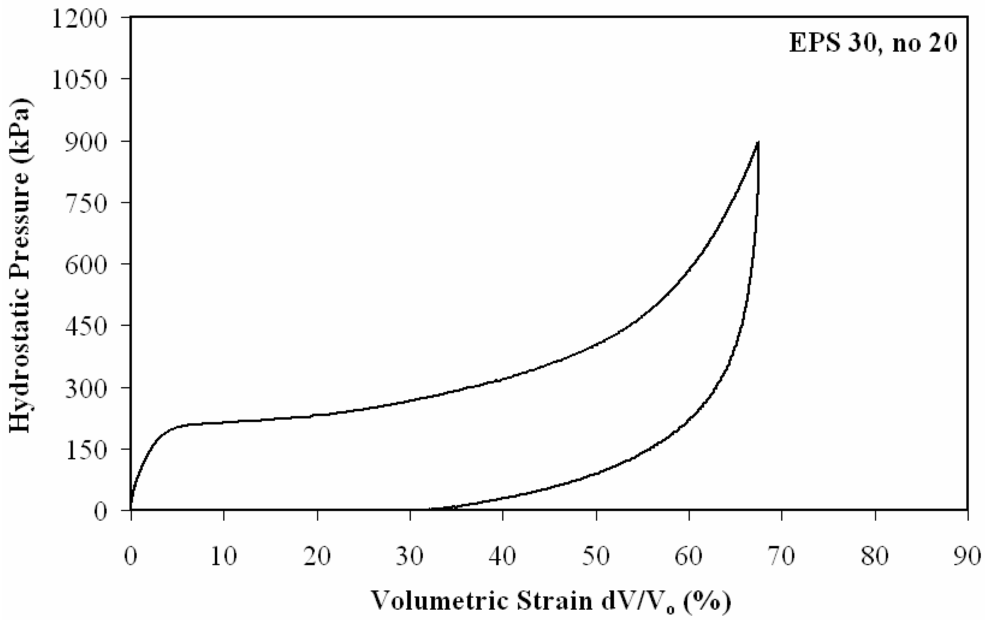

Figure 4.49. Pressure versus nominal volumetric strain in single hydrostatic loading of EPS 30 (compression direction is taken as positive)

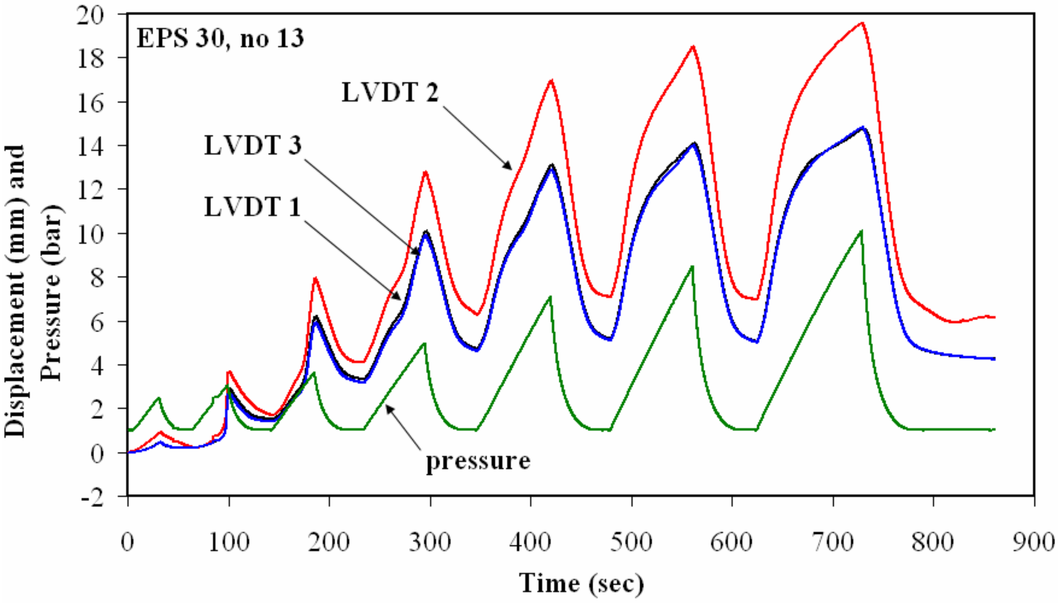

Figure 4.50. Displacement and pressure versus time in multiple hydrostatic loading of EPS 30 (compression direction is taken as positive)

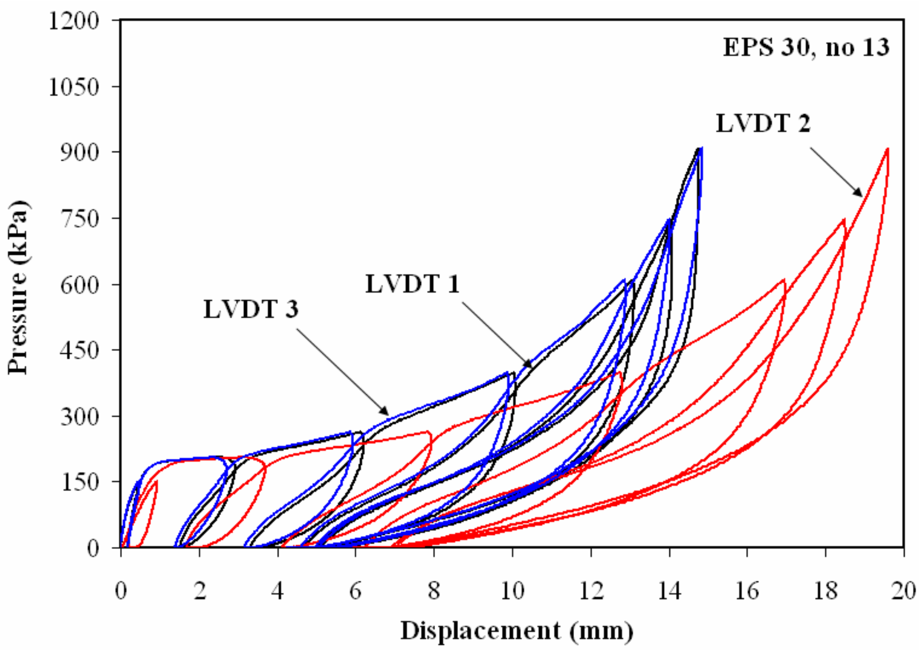

Figure 4.51. Pressure versus displacement in multiple hydrostatic loading of EPS 30 (compression direction is taken as positive)

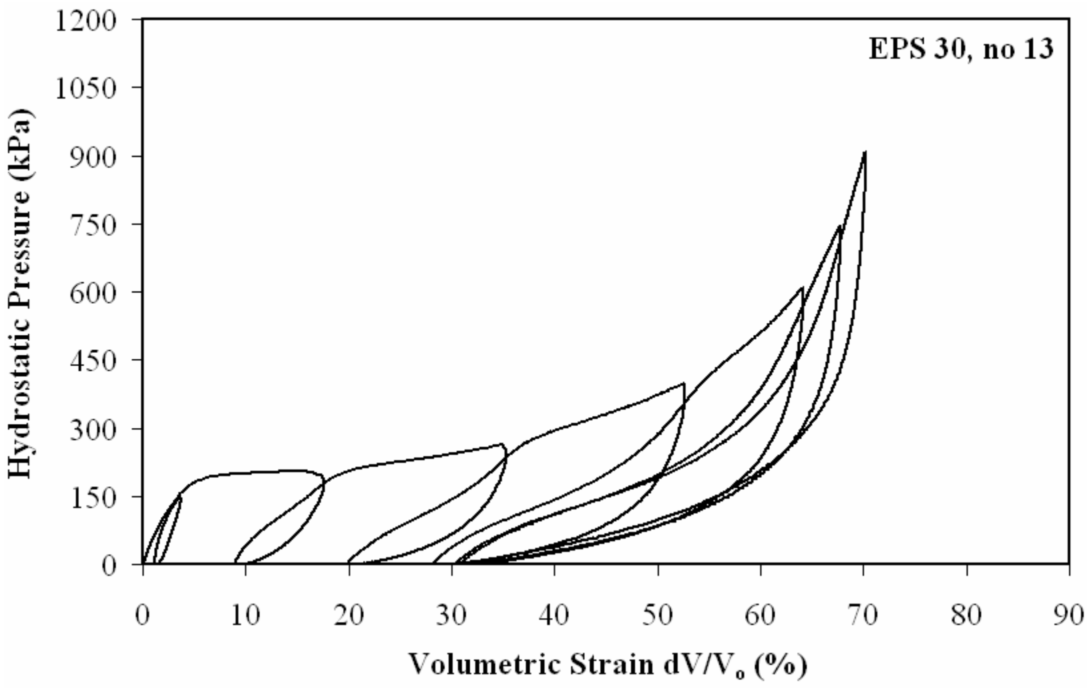

Figure 4.52. Hydrostatic pressure versus nominal volumetric strain in multiple hydrostatic loading of EPS 30 (compression direction is taken as positive)

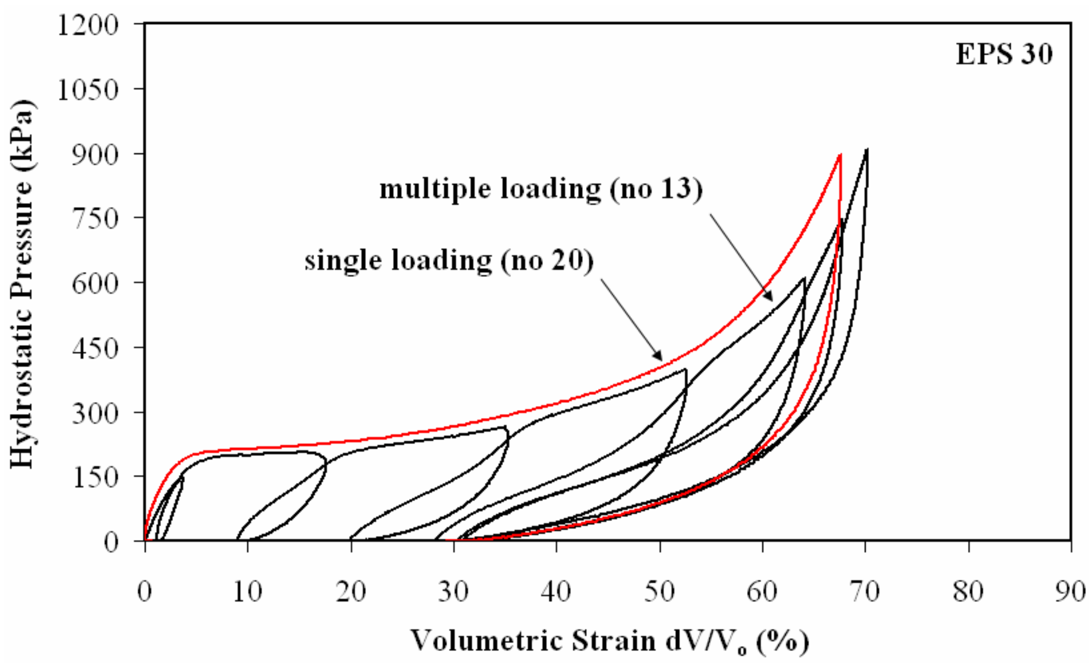

Figure 4.53. Hydrostatic pressure versus nominal volumetric strain in single and multiple hydrostatic loading of EPS 30 (compression direction is taken as positive)

Results of hydrostatic compression versus volumetric strain are given for PE 58 test no 21 in Figures 4.54–4.57. In Figure 4.54, displacement and pressure sensors measurements are given in time scale. In Figure 4.55, hydrostatic pressure versus displacement results are plotted for the three displacement sensors. In PE 58 test no 21, it is observed that there is a gap between the PE 58 specimen and the metal along the LVDT 1 direction at high pressure. In Figure 4.55, it is seen that the LVDT1 curve is not smooth as expected at pressure higher than 450 kPa. This uneven behavior should be due to the fact that after a pressure level, foam specimen stops sliding from the side of LVDT and continue its deformation from the opposite side, and a gap occurs between the metal plates and the foam. This phenomenon occurs when friction force between the bottom surface of foam and the metal plates becomes higher than the force exerted by the metal pins of LVDT's placed on lateral sides. Therefore hydrostatic pressure versus volumetric strain data given in Figure 4.57 for PE 58 no 21 are not reliable for pressure level higher than 450 kPa and volumetric strain level higher 65 per cent. Hydrostatic pressure data is used to define the shape of the yield surface in failure criteria. Hydrostatic pressure and volumetric strain level up to reliable limits can still be used to define the initial shape and evolvement of the yield surface during hardening. Similar results are given for multiple loading and unloading of PE 58 no 14 in Figures 4.58–4.62. In PE 58 test no 14, it is observed that there is a gap between the PE 58 specimen and the metal plate along the LVDT 3 and LVDT 2 direction at high pressure. In Figure 4.59, it is seen that the LVDT 3 and LVDT 2 curves are not smooth as expected at pressure level higher than 300 kPa. Therefore hydrostatic pressure versus volumetric strain data given in Figure 4.61 for PE 58 no 14 is not reliable for pressure level higher than 300 kPa and volumetric strain level higher 60 per cent. Hydrostatic pressure versus volumetric strain results are plotted together in Figures 4.63 and 4.64 for PE 58. It is seen that single loading path follows the multiple loading path as it were never unloaded before for hydrostatic loading.

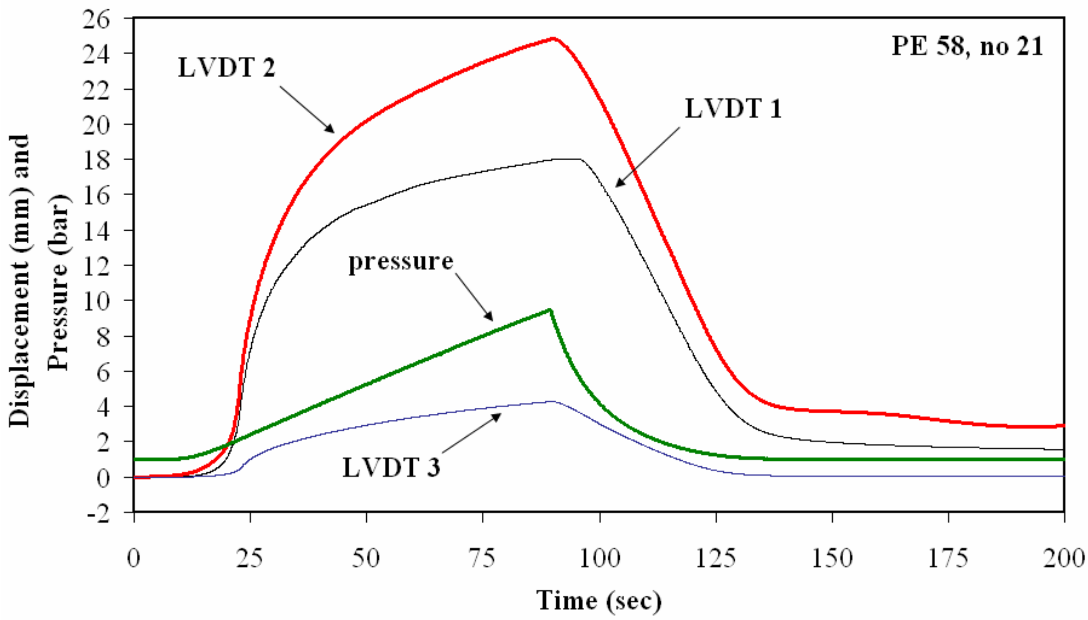

Figure 4.54. Displacement and pressure versus time in single hydrostatic loading of PE 58 (compression direction is taken as positive)

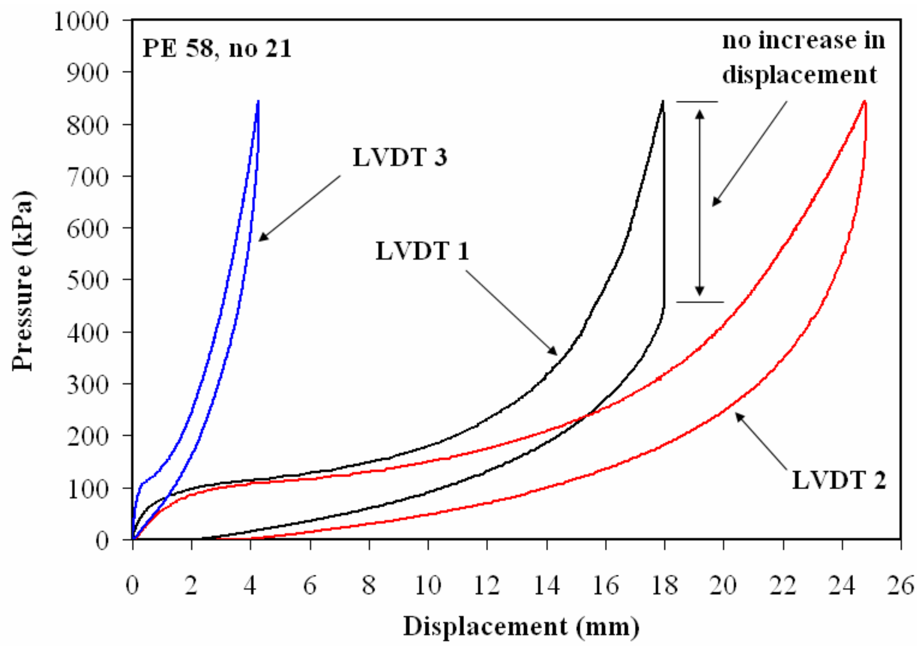

Figure 4.55. Pressure versus displacement in single hydrostatic loading of PE 58 (compression direction is taken as positive)

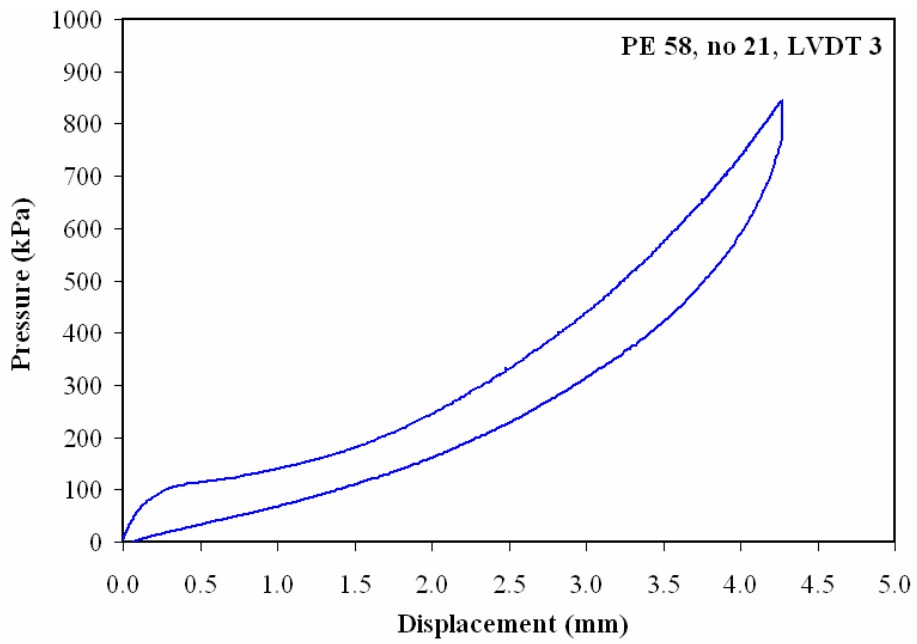

Figure 4.56. Pressure versus displacement measured by LVDT 3 in single hydrostatic loading of PE 58 (compression direction is taken as positive)

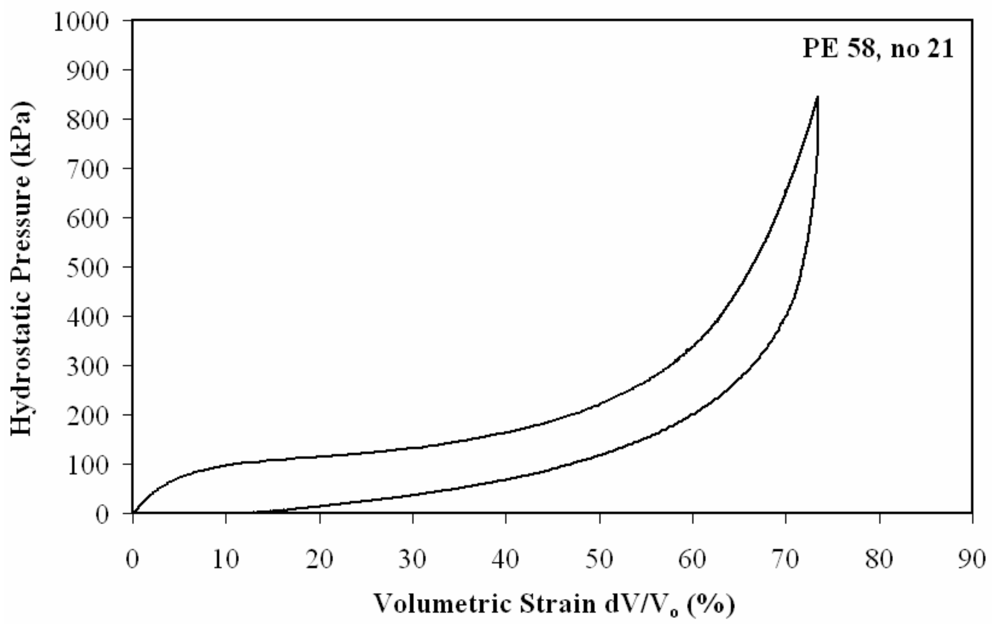

Figure 4.57. Hydrostatic pressure versus nominal volumetric strain for single loading of PE 58 (compression direction is taken as positive)

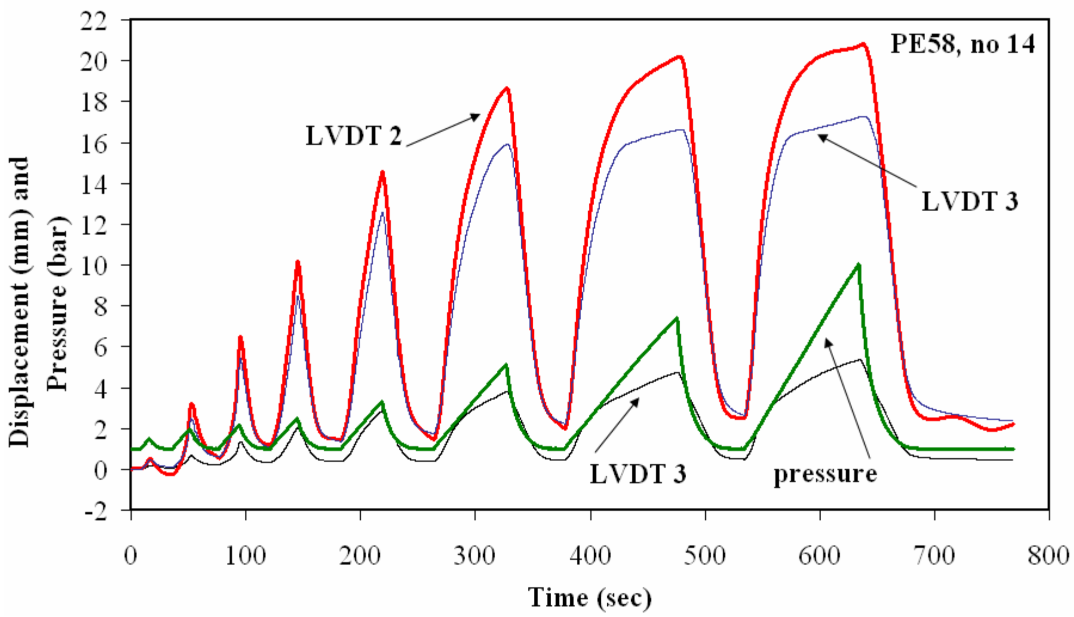

Figure 4.58. Displacement and pressure versus time in multiple hydrostatic loading of PE 58 (compression direction is taken as positive)

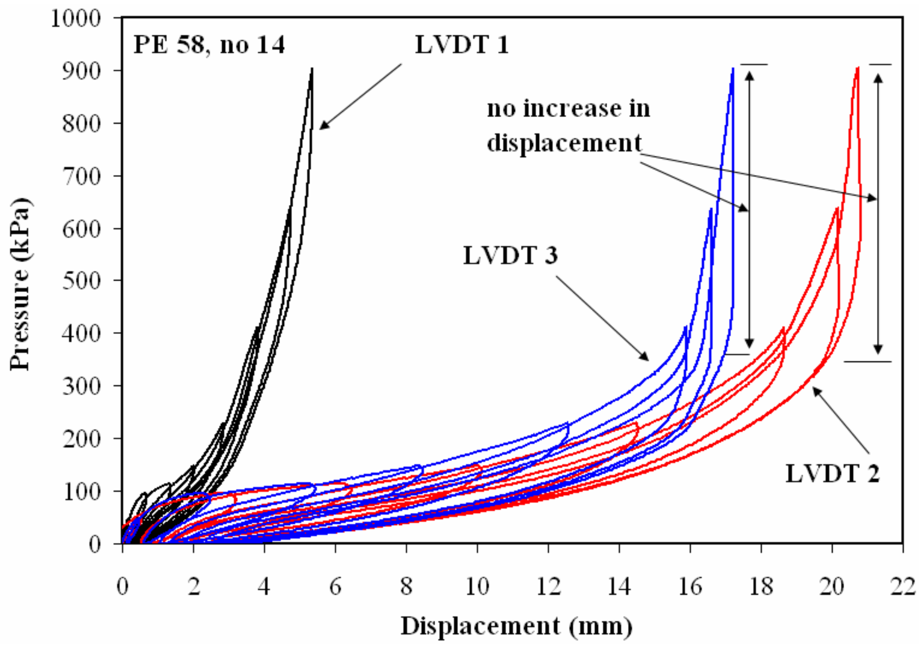

Figure 4.59. Hydrostatic pressure versus nominal volumetric strain in multiple hydrostatic loading of PE 58 (compression direction is taken as positive)

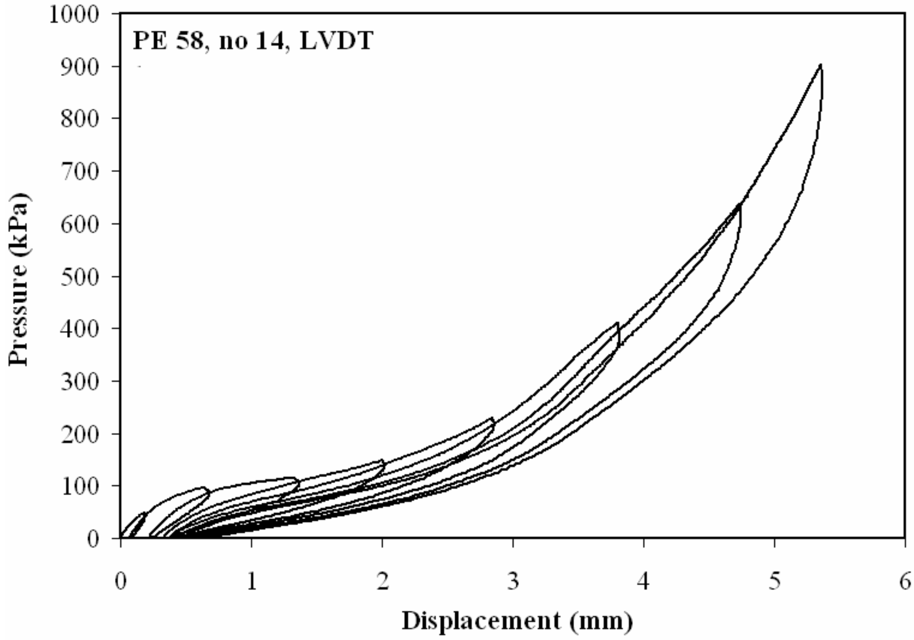

Figure 4.60. Pressure versus displacement measured by LVDT 1 in multiple hydrostatic loading of PE 58 (compression direction is taken as positive)

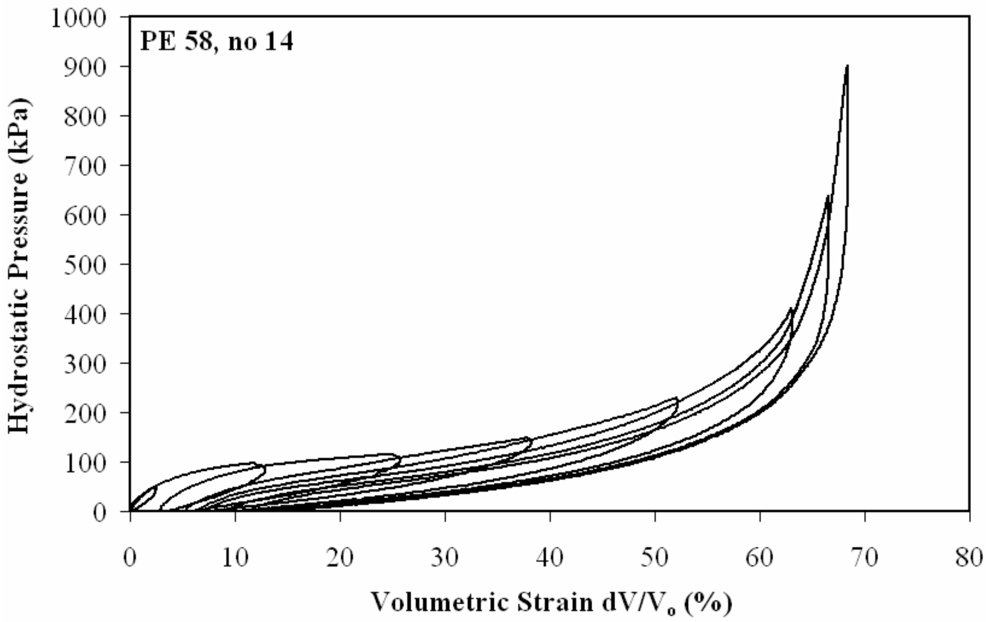

Figure 4.61. Hydrostatic pressure versus nominal volumetric strain in multiple hydrostatic loading of PE 58 (compression direction is taken as positive)

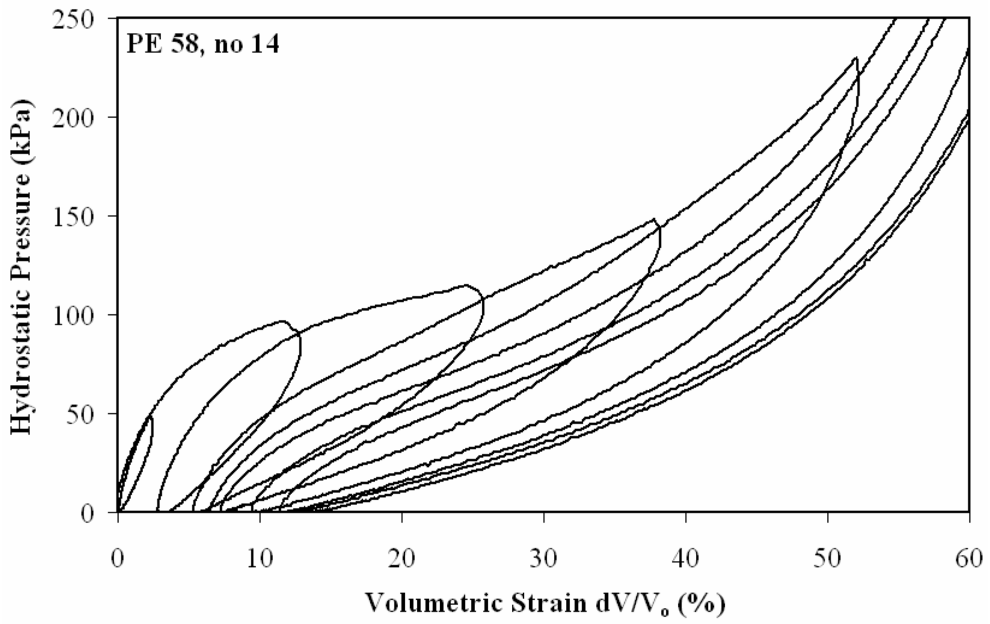

Figure 4.62. Hydrostatic pressure (up to 250 kPa) versus nominal volumetric strain (up to 60 per cent) in multiple hydrostatic loading of EPS 30 (compression direction is taken as positive)

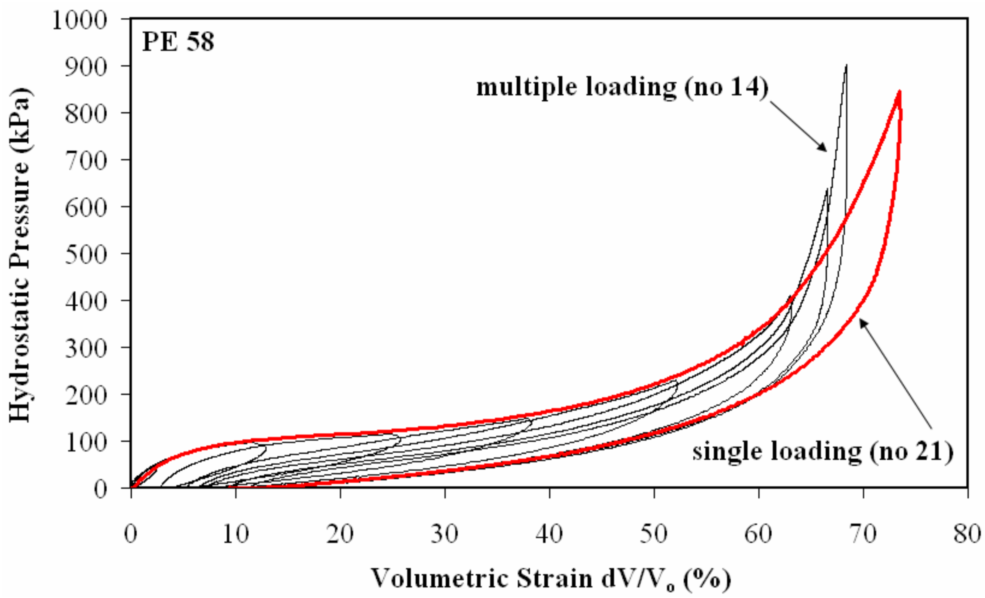

Figure 4.63. Hydrostatic pressure versus nominal volumetric strain in single and multiple hydrostatic loading of PE 58 (compression direction is taken as positive)

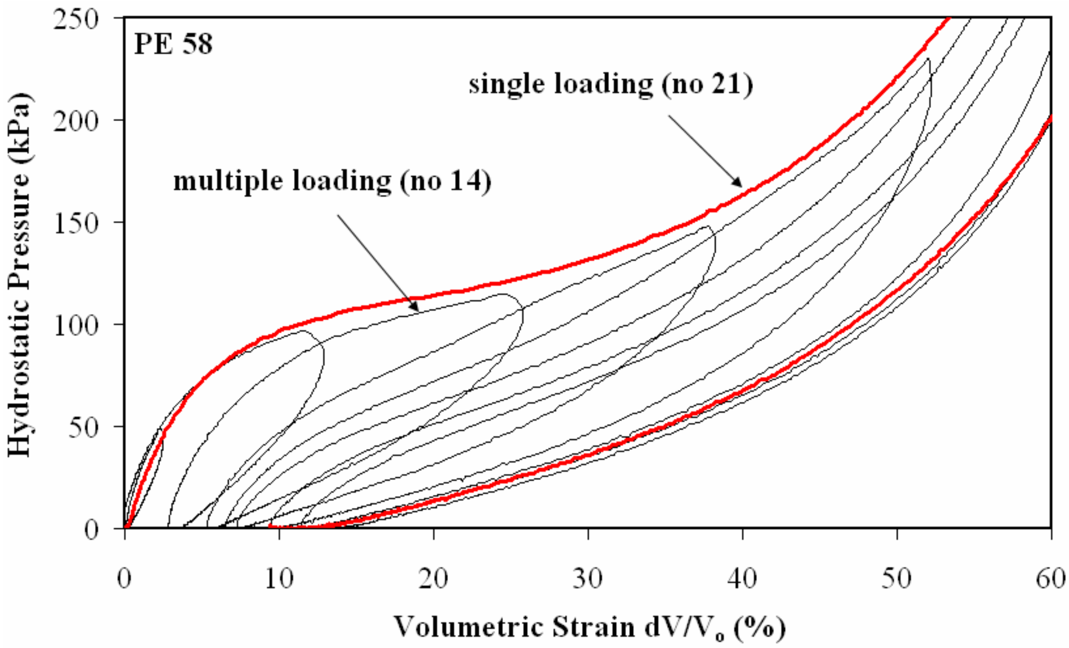

Figure 4.64. Hydrostatic pressure (up to 250 kPa) versus nominal volumetric strain (up to 60 per cent) in single and multiple hydrostatic loading of PE 58 (compression direction is taken as positive)

4.4. Mechanical Behavior Under Cylinder Indentation

A metal cylinder of 100 mm diameter is attached to the Zwick Z020 universal tensile testing machine for cylinder indentation tests. Specimens of $50 \times 50 \times 150$ mm^3 and $45 \times 50 \times 150$ mm^3 are used for cylinder indentation tests of EPS 30 and PE 58 respectively (Figures 4.65 and 4.66). In Figures 4.67–4.71, it can be seen how EPS 30 specimens deforms during and after the test. In Figure 4.72, force versus displacement for single and multiple loading and unloading of cylinder indentation tests are given for EPS 30. It is seen that fracture occurs at 23 mm indentation. Multiple loading path follows the single loading path as it were never unloaded before for cylinder indentation tests as seen in uniaxial compression, uniaxial tension, simple shear, and hydrostatic compression tests. In Figures 4.73–4.76, it can be seen how PE 58 specimens deforms during the test. In Figure 4.77, force versus displacement for single and multiple loading and unloading of cylinder indentation tests are given for PE 58. There is no fracture occurred in PE 58 specimens during cylinder indentation tests. Multiple loading path follows the single loading path as it were never unloaded before for PE 58 similar to EPS 30.

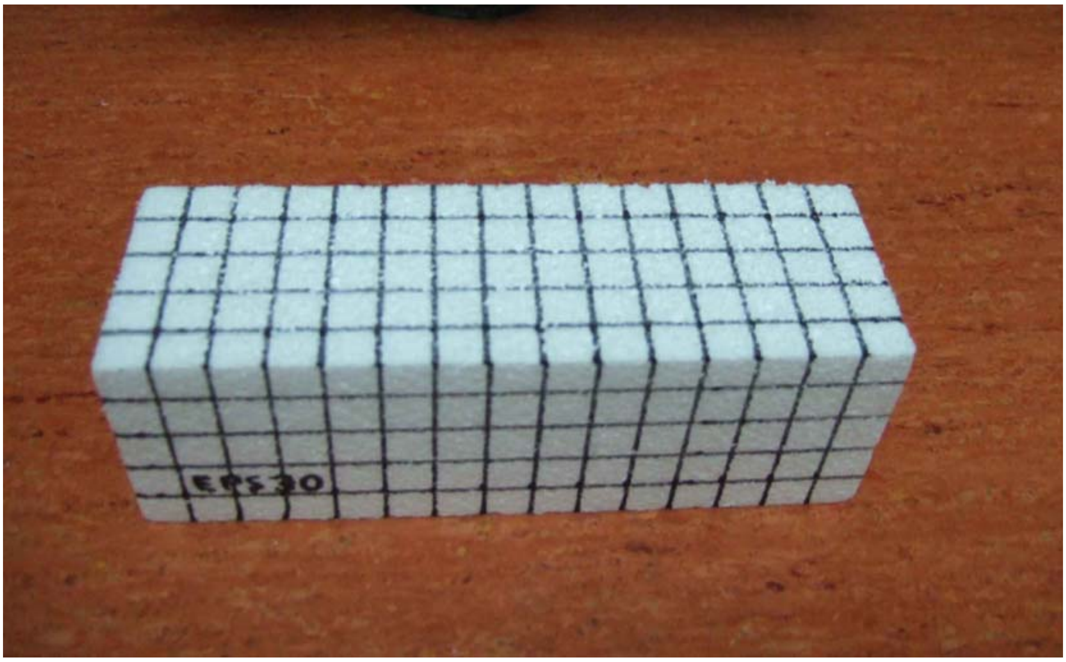

Figure 4.65. EPS 30 specimen used in cylinder indentation test

Figure 4.66. EPS 30 specimen before cylinder indentation test

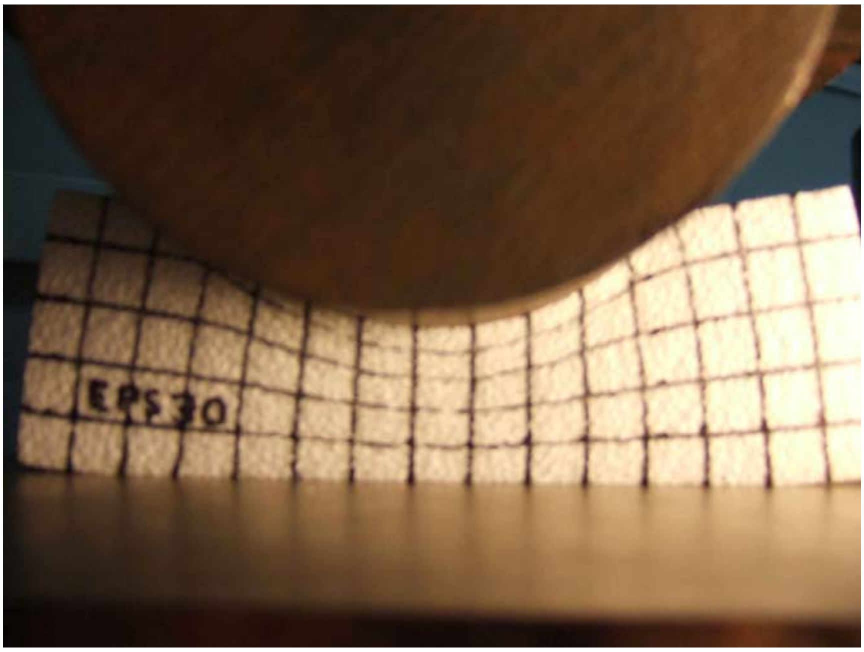

Figure 4.67. EPS 30 specimen in cylinder indentation test loaded up to 23.5 mm

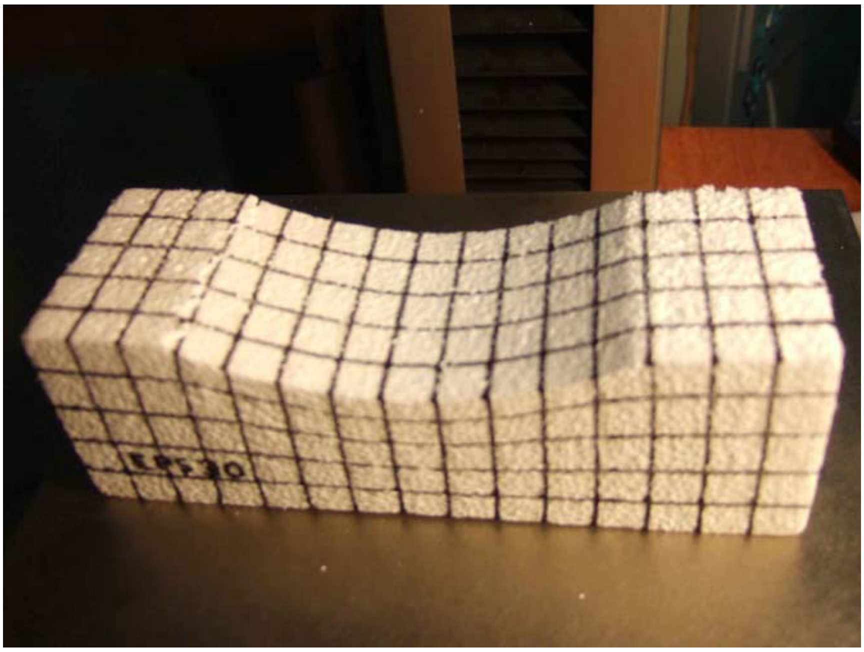

Figure 4.68. Top surface of EPS 30 specimen in cylinder indentation test after being loaded up to 23.5 mm

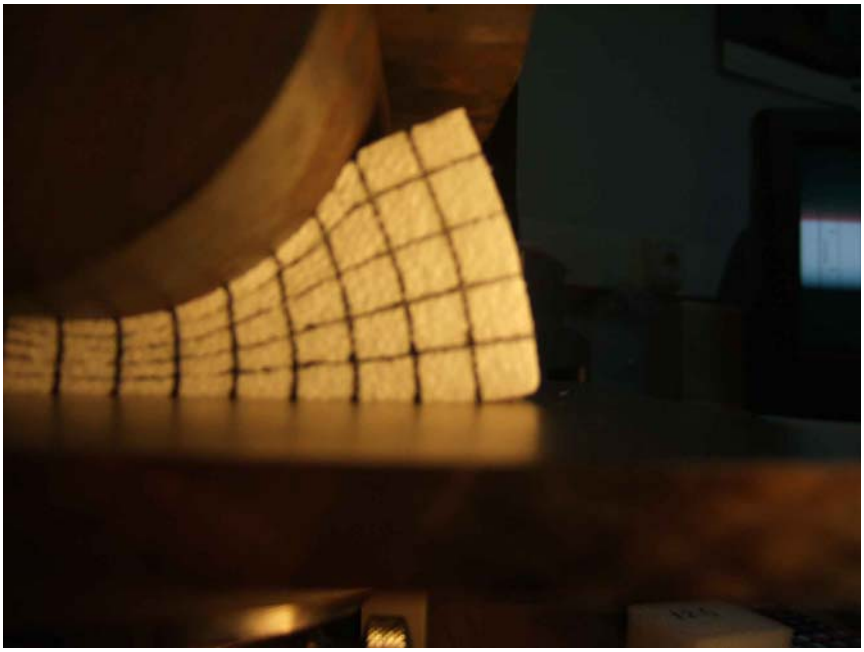

Figure 4.69. EPS 30 specimen in cylinder indentation test loaded third time up to 40.0 mm

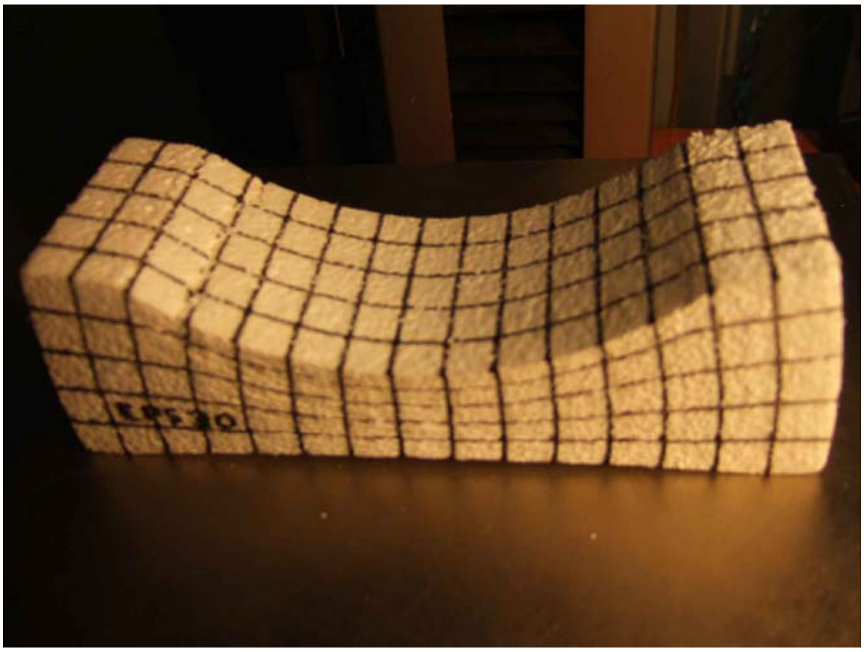

Figure 4.70. Top surface of EPS 30 specimen in cylinder indentation test after being loaded third time up to 40.0 mm

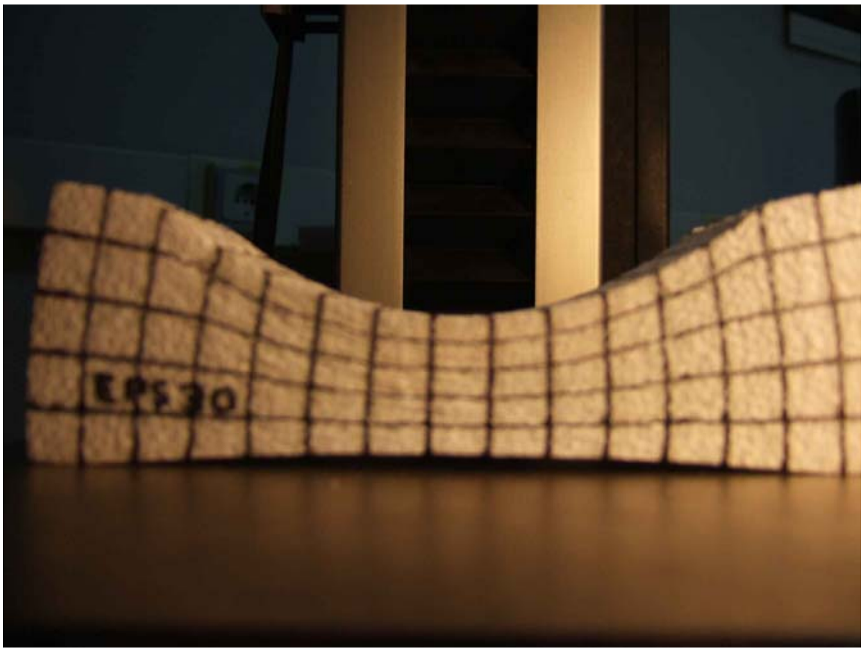

Figure 4.71. Side surface of EPS 30 specimen in cylinder indentation test after being loaded third time up to 40.0 mm

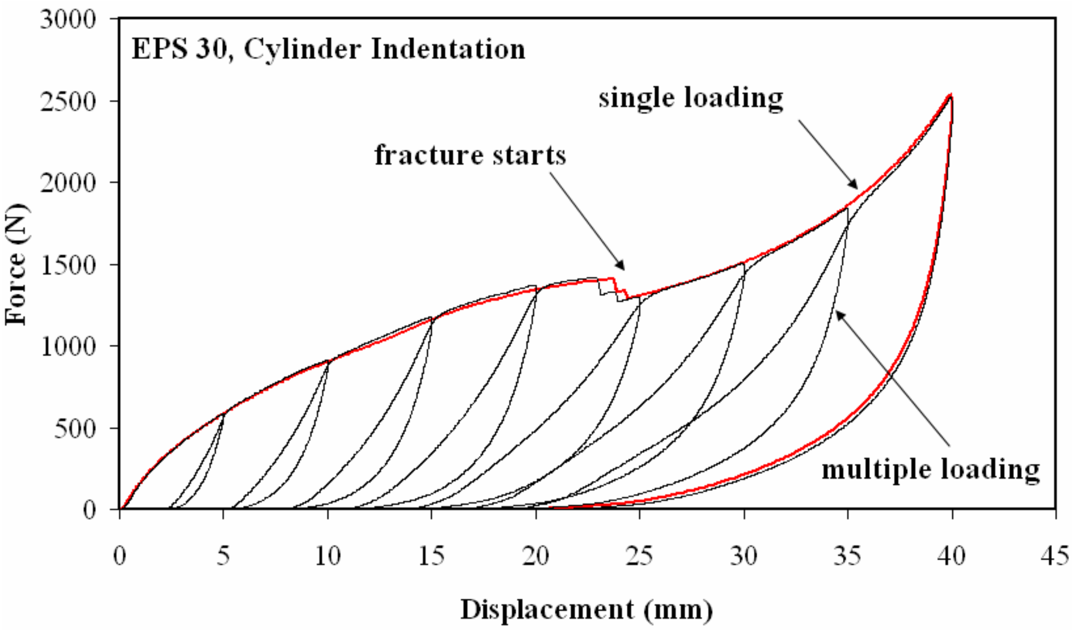

Figure 4.72. Force versus displacement for single and multiple cylinder indentation loading of EPS 30 (compression direction is taken as positive)

Figure 4.73. PE 58 specimen before cylinder indentation test

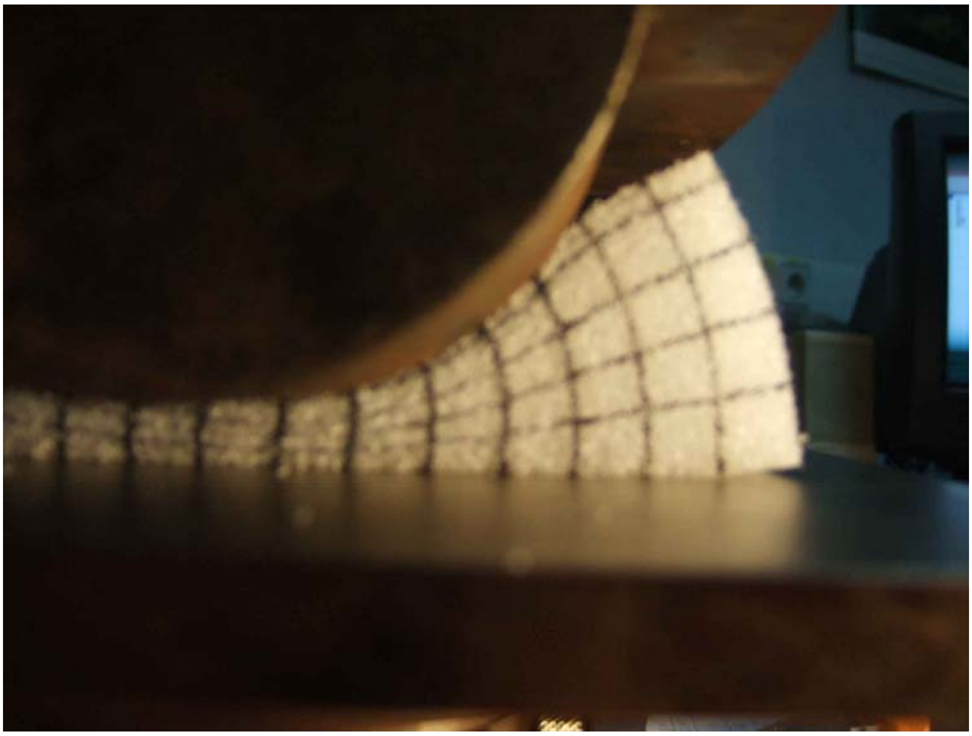

Figure 4.74. PE 58 specimen in cylinder indentation test loaded fourth time up to 36.0 mm

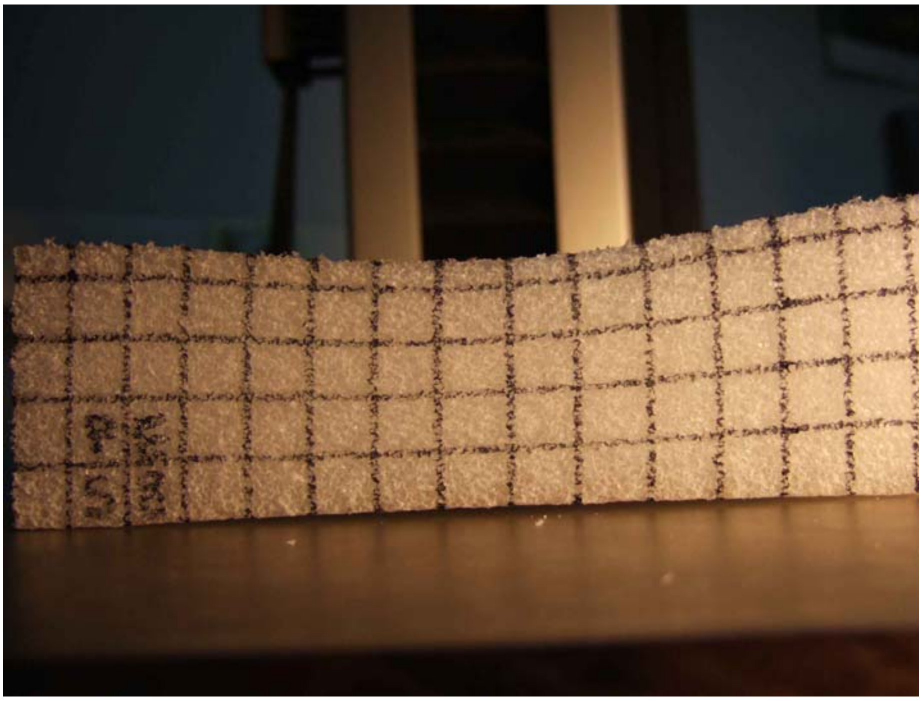

Figure 4.75. PE 58 specimen in cylinder indentation test after being loaded fourth time up to 36.0 mm

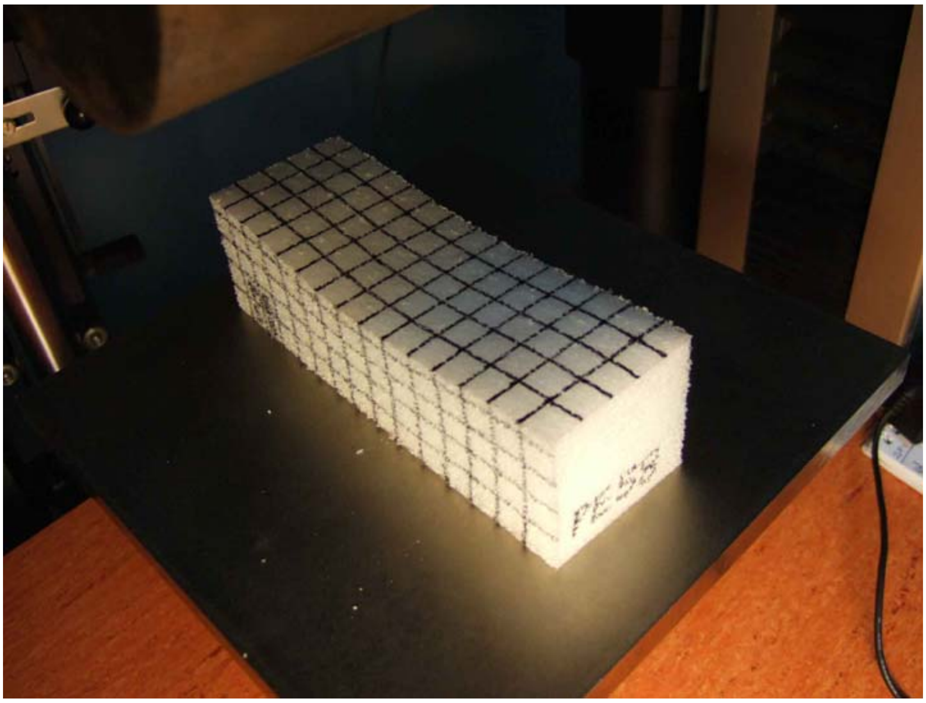

Figure 4.76. PE 58 specimen in cylinder indentation test after being loaded fourth time up to 36.0 mm

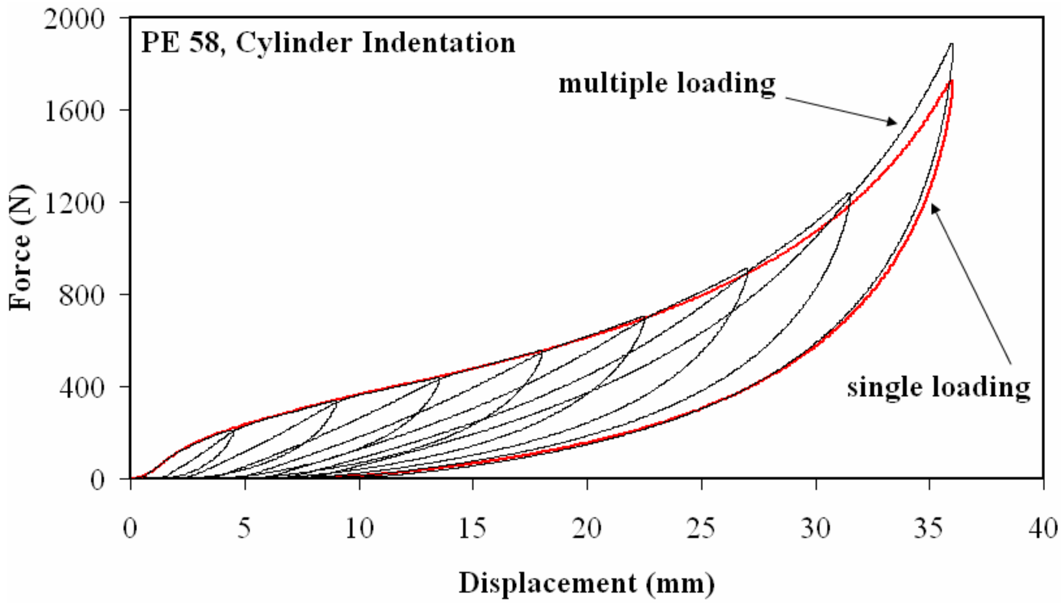

Figure 4.77. Force versus displacement for single and multiple cylinder indentation loading of PE 58 (compression direction is taken as positive)

4.5. Mechanical Behavior Under Block Indentation

A metal block of 50 mm width with 10 mm radius at the edges is attached to the Zwick Z020 universal tensile testing machine for block indentation tests (Figure 4.78). Specimens of 50 × 50 × 150 mm^3 and 45 × 50 × 150 mm^3 are used for block indentation tests of EPS 30 and PE 58 respectively. In Figures 4.79–4.87, it can be seen how EPS 30 specimens deforms during and after the test. In Figure 4.88, force versus displacement for single and multiple loading and unloading of cylinder indentation tests are given for EPS 30. Fracture in block indentation test occurs in the very beginning, therefore the force versus displacement curve is smooth, the decrease of the force due to fracture is not remarkable. Multiple loading path follows the single loading path as it were never unloaded before similar to cylinder indentation tests. In Figures 4.89–4.93, it can be seen how PE 58 specimens deforms during and after the block indentation test. In Figure 4.94, force versus displacement for single and multiple loading and unloading of cylinder indentation tests are given for PE 58. There is no fracture occurred in PE 58 specimens during the block indentation tests. Multiple loading path follows the single loading path as it were never unloaded before for PE 58 similar to EPS 30.

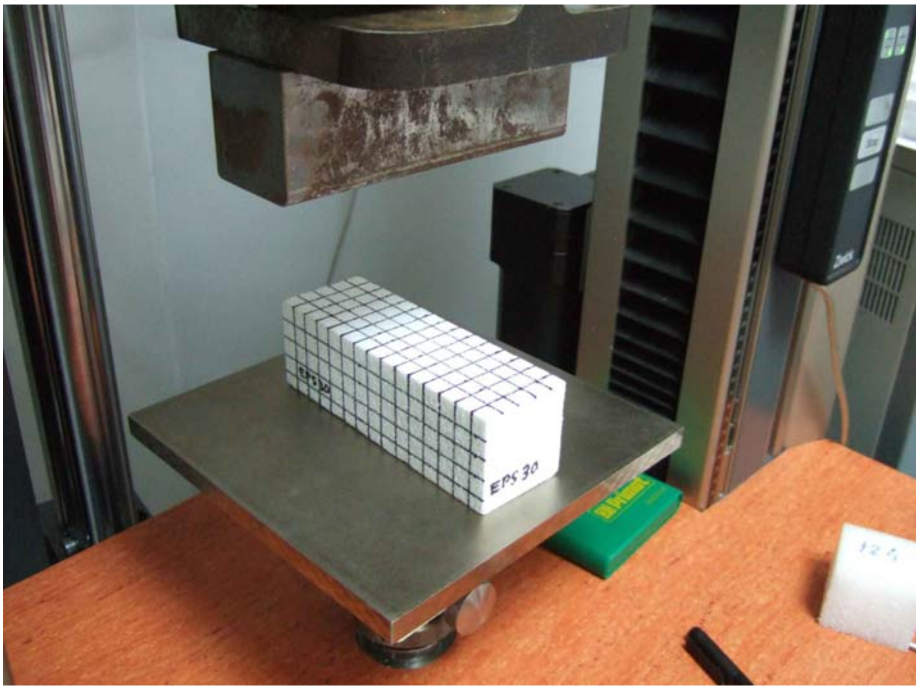

Figure 4.78. EPS 30 specimen in block indentation test setup

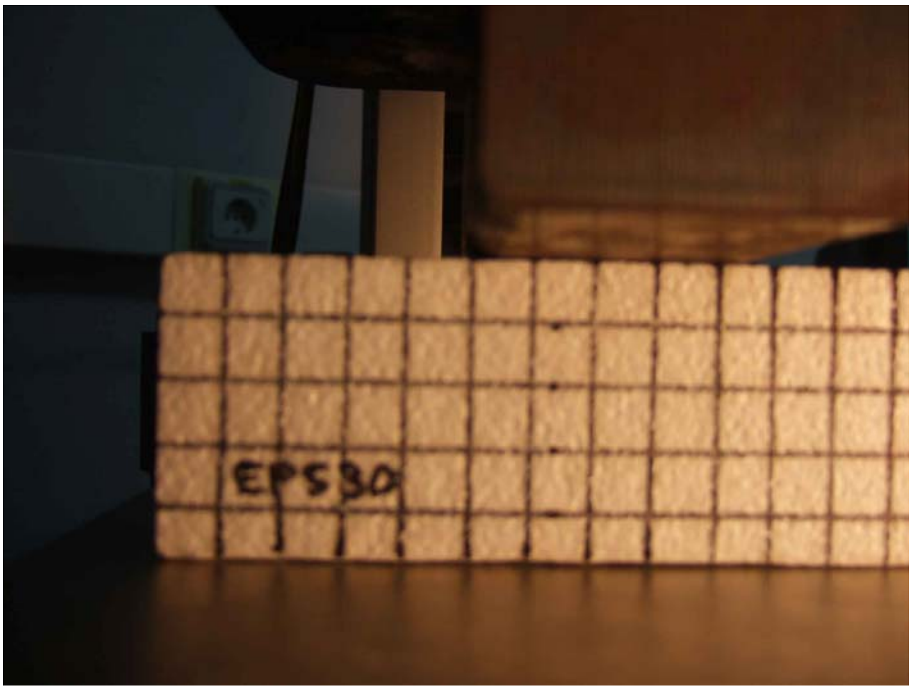

Figure 4.79. EPS 30 specimen at the beginning of block indentation test

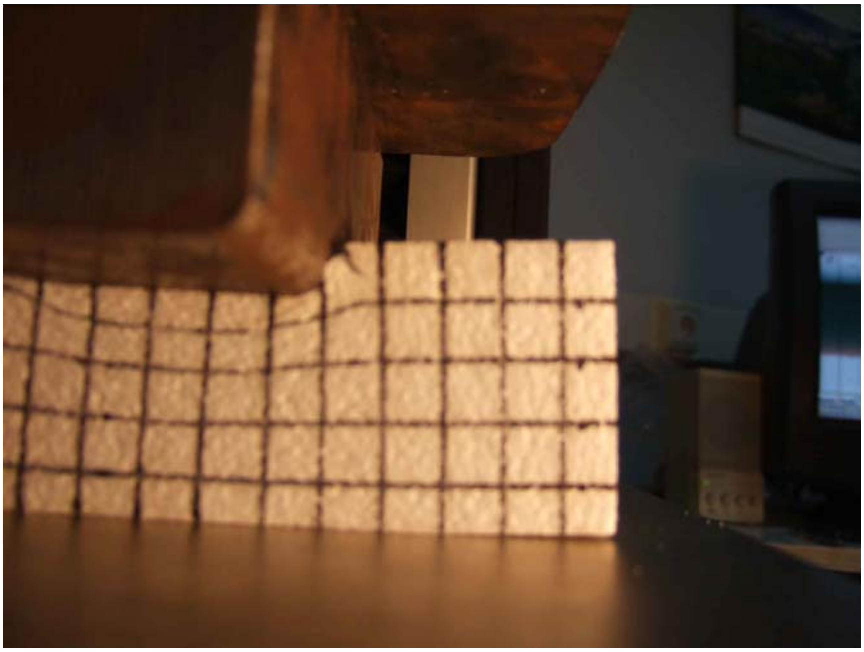

Figure 4.80. EPS 30 specimen in block indentation test loaded up to 11.7 mm

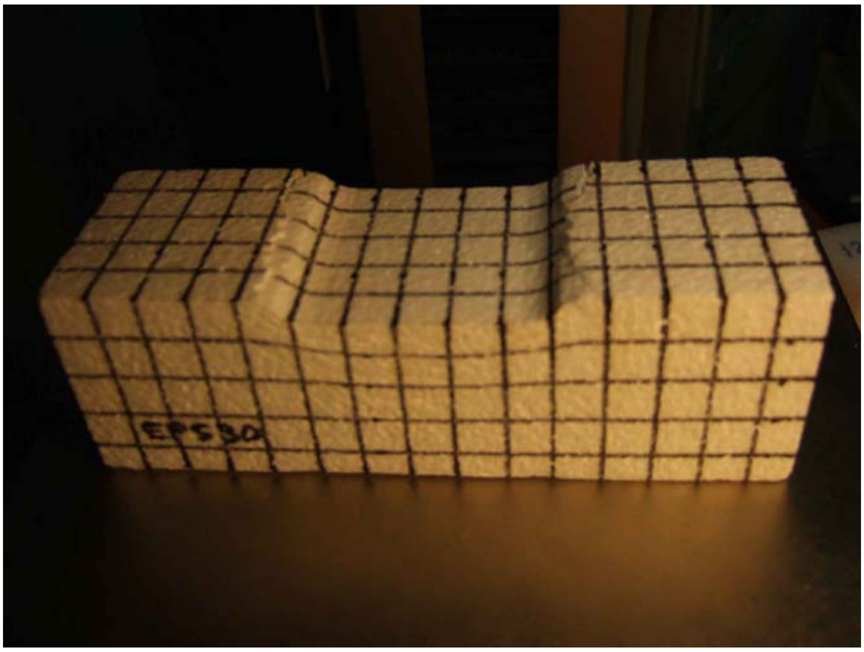

Figure 4.81. EPS 30 specimen in block indentation test after being loaded up to 11.7 mm

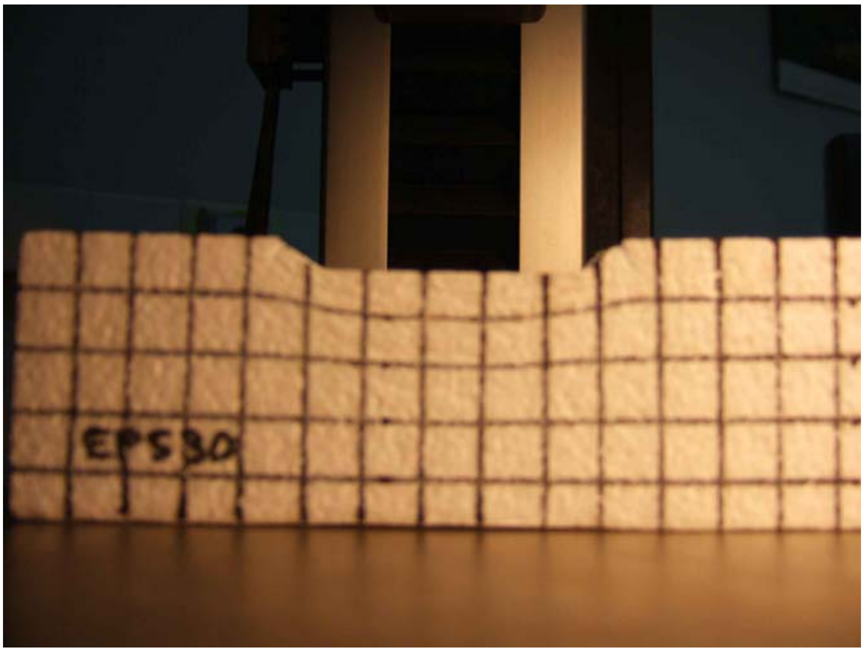

Figure 4.82. EPS 30 specimen in block indentation test after being loaded up to 11.7 mm

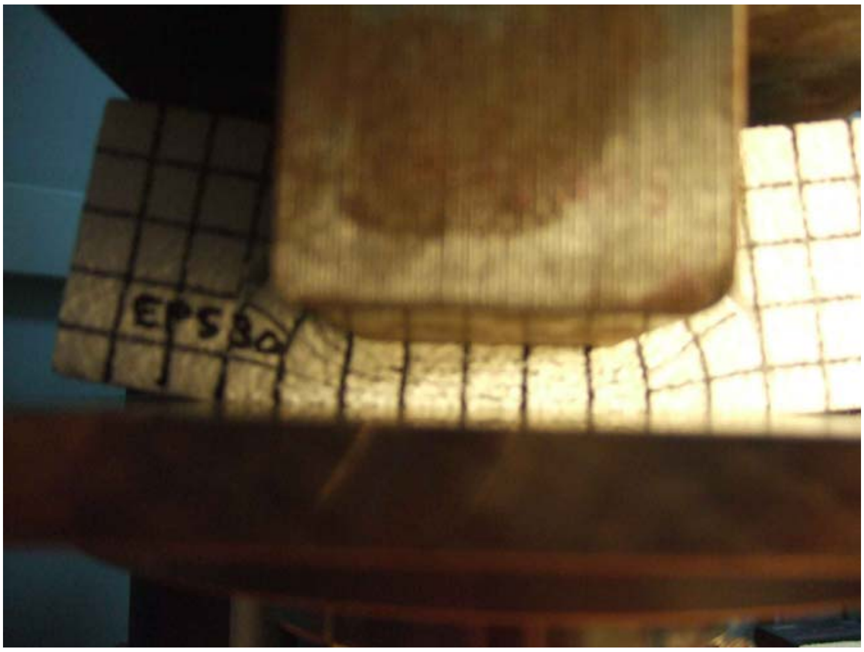

Figure 4.83. EPS 30 specimen in block indentation test loaded fourth time up to 40.0 mm

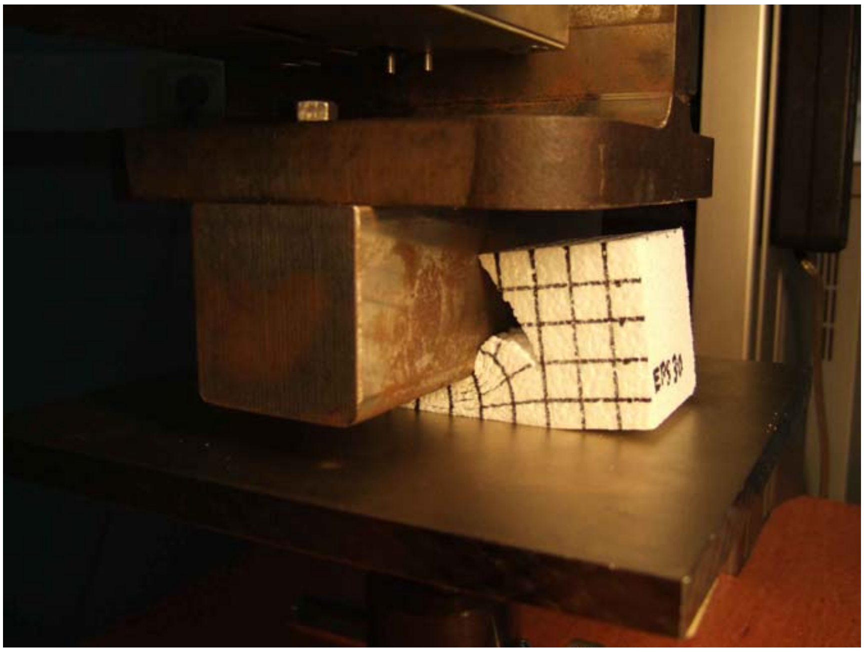

Figure 4.84. EPS 30 specimen in block indentation test loaded fourth time up to 40.0 mm

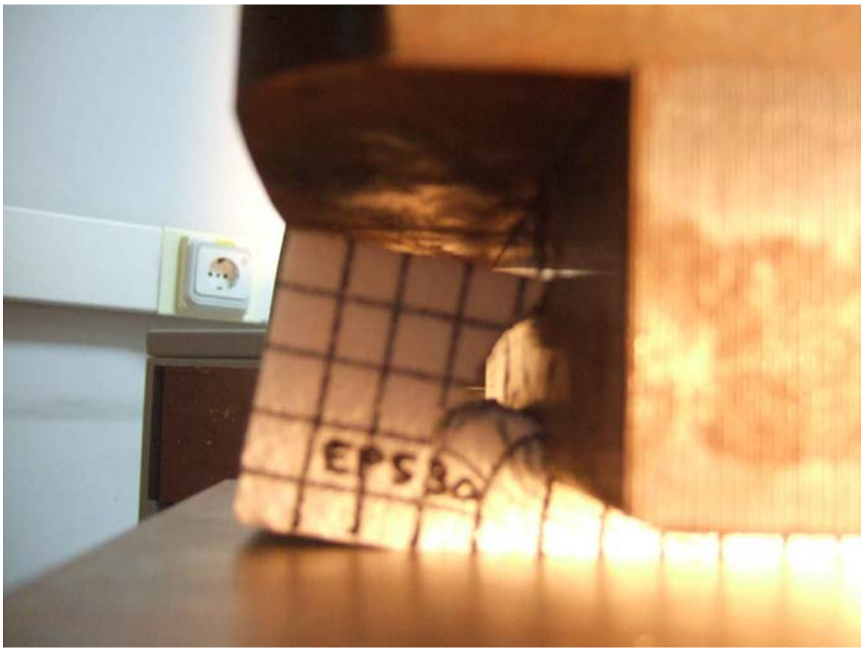

Figure 4.85. EPS 30 specimen in block indentation test loaded fourth time up to 40.0 mm

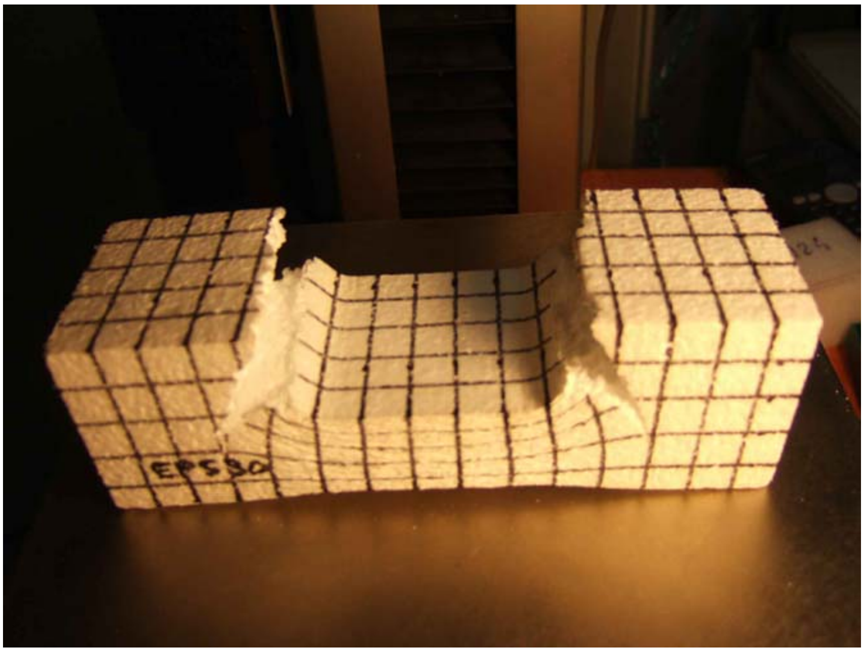

Figure 4.86. EPS 30 specimen in block indentation test after being loaded fourth time up to 40.0 mm

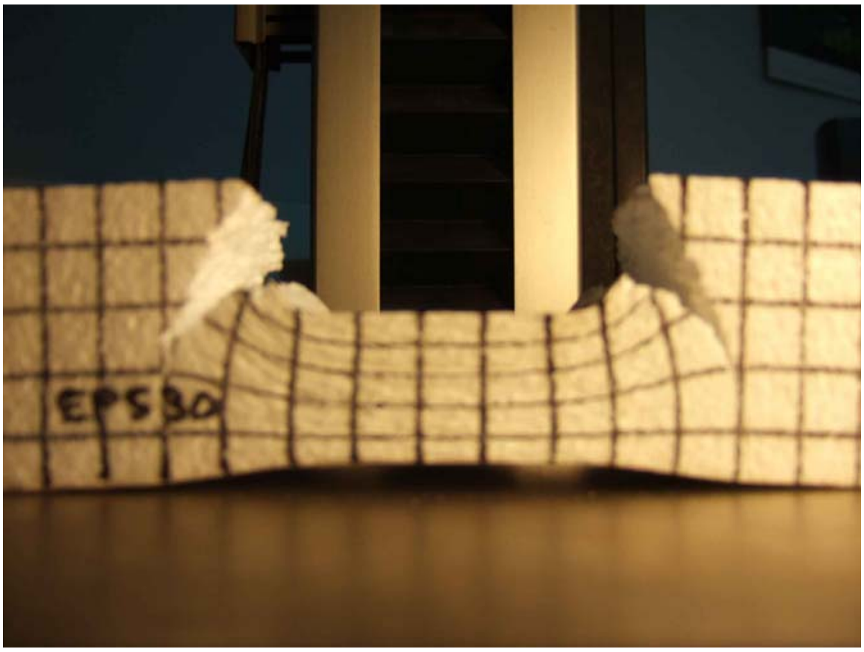

Figure 4.87. EPS 30 specimen in block indentation test after being loaded fourth time up to 40.0 mm

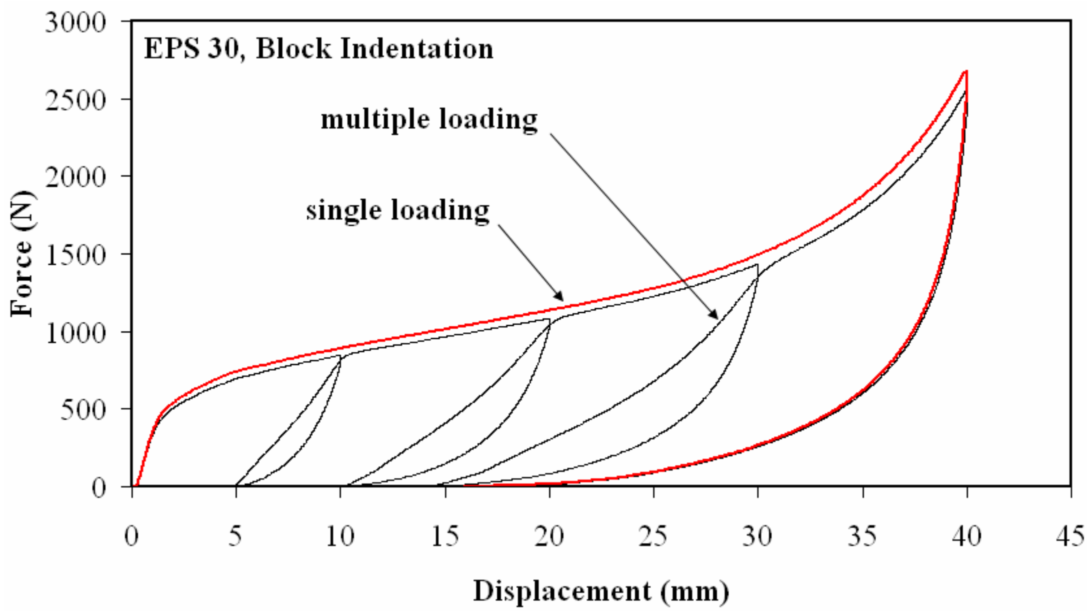

Figure 4.88. Force versus displacement for single and multiple block indentation loading of EPS 30 (compression direction is taken as positive)

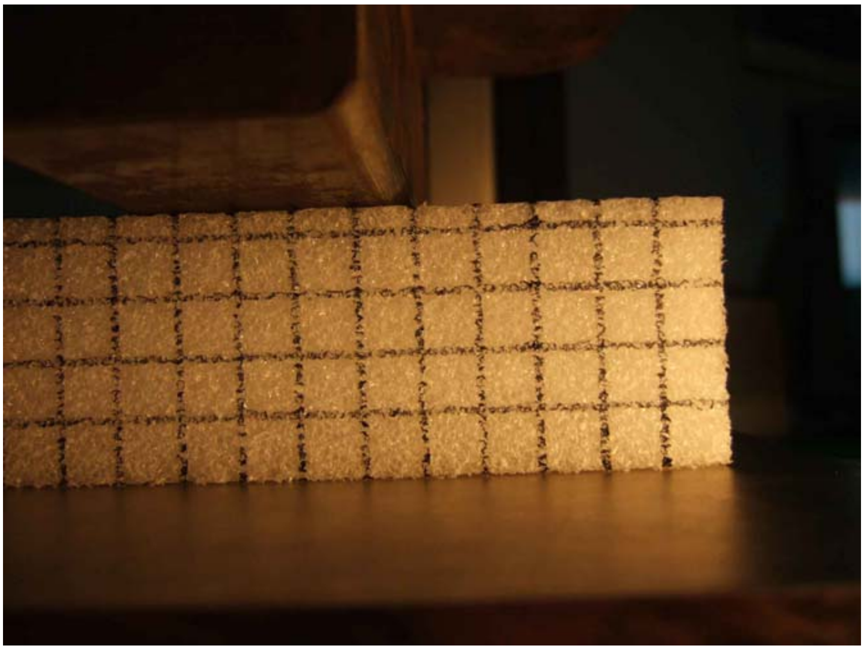

Figure 4.89. PE 58 specimen at the beginning of block indentation test

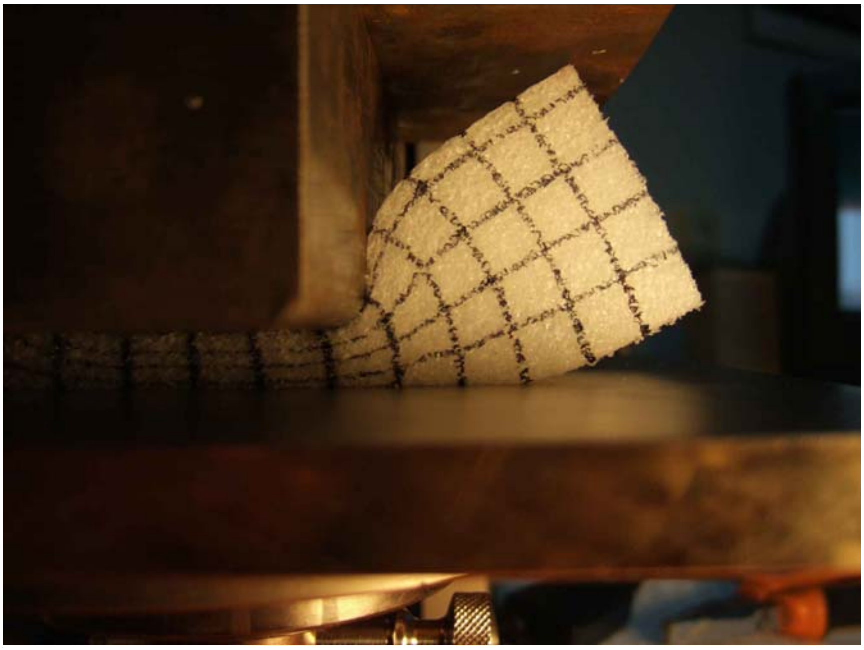

Figure 4.90. PE 58 specimen in block indentation test loaded fourth time up to 36.0 mm

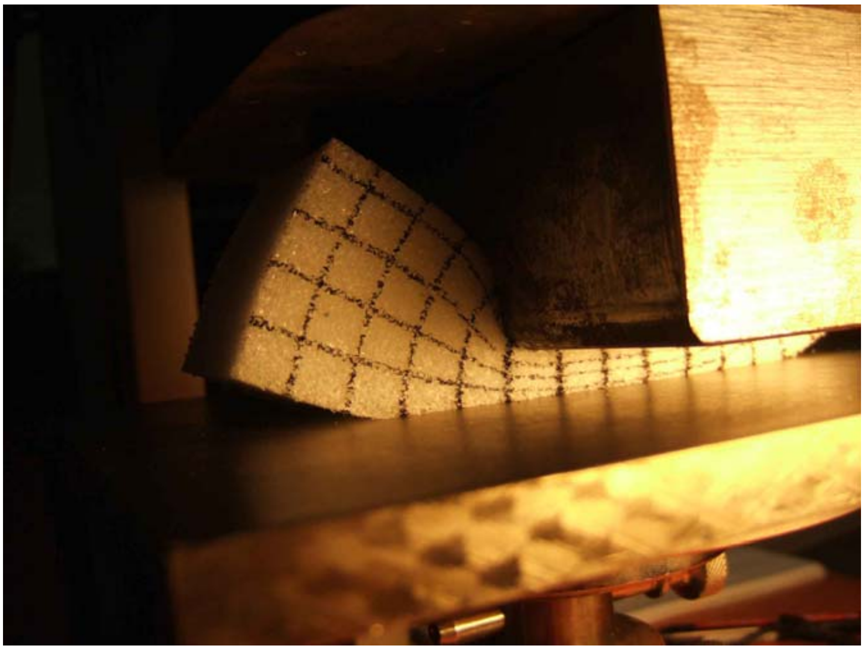

Figure 4.91. PE 58 specimen in block indentation test loaded fourth time up to 36.0 mm

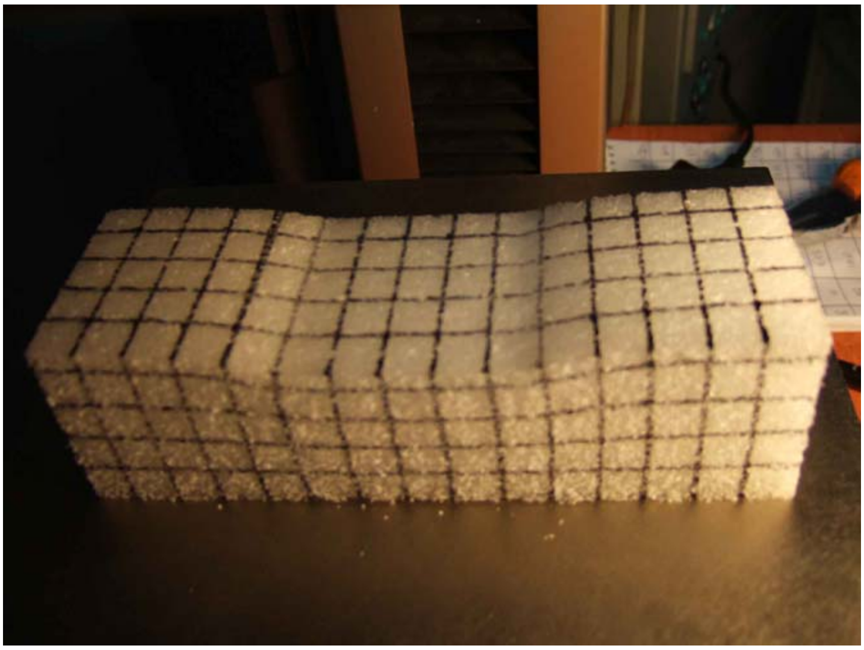

Figure 4.92. PE 58 specimen in block indentation test after being loaded fourth time up to 36.0 mm

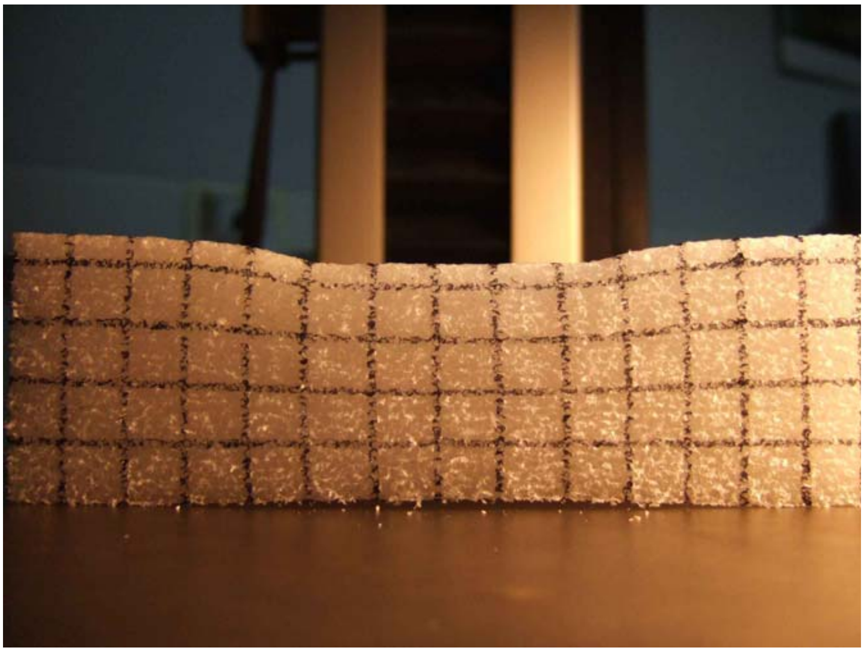

Figure 4.93. PE 58 specimen in block indentation test after being loaded fourth time up to 36.0 mm

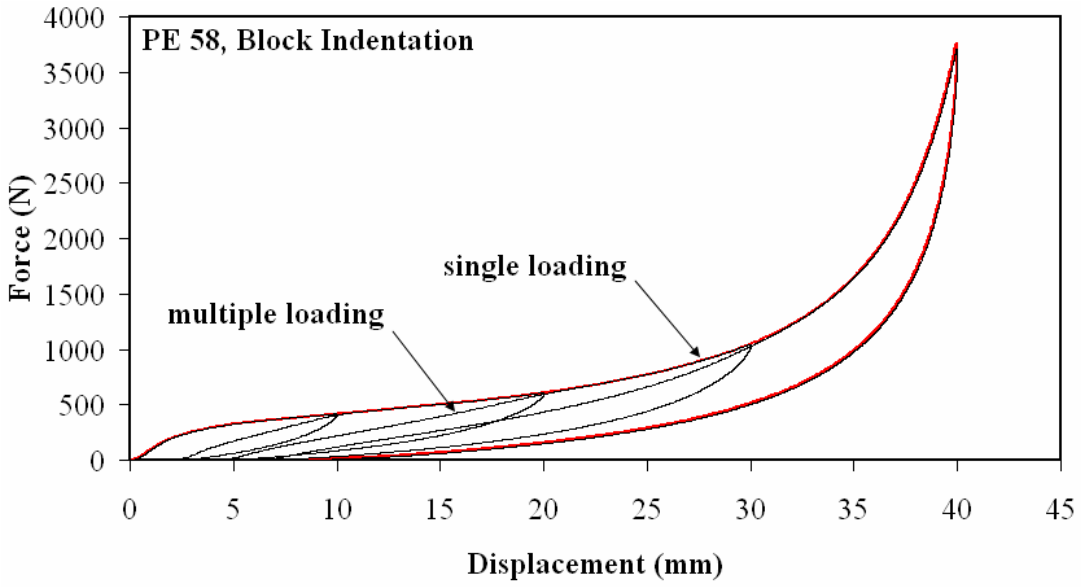

Figure 4.94. Force versus displacement for single and multiple block indentation loading of PE 58 (compression direction is taken as positive)

5. FINITE ELEMENT SIMULATION OF MULTIPLE GENERAL LOADING AND UNLOADING OF LOW DENSITY POLYMERIC FOAMS

In this chapter, results of uniaxial and hydrostatic compression, uniaxial tension, simple shear, and cylinder and block indentation tests are compared to those of finite element simulations performed by Abaqus Explicit version 6.7 for EPS 30 and PE 58. Elastic loading is modeled as linear in Abaqus, and there are two hardening options for yielding: volumetric and isotropic.

5.1. Crushable Foam Model with Volumetric Hardening

The yield surface for crushable foam with volumetric hardening is given in Figure 5.1 and defined by

$$F = \left[q^2 + \alpha^2 \left(p - p_0 \right)^2 \right]^{1/2} - B = 0 , \tag{5.1}$$

where p is the pressure stress,

$$p = -\frac{1}{3} trace(\sigma) = -\frac{1}{3}(\sigma_{11} + \sigma_{22} + \sigma_{33}), \tag{5.2}$$

and σ is stress tensor,

$$\sigma = \begin{bmatrix} \sigma_{11} & \sigma_{12} & \sigma_{13} \\ \sigma_{21} & \sigma_{22} & \sigma_{23} \\ \sigma_{31} & \sigma_{32} & \sigma_{33} \end{bmatrix}. \tag{5.3}$$

In Equation (5.1), q is the Von Mises stress defined as

$$q = \left[\frac{1}{2} \left((\sigma_{11} - \sigma_{22})^2 + (\sigma_{22} - \sigma_{33})^2 + (\sigma_{33} - \sigma_{11})^2 + 6\left(\sigma_{12}^2 + \sigma_{23}^2 + \sigma_{13}^2 \right) \right) \right]^{1/2} . \quad (5.4)$$

In Equation (5.1), B is the size of the vertical axis of the yield ellipse defined as

$$B = \alpha A = \alpha \frac{p_c + p_t}{2}, \quad (5.5)$$

where A is the size of the horizontal axis of the yield ellipse, and α is the shape factor of the yield ellipse that defines the relative magnitude of the axes defined as

$$\alpha = \frac{B}{A}. \quad (5.6)$$

In Equation (5.1), p_0 is the center of the yield ellipse on the *p*–axis which is defined as

$$p_0 = \frac{p_c - p_t}{2}, \quad (5.7)$$

where p_t is the strength of the material in hydrostatic tension and p_c is the yield stress in hydrostatic compression (always positive).

The yield surface is defined in Abaqus by providing the compression yield stress ratio, k, and the hydrostatic yield stress ratio, k_t, which are defined as

$$k = \frac{\sigma_c^0}{p_c^0}, \quad (5.8)$$

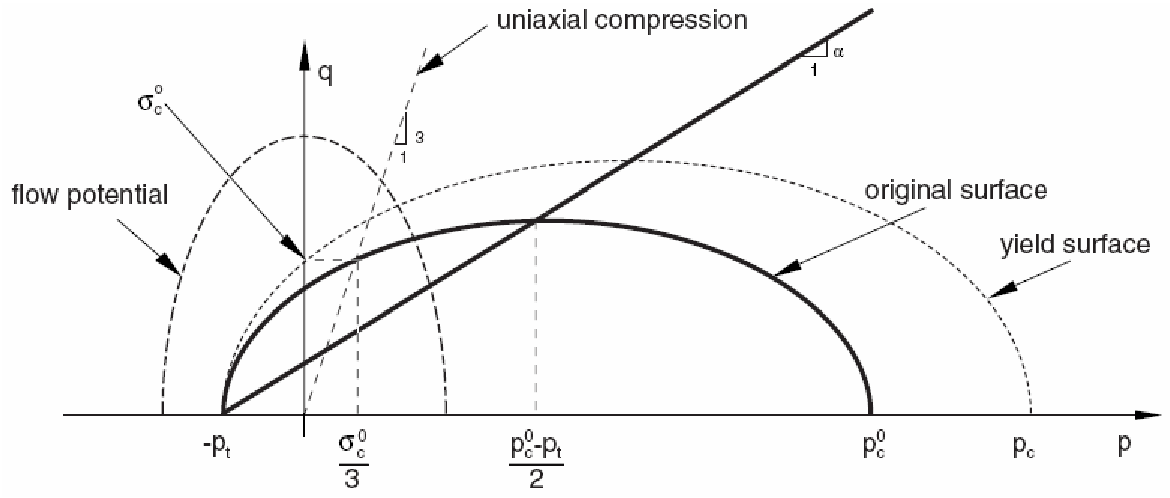

Figure 5.1. Yield surface and flow potential in the pressure stress (p)-Von Mises stress (q) plane for crushable foam with volumetric hardening [41]

and

$$k_t = \frac{p_t}{p_c^0}, \tag{5.9}$$

where σ_c^0 is the initial yield stress in uniaxial compression and p_c^0 is the initial yield stress in hydrostatic compression. Shape factor of the yield ellipse for volumetric hardening, α, can also be written in terms of compression yield stress ratio, k, and the hydrostatic yield stress ratio, k_t, as

$$\alpha = \frac{3k}{\sqrt{(3k_t + k)(3-k)}}. \tag{5.10}$$

In volumetric hardening, the plastic strain rate $\dot{\varepsilon}^{pl}$ is defined as

$$\dot{\varepsilon}^{pl} = \dot{\bar{\varepsilon}}^{pl} \frac{\partial G}{\partial \sigma}, \tag{5.11}$$

where G is the flow potential defined as

$$G = \sqrt{q^2 + \frac{9}{2} p^2} , \tag{5.12}$$

and $\dot{\bar{\varepsilon}}^{pl}$ is plastic strain rate defined as

$$\dot{\bar{\varepsilon}}^{pl} = \frac{\sigma : \dot{\varepsilon}^{pl}}{G} . \tag{5.13}$$

Flow potential in $q - p$ plane is an ellipse for volumetric hardening as given in Figure 5.1. Direction of flow given by the flow potential is along the stress direction in radial paths. It is not normal to the tangent to the yield surface at the load point; therefore the flow potential is non-associated.

The yield surface intersects the p axis at $-p_t$ and p_c. In volumetric hardening, the intersection point at $-p_t$ remains fixed, whereas p_c increases with densification. p_c is calculated by using the uniaxial compression test data input as a function of the volumetric compacting plastic strain $-\varepsilon_{vol}^{pl}$ as

$$p_c\left(\varepsilon_{vol}^{pl}\right) = \frac{\sigma_c\left(\varepsilon_{axial}^{pl}\right)\left[\sigma_c\left(\varepsilon_{axial}^{pl}\right)\left(\frac{1}{\alpha^2} + \frac{1}{9}\right) + \frac{p_t}{3}\right]}{p_t + \frac{\sigma_c\left(\varepsilon_{axial}^{pl}\right)}{3}} , \tag{5.14}$$

where $\varepsilon_{axial}^{pl} = \varepsilon_{vol}^{pl}$ in uniaxial compression.

There is strain rate dependency option for crushable foam material model with volumetric and isotropic hardening in Abaqus, but it is not used in simulations because the loading speeds in experiments and FE simulations are chosen to be the same (100 mm/min).

5.2. Crushable Foam Model with Isotropic Hardening

The yield surface for crushable foam with volumetric hardening is given in Figure 5.2, and defined as

$$F = \left[q^2 + \alpha^2 p^2 \right]^{1/2} - B = 0 . \tag{5.15}$$

In Equation (5.1), B is the size of the vertical axis of the yield ellipse defined as

$$B = \alpha p_c = \sigma_c \sqrt{1 + \left(\frac{\alpha}{3} \right)^2} , \tag{5.16}$$

The yield surface is an ellipse on the $q - p$ stress plane as seen in Figure 5.2. The yield surface is defined in Abaqus by providing only the compression yield stress ratio, k. Shape factor of the yield ellipse for isotropic hardening, α, can also be written in terms of compression yield stress ratio, k, as

$$\alpha = \frac{3k}{\sqrt{9 - k^2}} . \tag{5.17}$$

In volumetric hardening, the flow potential G is defined as

$$G = \sqrt{q^2 + \beta p^2} , \tag{5.18}$$

and β is a parameter that defines the shape of the flow potential ellipse on the $q - p$ plane, and it is related to the plastic Poisson's ratio υ_p by

$$\beta = \frac{3}{\sqrt{2}} \sqrt{\frac{1 - 2\upsilon_p}{1 + \upsilon_p}} . \tag{5.19}$$

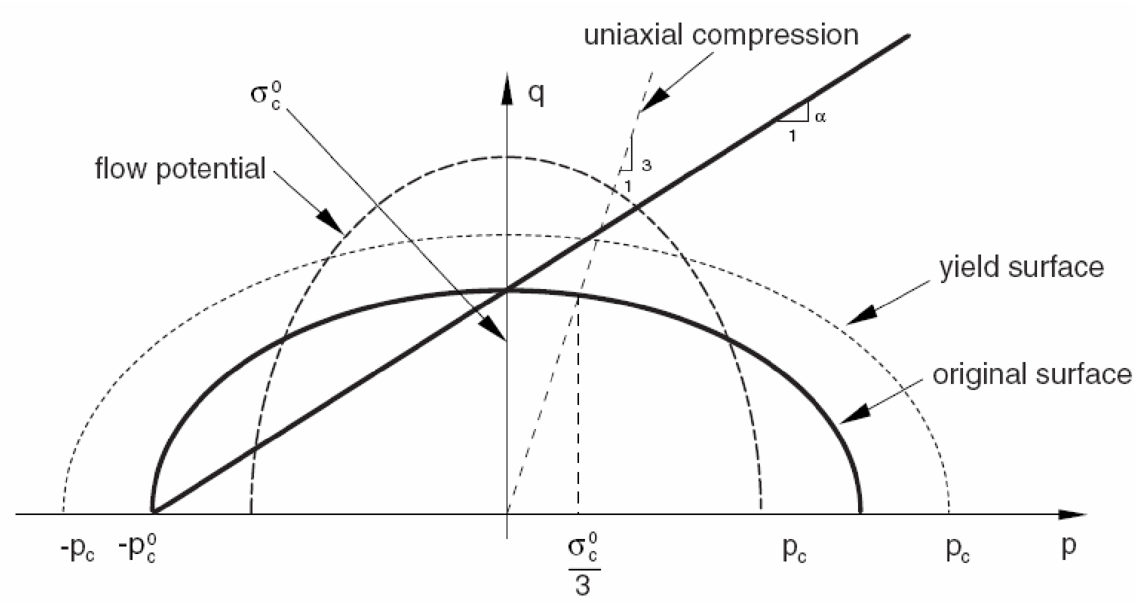

Figure 5.2. Yield surface and flow potential in the pressure stress (p)-Von Mises stress (q) plane for crushable foam with isotropic hardening [41]

The plastic flow is associated if α equals to β. Calculation method for p_c and rate dependency option for isotropic hardening are the same as volumetric hardening.

5.3. Finite Element Simulations

Finite element (FE) simulations are performed for uniaxial and hydrostatic compression, uniaxial tension, simple shear, and cylinder and block indentation tests by using Abaqus Explicit version 6.7. Crushable foam material model is used with both volumetric and isotropic hardening options. Experimental results are used for calculating the parameters needed to run the material model as well as to validate the FE results.

Crushable foam model requires elastic modulus and Poisson's ratio for linear elastic behavior. For yielding with volumetric hardening, it requires the compression yield stress ratio, k, the hydrostatic yield stress ratio, k_t, and the yield stress, σ_Y, with the absolute value of the axial plastic strain, ε_{axial}^{pl}, according to Equation (5.20) obtained from uniaxial compression test in a tabular format

$$\varepsilon_{axial}^{pl} = \ln(1 + \varepsilon_{nom}) - \varepsilon^{el}, \tag{5.20}$$

where ε_{nom} is the engineering strain with a negative value in compression. From observations in uniaxial compression experiments and as suggested Masso-Moreu and Mills [40], Poisson's ratio in the plastic region can be accepted as zero for EPS 30 and PE 58. Therefore engineering stress is accepted equal to true stress.

Equations (5.8) and (5.9) are used for calculation of the compression yield stress ratio, k, and the hydrostatic yield stress ratio, k_t. EPS 30 and PE 58 do not have a clear initial yield point in uniaxial and hydrostatic compression. There are very few experimental data for hydrostatic tension of foams in literature, and it is not possible to calculate exactly k_t either. Therefore it is preferred to define a range of values, to make simulations for different values of input parameters, and to compare the FE simulation results to those of experiments. Abaqus Theory Manual [41] recommends to use values between 0.05 and 0.1 for k_t. From the experimental results, k is expected to be approximately 0.85 and 2.0 for EPS 30 and PE 58 respectively. Poisson's ratio for elastic region, υ, and Poisson's ratio for plastic region, υ_p, are selected to be 0 and 0.1 for different materials defined in Abaqus. Material constants used to define EPS 30 are given in Tables 5.1 and 5.2 for crushable foam material model with volumetric hardening and isotropic hardening respectively. Similarly, the material constants used for PE 58 are given in Tables 5.3 and 5.4. The yield surfaces in the pressure stress (p) and Von Mises stress (q) plane obtained by using the material constants given in Tables 5.1–5.4 are given in Figures 5.3 and 5.4 for EPS 30 and PE 58 respectively. Units for stress used in Tables 5.1–5.4 are kPa. Although it is possible to guess the initial yield strength in uniaxial compression and hydrostatic compression tests, this is not the case for uniaxial tension and simple shear. Yield strength for uniaxial compression and hydrostatic compression found in experiments are used for the calculation of material constants given in Tables 5.1–5.3 and for yield ellipses given in Figures 5.3 and 5.4. Different values of yield strength for hydrostatic tension values are used in FE simulations. Yield strength values used in material constant calculations for uniaxial compression, hydrostatic compression, and hydrostatic tension are marked with dots in Figures 5.3 and 5.4. Yield strength values for uniaxial tension and simple shear are not given in Figures 5.3 and 5.4 because the yield points are not clear in stress–strain curves obtained by measurements. Yield strengths for uniaxial compression and uniaxial tension follow the dashed lines given in Figures 5.3 and 5.4 during hardening. Similarly, yield strengths for simple shear and hydrostatic tests follow the *y* axis and *x* axis respectively during hardening in Figures 5.3 and 5.4.

Table 5.1. Constants used for EPS 30 in crushable foam material model with volumetric hardening (unit of stress is kPa)

	E (kPa)	υ	σ_c^0	p_c^0	p_t	k	k_t	α	B	p_0
MAT1	5180	0	170	155	16	1.097	0.10	2.018	172.0	69.8
MAT2	5180	0	170	200	150	0.850	0.75	0.988	172.9	25.0
MAT3	5180	0	170	155	116	1.097	0.75	1.304	176.8	19.4
MAT3	5180	0.1	170	155	116	1.097	0.75	1.304	176.8	19.4
MAT5	5180	0.1	170	155	233	1.097	1.50	1.008	195.3	-38.8
MAT6	5180	0	170	200	20	0.850	0.10	1.622	178.4	90.0

Table 5.2. Constants used for EPS 30 in crushable foam material model with isotropic hardening (unit of stress is kPa)

	E (kPa)	υ	υ_p	σ_c^0	p_c^0	k	α	B
ISOMAT1	5180	0	0	170	155	1.10	1.178	182.6
ISOMAT2	5180	0	0	170	200	0.85	0.886	177.3
ISOMAT3	5180	0	0.1	170	200	0.85	0.886	177.3

Table 5.3. Constants used for PE 58 in crushable foam material model with volumetric hardening (unit of stress is kPa)

	E (kPa)	υ	σ_c^0	p_c^0	p_t	k	k_t	α	B	p_0
MAT1	2347	0.1	100	100	200	1.00	2.00	0.802	120.3	-50
MAT2	2347	0.1	100	100	100	1.00	1.00	1.061	106.1	0
MAT3	2347	0.1	100	100	10	1.00	0.10	1.861	102.3	45
MAT3	2347	0.1	100	100	300	1.00	3.00	0.671	134.2	-100
MAT5	2347	0.1	100	117.6	235	0.85	2.00	0.665	117.3	-58.8
MAT6	2347	0.1	100	90.9	182	1.10	2.00	0.899	122.5	-45.5

Table 5.4. Constants used for PE 58 in crushable foam material model isotropic hardening (unit of stress is kPa)

	E (kPa)	υ	υ_p	σ_c^0	p_c^0	k	α	B
ISOMAT1	2347	0.1	0	100	100.0	1.00	1.061	106.1
ISOMAT2	2347	0.1	0	100	117.6	0.85	0.886	104.3
ISOMAT3	2347	0.1	0	100	87.0	1.15	1.245	108.3

For uniaxial compression, foam is compressed between two rigid plates as seen in Figure 5.5. Single linear cubic element with reduced integration and hourglass control is used to model foam specimen with 50 × 50 × 50 mm^3 dimensions for EPS 30 and 45 × 50 × 50 mm^3 dimensions for PE 58. Contact is defined between the plates and the foam. Top rigid plate is moved downward 40 mm and 36 mm for EPS 30 and PE 58 respectively in simulations for uniaxial compression test. Top rigid plate is returned back to its initial position after unloading. Reaction force and displacement of the moving rigid plate are used for comparison of FE results to those obtained in experiments.

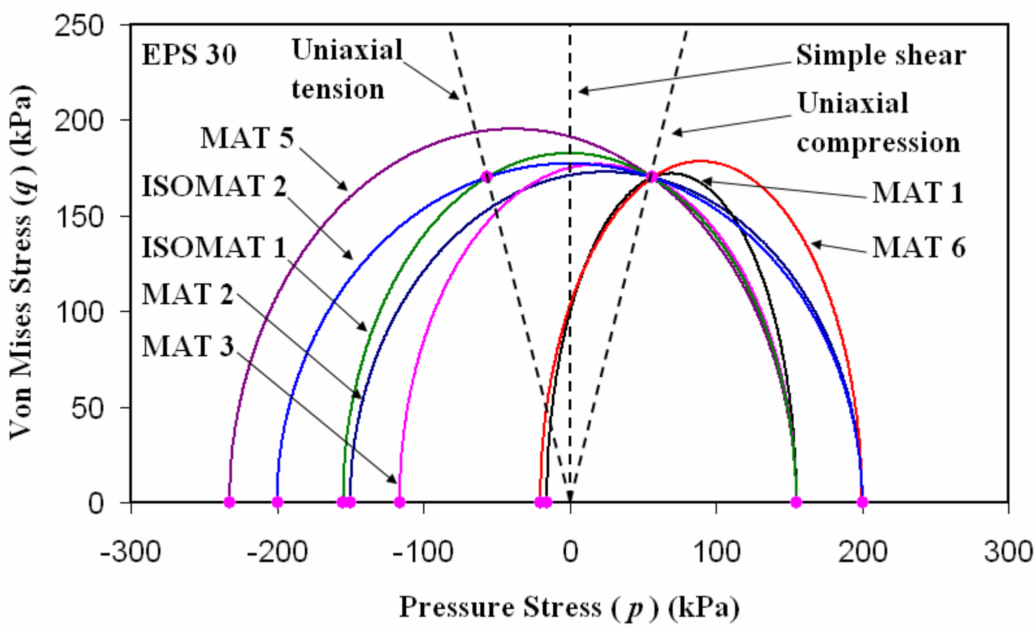

Figure 5.3. Yield surface in the pressure stress (p)-Von Mises stress (q) plane for different material constants of EPS 30 given in Tables 5.1 and 5.2

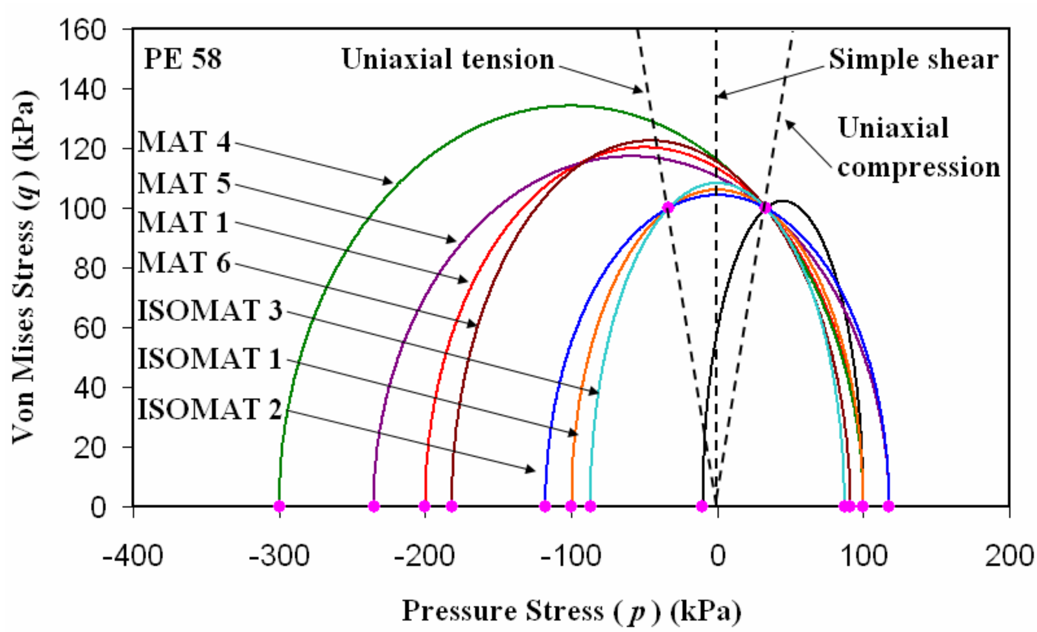

Figure 5.4. Yield surface in the pressure stress (p)-Von Mises stress (q) plane for different material constants of PE 58 given in Tables 5.3 and 5.4

For hydrostatic compression, foam specimen with 50 × 50 × 50 mm^3 dimensions for EPS 30 and 45 × 50 × 50 mm^3 dimensions for PE 58 are modeled with single linear cubic element with reduced integration and hourglass control. One corner of the foam is fixed and 10 bar pressure is applied on, and then removed from all of the surfaces as seen in Figure 5.5.

For uniaxial tension, foam specimen with 10 × 25 × 50 mm^3 dimensions is modeled with two linear cubic elements with reduced integration and hourglass control. Bottom surface of the foam is fixed, and displacement boundary condition is applied to the top surface as seen in Figure 5.6. Top surface is moved 10 mm upward and returned back to its initial position after unloading.

For simple shear, foam specimen with 50 × 50 × 100 mm^3 dimensions for EPS 30 and 45 × 50 × 100 mm^3 dimensions for PE 58 are modeled with two linear cubic elements with reduced integration and hourglass control. One of the side surfaces of foam is fixed, and displacement boundary condition is applied to the other side surface as seen in Figure 5.7. Side surface is moved 10 mm upward and returned back to its initial position after unloading.

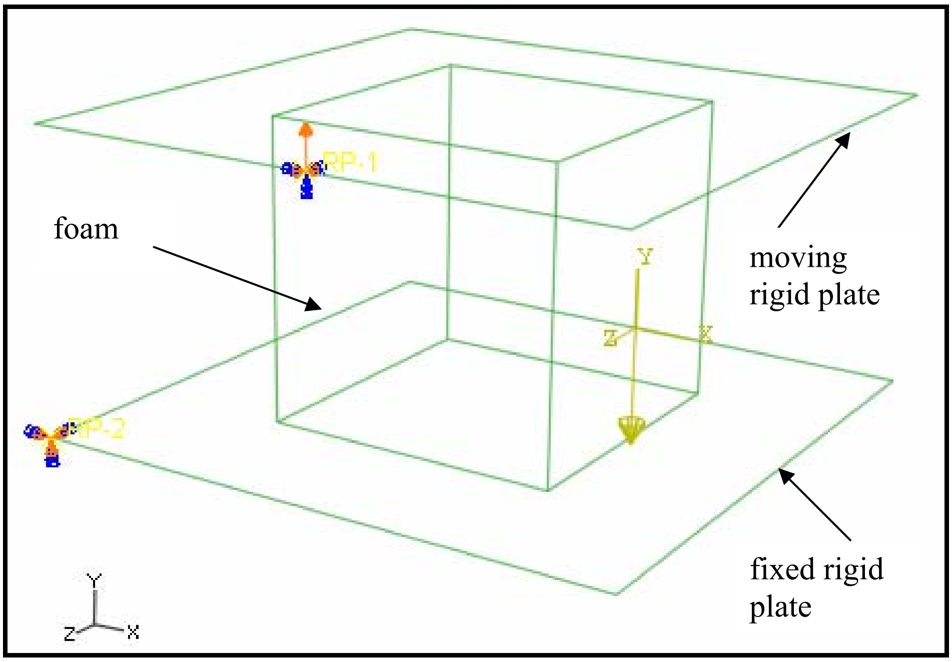

Figure 5.5. Finite element model for uniaxial compression

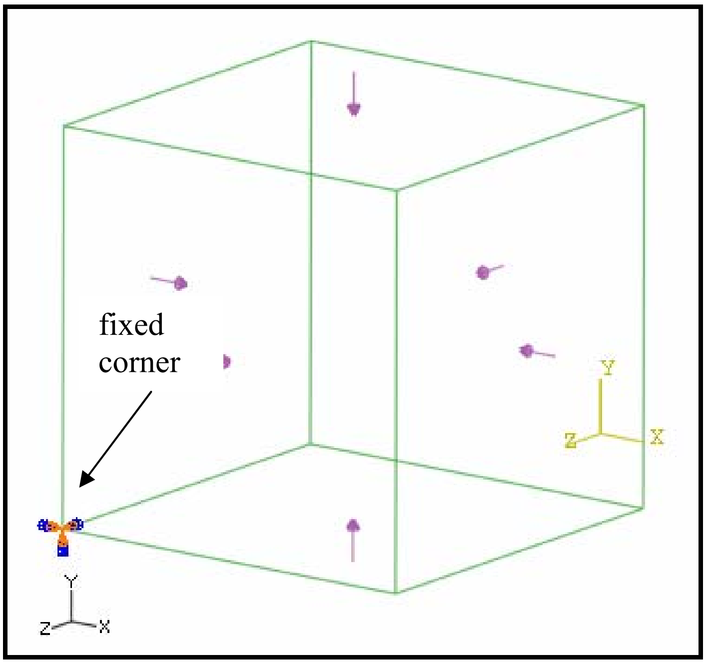

Figure 5.6. Finite element model for hydrostatic compression

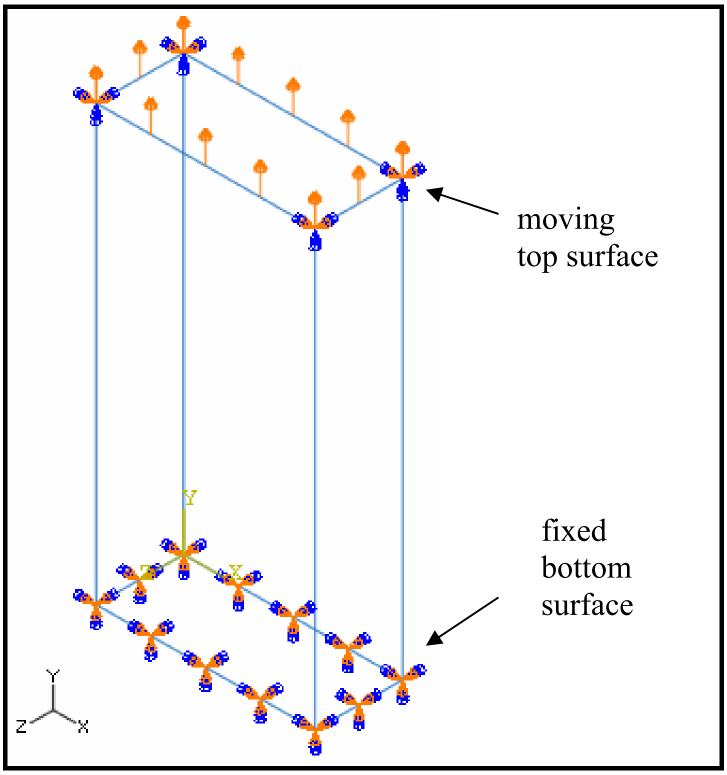

Figure 5.7. Finite element model for uniaxial tension

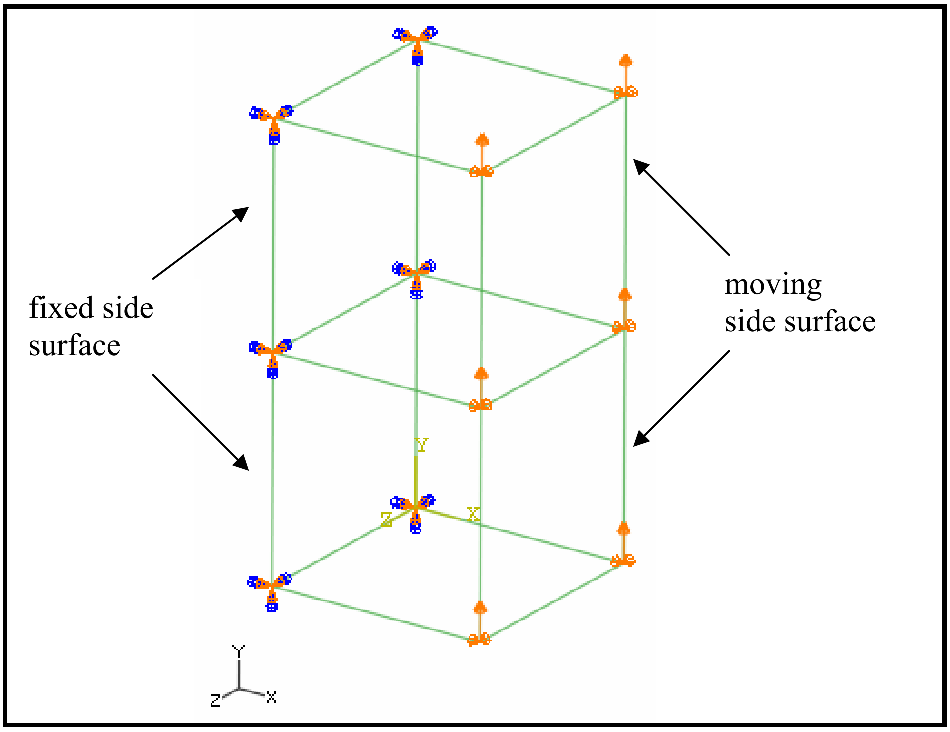

Figure 5.8. Finite element model for simple shear

FE simulations are performed for simple shear test of PE 58–ISOMAT 1 with two different mesh sizes: two (1 × 1 × 2) cubic elements in the first model and 54 (3 × 3 × 6) cubic elements in the second model are used. Side views of the two deformed FE models are given in Figure 5.9. Shear stress (S12) versus time plot for the elements in the two models is given in Figure 5.10. It is seen that for 10 mm deformation, the elements at the corners of FE model given in Figure 5.9 (b) are not in pure shear stress state. This behavior is also observed in simple shear tests performed by Zwick Z020 universal tensile testing machine. Except the corner elements, both FE models give the same shear stress value as seen in Figure 5.10. Therefore FE model with two cubic elements are used for FE simulations of simple shear test to reduce the FE model solution time for different material parameters given in Tables 5.1–5.4.

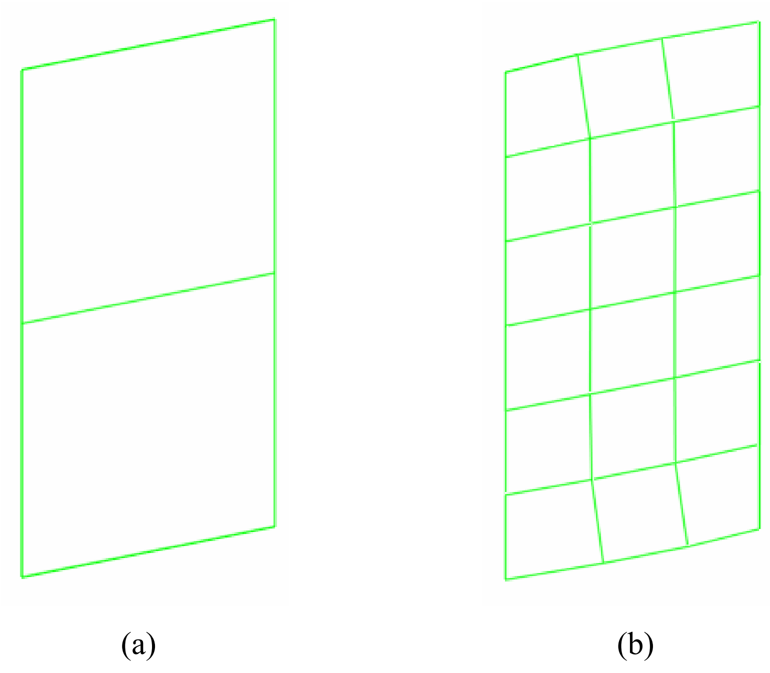

Figure 5.9. Deformed side views of finite element models used in simple shear test simulations: (a) FE model with 1 × 1 × 2 elements, (b) FE model with 3 × 3 × 6 elements

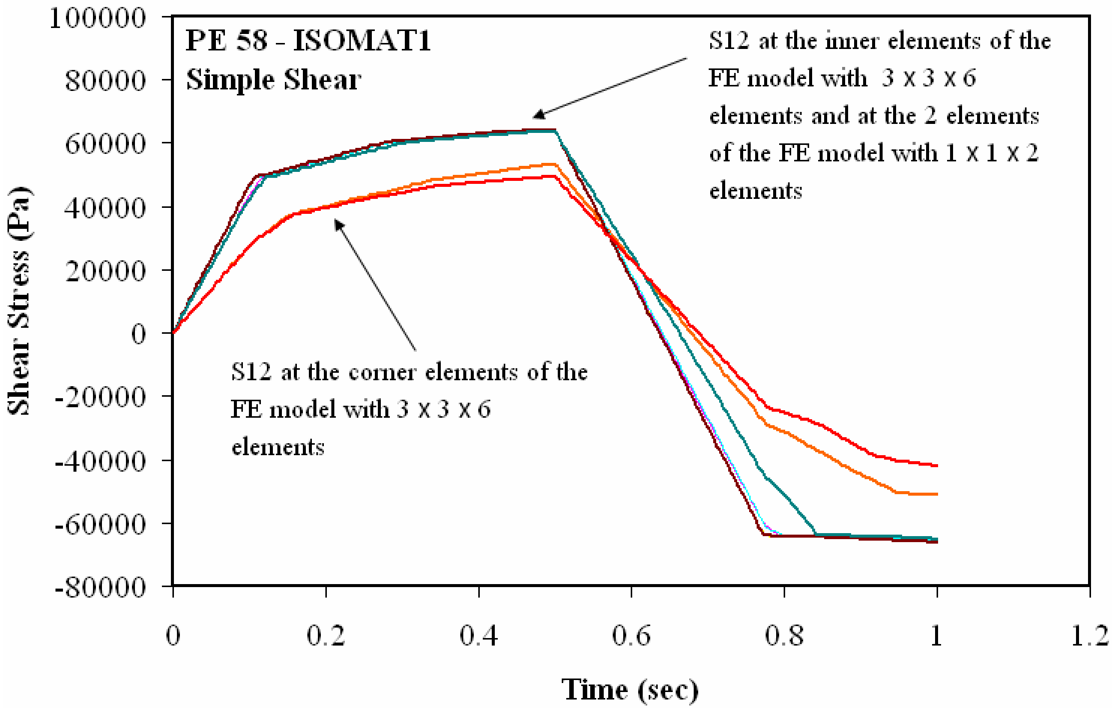

Figure 5.10. Shear stress (S12) versus time for PE58–ISOMAT1 material under simple shear

5.3.1. Effect of Mesh Size in Block Indentation

For cylinder and block indentation tests, foam specimens with $50\times50\times150$ mm^3 dimensions for EPS 30 and $45\times50\times150$ mm^3 dimensions for PE 58 are modeled by using two dimensional bilinear quadrilateral plane strain elements with reduced integration and hourglass control. 50 mm is used for plane strain thickness. Cylinder indenter with 100 mm diameter, block indenter with 50 mm width and 10 mm corner radius, and fixed bottom plates are modeled with two dimensional analytical rigid shells. FE models prepared for simulations of cylinder and block indentation tests are given in Figures 5.11 and 5.12 respectively. Bottom plate is fixed, and displacement boundary conditions are applied to the indenters. Contact is defined between the indenters and the foam. Reaction force and displacement of the indenters are used for comparison to test results. In FE models given in Figures 5.11 and 5.12, element length on the top edge of the foam is 5 mm, whereas it is 3 mm in Figure 5.13. In Figure 5.14, reaction force versus displacement plot for the block indenter is given for the fine and coarse meshes together with experimental result. It is seen that there is not a significant difference between the results. Cylinder indenter has a

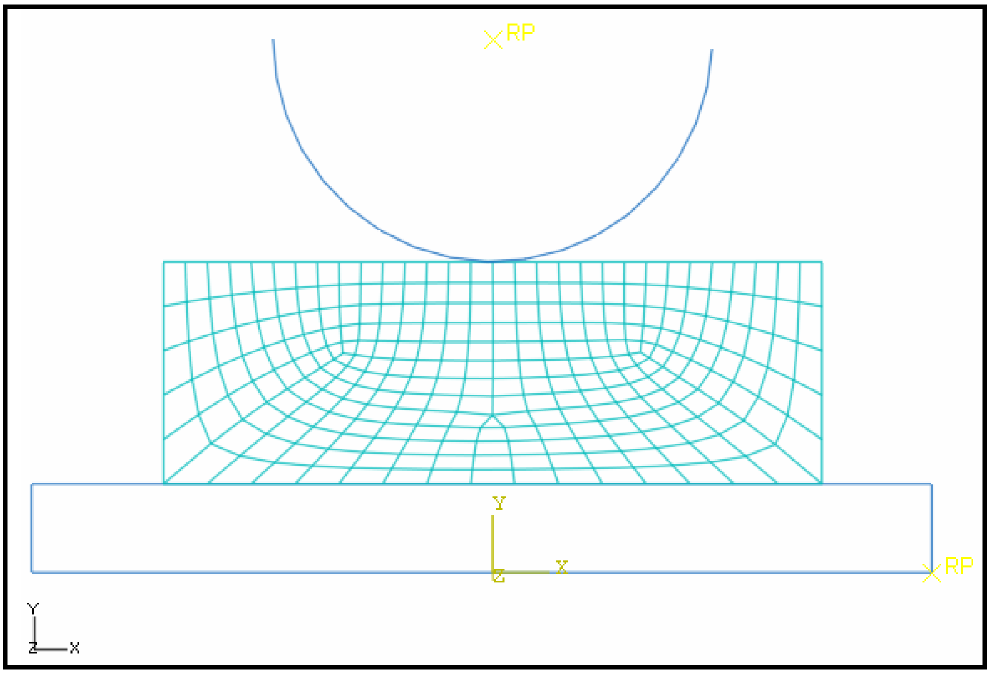

Figure 5.11. Finite element model for cylinder indentation

smoother surface compared to the block indenter, and there is no need to do such a comparison for cylinder. Therefore coarse mesh with 5 mm element length on the top edge of the foam will be used for the cylinder and block indentation test simulations with different material parameters.

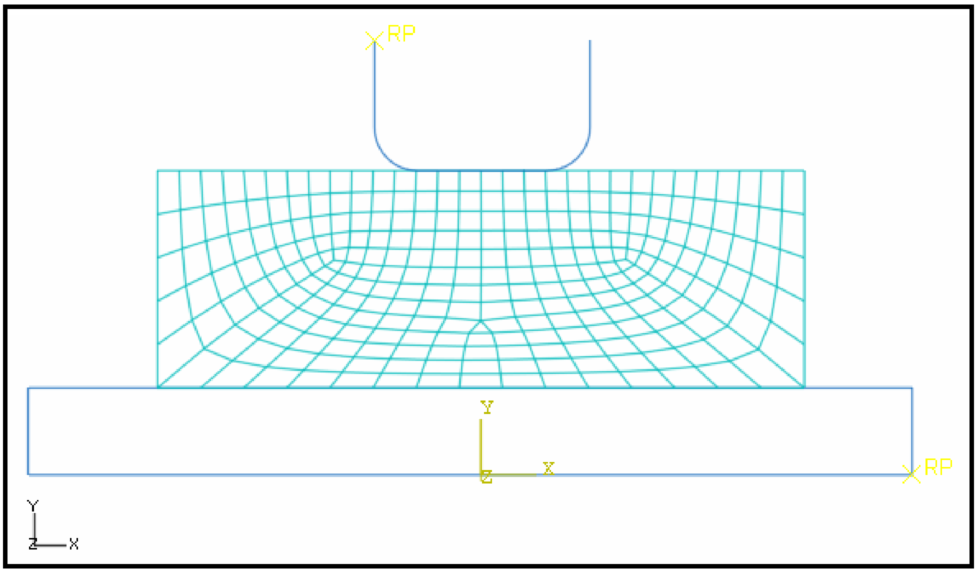

Figure 5.12. Finite element model for block indentation

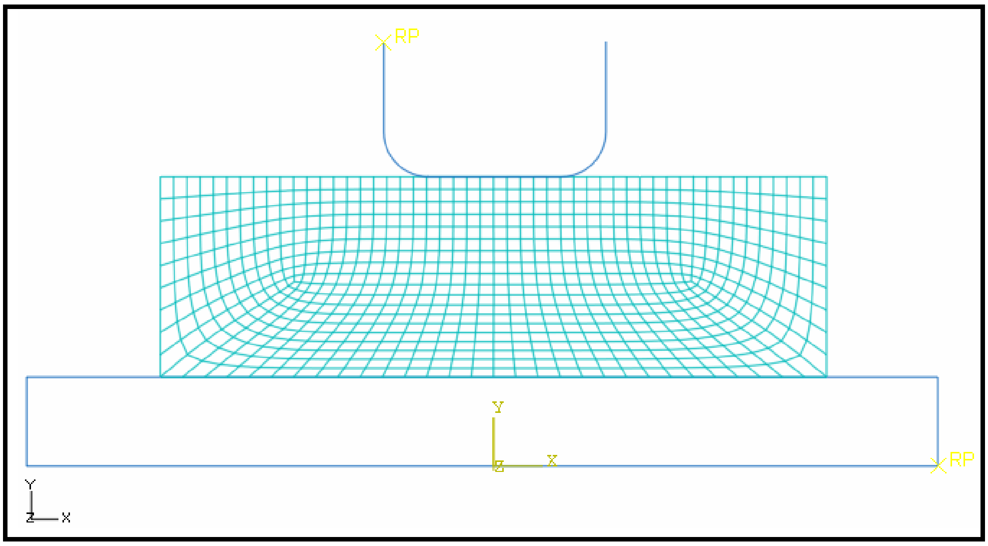

Figure 5.13. Finite element model for block indentation with fine mesh

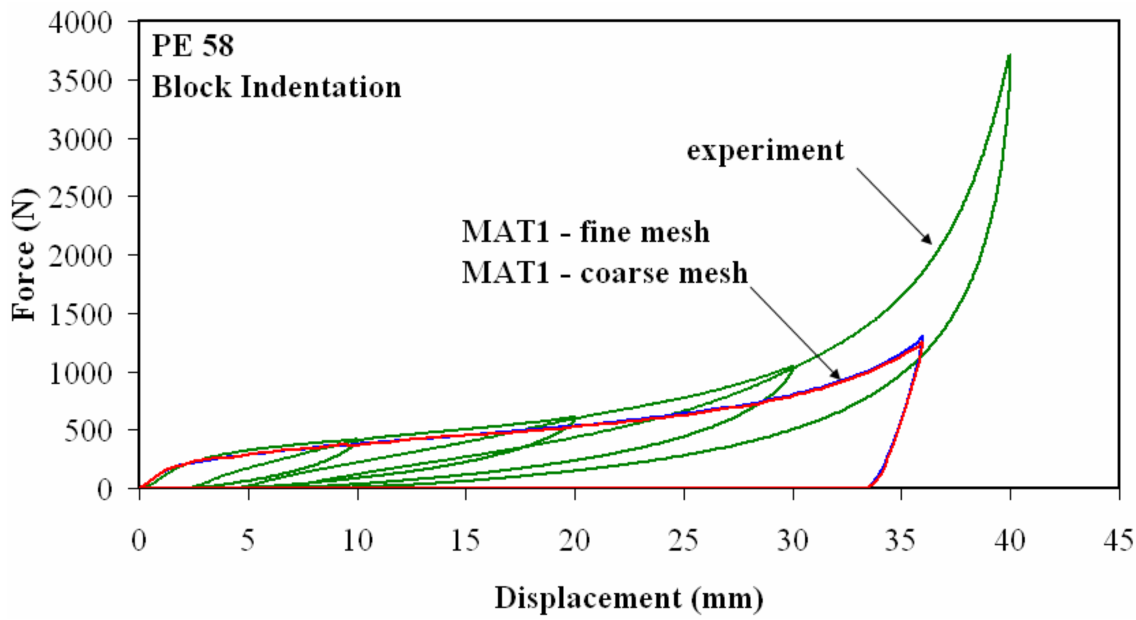

Figure 5.14. Force versus displacement for block indentation test and simulations with fine and coarse meshes, for PE 58 (compression direction is taken as positive)

5.3.2. Effect of Coefficient of Friction in Block Indentation

Contact is defined between the foam, indenter, and bottom plate in indentation test FE simulations. Effect of different values of coefficient of friction between the parts is investigated by performing simulations of block indentation test with PE58-ISOMAT1 materials. In Figures 5.15–5.18, deformation patterns are given for four different coefficients of friction: 0.001, 0.1, 0.3, and 0.5. It is observed that the deformation patterns for coefficient of friction 0.001 and 0.1 do not match to those observed in experiments. In Figure 5.19, force versus displacement is given for the block indentation test of PE 58-ISOMAT1 with different coefficients of friction together with the experimental result. Results are very close for coefficients of friction 0.3 and 0.5 compared to those obtained for 0.001 and 0.1. Abaqus Theory Manual [41] advises to use coefficient of friction as 0.3 between crushable foam and rigid surfaces. Therefore 0.3 is used as coefficient of friction in cylinder and block indentation test simulations with different material parameters.

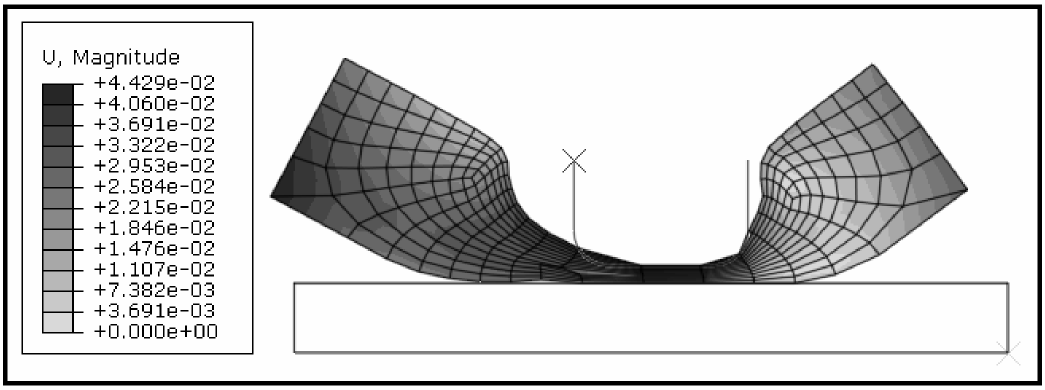

Figure 5.15. Deformation pattern for block indentation (PE 58 ISOMAT1 material with coefficient of friction equal 0.001)

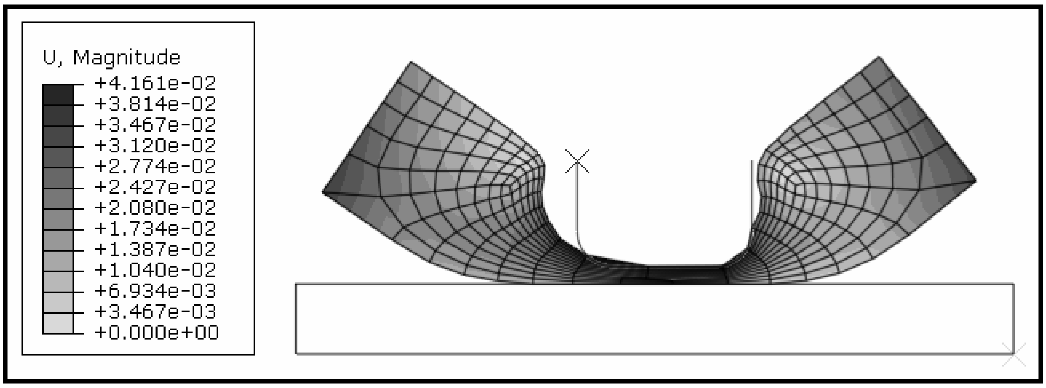

Figure 5.16. Deformation pattern for block indentation (PE 58 ISOMAT1 material with coefficient of friction equal 0.1)

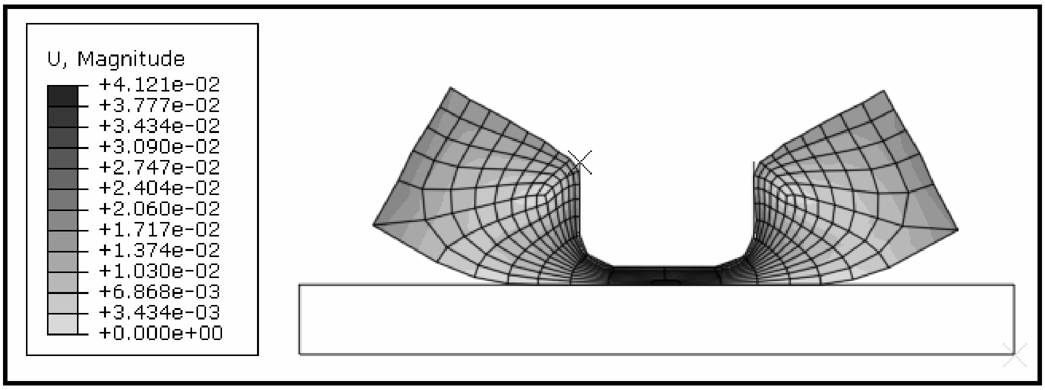

Figure 5.17. Deformation pattern for block indentation (PE 58 ISOMAT1 material with coefficient of friction equal 0.3)

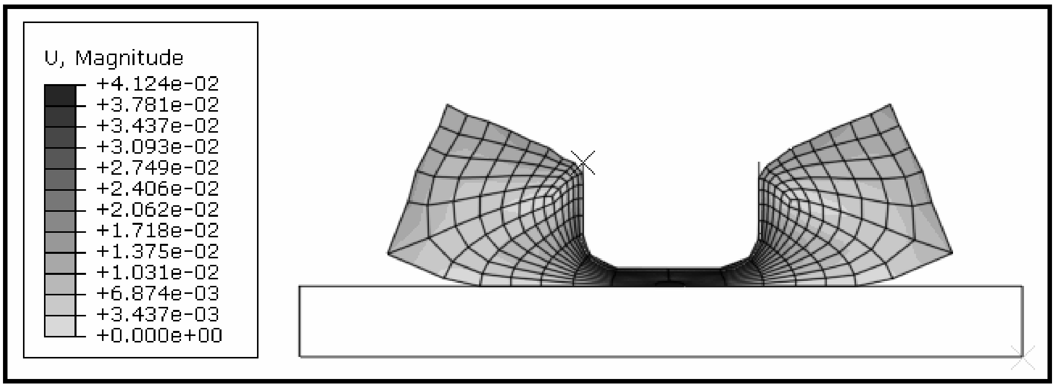

Figure 5.18. Deformation pattern for block indentation (PE 58 ISOMAT1 material with coefficient of friction equal 0.5)

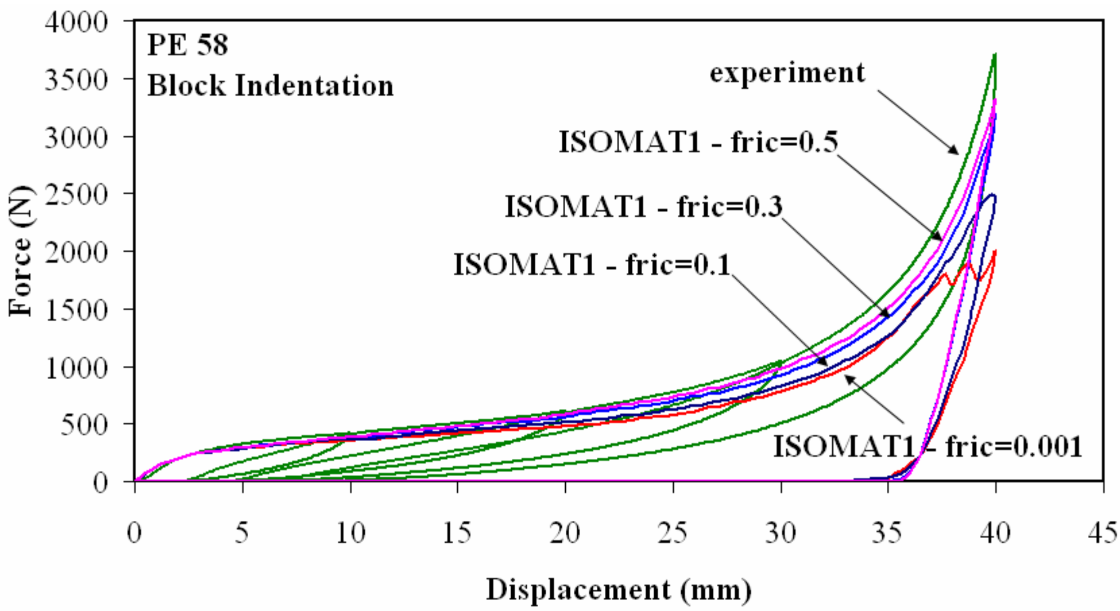

Figure 5.19. Force versus displacement for block indentation test and simulations with different coefficients of friction, for PE 58 (compression direction is taken as positive)

5.3.3. Finite Element Simulation Results for Different Material Parameters of EPS 30

Results of FE simulations for uniaxial compression are given in Figures 5.20–5.21 for EPS 30 with material constants given in Tables 5.1 and 5.2. Abaqus Theory Manual [41] suggested using zero for elastic Poisson's ratio and Masso-Moreu and Mills [40] suggested using 0.1. Poisson's ratio in elastic region is taken as 0.1 for materials MAT 4 and MAT 5, and FE results show that they differ from other materials with zero elastic Poisson's ratio in the densification region as given in Figure 5.20. Isotropic hardening requires plastic Poisson's ratio. As observed in the experiments performed in this study and as advised by Masso-Moreu and Mills [40], plastic Poisson's ratio is taken zero for most of the EPS 30 and PE 58 materials used in simulations. It is selected as 0.1 for material ISOMAT3 to see its effect on the results. FE results show that densification occur at lower strain values for ISOMAT3 compared to other materials which have zero plastic Poisson's ratio. The compression yield stress ratio, k, and the hydrostatic yield stress ratio, k_t, have no effect on the stress versus strain response in uniaxial compression because tabular input of compression test data is used for yielding in uniaxial compression. Simulation results for materials given in Tables 5.1 and 5.2 perfectly match to experiment data in loading except for materials with none zero elastic and plastic Poisson's ratio for uniaxial compression. Unloading response is modeled as linear in crushable foam model, and the measured unloading path is very different from the one calculated in FE simulation.

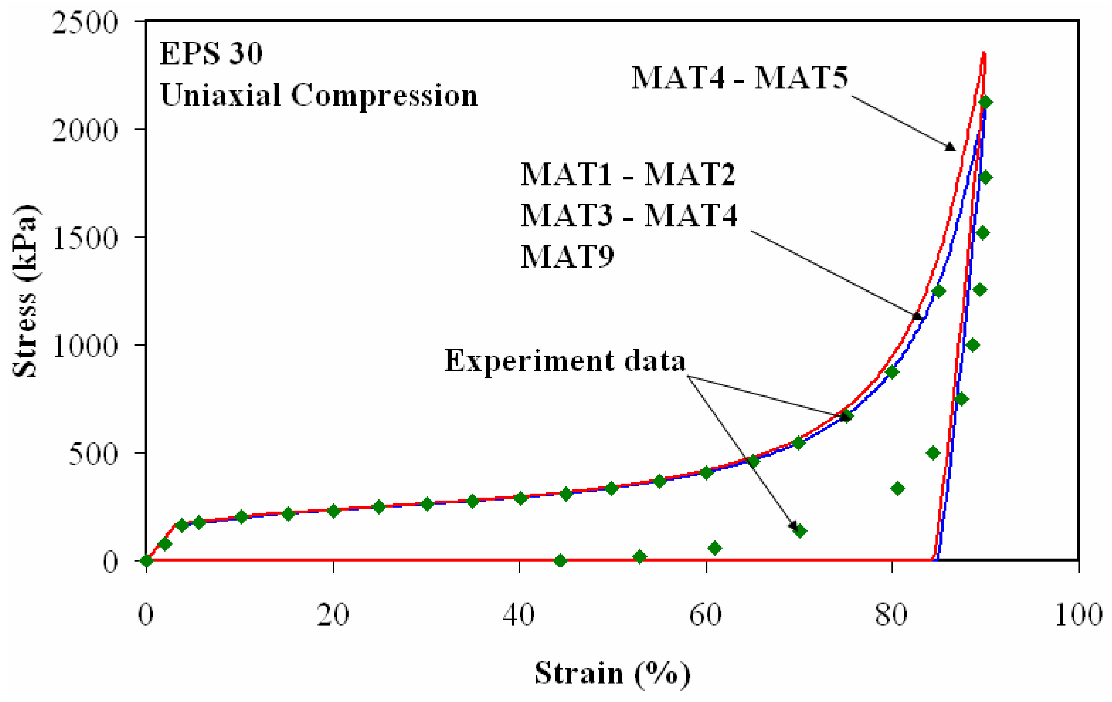

Figure 5.20. Stress versus strain for uniaxial compression test and simulations of EPS 30 (compression direction is taken as positive)

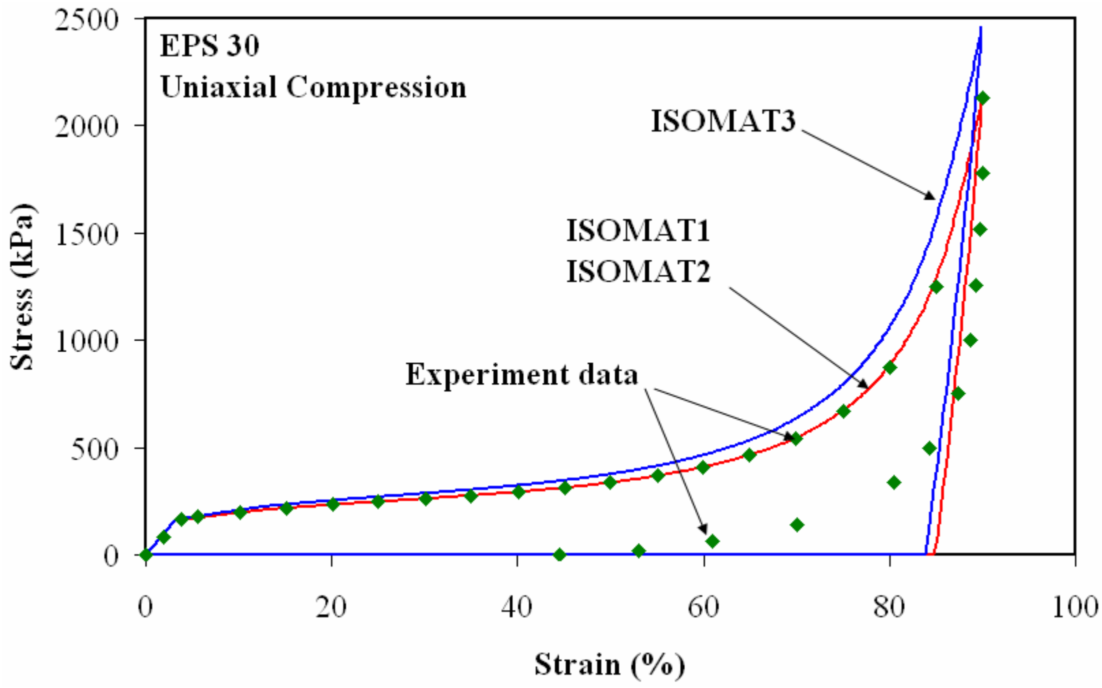

Figure 5.21. Stress versus strain for uniaxial compression test and simulations of EPS 30 (compression direction is taken as positive)

In Figures 5.22–5.24, hydrostatic pressure versus volumetric strain results are given for materials given in Tables 5.1 and 5.2 together with experimental data. Results do not match experimental results for elastic and densification regions. Stress level in plateau region is better predicted by most of the materials. Unloading path is again linear and very much deviated from measured one.

There is not a hardening effect for uniaxial tension and simple shear in volumetric hardening, because p_t remain fixed during expansion of yield surface. Yield strength values are much lower than expected. Linear hardening occur for materials with isotropic hardening but the yield stress values are much lower than the measured ones as seen in Figures 5.25–5.28. Unloading path is again linear and very much deviated from measured one.

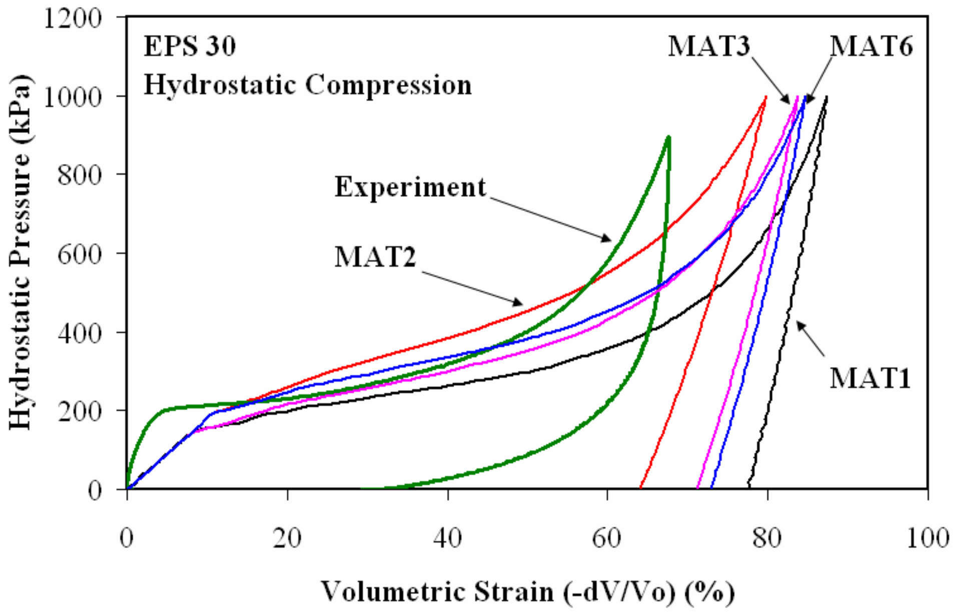

Figure 5.22. Hydrostatic pressure versus volumetric strain for hydrostatic compression test and simulations of EPS 30 (compression direction is taken as positive)

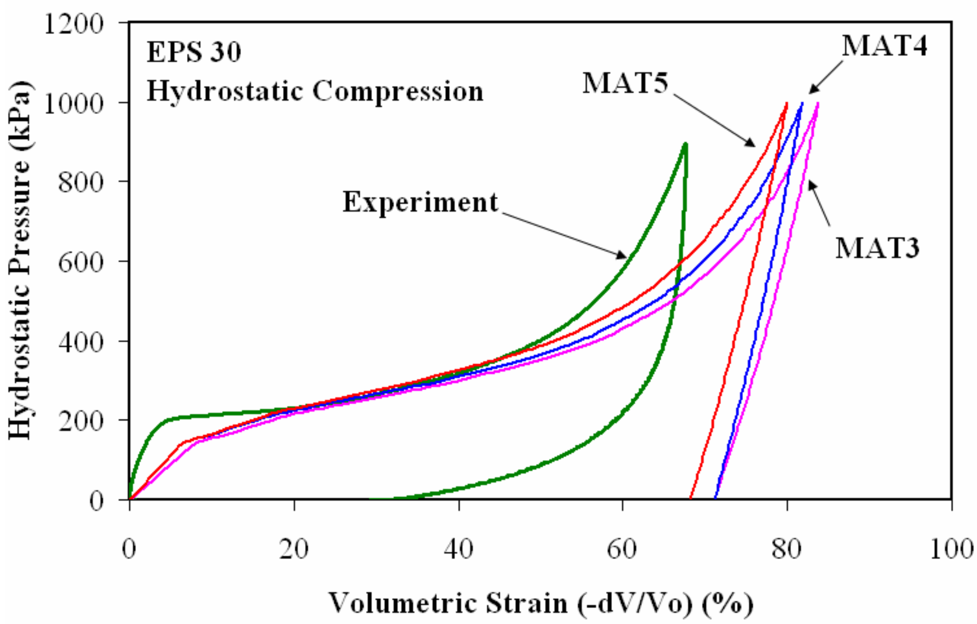

Figure 5.23. Hydrostatic pressure versus volumetric strain for hydrostatic compression test and simulations of EPS 30 (compression direction is taken as positive)

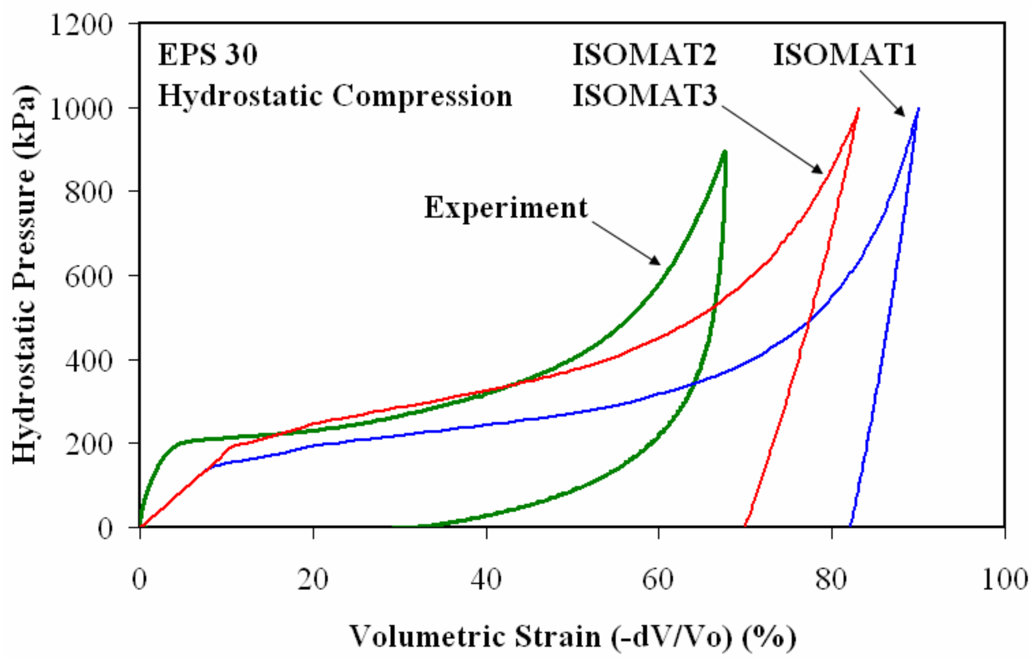

Figure 5.24. Hydrostatic pressure versus volumetric strain for hydrostatic compression test and simulations of EPS 30 (compression direction is taken as positive)

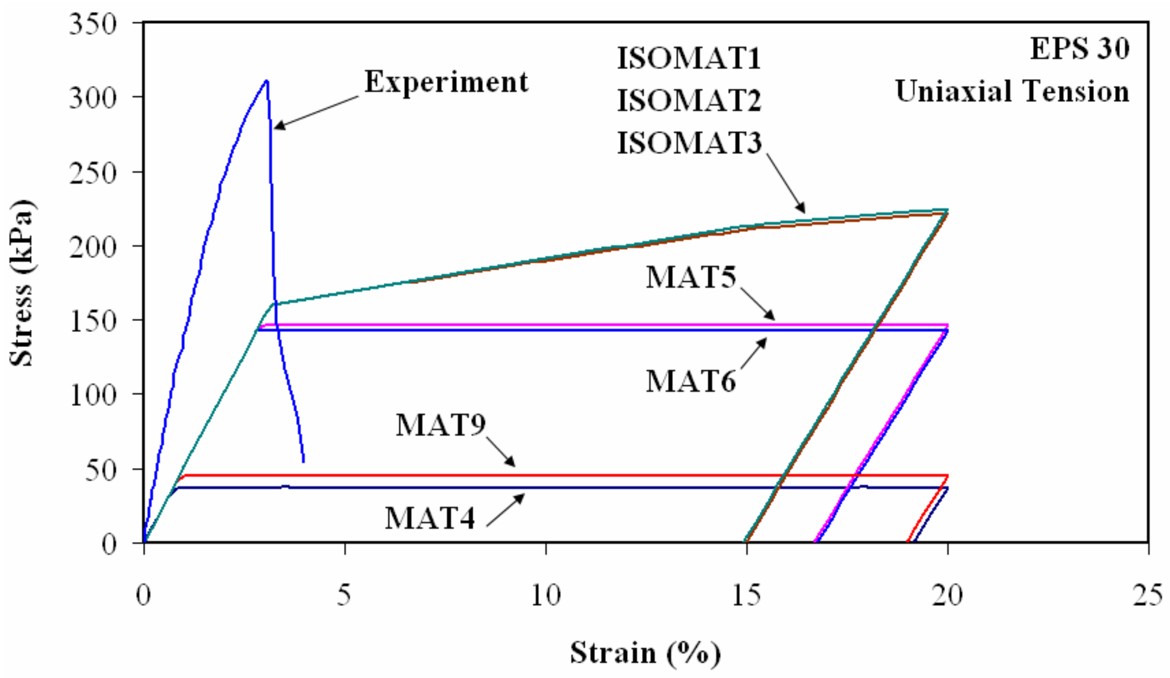

Figure 5.25. Stress versus strain for uniaxial tension test and simulations of EPS 30

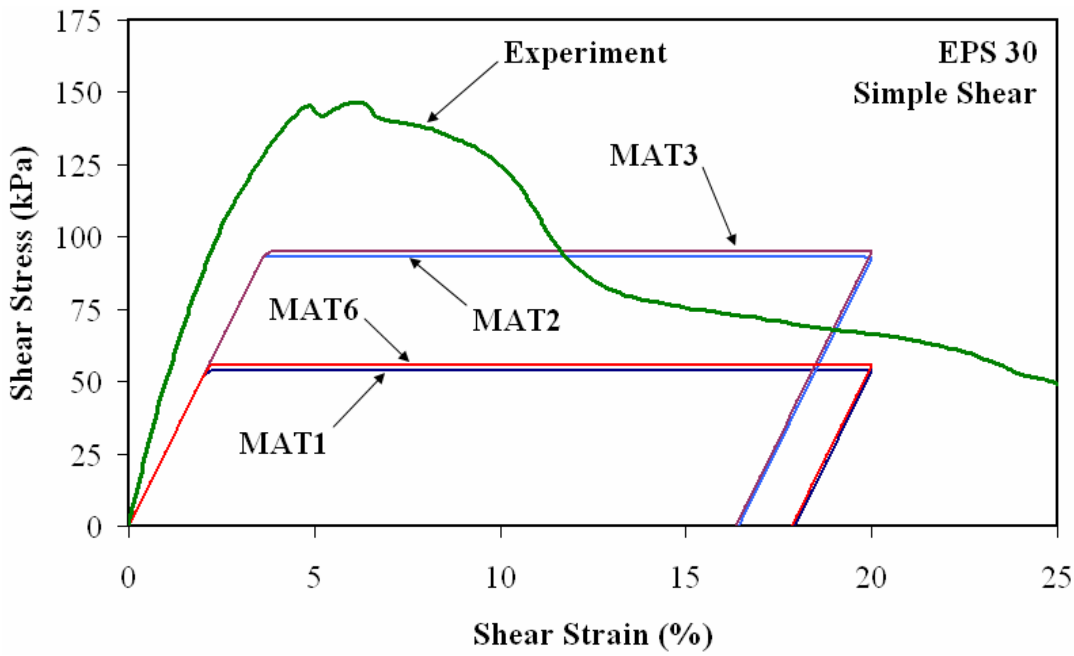

Figure 5.26. Stress versus strain for simple shear test and simulations of EPS 30

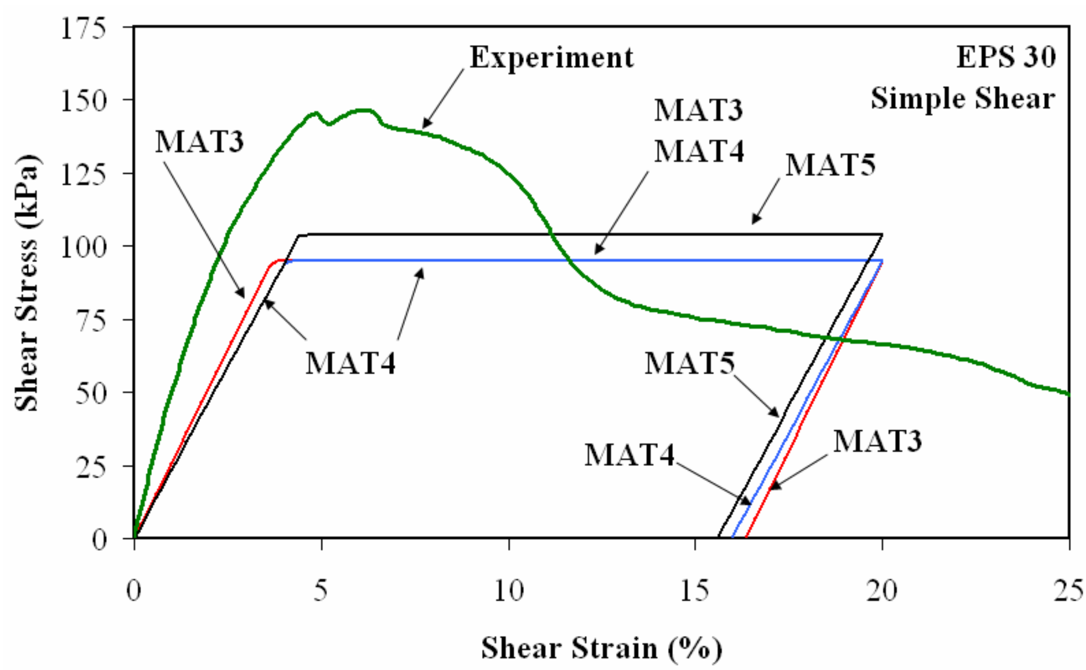

Figure 5.27. Stress versus strain for simple shear test and simulations of EPS 30

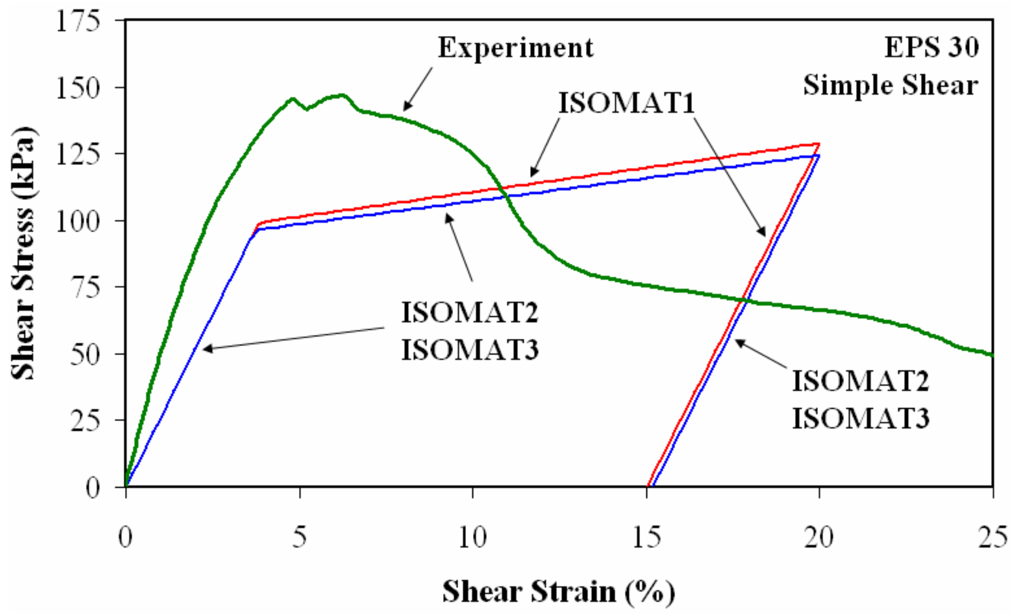

Figure 5.28. Stress versus strain for simple shear test and simulations of EPS 30

In Figures 5.29 and 5.30, force versus displacement results for cylinder indentation simulations are given for different constants given in Tables 5.1 and 5.2 respectively for EPS 30. Force response of foam is decreased when fracture starts during indentation. In FE simulation, fracture cannot be modeled for crushable foam materials, therefore there is not such a decrease in force response. Although fracture cannot be modeled in FE simulations, results are much better than the hydrostatic compression, uniaxial tension, and simple shear loading cases. This is mainly due to the fact that compression is the dominant loading mode in indentation. Contributions of other loading modes to the overall response are negligible for indentation. Deformation pattern of the cylinder indentation test for EPS 30-ISOMAT1 material given in Figure 5.31 is similar to the experiments. In Figures 5.32 and 5.33, force versus displacement results for block indentation simulations are given for different constants given in Tables 5.1 and 5.2 respectively for EPS 30. In block indentation tests, fracture occur in the very beginning of the test, therefore decrease in force response due to fracture is not remarkable from the force–displacement curve as it is in cylinder indentation test. Isotropic hardening materials give better results compared to volumetric hardening. Deformation pattern of the block indentation test for EPS 30-ISOMAT1 material given in Figure 5.34 is not similar to the one observed in experiments because fracture in foam cannot be modeled in FE simulation by Abaqus. Both in cylinder and block indentation simulations, unloading path is linear, and residual strain is not calculated correctly. Reloading path follows the unloading one without any hysteresis. Therefore absorbed energy in reloading is not calculated correctly with available material models.

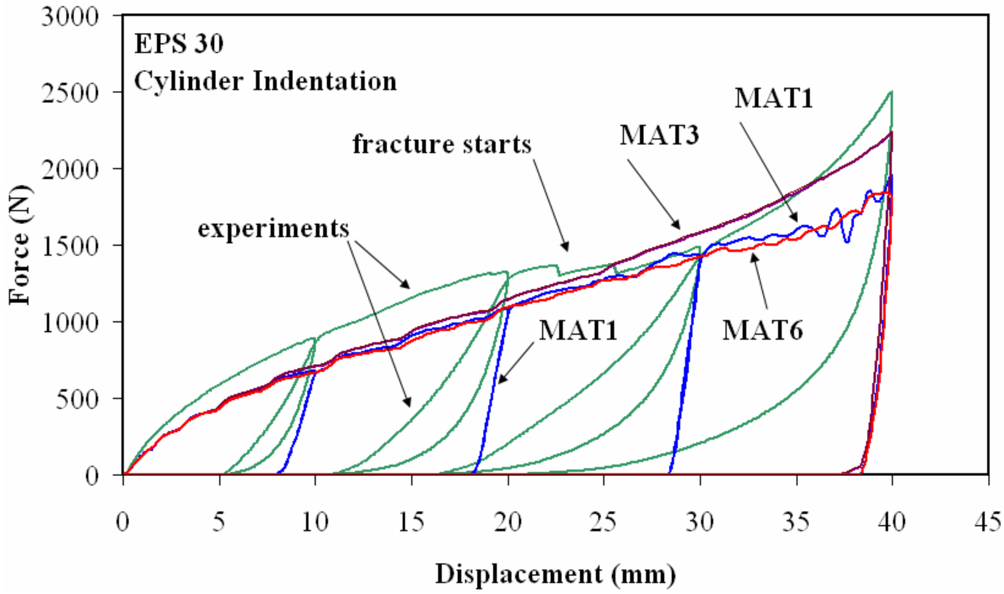

Figure 5.29. Force versus displacement for cylinder indentation test and simulations of EPS 30 (compression direction is taken as positive)

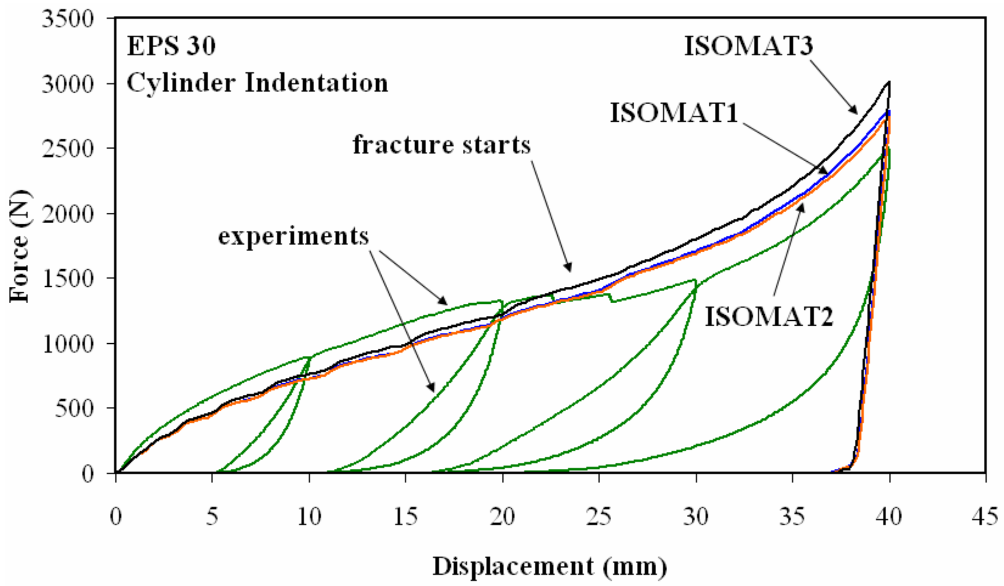

Figure 5.30. Force versus displacement for cylinder indentation test and simulations of EPS 30 (compression direction is taken as positive)

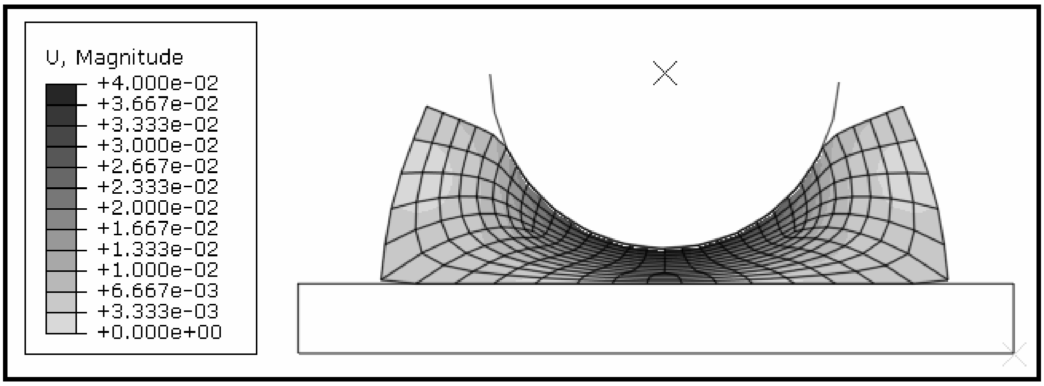

Figure 5.31. Deformation pattern for cylinder indentation (EPS 30–ISOMAT1 material)

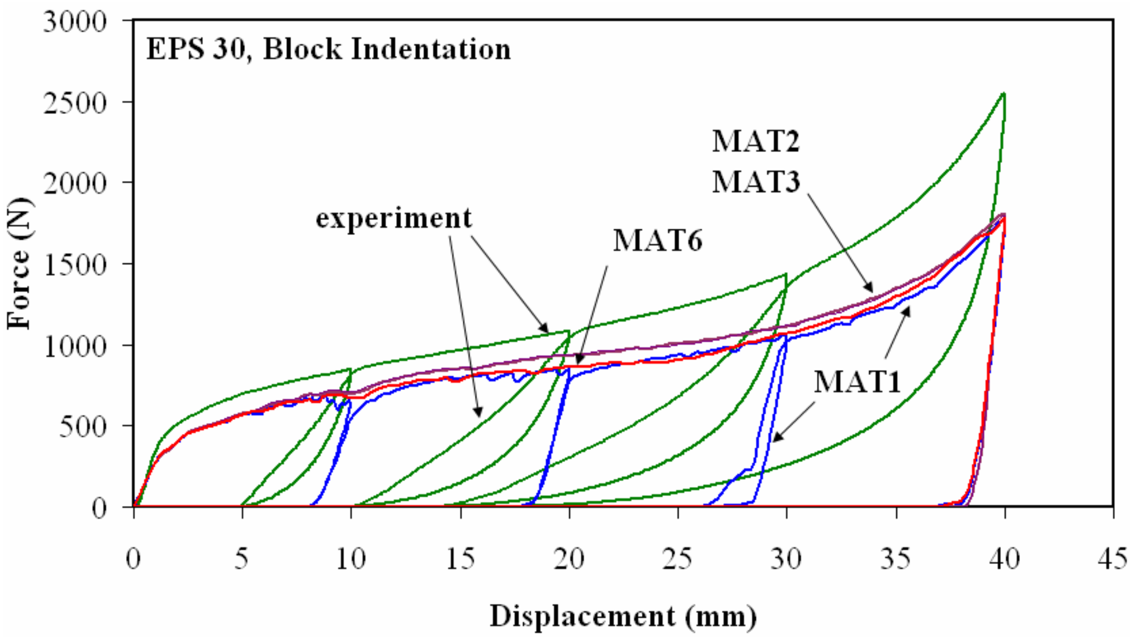

Figure 5.32. Force versus displacement for block indentation test and simulations of EPS 30 (compression direction is taken as positive)

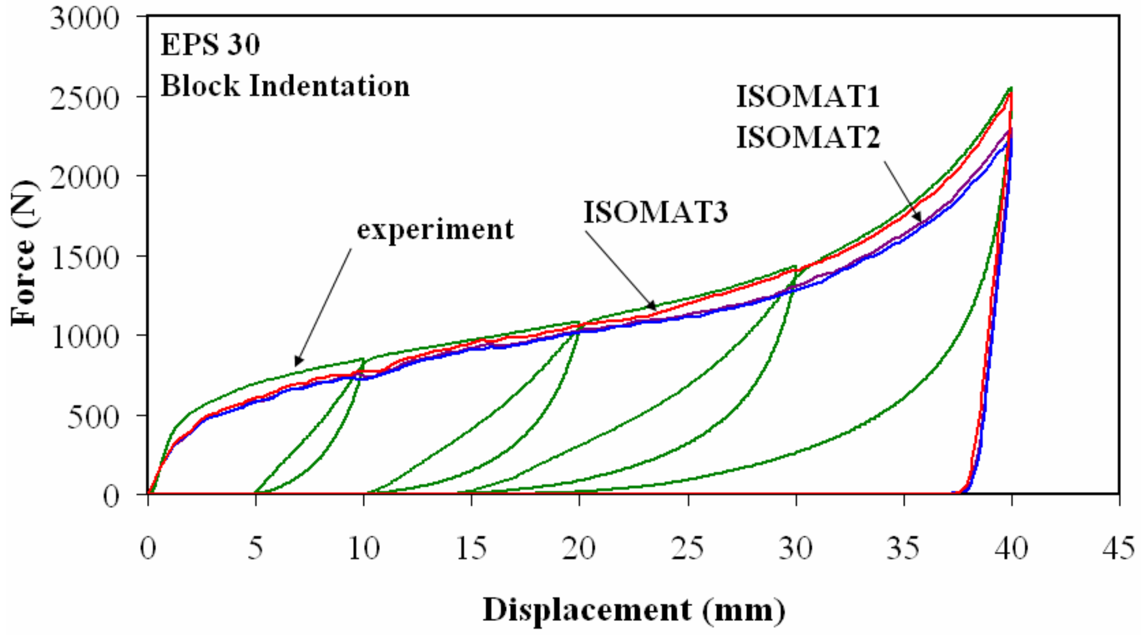

Figure 5.33. Force versus displacement for block indentation test and simulations of EPS 30 (compression direction is taken as positive)

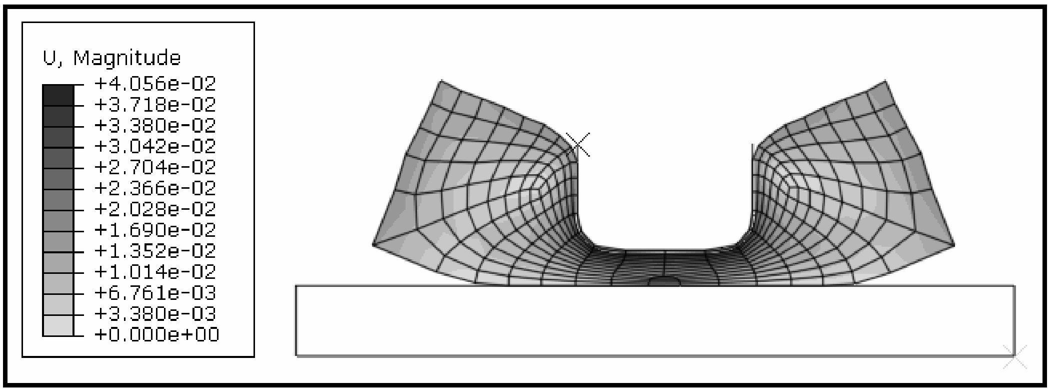

Figure 5.34. Deformation pattern for block indentation (EPS 30–ISOMAT1 material)

5.3.4. Finite Element Simulation Results for Different Material Parameters of PE 58

Results of FE simulations for uniaxial compression are given in Figure 5.35 for materials constants given in Tables 5.3 and 5.4 for PE 58. All PE 58 materials used in FE simulations have zero elastic and plastic Poisson's ratios, and all of the stress–strain curves for different materials coincide with experimental data. Unloading path is linear in crushable foam model and is very different from the measured unloading path. Hydrostatic compression, uniaxial tension, and simple shear results are given in Figures 36–42 for PE 58, and the results are similar to EPS 30 results. There is no hardening for volumetric hardening, linear hardening occur in isotropic hardening, and the yield stress values are much lower than the measured ones.

In Figures 5.43 and 5.44, force versus displacement for cylinder indentation simulations are given for different constants given in Tables 5.3 and 5.4 respectively for PE 58. Fracture does not occur in cylinder and block indentation tests with PE 58 as seen for EPS 30. Force versus displacement responses for materials with isotropic hardening are very close to those obtained in experiments. Deformation pattern in the cylinder indentation test for PE 58-ISOMAT1 material given in Figure 5.45 is similar to the one observed in experiments. In Figures 5.46 and 5.47, force versus displacement plots for block indentation simulations are given for different constants given in Tables 5.3 and 5.4 respectively for PE 58. Similar to cylinder indentation tests, materials defined with isotropic hardening give better results compared to those with volumetric hardening. Deformation pattern in the block indentation test for PE 58-ISOMAT1 material given in Figure 5.48 is similar to the one observed in experiments. Similar to EPS 30 materials, both in cylinder and indentation simulations, unloading path is linear and, residual strain is not calculated correctly. Load-displacement curve in reloading follows the linear unloading path without any hysteresis. Therefore absorbed energy in reloading is not calculated correctly with available material models for low density polymeric foams.

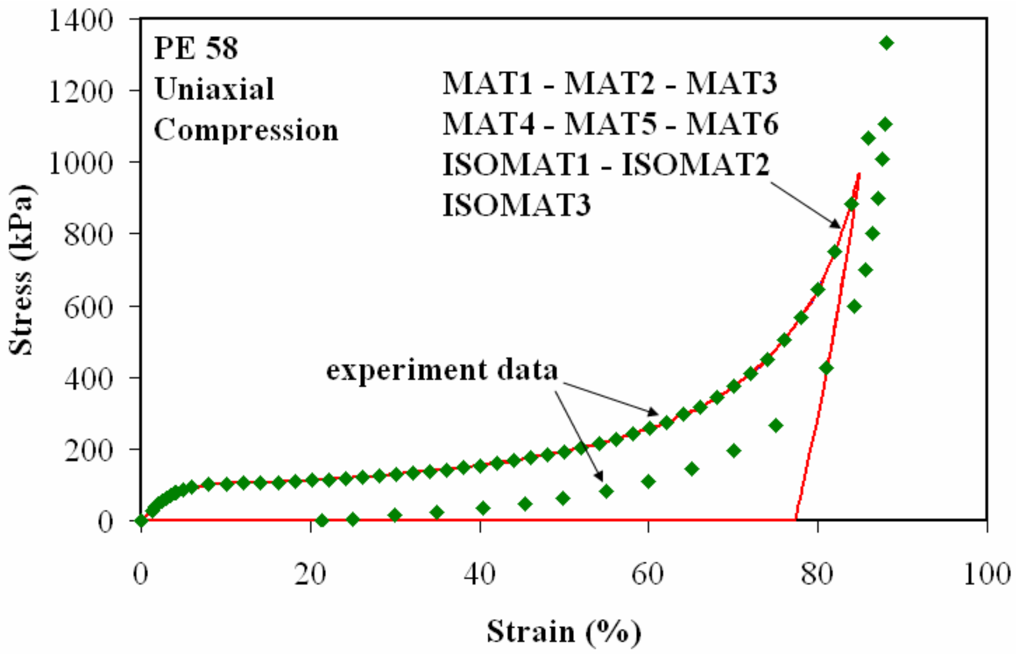

Figure 5.35. Stress versus strain for uniaxial compression test and simulations of PE 58 (compression direction is taken as positive)

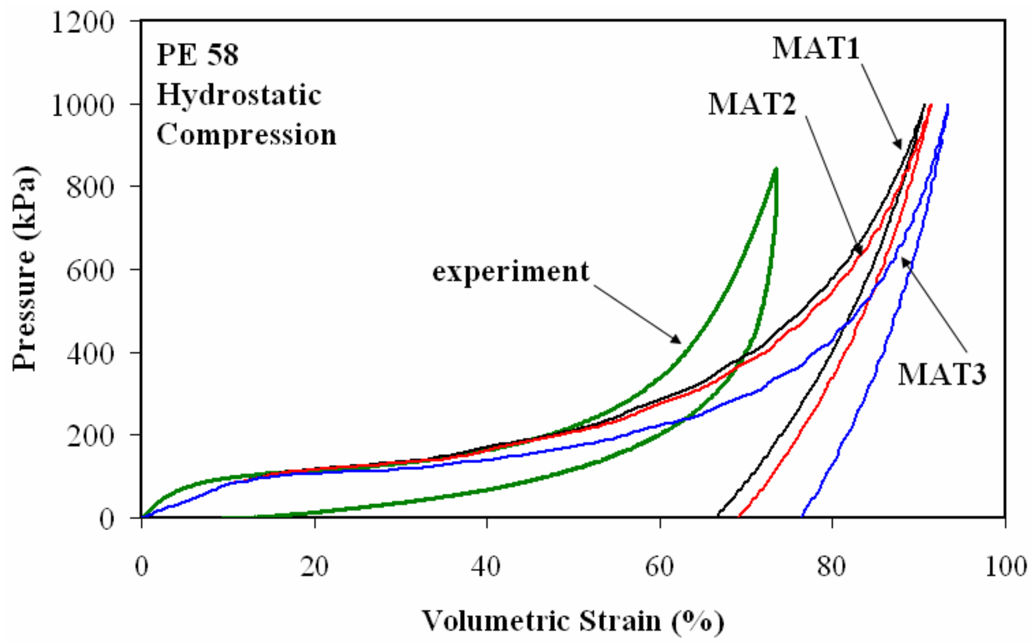

Figure 5.36. Hydrostatic pressure versus volumetric strain for hydrostatic compression test and simulations of PE 58 (compression direction is taken as positive)

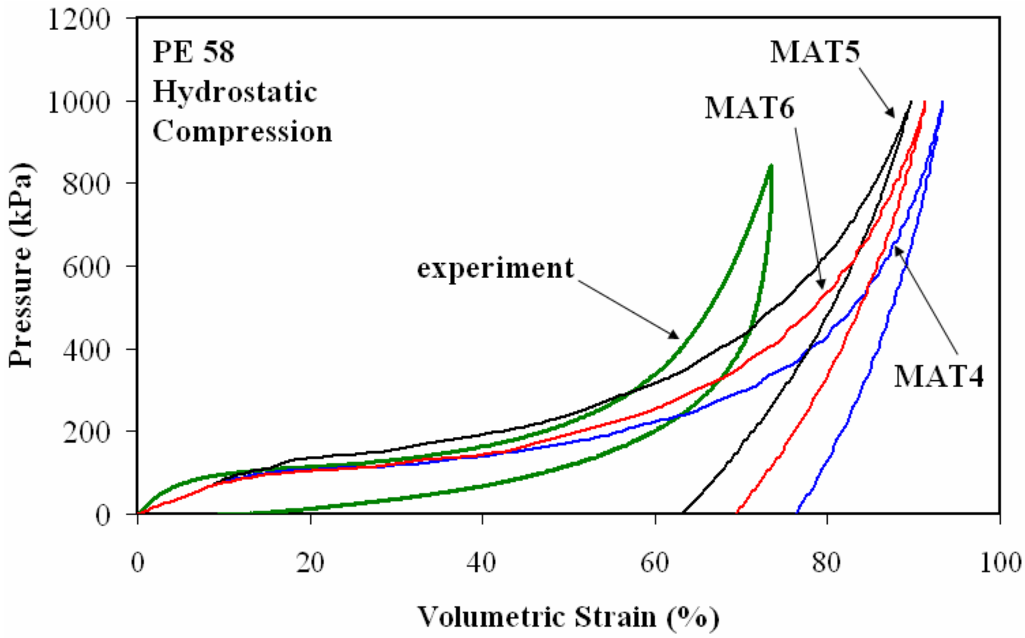

Figure 5.37. Hydrostatic pressure versus volumetric strain for hydrostatic compression test and simulations of PE 58 (compression direction is taken as positive)

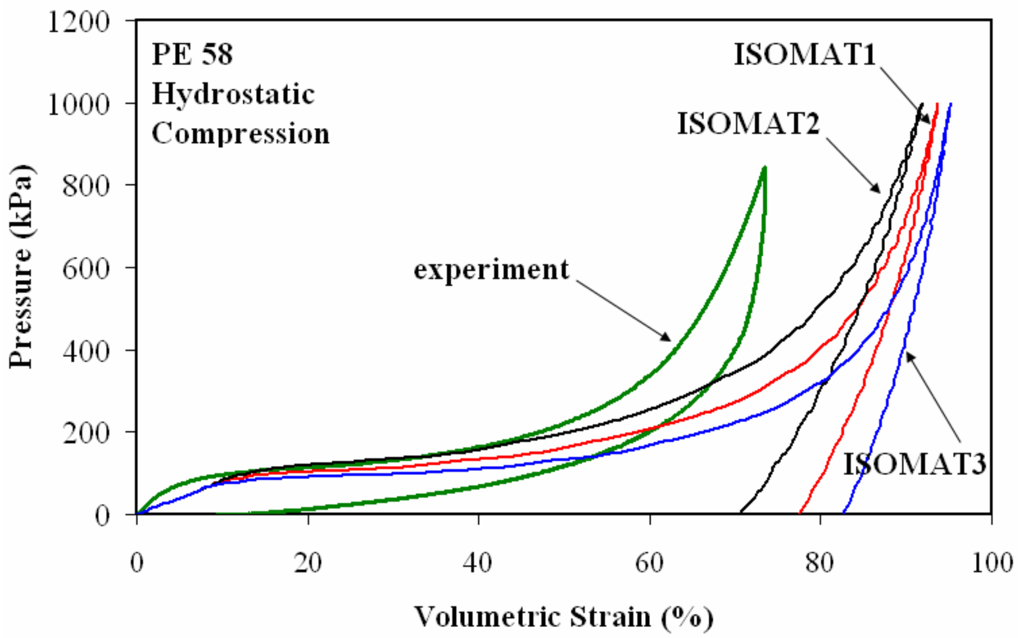

Figure 5.38. Hydrostatic pressure versus volumetric strain for hydrostatic compression test and simulations of PE 58 (compression direction is taken as positive)

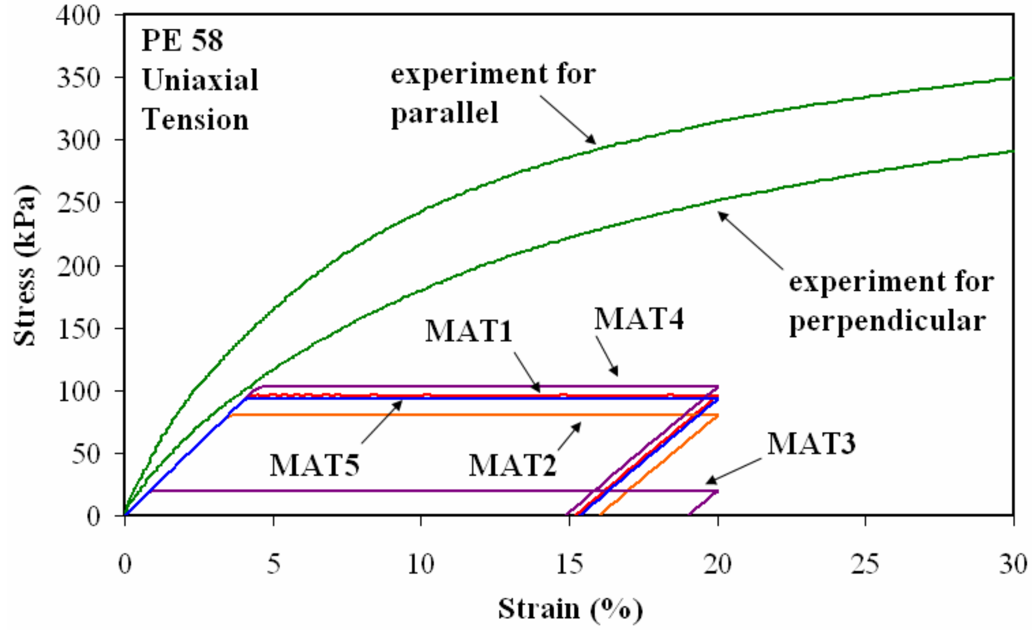

Figure 5.39. Stress versus strain for uniaxial tension test and simulations of PE 58

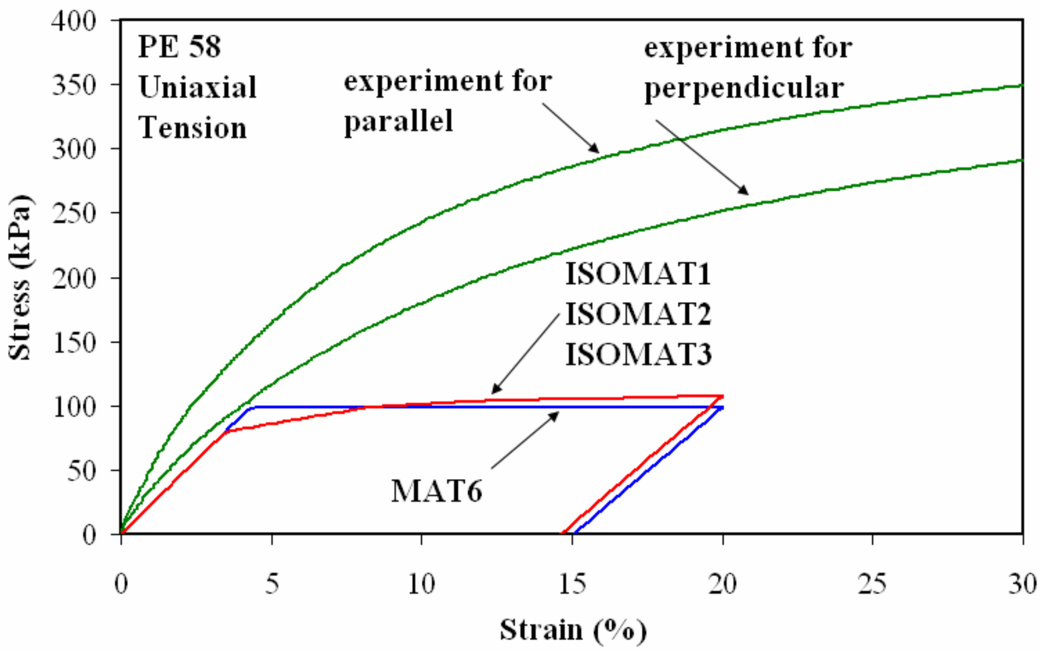

Figure 5.40. Stress versus strain for uniaxial tension test and simulations of PE 58

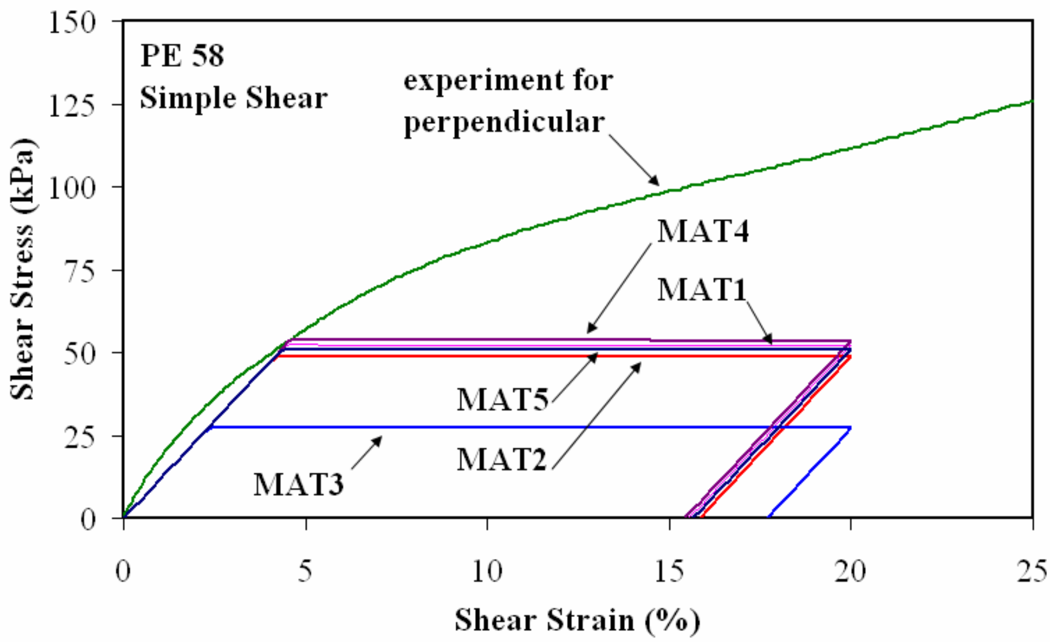

Figure 5.41. Stress versus strain for simple shear test and simulations of PE 58

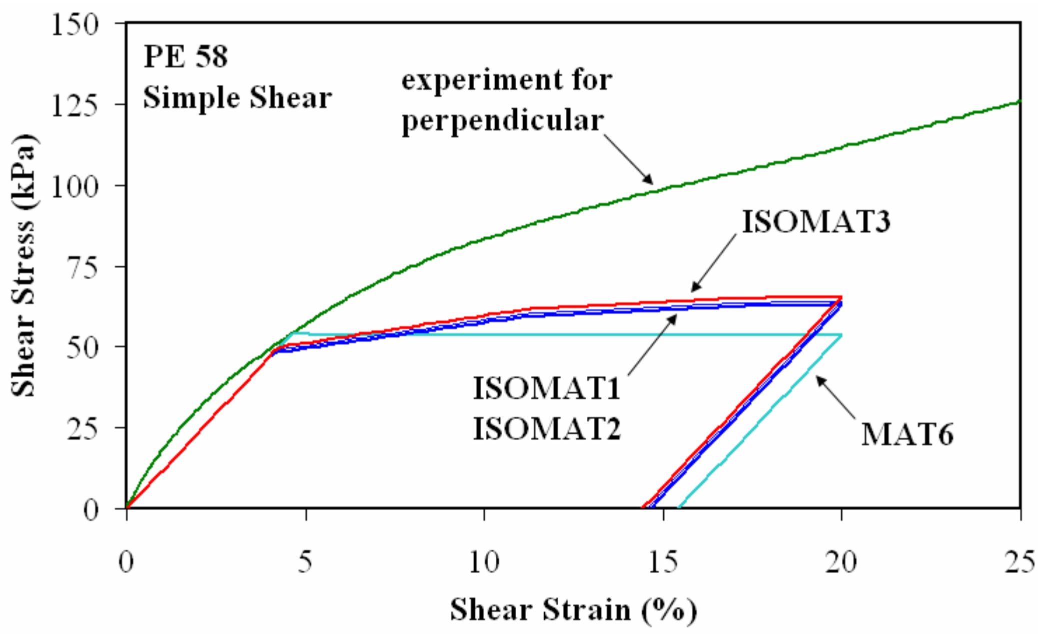

Figure 5.42. Stress versus strain for simple shear test and simulations of PE 58

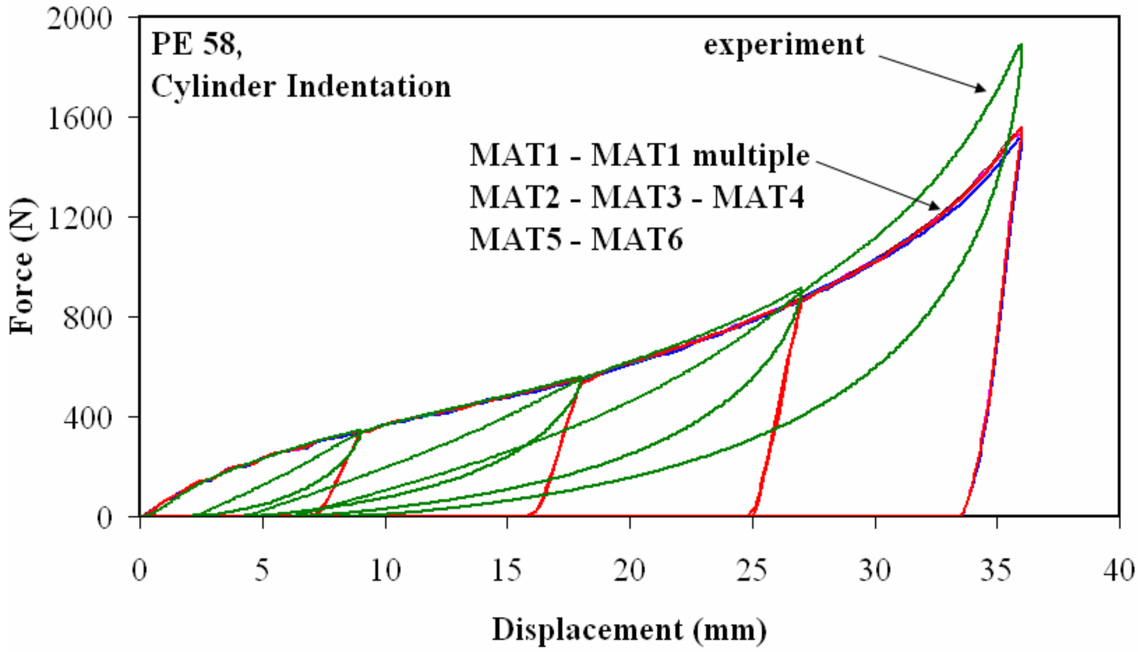

Figure 5.43. Force versus displacement for cylinder indentation test and simulations of PE 58 (compression direction is taken as positive)

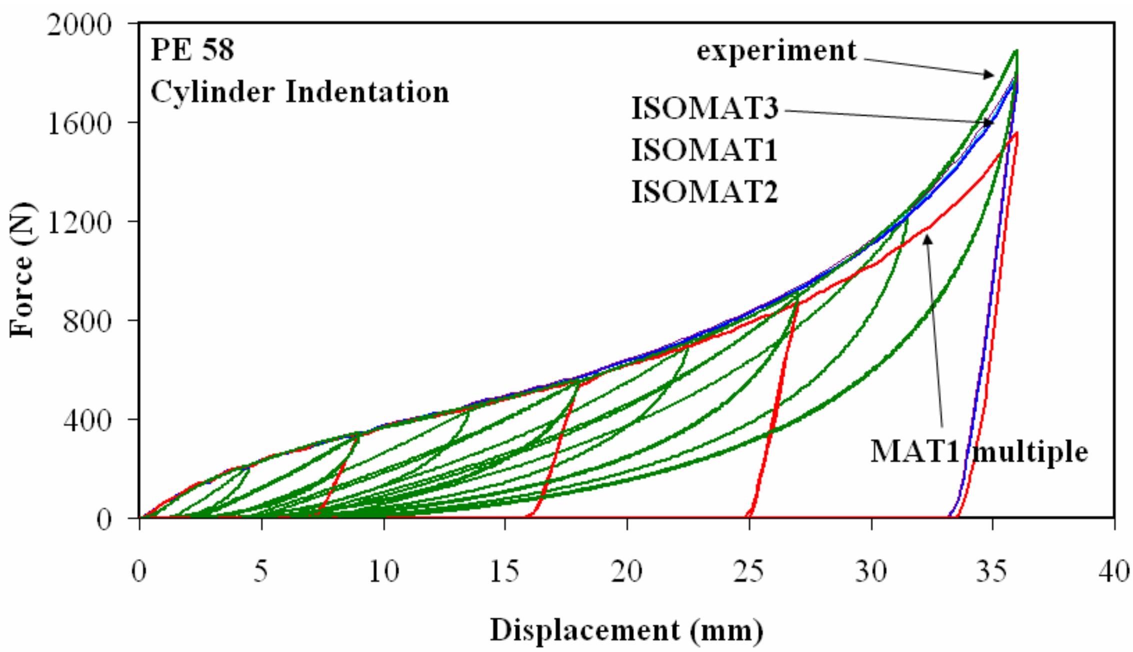

Figure 5.44. Force versus displacement for cylinder indentation test and simulations of PE 58 (compression direction is taken as positive)

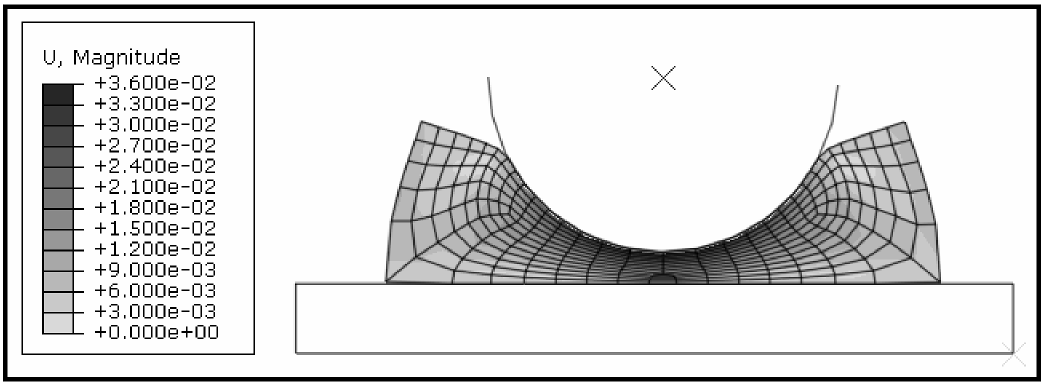

Figure 5.45. Deformation pattern for cylinder indentation (PE 58–ISOMAT1 material)

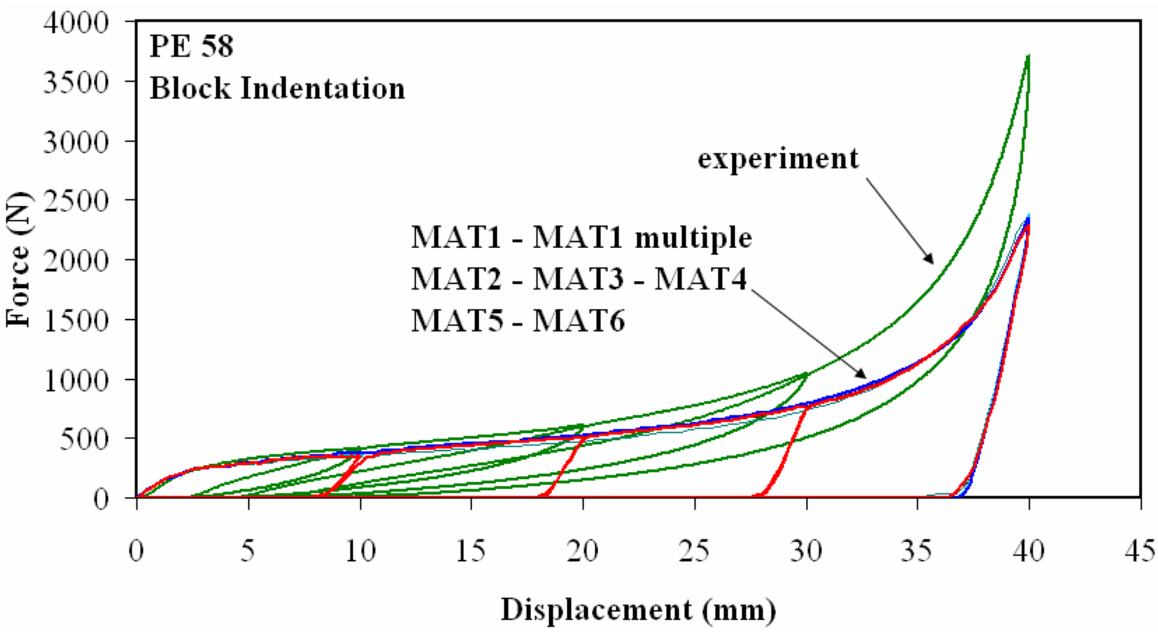

Figure 5.46. Force versus displacement for block indentation test and simulations of PE 58 (compression direction is taken as positive)

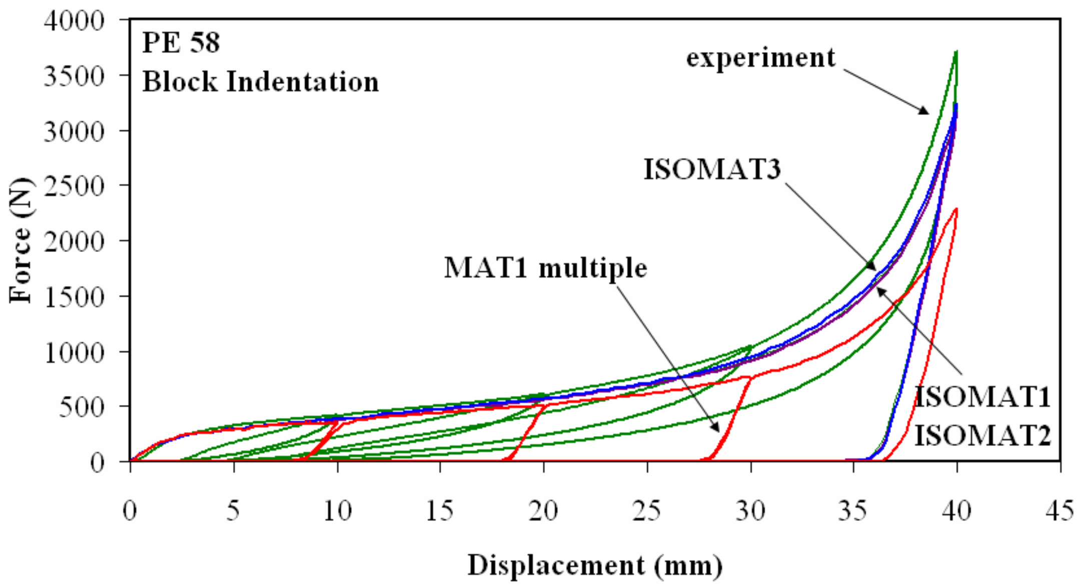

Figure 5.47. Force versus displacement for block indentation test and simulations of PE 58 (compression direction is taken as positive)

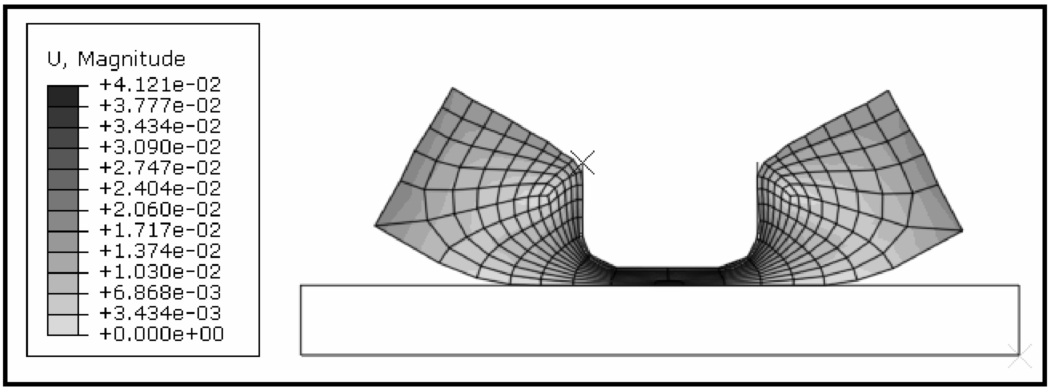

Figure 5.48. Deformation pattern for block indentation (PE 58–ISOMAT1 material)

6. SUMMARY AND CONCLUSIONS

In this study, mechanical behavior and energy absorption characteristics of low density polymeric foams under multiple loading and unloading are investigated for uniaxial and hydrostatic compression, uniaxial tension, simple shear, and block and cylinder indentation.

Constitutive models and energy absorption diagrams available in literature for uniaxial compressive loading are reviewed for multiple loading and unloading of EPS 30 and PE 58 foams. It is shown by uniaxial compression tests performed at Zwick Z020 universal tensile testing machine that for certain amount absorbed energy, reaction forces and deformations on the foam can increase multiple times when compared to single loading depending on the residual strain level occurred in previous loadings. Constitutive models available in literature for uniaxial compression have been developed for single loading only, unloading have not been modeled, and they have not been validated for reloading. A new phenomenological constitutive model for accurate calculation of load, deformation, and absorbed energy is proposed for multiple compressive loading and unloading. The proposed model is more appropriate than the existing ones for stress, strain, and energy absorption calculations in multiple compressive loading and unloading. A design procedure using the new proposed model for foams that are subjected to multiple compressive loading and unloading is presented.

A drop test rig is built for measuring compressive behavior of foams at high loading speed. Compression tests are successfully performed at the drop test rig, and the results are presented for EPS 30 and PE 58 foams. Speeds of the falling weight reached 1.57 m/s and 1.33 m/s at the beginning of the loading of EPS 30 and PE 58 specimens respectively from 1446 mm drop height. It is shown that the responses of EPS 30 in drop tests and in compression tests evaluated using Zwick Z020 are almost identical. In the case of PE 58 however, higher stress is obtained for the same level of strain in drop tests.

There are no available data in literature for multiple loading and unloading behavior of foams under hydrostatic compression, uniaxial tension, simple shear, and cylinder and block indentation. A hydrostatic compression test rig is built to study mechanical behavior of foams under multiple loading and unloading, and stress-strain results are presented for EPS 30 and PE 58. Similarly, tools to be used with Zwick Z020 universal tensile testing machine are prepared for uniaxial tension, simple shear, and cylinder and block indentation tests. Stress–strain results are presented for uniaxial compression, uniaxial tension, and simple shear of EPS 30 and PE 58 under multiple loading and unloading for loading in directions vertical, perpendicular, and parallel to extrusion directions of foam sheet. There is not a difference in stress-strain response of EPS 30 when tested in parallel and perpendicular directions under uniaxial compression, uniaxial tension, simple shear, and hydrostatic compression. However, a lower stress is obtained for the same strain level when testing EPS 30 in vertical loading direction. This is a result of expansion molding induced anisotropy. For PE 58, stress level obtained for the same strain level is much higher in parallel direction compared to the perpendicular direction for uniaxial compression, uniaxial tension, and hydrostatic compression. There is not much difference in stress-strain response for PE 58 when tested in perpendicular and vertical loading directions. PE 58 is extruded, and similarly, it is not isotropic.

Uniaxial compression, uniaxial tension, and hydrostatic compression test results are used as input parameters in finite element simulations. Simulations of uniaxial and hydrostatic compression, uniaxial tension, simple shear, and cylinder and block indentation tests are performed for EPS 30 and PE 58 materials using a broad range of parameters for crushable foam material model with volumetric and isotropic hardening. It is shown that the available finite element material model gives successful results for modeling of cylinder and block indentations of PE 58 where compression is the dominant loading mode and foam is not broken. Fracture of foam that occurs in cylinder and block indentation tests of EPS 30 cannot be modeled using Abaqus. In Abaqus, there is no hardening for uniaxial tension and simple shear loading cases in volumetric hardening, and only linear hardening is available in isotropic hardening, although nonlinear hardening is observed in experiments. Yield stress values calculated by Abaqus for uniaxial tension and simple shear loadings are much lower than the measured ones. However, the load-displacement response is successfully predicted by finite element simulations for single loading because compression is the dominant loading mode for cylinder and block indentation cases. The effect of shear and tension on results is negligible. In cases other than uniaxial compression and indentation, simulation results are not reliable. Unloadings for all loading cases are modeled as linear elastic without any hysteresis effect. Residual deformation and the energy released from foam during unloading are not calculated correctly. Load-displacement curve in reloading follows the same linear path as unloading. Therefore finite element material models available in Abaqus are not appropriate for multiple loading and unloading simulations of low density polymeric foams.

In the future, failure criteria for crushable foam models used in Abaqus should be improved for hardening in tension and shear. Fracture of foam should be modeled to make successful simulations of crushable foam materials. Modeling of unloading and reloading behavior should be improved to include nonlinear and hysteresis effects. Anisotropy of foam should be considered, and orthotropic and anisotropic foam material models should be implemented.

APPENDIX A: STRESS AND STRAIN REACHED AT THE END OF EACH LOADING FOR DIFFERENT ABSORBED ENERGY LEVELS OF EPS AND PE FOAMS

Table A.1. Stress and strain reached at the end of each loading for different absorbed energy levels for EPS 12 (unit of work, W, is kJ / cm^3)

	W= 3.71		W= 7.58		W= 15.3		W= 23.1		W= 30.9	
loading #	strain [%]	stress [kPa]	strain [%]	stress [kPa]	strain [%]	stress [kPa]	strain [%]	stress [kPa]	strain [%]	stress [kPa]
1	11.8	53	17.3	69	28.3	88	35.2	108	41.9	127
2	14.7	59	22.7	78	37.2	107	46.2	139	53.9	170
3	16.5	61	25.4	83	41.7	117	51.6	157	59.3	193
4	17.5	62	27.4	87	44.6	123	54.7	168	62.6	209
5	18.4	63	28.7	88	46.7	128	57.0	176	65.0	221
6	18.9	63	29.6	88	48.4	131	58.9	183	66.7	229
7	19.4	63	30.7	91	49.9	135	60.1	186	68.4	240
8	20.1	65	31.6	92	51.0	135	61.4	192	69.8	248
9	20.5	64	32.0	90	52.1	138	62.5	196	71.0	255
10	20.9	65	32.7	92	52.9	139	63.6	200	72.1	261

	W= 38.6		W= 46.0		W= 53.8		W= 61.5		W= 69.9	
loading #	strain [%]	stress [kPa]	strain [%]	stress [kPa]	strain [%]	stress [kPa]	strain [%]	stress [kPa]	strain [%]	stress [kPa]
1	47.1	148	55.9	171	57.4	190	60.9	215	64.4	240
2	60.0	206	68.2	250	70.5	289	73.7	339	77.1	395
3	65.4	240	73.5	300	75.8	354	78.8	423	81.9	503
4	68.7	264	76.9	340	78.8	399	81.6	486	84.6	586
5	71.0	282	79.3	374	80.9	440	83.8	549	86.5	670
6	72.6	294	81.3	413	82.6	476	85.2	597	-	-
7	74.2	309	82.8	445	84.0	512	86.5	655	-	-
8	75.5	321	84.3	484	85.1	545	87.7	721	-	-
9	76.5	332	85.6	529	86.1	574	-	-	-	-
10	77.7	347	86.6	568	-	-	-	-	-	-

	W= 77.6		W= 92.6		W= 109.4		W= 126.4	
loading #	strain [%]	stress [kPa]	strain [%]	stress [kPa]	strain [%]	stress [kPa]	strain [%]	stress [kPa]
1	67.6	269	72.1	326	77.8	411	80.4	504
2	79.8	460	83.9	606	88.0	819	89.6	1078
3	84.4	600	87.9	819	91.3	1148	-	-
4	86.9	714	90.2	1016	-	-	-	-
5	88.6	821	91.7	1218	-	-	-	-

Table A.2. Stress and strain reached at the end of each loading for different absorbed energy levels for EPS 20 (unit of work, W, is kJ / cm^3)

	W= 3.41		W= 6.91		W= 15.2		W= 22.5		W= 30.8	
loading #	strain [%]	stress [kPa]	strain [%]	stress [kPa]	strain [%]	stress [kPa]	strain [%]	stress [kPa]	strain [%]	stress [kPa]
1	5.92	103	9.8	114	16.3	129	22.0	141	27.3	153
2	7.28	107	13.1	122	23.3	142	32.1	161	39.6	182
3	8.16	108	15.3	127	28.0	151	38.1	176	46.9	206
4	8.72	107	17.2	130	31.1	158	42.3	188	50.9	222
5	9.28	108	18.4	131	33.7	164	44.9	196	53.7	233
6	9.76	109	19.5	133	35.4	167	46.7	200	55.6	241
7	10.2	109	20.2	132	36.8	169	48.3	205	56.8	244
8	10.4	106	22.9	132	38.0	172	49.6	209	58.0	250
9	10.8	109	23.2	132	38.8	172	50.1	201	58.9	253
10	10.9	104	23.4	133	39.6	173	51.4	213	59.7	254

	W= 38.5		W= 45.7		W= 53.9		W= 61.8		W= 69.5	
loading #	strain [%]	stress [kPa]	strain [%]	stress [kPa]	strain [%]	stress [kPa]	strain [%]	stress [kPa]	strain [%]	stress [kPa]
1	31.8	165	36.5	176	41.0	189	45.4	202	48.7	218
2	46.1	206	51.6	230	57.2	261	62.4	294	65.9	333
3	53.4	238	59.2	273	64.4	315	69.2	358	72.1	411
4	57.6	261	63.0	299	67.9	347	72.6	399	75.1	459
5	60.0	274	65.4	318	70.2	371	74.6	425	77.1	494
6	61.6	283	67.0	330	71.8	388	76.2	448	78.6	525
7	63.0	290	67.9	325	72.9	399	77.3	465	79.8	553
8	64.1	296	69.5	350	73.9	410	78.3	480	80.9	581
9	64.9	299	70.2	350	74.9	424	79.3	500	81.7	599
10	65.6	300	71.3	367	75.6	429	80.1	516	82.4	620

	W= 76.9		W= 92.6		W= 107.8		W= 123.6		W= 138.8	
loading #	strain [%]	stress [kPa]	strain [%]	stress [kPa]	strain [%]	stress [kPa]	strain [%]	stress [kPa]	strain [%]	stress [kPa]
1	52.7	234	59.3	273	64.5	317	68.3	369	73.3	430
2	69.7	374	75.4	473	79.8	587	82.6	740	86.3	908
3	75.6	468	80.7	609	84.5	774	86.7	1001	90.1	1265
4	78.5	528	83.3	698	86.8	905	88.8	1199	91.8	1512
5	80.4	573	84.9	769	88.3	1017	90.1	1360	93.0	1734
6	81.8	609	86.3	842	89.5	1129	91.1	1500	-	-
7	83.0	652	87.3	897	90.4	1225	-	-	-	-
8	84.0	688	88.2	966	-	-	-	-	-	-
9	84.7	703	-	-	-	-	-	-	-	-
10	85.5	742	-	-	-	-	-	-	-	-

Table A.2. Continued

	W= 153.5		W= 172.2	
loading	strain	stress	strain	stress
#	[%]	[kPa]	[%]	[kPa]
1	75.9	502	79.6	585
2	87.9	1125	90.5	1364
3	90.9	1533	93.4	1935
4	92.7	1929	-	-

Table A.3. Stress and strain reached at the end of each loading for different absorbed energy levels for EPS 30 (unit of work, W, is kJ / cm^3)

	W= 2.98		W= 6.80		W= 14.5		W= 22.5		W= 30.3	
loading	strain	stress	strain	stress	strain	stress	strain	stress	strain	stress
#	[%]	[kPa]	[%]	[kPa]	[%]	[kPa]	[%]	[kPa]	[%]	[kPa]
1	4.22	195	6.62	206	10.0	229	12.9	240	15.7	254
2	4.52	178	8.08	215	13.9	245	19.1	261	24.0	279
3	4.80	181	9.28	220	16.7	256	23.8	275	30.2	297
4	5.02	182	10.2	222	23.0	275	27.6	287	35.1	312
5	5.16	176	10.9	219	23.7	271	30.7	296	39.3	327
6	5.28	174	11.6	228	25.0	279	33.3	304	42.4	338
7	5.50	180	12.2	227	26.0	282	35.6	311	45.1	349
8	5.58	176	12.8	227	27.0	283	37.3	316	47.1	358
9	5.60	171	13.0	218	27.9	286	39.0	322	49.1	368
10	5.76	176	13.5	223	28.8	290	40.4	326	50.6	374

	W= 38.1		W= 46.0		W= 53.8		W= 60.5		W= 69.1	
loading	strain	stress	strain	stress	strain	stress	strain	stress	strain	stress
#	[%]	[kPa]	[%]	[kPa]	[%]	[kPa]	[%]	[kPa]	[%]	[kPa]
1	18.8	268	22.4	266	25.3	277	27.4	292	31.7	287
2	28.5	298	34.7	301	39.2	319	42.3	341	48.6	348
3	36.1	321	43.6	332	48.9	360	52.8	397	59.5	422
4	41.9	343	50.0	363	55.7	402	59.6	453	66.1	494
5	46.5	364	54.9	393	60.3	440	64.3	506	70.0	552
6	49.9	383	58.1	417	63.6	473	67.2	546	72.7	600
7	52.7	399	60.7	440	66.0	500	69.4	580	74.7	644
8	54.8	413	62.7	457	67.7	521	71.1	613	76.1	672
9	56.6	426	64.2	471	69.1	539	71.8	555	77.4	704
10	58.0	437	65.4	483	70.4	558	73.9	666	78.6	745

Table A.3. Continued

	W= 76.7		W= 84.4		W= 91.9		W= 106.6		W= 122.8	
loading #	strain [%]	stress [kPa]	strain [%]	stress [kPa]	strain [%]	stress [kPa]	strain [%]	stress [kPa]	strain [%]	stress [kPa]
1	32.9	306	36.5	307	38.3	320	48.7	319	52.6	349
2	50.9	381	55.5	399	58.2	430	69.4	508	73.1	611
3	61.8	473	66.5	517	69.1	574	77.9	716	80.8	894
4	68.3	564	72.5	628	74.7	708	82.0	891	84.4	1134
5	72.1	640	75.9	720	77.9	815	84.5	1033	86.7	1351
6	74.7	706	78.3	797	80.1	911	86.1	1157	88.2	1547
7	76.6	758	79.9	862	81.7	992	87.6	1298	89.4	1747
8	78.0	806	81.3	921	83.1	1087	88.7	1429	-	-
9	79.3	855	82.4	987	84.1	1147	89.5	1533	-	-
10	80.2	891	83.4	1047	85.2	1244	90.3	1667	-	-

	W= 139.5		W= 154.1		W= 170.9		W= 189.0		W= 202.7	
loading #	strain [%]	stress [kPa]	strain [%]	stress [kPa]	strain [%]	stress [kPa]	strain [%]	stress [kPa]	strain [%]	stress [kPa]
1	57.5	376	60.8	415	66.0	456	69.2	505	72.0	566
2	77.8	725	80.3	876	84.1	1060	86.3	1242	87.8	1493
3	84.7	1094	86.4	1363	89.3	1671	91.3	2031	92.1	2431
4	87.9	1416	89.3	1786	91.9	2223	-	-	-	-
5	89.9	1700	91.1	2195	-	-	-	-	-	-

	W= 219.1		W= 238.0		W= 253.8	
loading #	strain [%]	stress [kPa]	strain [%]	stress [kPa]	strain [%]	stress [kPa]
1	74.4	628	77.7	698	80.3	792
2	89.3	1749	91.5	2029	92.8	2404
3	93.3	2911	-	-	-	-

Table A.4. Stress and strain reached at the end of each loading for different absorbed energy levels for PE 24 (unit of work, W, is kJ / cm^3)

	W= 4,05		W= 8,21		W= 16,5		W= 24,8		W= 33,2	
loading #	strain [%]	stress [kPa]	strain [%]	stress [kPa]	strain [%]	stress [kPa]	strain [%]	stress [kPa]	strain [%]	stress [kPa]
1	19.9	36	29.2	49	43.1	77	51.9	107	60.6	136
2	23.4	40	34.1	57	48.5	92	57.1	129	65.5	165
3	24.6	40	35.1	58	49.7	94	58.3	133	66.4	170
4	25.5	41	36.0	60	50.4	97	58.4	133	67.1	175
5	25.5	41	36.4	60	50.7	97	59.2	137	67.3	175
6	25.9	41	36.9	61	51.0	98	59.2	136	67.6	176
7	26.4	42	36.9	60	51.3	98	59.9	140	67.8	178
8	26.4	41	37.4	62	51.4	98	59.7	138	68.1	180
9	26.7	42	37.6	62	51.6	99	59.6	137	68.0	178
10	26.7	41	37.6	62	51.5	98	59.8	138	68.2	180

	W= 41,3		W= 49,6		W= 57,7		W= 66,0		W= 82,0	
loading #	strain [%]	stress [kPa]	strain [%]	stress [kPa]	strain [%]	stress [kPa]	strain [%]	stress [kPa]	strain [%]	stress [kPa]
1	65.1	171	69.7	212	73.0	253	76.1	297	81.0	409
2	70.0	212	73.7	258	77.1	314	79.4	359	84.1	513
3	70.7	218	74.5	267	77.8	324	80.0	370	84.9	541
4	71.2	222	74.9	270	78.3	332	80.5	380	85.3	551
5	71.6	225	75.3	276	78.7	338	80.5	378	85.4	556
6	71.8	227	75.3	274	79.0	343	81.0	391	85.8	571
7	72.1	229	75.6	278	79.1	344	81.1	390	85.9	570
8	72.0	227	75.6	277	79.1	342	81.3	394	86.0	578
9	72.2	229	76.0	282	79.5	351	81.3	395	86.2	587
10	72.6	233	76.0	281	79.4	347	81.4	397	86.3	586

	W= 98,2		W= 114,0		W= 158,5		W= 174,3		W= 190,7	
loading #	strain [%]	stress [kPa]	strain [%]	stress [kPa]	strain [%]	stress [kPa]	strain [%]	stress [kPa]	strain [%]	stress [kPa]
1	85.1	529	88.0	679	90.4	932	90.3	1093	93.5	1388
2	87.5	649	89.9	820	92.3	1195	92.0	1376	94.8	1705
3	87.9	665	90.4	854	92.8	1261	92.3	1426	95.0	1753
4	88.1	673	90.7	883	93.0	1291	92.7	1509	95.2	1765
5	88.4	692	90.8	886	93.4	1377	92.7	1497	95.6	1909
6	88.6	704	90.9	888	93.4	1352	92.7	1486	95.5	1865
7	88.6	699	91.0	902	93.7	1403	93.1	1579	95.7	1900
8	88.8	709	91.2	918	93.8	1412	93.2	1612	95.8	1962
9	88.9	718	91.2	915	94.0	1471	93.3	1638	95.8	1925
10	89.0	719	91.4	931	94.0	1441	93.4	1663	96.0	2010

Table A.5. Stress and strain reached at the end of each loading for different absorbed energy levels for PE 32 (unit of work, W, is kJ / cm^3)

	W= 3,34		W= 6,85		W= 13,9		W= 20,9		W= 27,9	
loading #	strain [%]	stress [kPa]	strain [%]	stress [kPa]	strain [%]	stress [kPa]	strain [%]	stress [kPa]	strain [%]	stress [kPa]
1	11.3	53	17.3	62	28.2	74	37.1	90	43.9	110
2	13.1	55	21.0	65	35.0	86	44.6	110	51.8	138
3	14.1	55	23.0	67	37.3	90	47.0	117	54.1	146
4	14.7	55	23.8	67	38.7	93	48.2	120	55.1	150
5	15.1	55	24.8	68	39.4	94	48.9	121	55.8	153
6	15.6	55	25.4	69	39.9	95	49.4	123	56.3	155
7	15.8	55	25.6	68	40.5	96	49.7	123	56.7	157
8	16.0	55	26.0	69	40.6	96	50.1	125	56.9	157
9	16.1	54	26.5	69	40.9	96	50.3	125	57.2	158
10	16.4	55	26.5	68	41.1	96	50.5	125	57.4	159
	W= 35,0		W= 41,9		W= 48,8		W= 55,7		W= 69,7	
loading #	strain [%]	stress [kPa]	strain [%]	stress [kPa]	strain [%]	stress [kPa]	strain [%]	stress [kPa]	strain [%]	stress [kPa]
1	50.2	129	55.5	150	59.8	175	62.7	198	69.8	259
2	58.0	165	63.3	197	67.2	231	70.5	271	76.1	350
3	60.0	175	65.1	208	68.8	245	72.3	291	77.3	371
4	61.0	180	66.0	215	69.6	252	73.2	300	78.1	384
5	61.7	184	66.5	218	70.1	255	73.8	306	78.5	391
6	62.1	186	66.8	220	70.4	258	74.2	312	78.8	396
7	62.3	187	67.3	224	70.3	254	74.3	311	78.9	398
8	62.6	188	67.4	224	71.0	264	74.8	318	79.2	403
9	62.7	188	67.7	226	71.2	265	74.9	318	79.3	407
10	63.0	190	67.9	227	71.3	265	75.1	321	79.5	409
	W= 83,4		W= 96,3		W= 110,5		W= 123,7		W= 137,0	
loading #	strain [%]	stress [kPa]	strain [%]	stress [kPa]	strain [%]	stress [kPa]	strain [%]	stress [kPa]	strain [%]	stress [kPa]
1	74.3	331	77.9	407	81.6	498	83.8	614	85.4	721
2	79.9	460	83.0	570	86.0	700	87.8	878	89.3	1093
3	81.1	493	84.0	611	86.9	746	88.7	955	90.1	1188
4	81.5	504	84.6	633	87.4	777	89.0	978	90.6	1265
5	82.1	522	84.9	643	87.7	797	89.3	1002	90.6	1243
6	82.3	526	84.9	643	87.9	808	89.5	1031	91.0	1304
7	82.6	538	85.4	668	88.1	818	89.7	1050	91.1	1325
8	82.7	542	85.4	666	88.3	832	89.8	1061	91.2	1323
9	82.8	544	85.6	675	88.3	824	89.8	1054	-	-
10	82.9	543	84.9	676	88.4	832	90.0	1076	-	-

Table A.5. Continued

	W= 151,0		W= 163,6		W= 175,1		W= 188,3		W= 199,6	
loading #	strain [%]	stress [kPa]	strain [%]	stress [kPa]	strain [%]	stress [kPa]	strain [%]	stress [kPa]	strain [%]	stress [kPa]
1	87.9	868	89.8	1041	89.5	1216	92.4	1417	92.9	1653
2	91.1	1259	92.5	1510	92.4	1891	94.8	2033	95.0	2408
3	91.6	1339	93.1	1624	92.9	2041	95.3	2173	95.4	2554
4	91.9	1380	93.3	1652	93.3	2174	95.5	2262	94.9	2162
5	92.2	1417	93.6	1736	93.3	2140	95.9	2465	95.9	2805

Table A.6. Stress and strain reached at the end of each loading for different absorbed energy levels for PE 58 (unit of work, W, is kJ / cm^3)

	W= 3,95		W= 8,34		W= 17,0		W= 25,7		W= 34,5	
loading #	strain [%]	stress [kPa]	strain [%]	stress [kPa]	strain [%]	stress [kPa]	strain [%]	stress [kPa]	strain [%]	stress [kPa]
1	8.47	92	13.5	94	21.8	107	28.5	121	36.6	136
2	9.33	92	16.4	97	28.1	118	37.1	143	46.0	169
3	10.0	93	18.4	98	31.0	123	40.6	153	49.7	184
4	10.5	93	19.6	98	32.7	126	42.5	158	51.2	189
5	10.7	91	20.4	99	33.9	128	43.8	162	52.3	194
6	10.9	90	21.1	99	34.4	128	44.6	164	53.1	197
7	11.2	91	21.4	98	35.1	129	45.0	164	53.7	200
8	11.4	90	21.9	99	35.6	130	45.6	166	54.0	201
9	11.6	90	22.1	98	36.0	131	46.0	168	54.5	204
10	11.8	90	22.3	98	36.5	132	46.3	168	54.4	201

	W= 43,1		W= 51,6		W= 60,3		W= 68,9		W= 77,7	
loading #	strain [%]	stress [kPa]	strain [%]	stress [kPa]	strain [%]	stress [kPa]	strain [%]	stress [kPa]	strain [%]	stress [kPa]
1	42.8	156	47.6	176	53.5	201	57.4	228	60.8	254
2	52.5	199	57.8	234	63.3	274	67.2	322	70.2	366
3	55.7	217	61.0	257	66.0	301	69.7	354	72.9	412
4	57.2	225	62.5	269	67.3	315	70.9	371	74.0	432
5	58.1	231	63.5	278	68.3	327	71.7	383	74.7	443
6	58.9	236	64.1	282	68.8	331	72.2	389	75.3	458
7	59.4	238	64.4	283	69.0	332	72.6	395	75.5	459
8	59.7	239	64.7	286	69.4	336	73.0	404	75.9	468
9	60.1	242	65.1	290	69.8	342	73.1	403	76.2	477
10	60.4	243	65.5	293	70.0	345	73.3	405	76.5	482

Table A.6. Continued

loading #	W= 86,0 strain [%]	W= 86,0 stress [kPa]	W= 94,6 strain [%]	W= 94,6 stress [kPa]	W= 102,8 strain [%]	W= 102,8 stress [kPa]	W= 119,2 strain [%]	W= 119,2 stress [kPa]	W= 135,5 strain [%]	W= 135,5 stress [kPa]
1	63.8	285	66.8	319	68.9	354	73.7	441	77.4	537
2	73.0	421	75.4	478	77.4	545	81.4	710	84.3	886
3	75.3	471	77.6	539	79.6	620	83.2	810	85.9	1015
4	76.4	497	78.6	568	80.6	658	83.9	849	86.7	1086
5	77.1	513	79.3	589	81.2	683	84.6	898	87.3	1143
6	77.6	525	79.6	600	81.6	696	84.8	904	87.6	1162
7	77.8	528	79.9	604	82.0	714	85.2	936	87.9	1213
8	78.1	539	80.2	621	82.2	724	85.6	964	88.1	1217
9	78.3	543	80.4	626	82.4	730	85.8	981	88.3	1240
10	78.5	548	80.7	635	82.6	741	86.0	995	88.4	1251

loading #	W= 151,8 strain [%]	W= 151,8 stress [kPa]	W= 168,6 strain [%]	W= 168,6 stress [kPa]	W= 185,8 strain [%]	W= 185,8 stress [kPa]	W= 199,1 strain [%]	W= 199,1 stress [kPa]	W= 217,3 strain [%]	W= 217,3 stress [kPa]
1	80.4	654	82.8	785	84.9	942	86.6	1130	88.5	1310
2	86.6	1107	88.4	1347	89.9	1639	91.1	1988	92.7	2286
3	88.0	1271	89.8	1565	91.1	1912	92.2	2299	93.6	2639
4	88.7	1359	90.3	1652	91.7	2044	92.7	2467	94.2	2891
5	89.2	1445	90.8	1751	92.1	2148	93.1	2639	94.64	3399

REFERENCES

1. Gibson, L. J. and M. F. Ashby (editors), *Cellular Solid: Structure and Properties*, Cambridge University Press, Cambridge, 1997.

2. *Styropor Technical Information: Packaging*, BASF, Ludwigshafen, Germany, 2007.

3. *Cellular Polystyrene for Packaging–Requirements and Testing*, DIN 55471, 1983.

4. Rusch, K. C., “Load Compression Behavior of Flexible Foams”, *Journal of Applied Polymer Sciences*, Vol. 13, No. 11, pp. 2297-3311, 1969.

5. Rusch, K. C., “Load Compression Behavior of Brittle Foams”, *Journal of Applied Polymer Sciences*, Vol. 14, No. 5, pp. 1263-1273, 1970.

6. Rusch, K. C., “Energy Absorbing Characteristics of Foamed Polymers”, *Journal of Applied Polymer Sciences*, Vol. 14, No. 6, pp. 1133-1147, 1969.

7. Meinecke, E. A. and D. M. Schwaber, “Energy Absorption in Polymeric Foams-I. Prediction of Impact Behavior from Instron Data for Foams with Rate-Independent Modulus”, *Journal of Applied Polymer Sciences*, Vol. 14, No. 9, pp. 2239-2248, 1970.

8. Nagy, A., W. L. Ko and U. S. Lindholm, “Mechanical Behavior of Foamed Materials under Dynamic Compression”, *Journal of Cellular Plastics*, Vol. 10, No. 5, pp. 127-134, 1974.

9. Sherwood, J. A. and C. C. Frost, “Constitutive Modeling and Simulation of Energy Absorbing Polyurethane Foam Under Impact Loading”, *Polymer Engineering and Science*, Vol. 32, No. 16, pp. 1138-1146, 1992.

10. Chou, C. C., Y. Zhao, G. G. Lim, and G. S. Song, "A Constitutive Model for Polyurethane Foams with Strain-Rate and Temperature Effects", *SAE Technical Paper Series,* No. 980967, pp. 1-12, 1998.

11. Liu, Q. and G. Subhash, "A Phenomenological Constitutive Model for Foams Under Large Deformations", *Polymer Engineering and Science*, Vol. 44, No. 3, pp. 463-473, 2004.

12. Liu, Q., G. Subhash and X. L. Gao, "A Parametric Study on Crushability of Open-Cell Structural Polymeric Foams", *Journal of Porous Materials*, Vol. 12, No. 3, pp. 233-248, 2005.

13. Avalle, M., G. Belingardi and A. Ibba, "Mechanical Models of Cellular Solids: Parameter Identification From Experimental Tests", *International Journal of Impact Engineering*, Vol. 34, No. 1, pp. 3-27, 2007.

14. Miltz, J. and O. Ramon, "Energy Absorption Characteristics of Polymeric Foams Used as Cushioning Materials", *Polymer Engineering and Science*, Vol. 30, No. 2, pp. 129-133, 1990.

15. Avalle, M., G. Belingardi and R. Montanini, "Characterization of Polymeric Structural Foams Under Compressive Impact Loading by Means of Energy-Absorption Diagrams", *International Journal of Impact Engineering*, Vol. 25, No. 2, pp. 455-472, 2001.

16. Juntikka, R. and S. Hallstrom, "Weight-Balanced Drop Test Method for Characterization of Dynamic Properties of Cellular Materials", *International Journal of Impact Engineering*, Vol. 30, No. 5, pp. 541-554, 2003.

17. Shim, V. P. M. and K. Y. Yap, "Modelling Impact Deformation of Foam–Plate Sandwich Systems", *International Journal of Impact Engineering*, Vol. 19, No. 7, pp. 615-636, 1997.

18. Frew, D. J., M. J. Forrestal and W. Chen, “A Split Hopkinson Pressure Bar Technique to Determine Compressive Stress-Strain Data for Rock Materials”, *Experimental Mechanics*, Vol. 41, No. 1, pp. 40-46, 2001.

19. Sawas, O., N. S. Brar and R. A. Brockman, ‘‘Dynamic Characterization of Compliant Materials Using an All-Polymeric Split Hopkinson Bar’’, *Experimental Mechanics*, Vol. 38, No. 3, pp. 204–210, 1998.

20. Gray, G. T. and W. R. Blumenthal, ‘‘Split-Hopkinson Pressure Bar Testing of Soft Materials’’, *Mechanical Testing and Evaluation-Metals Handbook*, pp. 488–496, American Society for Metals, Ohio, 2000.

21. Chen, W., B. Zhang and M. J. Forrestal, ‘‘A Split Hopkinson Bar Technique for Low-Impedance Materials’’, *Experimental Mechanics*, Vol. 39, No. 2, pp. 81–85, 1999.

22. Chen, W., F. Lu and B. Zhou, ‘‘A Quartz Crystal Embedded Split Hopkinson Bar for Soft Materials’’, *Experimental Mechanics*, Vol. 40, No. 1, pp. 1–6, 2000.

23. Chen, W., F. Lu, D. J. Frew and M. J. Forrestal, “Dynamic Compression Testing of Soft Materials”, *Journal of Applied Mechanics*, Vol. 69, No. 3, pp. 214–223, 2002.

24. Gibson, L. J., M. F. Ashby, J. Zhang and T. C. Triantafillou, “Failure Surfaces for Cellular Materials Under Multiaxial Loads–I. Modelling”, *International Journal of Mechanical Sciences*, Vol. 31, No. 9, pp. 635-663, 1989.

25. Triantafillou, T. C., J. Zhang, T. L. Shercliff, L. J. Gibson and M. F. Ashby, “Failure Surfaces for Cellular Materials Under Multiaxial Loads–II. Comparison of Models with Experiements”, *International Journal of Mechanical Sciences*, Vol. 31, No. 9, pp. 665–678, 1989.

26. Deshpande, V. S. and N. A. Fleck, “Isotropic Constitutive Models for Metallic Foams”, *Journal of the Mechanics and Physics of Solids*, Vol. 48, No. 6, pp. 1253-1283, 2000.

27. Zhang, J., Z. Lin, A. Wong, N. Kikuchi, V. C. Li, A. F. Yee and G. S. Nusholtz, "Constitutive Modeling and Material Characterization of Polymeric Foams", *Transactions of the ASME*, Vol. 119, No. 3, pp. 284-291, 1997.

28. Zhang, J., N. Kikuchi, V. C. Li, A. F. Yee and G. S. Nusholtz, "Constitutive Modeling of Polymeric Foam Material Subjected to Dynamic Crash Loading", *International Journal of Impact Engineering,* Vol. 21, No. 5, pp. 369-386, 1998.

29. William, M. L., R. L. Landel and J. D. Ferry, "The Temperature Dependence of Relaxation Mechanisms Amorphous Polymers and Other Glass–Forming Liquids", *Journal of American Chemical Society*, Vol. 77, No. 14, pp. 3701-3707, 1955.

30. Deshpande, V. S. and N. A. Fleck, "Multi-Axial Yield Behaviour of Polymer Foams", *Acta Materiala*, Vol. 49, pp. 1859-1866, 2001.

31. Arcan, M., Z. Hashin and A. Voloshin, "A Method to Produce Uniform Plane Stress States with Applications to Fiber Reinforced Materials", *Experimental Mechanics*, Vol. 18, No. 4, pp. 141-146, 1978.

32. Moreu, Y. M. and N. J. Mills, "Rapid Hydrostatic Compression of Low-Density Polymeric Foams", *Polymer Testing*, Vol. 23, No. 3, pp. 313-322, 2004.

33. Cridland, L. and W. G. Wood, "A Hydrostatic Tension Test of a Brittle Material", *The International Journal of Fracture Mechanics*, Vol. 4, No. 3, pp. 277-285, 1968.

34. Faruque, O., N. Liu and C. C. Chou, "Strain Rate Dependent Foam Constitutive Modeling and Applications", *SAE Technical Paper Series,* No. 971076, pp. 221-229, 1997.

35. Chou, C. C., Y. Zhao, L. Chai, J. Co and G. G. Lim, "Development of Foam Models As Applications to Vehicle Interior", *SAE Technical Paper Series,* No. 952733, pp. 335-348, 1995.

36. Gilchrist, A. and N. J. Mills, “Impact Deformation of Rigid Polymeric Foams: Experiments and FEA modeling”, *International Journal of Impact Engineering*, Vol. 25, No. 8, pp. 767-786, 2001.

37. Mills, N. J. and A. Gilchrist, “Shear and Compressive Impact of PP Bead Foam”, *Cellular Polymers*, Vol. 18, No. 3, pp. 157–174, 1999.

38. Mills N. J. and A. Gilchrist, “The Effects of Heat Transfer and Poisson’s Ratio on The Compressive Response of Closed-Cell Polymer Foams”, *Cellular Polymers*, Vol. 16, No. 2, pp. 87–109, 1997.

39. Bilkhu, S. S., M. Founas and G. S. Nusholtz, “Material Modelling of Structural Foams in FEA Using Compressive Uniaxial and Triaxial Data”, *SAE Technical Paper Series*, No. 930434, pp. 1–7, 1993.

40. Masso-Moreu, Y. and N. J. Mills, “Impact Compression of Polystyrene Foam Pyramids”, *International Journal of Impact Engineering*, Vol. 28, No. 6, pp. 653-676, 2003.

41. *Abaqus 6.7 Theory Manual*, Simulia-Dassault Systèmes, 2007.